

UC San Diego

UC San Diego Electronic Theses and Dissertations

Title

Defect Mitigation in Additive Manufacturing under Low and High Energy Processing Conditions

Permalink

<https://escholarship.org/uc/item/8tx2v47r>

Author

Olumor, Ifeanyichukwu Donald

Publication Date

2023

Peer reviewed|Thesis/dissertation

UNIVERSITY OF CALIFORNIA SAN DIEGO
SAN DIEGO STATE UNIVERSITY

Defect Mitigation in Additive Manufacturing under Low and High Energy Processing
Conditions

A dissertation submitted in partial fulfilment

of the requirements for the degree of

Doctor of Philosophy

in

Engineering Sciences (Mechanical and Aerospace Engineering)

by

Ifeanyichukwu Donald Olumor

Committee in charge:

San Diego State University

Professor Eugene A. Olevsky, Co-Chair

Assistant Professor Elisa Torresani

University of California San Diego

Professor Marc Meyers, Co-Chair

Professor Garay Javier

Professor Jian Luo

2023

Copyright

Ifeanyichukwu Donald Olumor, 2023

All rights reserved.

The dissertation of Ifeanyichukwu Donald Olumor is approved, and it is acceptable in quality and form for publication on microfilm and electronically:

Co-Chair

Co-Chair

University of California San Diego

San Diego State University

2023

DEDICATION

To Kemka, my little man

TABLE OF CONTENTS

Dissertation Approval Page.....	iii
Dedication.....	iv
Table of Contents.....	v
List of Figures.....	xi
List of Tables.....	xix
Acknowledgements.....	xx
Vita.....	xxiii
Abstract of the Dissertation.....	xxv
Chapter 1	
Introduction: Additive Manufacturing.....	1
1.1. Selective laser melting.....	4
1.2. Binder/Solvent Jetting.....	6
1.2.1. Sintering of Binder/Solvent Jetting components.....	8
1.2.2. Sintering thermodynamics and kinetics.	9
1.3. Defects in additive manufacturing.....	10
1.3.1. Pre-process or powder related defects.	11
1.4. In-process related defects in SLM and B/SJ AM.....	17
1.4.1. Porosity in selective laser melting AM.....	18
1.4.2. Part distortion in laser powder bed fusion AM.....	20
1.4.3. Cracks in laser powder bed fusion AM.....	22
1.5. Defects in binder/solvent jetting AM.....	23
1.5.1. Porosity in binder jetting AM.....	23

1.5.2.	Part distortion in binder/solvent jetting AM.....	23
1.5.3.	Cracks in binder jetting AM.....	24
1.6	Post-processing-related defects.....	25
1.7	Defects characterization.....	26
1.8	Defects mitigation.....	29
1.8.1	Pre-printing defect mitigation strategies.....	30
1.8.2	In-printing defect mitigation strategies.....	32
1.8.3	Defects mitigation in selective laser melting.....	33
1.8.4	Defects mitigation in binder and solvent jetting.....	34
1.9	Post-printing defect mitigation strategies.....	36
1.10	Simulation and modeling of powder spreading in AM processes.....	37
CHAPTER 2		
	Research Incentives and Objectives.....	40
2.0	Research motivation/justification.....	40
2.1	Research objectives and Scope.....	40
2.2	Major research tasks.....	42
2.3	Dissertation format.....	44
Chapter 3		
	Optimization of Low Energy Based AM for Defects Free Parts.....	46
3.1	Binder jetting vs solvent jetting: Determining the best processing route.....	46
3.1.1	Materials and experimental methods.....	50
3.1.1.1	Powder pre-processing for BJ/SJ.....	50
3.1.1.2	BJ and SJ 3D printing processes.....	51

3.1.1.3	Post-BJ/SJ Debinding and sintering.....	52
3.1.1.4	Characterization of BJ/SJ-ed sintered components.....	53
3.1.2	Results and Discussions.....	53
3.1.2.1	Powder characterization/ BJ/SJ printing.....	53
3.1.2.2	Curing of BJ/SJ printed samples.....	54
3.1.2.3	Debinding analysis of BJ/SJ printed samples.....	55
3.1.2.4	Effect of printing parameters and processing route on the green density of BJ/SJ printed parts.....	57
3.1.2.5	Relative density of BJ/SJ-ed sintered SS316L components.....	59
3.2	Influence of powder morphology on BJ/SJ-ed green and BJ/SJ-ed sintered part density.....	60
3.3	Optimizing powder bed spreading in BJ AM: Experimentally validated modeling.....	64
3.3.1	Selection of deposited powder layer thickness in Binder Jetting.....	64
3.3.2	Powder spreading during binder jetting.....	64
3.3.3	Discrete element modeling of powder spreading in BJ.....	68
3.3.3.1	Parameters of particle interaction in BJ.....	68
3.3.3.2	Schematics of virtual experiments on BJ.....	70
3.3.4	Density evolution during powder spreading in BJ.....	72
3.3.5	Shape distortion during powder spreading with a blade.....	75
3.3.6	Shape distortion during powder spreading with a roller.....	78
3.3.7	DEM simulation of bimodal powder packing for improved packing density in BJ.....	79
3.3.8	Experimental verification of DEM simulation of BJ.....	80

3.4	Influence of powder size distribution on BJ/SJ-ed green and BJ/SJ-ed sintered parts density.....	86
3.5	Process optimization for the SJ process.....	89
3.5.1	SJ Materials and Method.....	89
3.5.2	S/N analysis from Taguchi DOE for the SJ optimization.....	91
3.5.3	Regression analysis of SJ.....	93
3.6	Pressure assisted solvent jetting.....	94
3.7	Chapter conclusions.....	98
Chapter 4		
	Optimization of High Energy Based AM for Defects Free Parts.	101
4.1	Qualitative examination of SLM printed SS316L single tracks.	103
4.1.1	Effects of SLM process parameters on printed SS316L single tracks.....	103
4.1.2	SLM Materials and Methods.....	104
4.1.3	Results and Discussion.....	105
4.2	Effect of laser dwell time on pore elimination in SLM of WC reinforced SS316L matrix composite: Experimentally validated modeling.....	108
4.2.1	Background to the study.....	108
4.2.2	SLM Materials and Methods.....	112
4.2.3	Setup of virtual experiment on SLM of WC reinforced SS316L matrix composite.....	115
4.2.4	Results and Discussion.....	117
4.3	Effect of volumetric energy density and laser dwell time on relative density of SLM processed bulk SS316L parts.....	127

4.3.1	Background to the SLM of bulk SS316L study.....	127
4.3.2	SLM of bulk SS316L experimental procedure.....	128
4.3.3	Results and Discussion.....	130
4.4	Process optimization for the SLM processing of pure SS316L parts.....	135
4.4.1	SLM Materials and Methods.....	136
4.4.2	Results and Discussion.....	139
	4.4.2.1 Relative density variation and S/N analysis from Taguchi DOE.....	140
	4.4.2.2 Microstructural analysis of SLM processed parts.....	143
	4.4.2.3 Regression analysis of SLM processing.....	146
4.5	SLM processing of WC-SS316L composite and functionally graded WC-SS316L system.	147
4.5.1	SLM Materials and Methods.....	148
4.5.2	Results and Discussions.....	150
4.6	Chapter conclusions.....	152
Chapter 5		
	Additive Manufacturing and Spark Plasma Sintering as Effective Routes for Manufacturing of SS316L and SS316L-WC Composites: A Comparative Study.....	154
5.1	Introduction to comparative study.....	154
5.2	Materials and Methodology utilized in comparative study.....	156
	5.2.1 Powders and powder preparation.....	156
	5.2.2 Selective laser melting.....	157
	5.2.3 Solvent jetting.....	158
	5.2.4 Spark plasma sintering.....	159

5.2.5	Characterization.....	161
5.3	Results and Discussions.....	162
5.3.1	Powder milling and flowability test.....	162
5.3.2	Sintering of solvent jetted samples.....	163
5.3.3	Relative density of SJ, SLM and SPS processed samples.....	165
5.3.4	Microstructure of samples.....	166
5.3.5	XRD analysis.....	171
5.3.6	Micro hardness of processed composite samples.	173
5.3.7	Property anisotropy in the SLM and SJ processed samples.....	174
	5.3.7.1 Microstructural anisotropy.....	174
	5.3.7.2 Tensile strength anisotropy.....	177
5.4	Chapter conclusion.....	178
Chapter 6		
	General conclusions.....	181
6.1	Summary of goals reached.....	181
6.2	Scientific and engineering novelty of the conducted work.....	184
	References.....	185

LIST OF FIGURES

Figure 1.1 Classification of AM techniques based on energy requirement (highlighted path represents techniques explored in this work)	2
Figure 1.2 Schematic of the SLM process.....	4
Figure 1.3 Schematic of the binder jetting process.....	6
Figure 1.4 Scanning electron microscopy image showing (a) balling effect in SLM-processed commercial pure titanium [66] and (b) lack of fusion porosity in SLM-processed SS316L (current work), with the red arrows indicating unmelted SS316L particles.....	20
Figure 1.5 A typical powder bed highlighting the various possible defects [85]	21
Figure 1.6 Schematic of the sintering behavior of monomodal and bimodal powder mixtures showing the mechanism of sintering anisotropy and crack introduction in a bimodal powder mixture [101]	26
Figure 1.7 Packing density variation with composition for a bimodal powder mixture [101].....	32
Figure 1.8 SLM processing map developed by Gong and his co-workers [117]	33
Figure 2.1 Schematic of the structure of the research.....	43
Figure 3.1 Printer set up for showing the attached colorpod run set up.....	49
Figure 3.2 SEM images of as received (a) SS316L powders and (b) Nickel powders.....	50
Figure 3.3 Images of printed samples (a) binder jetted SS316L cube, (b) solvent jetted SS316L cube, (c) solvent jetted Ni cubes, (d) solvent jetted SS316L gear and (e) solvent jetted SS316L wristwatch case.....	54
Figure 3.4 SEM micrographs of solvent jetted SS316L samples after curing (a) 90%SS316L, (b) 95% SS316L and (c) 99% SS316L.....	55
Figure 3.5 Mass loss profile of (a) binder mixture, (b) SS316L powder and (c) printed SS316L	

cube.....	56
Figure 3.6 SEM micrographs of sintered SS316L showing evidence of oxidation before debinding optimization.....	57
Figure 3.7 Effect of printing parameters on green density of printed parts (a) Solvent jetted SS316L, (b) Binder jetted SS316L, (c) Solvent jetted Ni and (d) Binder jetted Ni.....	58
Figure 3.8 Sintered SS316L after SJ and debinding (a) 99% SS316L cube, (b) 90% SS316L cube and (c) gear.....	59
Figure 3.9 SEM micrographs after spreading a single layer of the (a) water atomized powder (b) gas atomized powder (c) magnified image of the water atomized powder within the spread layer (d) magnified image of the gas atomized powder within the spread layer. Red arrows indicate binder.....	61
Figure 3.10 Water and gas atomized samples after printing and sintering at 1350 °C.....	62
Figure 3.11 SEM micrograph of etched (a) water atomized powder at 1250 °C (b) gas atomized powder at 1250 °C (c) water atomized powder at 1380 °C (d) gas atomized powder at 1380 °C. The red arrows indicate SiO ₂ impurities and yellow arrows indicate pores.....	63
Figure 3.12 Schematic of virtual experiment with powder spreading during binder jetting (a) blade spreader (b) roller spreader.....	70
Figure 3.13. Discrete Element model of powder bed and (a) blade (b) roller powder spreading....	71
Figure 3.14 Relative density distribution along powder bed in Layer 1 after spreading with different H _f for the fixed H _i =8.25d: a) narrow 8d blade; b) wide 40d blade.....	73
Figure 3.15 Effect of roller speed on packing density across spread layer.....	74
Figure 3.16 Shape distortion of previously glued powder elements:(a) general view of powder bed; (b) blue glued powder element and red free powder elements are shown.....	75

Figure 3.17 Distortion of bound powder elements after passage of wide blade.....	76
Figure 3.18 Distortion of the glued 12d-wide element after blade passage.....	76
Figure 3.19 Distortion angle as a function of parameters of deposited layer: a) distortion angle as a function of H_i for the fixed $H_f = 2.75d$; b) distortion angle as a function of H_f for the fixed $H_i = 8.25d$	77
Figure 3.20 Distortion of previously printed part resulting from various rotational speeds.....	78
Figure 3.21 Effect of roller rotational and translational speeds on the distortion of the previously printed layer for a fixed $H_f = 2.75d$	78
Figure 3.22 DEM modeling result of bimodal powder packing.....	79
Figure 3.23 Schematics of experimental set up (a) designed shape for printing (b) after printing, curing and depowdering.....	80
Figure 3.24 Different configurations of blade/sample thickness.....	81
Figure 3.25 Distortion (Layer shifting) of printed base for SS316L.....	82
Figure 3.26 Distortion angle vs final layer height for printed TNZT samples at different values.....	83
Figure 3.27 Samples printed with; (a) $U = 5$ at $H_f = 750 \mu\text{m}$ (b) $U = 15$ at $H_f = 750 \mu\text{m}$, (c) $U = 1$ at $H_f = 750 \mu\text{m}$, (d) $U = 3$ at $H_f = 750 \mu\text{m}$ (e) $U = 1$ at $H_f = 550 \mu\text{m}$, (f) $U = 3$ at $H_f = 550 \mu\text{m}$	84
Figure 3.28 Experimental and theoretical results for different U values for $L = 3 \text{ mm}$. Index e and m indicates experimental and modeling values respectively.....	85
Figure 3.29 particle size distribution of (a) unprocessed powder, and processed powder for the size ratios (b) 2.53 (c) 3.00 (d) 3.53.....	87
Figure 3.30 Effect of powder processing on green and relative densities of processed	

samples.....	88
Figure 3.31 SEM micrograph of samples processed with (a) unprocessed water atomized powder (b) processed with 15+53 μm size group bimodal powder. Yellow arrows indicate SiO_2 impurities and red arrows indicate pores.....	89
Figure 3.32 The main effects plots for the mean values of (a) relative density and (b) S/N ratio on the parameters investigated.....	92
Figure 3.33 SEM micrograph of fully sintered part after optimization.....	94
Figure 3.34 Schematics of the QIP process following [132]	95
Figure 3.35 Steps involved in the ex-situ pressure assisted solvent jetting.....	96
Figure 3.36 Samples (a) before compaction (b) after compaction with a single layer of powder above and below the sample during compaction (c) after compaction with several layer of powder above and below the sample during compaction.	98
Figure 4.1 Schematic of single-track printing process.....	105
Figure 4.2 SEM images of Single-track specimens processed on a copper substrate at (a) 200 mm/s (b) 600 mm/s (c) 1000 mm/s; and processed on a steel plate at (d) 200 mm/s (e) 600 mm/s (f) 1000 mm/s.....	106
Figure 4.3 SEM micrographs of polished and etched single track specimens on a steel substrate processed at (a) 200 mm/s (b) 600 mm/s (c) 1000 mm/s. Red arrows indicating partially or unmelted SS316 particles within the molten track.....	107
Figure 4.4 Printed single track, single layer specimens printed at (a) 200 mm/s (b) 600 mm/s (c) 1000 mm/s. Red arrows indicating areas with lack of fusion, and yellow arrow indicating the build direction.....	108
Figure 4.5 SEM micrographs of (a) SS316L powder (b) WC powder and (c) photograph of	

presentative composite single tracks after laser passage.....	115
Figure 4.6 SEM micrographs of single-track samples printed with 0.3 volume fraction WC for dwell times of (a) 2.5 ms (b) 1.65 ms (c) 1.25 ms (d) 1 ms (e,f) 0.85 ms. Red arrows indicate pores. The direction of the laser beam is into the plane.....	118
Figure 4.7 SEM micrographs of single-track samples printed with 0.35 volume fraction WC for dwell times of (a) 2.5 ms, (b) 1.65 ms, (c) 1.25 ms (d) 0.85 ms. Red arrows indicate pores. The direction of the laser beam is into the plane.....	119
Figure 4.8 SEM micrographs of single-track samples printed with 0.4 volume fraction WC for dwell times of (a) 5 ms, (b) 2.5 ms, (c) 1.25 ms (d) 0.85 ms. Red arrows indicate pores. The direction of the laser beam is into the plane for (a) and (b), and as indicated by the white arrows in (c) and (d).....	120
Figure 4.9 Effect of dwell time on pore sizes of single tracks with different vol fraction of WC.....	121
Figure 4.10 Kinetics of pore collapse for the various pore sizes considered.....	124
Figure 4.11 DEM simulation of powder packing (a) Powder packing of small and large particles (b) results with small particles removed (c) large particles allowed to settle freely (d) evolution of WC packing fraction over time.....	125
Figure 4.12 Effect of volume fraction of WC on critical time interval for pore-free laser treatment for the various initial pore sizes considered in model estimate and comparison with experimental observations.....	126
Figure 4.13 Effect of simultaneously varying E_{VH} , E_{VL} and dwell time on relative density of processed parts.....	130
Figure 4.14 Effect of varying E_{VL} at a constant E_{VH} , on relative density of processed parts.....	131

Figure 4.15 Effect of varying E_{VH} at a constant E_{VL} , on relative density of processed parts.....	132
Figure 4.16 Effect of varying E_{VL} and E_{VH} , at a constant dwell time on relative density of processed parts.	133
Figure 4.17 Effect of a constant E_{VL} and E_{VH} , and varying dwell time on relative density of processed parts when hatch spacing is not set equal to the laser diameter.....	134
Figure 4.18 Effect of a constant E_{VL} and E_{VH} , and varying dwell time on relative density of processed parts when hatch spacing is set equal to the laser diameter.....	135
Figure 4.19 Printed samples (a) Group A after depowdering (b) Groups B, C, D and E before depowdering.....	139
Figure 4.20 The main effects plots for the mean values of (a) relative density and (b) S/N ratio on the Parameters investigated.....	142
Figure 4.21 Select SEM micrographs of samples processed at 50 μm layer thickness.....	143
Figure 4.22 Select SEM micrographs of samples processed at 75 μm layer thickness.....	144
Figure 4.23 Select SEM micrographs of samples processed at 100 μm layer thickness.....	144
Figure 4.24 Select SEM micrographs of samples processed at 125 μm layer thickness.....	145
Figure 4.25 Select SEM micrographs of samples processed at 150 μm layer thickness.....	145
Figure 4.26 SEM micrograph of sample processed using the optimized processing Parameters.....	147
Figure 4.27 SEM micrographs of the (a) SS316L powder (b) WC powder.....	148
Figure 4.28 Schematic describing the SLM setup for the processing of functionally graded SS316L-WC (a) at start of printing (b) at the end of printing (c) actual powder bed in the build platform after sample removal.....	149
Figure 4.29 SEM micrographs of the processed (a) composites and functionally graded SS316L-	

WC (b) with un-optimized parameters (c) with optimized parameters.....	151
Figure 5.1 SEM micrographs of powders (a) SS316L (b) WC.....	157
Figure 5.2 Optimized parameters of the spark plasma sintering process.....	160
Figure 5.3 Composite powder mixture (a) before milling (b) after milling (c) during SLM powder spreading. Green and red arrows indicate SS316L and WC particles respectively.....	163
Figure 5.4 Sintered composite samples (a) sintering at 1380 °C for 4 H (b) sintering at 1300 °C for 4 H.....	164
Figure 5.5 Representative TGA data for pure SS316L and samples with various WC volume fraction additions.....	165
Figure 5.6 Final relative densities of processed samples.....	166
Figure 5.7 Micrographs of etched pure SS316L samples processed by (a) solvent jetting (b) selective laser melting (c) spark plasma sintering (d) spark plasma sintering for regions close to the graphite tooling.....	167
Figure 5.8 Micrographs of the various composite samples processed.....	168
Figure 5.9 SEM micrographs of 15%WC composite composition processed by SJ and corresponding EDS mapping data.....	169
Figure 5.10 SEM micrographs with the yellow lines representing lines across which EDS line scans were conducted for (a) the edge of the SPS processed pure SS316L samples (b) the center of the SPS processed samples with 15%WC composition (c) SLM with 15%WC composition.....	171
Figure 5.11 Selected XRD patterns of processed samples showing formation and growth of new phases for the different processing techniques.....	172

Figure 5.12 Effect of WC content on the micro hardness values of the processed samples for all manufacturing techniques investigated.....	173
Figure 5.13 SEM micrograph of SJ processed SS316L sample along cross-sections (a) parallel (b) perpendicular to the build direction of. Red arrow and dot indicate the build direction.....	174
Figure 5.14 Microstructural details of the SLM processed SS316L (a) parallel to build direction. The yellow arrow indicates the build direction and black arrow indicates the melt pool boundary. (b) perpendicular to build direction. The yellow dot indicates the build direction and black arrow indicates the melt pool boundary (c) high magnification image from (a). The yellow arrow indicates the melt pool boundary.....	175
Figure 5.15 Microstructure of the annealed SLM processed SS316L.....	176
Figure 5.16 Load vs extension curves for SLM processed samples with (a) tensile strength perpendicular to the build direction (b) tensile strength parallel to the build direction; SJ processed samples with (c) tensile strength perpendicular to the build direction (d) tensile strength parallel to the build direction.....	178
Figure 6.1 Flowchart of the completed work.....	183

LIST OF TABLES

Table 1.1 SLM processing parameters.....	5
Table 3.1 Effect of relative green density on final relative density of sintered part.....	60
Table 3.2 Properties of water and gas atomized powders.....	60
Table 3.3 Green and sintered relative density of processed samples.....	62
Table 3.4 Estimated relative densities for the processed and unprocessed powders.....	87
Table 3.5 Factors and levels implemented in Minitab 17 for the SJ optimization.....	90
Table 3.6 S/N ratio and relative densities of green parts obtained from Taguchi’s L ₉ Orthogonal Array for the SJ AM processing technique.....	91
Table 4.1 Printing parameters for single track experiments of WC-SS316L MMC.....	113
Table 4.2 Discrete element method parameters for the simulations.....	116
Table 4.3 SLM parameters for processing bulk SS316L.....	129
Table 4.4 Factors and levels implemented in Minitab 17 for the SLM optimization.....	136
Table 4.5 Result of the Taguchi DOE.....	137
Table 4.6 S/N ratio and relative densities obtained from Taguchi’s L ₂₅ Orthogonal Array.....	140
Table 4.6 S/N ratio and relative densities obtained from Taguchi’s L ₂₅ Orthogonal Array (Cont’d).....	141
Table 4.7 Optimized SLM process parameters at a constant laser power and hatch spacing.....	146

ACKNOWLEDGEMENTS

In the course of my PhD studies, I have enjoyed the tremendous support and mentorship of Professor Eugene A. Olevsky. I will always recall the first e-mail response I received from him as a prospective doctoral student, and the subsequent interview via skype. After that interview session, I knew that the mentorship I needed to be grounded in the science and engineering of powder technology would be readily available for me here at the SDSU Powder Technology Laboratory. I am happy to say that all my expectations were exceedingly surpassed! I therefore would like to say a very big thank you to Professor Eugene A. Olevsky for the opportunity to be a part of the Lab and his great mentorship.

My deep appreciation also goes to my co-advisor, Professor M.A. Meyers, whose valuable tutelage, discussions, and mentorship guided me through my PhD studies. I would also like to thank my committee members: Professors Javier Garay and Jian Luo, and Assistant Professor Elisa Torresani for their tutelage and guidance. I must especially thank Dr Maximenko for his highly constructive criticisms. A special thank you goes to all my colleagues at the SDSU Powder Technology Laboratory: Dr. Maximenko, Dr. Torresani, Dr. Geuntak Lee, Dr Woody, Miss Carrillo, Mr. Alberto, Mr. Runjian, and Miss Maria.

Lastly, I would like to thank my family for their full support and encouragement. My wife, Onyinyechi, whom I met during this period was a continuous source of inspiration and encouragement. Thank you for all you do. A big thank you to my mum for her prayers every night. To my dad and my siblings Chioma, Chukwubuzor, Chineye and Oluchukwu, thank you all for the encouragement.

Parts of Chapter 3 have been published in the Rapid Prototyping Journal (I.D., Olumor, L. Geuntak, and E. Olevsky, (2021), "Effect of process route on powder three-dimensional-printing of metal powders", Rapid Prototyping Journal, Vol. 27 No. 2, pp. 399-406). The dissertation author is the primary investigator and author of this paper.

Parts of Chapter 3 have also been published in the Powder Technology Journal (A.L. Maximenko, I.D. Olumor, A.P. Maidaniuk, and E.A. Olevsky, (2021), "Modeling of effect of powder spreading on green body dimensional accuracy in additive manufacturing by binder jetting", Powder Technology, Vol. 385, pp 60-68). The dissertation author is the primary experimentalist and co-author of this paper.

Other parts of Chapter 3 are being prepared for publication (I.D. Olumor, E. Torresani, A.L. Maximenko, E.A. Olevsky, (2023) "Pressure assisted binder jetting". Prepared for publication). The dissertation author is the primary investigator and author of this paper.

Parts of Chapter 4 have been published in the Journal of Materials Research and Technology, (I.D. Olumor, A.L. Maximenko, E.A. Olevsky, (2022), "Effect of laser dwell time on pore elimination in powder bed fusion of metal matrix composites: experimentally validated modeling", Journal of Materials Research and Technology, Vol 21, pp 4994-5003). The dissertation author is the primary investigator and author of this paper.

Parts of Chapter 5 have been submitted for publication in the Journal of Materials Science and Engineering: A (I.D. Olumor, M. Wiśniewska, E. Torresani, and E.A. Olevsky, (2023), "Additive manufacturing and spark plasma sintering as effective routes for manufacturing of AISI 316L Austenitic Stainless Steel-WC composites". Journal of Materials Science and Engineering: A. Submitted for publication). The dissertation author is the primary investigator and author of this paper.

Parts of Chapter 5 are also being prepared for publication (I.D. Olumor, E. Torresani, A.L. Maximenko and E.A. Olevsky, (2023), “Property anisotropy in SLM and SJ processed SS316L”. Prepared for publication). The dissertation/thesis author was the primary investigator and author of this paper.

VITA

- 2008 Bachelor of Science in Metallurgical and Materials Engineering, Obafemi Awolowo University, Ile Ife, Nigeria
- 2012 Master of Science in Materials Science and Engineering, Obafemi Awolowo University, Ile Ife, Nigeria
- 2023 Doctor of Philosophy in Engineering Sciences (Mechanical and Aerospace Engineering), University of California San Diego and San Diego State University, USA.
- 2018-2023 Research Scholar, San Diego State University, USA.

PUBLICATIONS

1. I.D. Olumor, A.L. Maximenko, and E.A. Olevsky (2022), Effect of laser dwell time on pore elimination in powder bed fusion of metal matrix composites: experimentally validated modeling, *Journal of Materials Research and Technology*, Vol 21, Pages 4994-5003.
2. A.L. Maximenko, I.D. Olumor, A.P. Maidaniuk, E.A. Olevsky, Modeling of effect of powder spreading on green body dimensional accuracy in additive manufacturing by binder jetting, *Powder Technology*, Vol. 385, Pages 60-68,
3. Olumor, I.D., Geuntak, L. and Olevsky, E. (2021), "Effect of process route on powder three-dimensional-printing of metal powders", *Rapid Prototyping Journal*, Vol. 27 No. 2, Pages 399-406.

4. I.D. Olumor, M. Wiśniewska, E. Torresani, and E.A. Olevsky, (2023), “Additive manufacturing and spark plasma sintering as effective routes for manufacturing of AISI 316L Austenitic Stainless Steel-WC composites”. Journal of Materials Science and Engineering: A. Submitted for publication.
5. Property anisotropy in SLM and SJ processed SS316L. Prepared for publication.
6. Pressure assisted binder jetting. Prepared for publication.

FIELDS OF STUDY

Major field: Engineering Sciences (Mechanical and Aerospace Engineering)

Studies in Sintering and Powder Technologies

Prof. E.A. Olevsky

Studies in Mechanical Behavior of Materials

Prof. E.A. Olevsky and Prof. M.A. Meyers

ABSTRACT OF THE DISSERTATION

Defect Mitigation in Additive Manufacturing under Low and High Energy Processing
Conditions

by

Ifeanyichukwu Donald Olumor

Doctor of Philosophy in Engineering Sciences (Mechanical and Aerospace Engineering)

University of California San Diego, 2023

San Diego State University, 2023

Professor Eugene A. Olevsky, Co-Chair

Professor Marc A. Meyers, Co-Chair

In recent times, research efforts have been focused on Additive Manufacturing (AM) technologies, be it high or low energy-based, due to the ability to produce very complex and near-net shaped components. The overall aim of any AM technique is to produce parts that have industrial applicability. However, additively manufactured parts exhibit low service life as a result of part failure during use. These part failures usually arise due to the presence of defects such as

excessive porosity, part distortion and property anisotropy. In order to meet the aspirations of using parts manufactured via AM without the fear of catastrophic failure, there is therefore the need for research efforts to be geared towards developing novel approaches to mitigating and eliminating unintentional defects in additively manufactured parts.

This body of research work aims to improve on the current understanding of the defect mitigation strategies in additively manufactured parts by contributing towards accelerating new discoveries of innovative approaches in eliminating detrimental defects in high and low energy AM processes. We explored the Binder/Solvent Jetting and the Selective Laser Melting AM technologies when considering low-energy and high-energy based AM processes respectively, with a focus on mitigating excessive porosity and part distortion defects.

Our approach to the research work was fundamental in nature, involving both experimental and analytical considerations from both a macroscopic and microscopic point of view and has taken the form of understanding the influence of process parameters on defect formation. We developed novel and innovative approaches to optimizing the AM processes for the production of defects free parts, and further systematically developed empirical relations between process parameters and output variables such as final part density and degree of distortion to help control defect formation from experimental observations and analytical considerations. For example, An empirical equation describing the distortion strain as a function of powder spreading parameters during binder jetting AM is suggested as an approximation of the numerical modeling results, while the results on selective laser melting of metal-matrix-composites show that the filling of the pores between rigid inclusions by the molten matrix is dependent on the laser dwell time, which in turn, depends on the volume fraction of ceramic reinforcement, initial pore sizes between

inclusions and materials properties of the matrix phase such as viscosity, surface energy and initial pore sizes between rigid inclusions.

Our developed process parameters were used with great success in manufacturing defects free AISI 316L austenitic stainless steel (SS316L) alloy, (SS316L)-WC and functionally graded (SS316L)-WC metal-matrix-composites. Furthermore, a comparative study was conducted to investigate the influence of the various AM processing route on the process-structure-property relationship of processed parts, with results indicating that due to the differences in the kinetics of the various processing routes investigated, different microstructures and hence mechanical properties can be realized.

Chapter 1

Introduction: Additive Manufacturing

Additive manufacturing (AM) is a term used to describe a collection of manufacturing technologies that involves the fabrication of parts in a layer-wise manner. This differs from other conventional manufacturing methods where parts are made by adding constituent materials all at once like casting or removing materials as in the case of machining [1]. The first recorded AM process, according to Akmal et al. occurred in the 1980's, where a UV-laser was employed in curing a polymer resin in a process now known as stereolithography [2].

There is currently a wide range of AM process techniques that are being used to manufacture parts made of polymers, metals, ceramics, and composites. These AM process techniques differ one from the other by the method in which the starting material is supplied, how these are consolidated, and the energy requirement for the process. According to the technical committees ASTM F42 and ISO 261, the common AM technologies can be classified into seven categories viz; binder jetting (BJ), powder bed fusion (PBF), directed energy deposition (DED), material jetting (MJ), Material extrusion (ME), sheet lamination (SL), and vat photopolymerization (VPP) [3]. Furthermore, these AM processes can be divided into two broad categories based on their energy requirements [4, 5], and this is represented schematically in Figure 1.1, with the highlighted paths indicating the case studies for the thesis.

On the one hand, high energy AM is a broad class of AM techniques that require quite a substantial amount of energy, usually to fuse starting materials together. One such method is the Powder bed fusion AM technique. The PBF is an AM technique in which the raw material is supplied through a bed of powder [6]. The powder is melted using a laser beam, as in the case of selective laser melting (SLM) [7] or sintered using a laser beam, as in the case of selective laser

sintering (SLS) [8]. These AM techniques are generally called laser powder bed fusion (LPBF). Another way to consolidate a powder bed is using an electron beam, called electron beam powder bed fusion (EPBF) [9]. Another well-known high energy AM technique is the so-called direct energy deposition, where powder or a metal wire is focused or fed respectively through a nozzle into the path of a laser beam, which then melts and deposits the molten feed material onto a substrate [10].

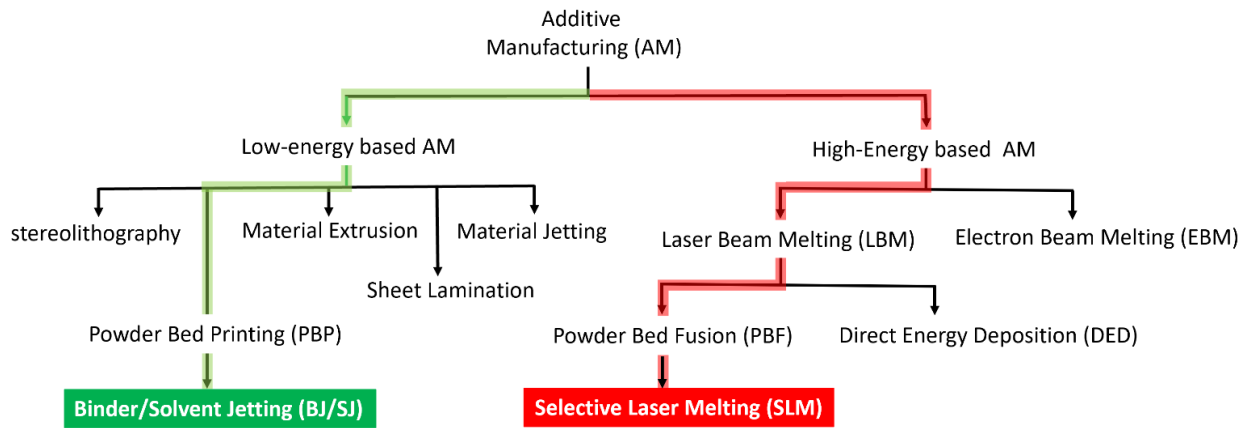


Figure 1.1 Classification of AM techniques based on energy requirement (highlighted path represents techniques explored in this work).

On the other hand, low energy AM techniques are those AM techniques that do not require high amount of energy input during the printing stage. One such method is the Binder Jetting (BJ), sometimes called the Solvent Jetting (SJ) AM technique, which like the PBF AM process is a powder-bed-based AM technology. The terms binder jetting and solvent jetting are seldom used interchangeably even though they describe slightly different techniques. The slight difference will be expatiated on in a subsequent section. However, for simplicity, we will refer to them as the Binder/Solvent Jetting (B/SJ) AM technique when speaking in general terms throughout this work.

Unlike in SLM, in the case of the B/SJ, the powder bed is not fused directly during printing, but instead the part consolidation is carried out in a different step, thereby effectively separating

the AM process into two stages; the printing stage and the consolidation stage [11]. In the printing stage, liquid binding agents are selectively deposited onto the build bed, based on a CAD model which is transmitted into the printing machine in the form of an stl file. After printing, a rather fragile part is made which is then cured to slightly increase its strength enough to be handled [12]. After curing, the printed part is de-powdered, a process that involves the removal of surrounding loose powder. The next step, known as the debinding and consolidation or sintering step is carried out. Here, the printed parts are subjected to thermal or sintering environments in order to consolidate the printed part [13].

In recent times, additive manufacturing of metals has drawn the attention of the manufacturing industry due to its ability to produce geometrically complex shapes, which hitherto was, and remains, a major challenge with the more conventional manufacturing processes like casting and the various forming processes that can include forging, extrusion and rolling [14]. Often, these conventional manufacturing processes are combined with subtractive processes like machining or additive processes like welding etc. in a bid to produce finished parts. Still, the complexity of parts produced by the combination of these different manufacturing processes do not compare to parts manufactured with a single additive manufacturing step [15]. Despite this advantage of AM processes over the more conventional manufacturing processes, the AM processes are faced with peculiar challenges, limiting their wide industrial applicability.

The AM techniques of interest in this work are the selective laser melting and the binder/solvent jetting techniques. The following sections will focus on these technologies, highlighting the current defects encountered by both techniques and defects mitigating steps being explored.

1.1 Selective laser melting

Selective laser melting is a PBF AM technology that can be applied to metals and non-metals like ceramics. Just like other AM technologies, SLM can be used to produce near net shaped parts. In this AM method, a computer-generated 3D file is aligned with processing parameters and sliced to several 2D files corresponding to the cross section of the parts after every given layer. This process is usually done using a computer software such as magics. The print process then involves the deposition and spreading of a powder layer over a build plate or previously printed layer according to a pre-defined layer thickness, followed by selectively melting the powder with a high energy laser beam in accordance with the cross section of each layer. After this, the build platform is lowered to a distance corresponding to the layer thickness and a fresh powder is spread over the melted layer. The process repeats itself until the entire 3D part is built. The SLM process is able to quickly build parts with highly complex shapes without the need for post process machining operations. Figure 1.2 illustrates the SLM process, highlighting the several process parameters.

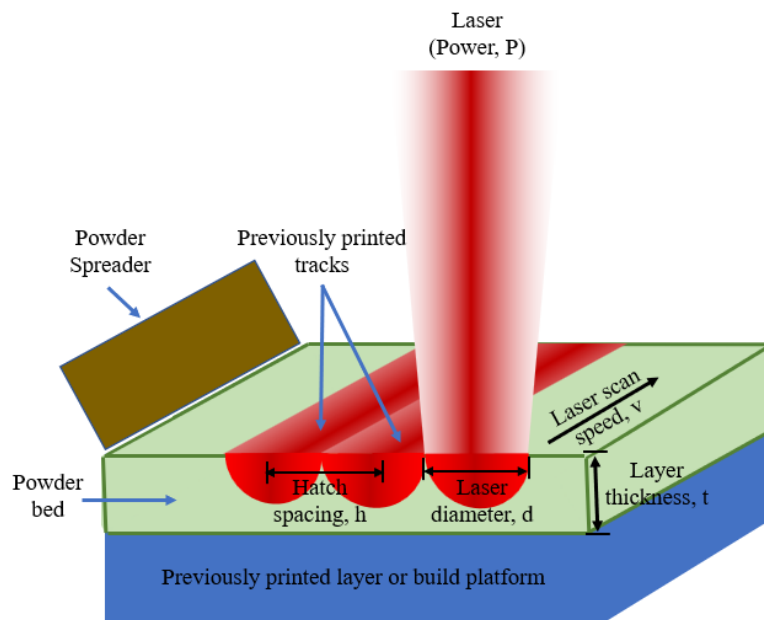


Figure 1.2 Schematic of the SLM process

In order to achieve a successful SLM process, several parameters must be taken into account. These parameters are generally classified into two broad categories viz i) materials related parameters and ii) processing related parameters. Table 1.1 shows the various parameters to be considered during SLM.

Table 1.1 SLM processing parameters

Materials related parameters	Process related parameters
Thermal conductivity	Laser power
Laser absorptivity	Laser scan speed
Particle morphology	Hatch spacing
Particle size distribution	Layer thickness
viscosity	Laser scan strategy
Surface tension/wettability	Temperature of build bed
Melting temperature	Atmosphere of build chamber
Chemical composition	Recoater speed

The important processing parameters involved in SLM include laser power (P), scanning speed (v), hatch spacing (h), layer thickness (d), and scanning strategy. These parameters are chosen in such a way as to ensure an appropriate and uniform energy density across the powder bed. Several expressions have been used to define the energy density during SLM. According to several authors [16-19], the energy density is usually expressed as a volumetric energy density with the expression:

$$E_v = \frac{P}{v.h.t} \quad (1.1)$$

where E_v is the volumetric energy density with a unit of J/mm^3

Some authors would substitute the hatch spacing, h for the laser diameter d while estimating the volumetric energy density. Other authors such as Jiang et al. [20] use the planar or surface energy density with units of J/mm^2 given as:

$$E_p = \frac{P}{v.h} \quad (1.2)$$

where E_p is the planar energy density

The expression of the energy density in equation (1.2) is particularly useful when dealing with single layer SLM processes. Furthermore, a few others [21, 22] have estimated the energy density as a linear energy density which is particularly useful when dealing with single track processes and expressed as

$$E_l = \frac{P}{v} \quad (1.3)$$

where E_l is the linear energy density with a unit of J/mm.

1.2 Binder/Solvent Jetting

ASTM F2792 defines binder jetting as “an additive manufacturing process in which a liquid bonding agent is selectively deposited to join powder materials”. This process is quite similar to the SLM, but instead of a high energy laser, a liquid binder jet, supplied through an inkjet printer head, is used to selectively bond powder particles on a powder bed as shown in Figure 1.3.

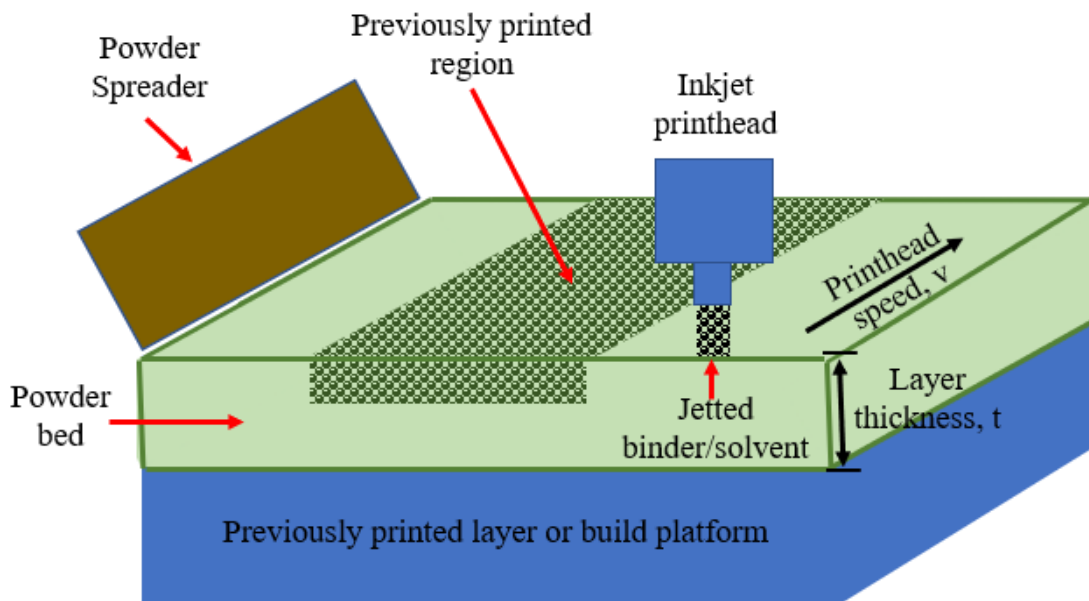


Figure 1.3 Schematic of the binder jetting process

The parts printed by B/SJ are very fragile as mentioned earlier and are referred to as green bodies. These usually need additional post printing steps like sintering, hot isostatic pressing (HIP) and liquid infiltration before the parts can be useful [11, 23]. The major and probably only difference between the binder jetting and the solvent jetting techniques is in the mode of the application of the binder. In the case of the binder jetting, a liquid polymeric binder is jetted directly from the inkjet printhead onto the powder bed, while in the case of the solvent jetting, a polymeric binder in granular form is premixed with the powder to be printed and spread on the build plate. A binder activator called the solvent is then jetted from the inkjet printhead onto the powder bed. The solvent, on contact with the binder particles, activates the binder which then binds the powder to be printed.

In very recent times, the B/SJ of metallic parts has been attracting the attention of both researchers and industrial partners. This is because of the advances in sintering science. Metal alloys like Inconel, several classes of stainless steels and nickel-chromium alloys, etc. have been successfully binder/solvent jetted and advances made to sinter them to near full density. Without fully consolidating B/SJ parts, their industrial applicability becomes limited to only applications that require a porous structure as in the case of certain biomedical applications. As such, for B/SJ components to find full industrial use, sintering becomes an important post printing step. To this end, several studies, both experimental and modeling, are ongoing to fully understand the sintering kinetics of B/SJ components.

Several models used in predicting the sintering behavior of green bodies produced by conventional powder technology methods such as metal injection molding (MIM) are being used to predict the sintering behavior of B/SJ components with varying degrees of success. One such model that has been quite successful is the Olevsky's continuum sintering model [24]. This model

has been used with great success to predict sintering kinetics and shrinkage anisotropy of B/SJ alloys and ceramic components [25-27].

1.2.1 Sintering of Binder/Solvent Jetting components

A very crucial step in B/SJ is the sintering step, without which the printed part has no engineering value, especially when it comes to structural applications. In this step, high temperature induced atomic diffusion helps for densification of printed green part. This densification results in improved microstructural and mechanical properties. Parts printed usually exhibit high levels of porosity which depends on the powder characteristics, spreading mechanism and other printing dynamics. These initial porosities can range from about 40% for metals to as high as 75% for ceramics. Because of this high level of porosity in printed parts, they exhibit high surface areas, thus the bid to reduce these surface areas serves as the driving force for sintering of the printed parts.

The sintering process can be divided into 3 stages viz: the initial, the intermediate and the final sintering stages [24, 28, 29]. The initial stage occurs at low temperatures with surface diffusion serving as the dominant mode of mass transport. In this stage, necks form between particles without any dimensional change or reduction in porosity. The next stage which is the intermediate sintering stage begins at higher temperatures and involves the growth of the previously formed necks [29, 30]. In this stage, atomic diffusion occurs across lattice and grain boundaries, resulting in significant densification of the part. The pore structure during this stage is interconnected. As the temperature is further increased, the porosity of the part is further reduced and the pores become isolated, leading to the final stage of sintering. In this final sintering stage, the pores are further reduced until full densification is achieved with the part exhibiting a well-developed microstructure. This final sintering stage is also characterized by grain growth [29, 31].

1.2.2 Sintering thermodynamics and kinetics.

The fundamental force driving the sintering process is the minimization of surface area and/or surface energy. In order for a porous body to reach a state of lower energy, mass transportation occurs between particles with the aim of minimizing the total free surface of the system. Just like in conventional powder metallurgy, in binder jetting, the morphology of the starting powder influences the densification behavior of the printed part. According to German [30] fine powder particle exhibits a higher driving force for sintering, resulting in densification occurring at lower sintering temperatures when compared with the sintering behavior of coarse powder particles.

The kinetics of sintering can be viewed from two broad mechanisms known as solid-state and liquid-phase sintering. During solid-state sintering, consolidation occurs in the solid state without formation of any liquid phase by heating the material below the solidus temperature. In this case, the diffusion-controlled mechanisms govern the sintering process. This is usually the preferred mechanism in sintering of B/SJ parts, as the integrity of the printed part is guaranteed. On the other hand, when the porous part is heated to temperatures above the solidus line, resulting in the formation of a liquid phase, the liquid phase sintering mechanism comes to effect. The mechanism that plays out during a sintering process is dependent on the chemistry of the materials involved and the sintering conditions. It is therefore important to fully understand the high temperature behavior of the material system being sintered in order to make the right choice of the sintering parameters such as heating rate, holding temperature and holding time etc.

As parts densify during sintering, these parts experience shrinkage. Reports have shown that for BJ parts, the shrinkage is anisotropic in nature [26, 27]. Several reasons have been attributed to this observed anisotropy, and one such reason is the layer-wise nature of the printed

porous part. It is postulated that because of the differences between inter-layer and intra-layer porosity and pore distribution, non-uniformity in densification occurs as sintering progresses, resulting in shrinkage anisotropy. Results have shown that there is higher part shrinkage parallel to the build direction when compared to shrinkage perpendicular to the build direction [32].

1.3 Defects in additive manufacturing

Additive manufacturing is still a budding technology, hence the processing-microstructure-property relationships are yet to be fully understood [33]. Just like all other conventional manufacturing techniques, AM techniques are associated with manufacturing defects which can lead to potential part failure during service. During AM processes, several defects are encountered which may be divided into three categories viz; 1) Pre-process or Powder-related defects [34]; 2) In-process-related defects which are peculiar to the AM techniques involved [35]; and 3) Post-processing-related defects [34, 36].

The pre-process related defects concern the defects associated with the starting powder material which are subsequently transferred to the manufactured parts. These defects are common to all powder-based AM techniques, and they include such defects that arise as a result of undesirable powder morphology, powder particle size/size distribution, powder surface contaminants and trapped gases within the starting powder particles leading to excessive powder porosity. On the other hand, both in-process and post-process defects are unique to the AM technique in question, and their features, properties and mode of formation are dependent on the process technique parameters. Hence to mitigate these defects, the process parameters for the given AM technique must be well understood.

1.3.1 Pre-process or powder related defects

In metal AM, the properties of the metal powder are very crucial factors in determining the success of a printing operation. Of particular interest are the mechanical and geometric properties of the powder. The mechanical properties such as the powder apparent/tapped density, internal porosity and flowability are generally influenced by the physical properties which include particle morphology and size/size-distribution [37]. To fully understand the influence of starting powder on properties of the final printed part, one must take a closer look at the starting powder characteristics or properties amongst which includes powder morphology, internal and surface porosity in starting powder, powder size & size distribution, powder flowability, and powder apparent/tapped density

a) Powder morphology

The particle morphology of any given powder influences its flowability and apparent/tapped density. The shape of the powder particles is dependent on its processing route. Usually, there are two very common ways of manufacturing powders for metal additive manufacturing which include gas atomization (GA) and water atomization (WA) [38]. Other less common methods of powder manufacturing for the purpose of metal additive manufacturing include plasma atomization (PA) and plasma rotation electrode process (PREP).

Generally speaking, PA and PREP powders are highly spherical in shape and exhibit very high surface quality, but are extremely expensive, while GA powders show some high level of sphericity, but with some surface irregularities [39, 40]. On the other hand, WA powders are very cost-effective powders with irregular shapes [41]. Studies have shown that the morphology of the starting powder affects the final density of manufactured parts because it influences the powder

bed topography uniformity [42]. To maximize powder bed topography uniformity, particle sphericity and smoothness must be improved on.

A study by [43] on the effect of moisture content on spreadability shows that powder morphology greatly influences the moisture absorptivity of a given powder. Powders with high moisture content leads to agglomeration and segregation during spreading. Their findings also show that spreading of such powders results in formation of distortion lines on the spread powder surface, leading to defective parts. Also, studies by Lerma et al. [44] show that powders with high sphericity and low surface roughness exhibits about 50% increase in packing density when compared to their counterparts with irregular shapes and rough surface finish.

b) Internal and Surface Porosity in starting powder

It has been shown that porosities within and on the surfaces of powder particles are usually transferred to the finished parts and are thus unwanted characteristics of the starting powder. Of the various powder morphology types, the WA powders have been shown to exhibit highest internal and surface porosity [42, 45]. GA powders also exhibit internal porosity to a lesser degree resulting from gases trapped within the solidifying powder particles [42]. Among the available powder types, the PREP powder exhibits the least internal and surface porosity [46]. One way of visualizing and characterizing internal porosity is by optical or scanning electron microscopy of polished cross sections of the powder particles [40, 47].

c) Powder Size & Size Distribution

Powders for additive manufacturing usually come in different sizes and size distributions. Powders will have varying size ranges depending on the synthesis method outlined previously. The aim in carefully selecting powder size and size distribution is to ensure excellent flowability

during powder bed spreading and ability to achieve high powder packing after spreading individual powder layers [48, 49].

A convention in LPBF is to select powders with average particle diameters less than the laser or electron beam diameter. Also, consideration should be given to the layer thickness when considering powder particle sizes. The current convention is to select powders with average particle diameters that are much smaller than the intended printing layer thickness.

Powders with a wide particle size distribution that also contains large number of fine particles usually encounter the so-called segregation effect during spreading. This is usually a problem encountered during the spreading of composite powders involving large rigid particle inclusions. Usually, when these inclusions are larger than 3 times the particle diameter of the matrix powder, they tend to segregate during powder spreading resulting in non-uniform distribution of the particulate reinforcements.

There are a few contradictory reports on particle segregation during powder spreading. For example, according to the results of Lemar et al [44] during powder spreading, large particles segregate near the beginning of spreading, while smaller particles segregate at the end, when the spreading blade approaches the other end of the build plate. Meanwhile, another study [50] shows that the smaller particles segregate at the beginning, leaving the larger particles to segregate towards the end of the spreading operation. In either case, segregation leads to poor powder bed uniformity and non-uniform powder bed density and must thus be avoided.

d) Powder flowability

To an extent, the flowability of metal powders determines their printability. Powders with poor flowability generally tend to be difficult to print. This is because poor flowability hinders good layer spreading during printing, resulting in un-even layer surface after powder spreading. To date,

there are limited studies on powder spreadability in AM, and as such, more experimental and theoretic efforts need to be focused on this aspect of AM. Currently, powders used in additive manufacturing come in either spherical or irregular shapes, and particle size distribution are usually either monomodal or bimodal. These powder properties influence the flowability of the powder. The ability of a powder to flow during AM is a very crucial factor because the powder supply rate through the powder feeder, spreading and packing efficiency depends on it [51].

Results have shown that the flowability of any given powder is very much dependent on the particle shape, size and size distribution resulting from the effect of surface friction between particles during powder-powder interaction as powder flows across the build area [52]. Thus, it's been argued that since fine powders have a larger apparent surface area when compared to coarse powders, they exhibit higher interparticle friction and hence lower flow characteristics [51, 53].

The presence of satellites, particularly with irregularly shaped WA powders also contribute to their observed poor flowability compared to the more regularly shaped GA and PREP powders due to mechanical interlocking between surface irregularities. One other factor that affects flowability is particle agglomeration resulting from high moisture content of the powder. Results have shown that powders with high moisture content are more susceptible to agglomeration resulting in reduced flowability [54].

Powder size distribution, morphology and surface features can also affect the powder efficiency as shown by Zhao and his coworkers [51]. Their work on Inconel 718 showed that flow efficiency is best with PREP powders due to the high particle sphericity and the thin surface oxide film, concluding that if the environmental factors are well controlled during powder handling, PREP has a natural advantage over GA in terms of flowability.

Another factor that influences the ability of a powder to form a uniform powder bed is the speed of the spreader. In the case of a spreading blade, results have shown that better uniformity of the spread layer is achieved with low translational speeds in the range of 80 mm/s [55, 56]. When considering the action of a roller, both the translation and rotational speeds come to play, as such, careful thought is given to the choice of the speeds to ensure the spreading of a uniform powder bed.

Several measuring techniques have been developed to measure powder flowability amongst which include Hall flowmeter, and Rheometer, amongst others. In the hall flowmeter measuring technique, the principle is such that the time taken for a fixed mass of powder to freely flow through a funnel with a given outlet diameter, known as the so-called Hall Flowmeter funnel, is used as an indication of how easily a powder flows. Usually, A mass of 50 g of powder is placed in a cone shaped funnel and allowed to freely flow out under the influence of gravity. The time taken for the powder to completely exit the funnel is noted and used to estimate the powder flow rate, using eq (1.4), known as the Hall Flow rate expressed as time per sample mass, following the ASTM B213 test method [57].

$$\text{Powder flowability (g/s)} = \text{mass of powder (g)/time taken to completely exit funnel (s)} \quad (1.4)$$

This value is used as an indication of flowability. On the other hand, another method used to indicate flowability known as the Rheometer employs the principles of the FT4 Freeman rheometer [56]. In this case, flowability of a powder is measured by the energy required to establish flow when a rotating blade moves either downwards (confined test) or upwards (unconfined test) through the powder and is measured as basic flowability energy (BFE) for confined test or surface energy (SE) for unconfined test, normalized by the powder mass and with units of mJ/g.

Results have shown that even though the results from the various flow measuring techniques can serve as useful indicators of flow properties, there have been inconsistencies in reported results. For example, results by Freeman [56] have shown that the inter-particle friction and particle-particle cohesive forces are not adequately explained by only one given method. In particular, he noted that the Hall Flow measurement is not sensitive enough to capture differences among different powders. Also, Clayton and coworkers also showed variation in measured flowability of powders with similar size distributions from different suppliers and manufacturing processes [58].

Snow and coworkers [59] have shown from their experimental work on powder spreadability during AM that the angle of repose is one of the best indicators of spreadability. Their results show that powder with lower angle of repose exhibit better spreadability as compared with those of high angle of repose. Also, they proposed that to improve the spreadability of powders with high angle of repose values, spreading should be carried out at very low translational speeds.

e) Powder apparent/tapped density

The apparent and tapped densities of a powder are important properties considered in powder technology and additive manufacturing. They are of importance because they serve as a measure of powder packing during powder spreading in additive manufacturing. The apparent density of a powder measures the fraction of space freely occupied by the powder particle in a given volume. This property may be measured by the use of a Hall Flowmeter funnel where the powder is allowed to flow freely under the influence of gravity through an opening and made to fill a container placed below, following ASTM B212 test method [60]. After filling is complete,

the mass of the powder and total volume of the container are measured and used to estimate the apparent density as follows;

$$\text{Apparent density} = \text{mass of powder/volume of container} \quad (1.5)$$

Tapped density, on the other hand, is a measure of a powder's ability to fill a container after a defined number of taps. Usually, tapping the container results in better consolidation of the powder, leading to an increased density compared to the powder's apparent density. This test simulates vibrations that may occur during the additive manufacturing processes. The difference between the apparent and tapped density values indicates the sensitivity of a powder to possible vibrations during the additive manufacturing processes [56].

1.4 In-process related defects in SLM and B/SJ AM

In the case of the SLM defects, in-process related defects resulting from the laser-powder interaction is the most common and pronounced means of defects formation during metal AM processing [61-63], and can include powder spreading anomalies, balling, lack of fusion porosity, keyhole porosity, microstructural inhomogeneity and impurities, loss of alloying elements, spattering, residual stresses, parts distortion, and surface finish roughness [35].

The major defect plaguing B/SJ is distortion and excessive porosity of green parts leading ultimately to undesirable physical and mechanical properties of finished parts. Part distortion generally occur during printing of the green part and can be retained in the finished part after post printing operations like sintering. It is also well understood in the field of powder technology that the porosity of green parts affects the eventual porosity of the part after sintering [28], therefore in order to optimize final part density, green density must be optimized. Several reasons account for the introduction of defects during B/SJ AM including insufficient or excessive binder saturation

[64], insufficient curing [13], effect of roller or blade motion [65], inherent porosity within powder feedstock [66], etc.

To fully mitigate part defects in B/SJ AM parts, consideration must be given to powder feedstock, printing parameters and post printing operation parameters. It's been shown by previous authors that printing parameters optimization is a necessity for defect free B/SJ AM parts. In particular, Lee et al., [67] Bai et al., [13] and Mostafaei et al.,[64] amongst others have shown that optimizing printing parameters such as layer height, binder saturation, powder spreading speed, etc, aid in producing defect free part. One important post processing defect that needs mentioning is oxidation of parts during debinding or sintering of BJ AM parts. This has necessitated the need for debinding and sintering optimization. In order to mitigate these defects, the temperature profile and atmosphere during debinding and sintering must be carefully selected [68, 69].

In both AM processes, patterned porosity must be avoided at all costs as cracks are easily propagated across such pore structures leading to catastrophic failure of parts. Results from previous authors [70, 71] have shown that shape, size, and location of pores affects the mechanical properties of parts manufactured via both B/SJ and PBF additive manufacturing processing techniques, and as such, must be avoided.

1.4.1 Porosity in selective laser melting AM

There are several types and origins of porosity in PBF AM and thus require different strategies to be mitigated. Generally, when dealing with metal alloys, three different types of porosity are observed in LPBF, namely, keyhole porosity, lack-of-fusion porosity, and gas porosity [72]. When dealing with metal matrix composites (MMCs), one key porosity that is often encountered is the porosity resulting from insufficient pore filling time [73]. In this work, we have

focused on pores resulting from lack of fusion in terms of alloy systems, and pores resulting from insufficient pore filling time in terms of MMC systems.

Several works have been done to investigate pores resulting from melting mode of the melt track. With the improper melting mode, phenomenon such as lack of fusion, balling and keyhole formation may result in excessive porosity within parts known as lack of fusion porosity, balling pores, and keyhole pores respectively. The origin for the formation of these pores has been given as; melt instabilities due to hydrodynamic factors [74], insufficient dwell time allowing melt spreading [73], and poor wettability resulting from oxidation [75].

Lack of fusion porosity has been shown to correlate with gaps in-between the melt tracks known as hatch spacing [76], thus the major cause of lack-of-fusion porosity is insufficient overlap between melt pools resulting in un-melted regions [77]. Another cause of LOF porosity as shown in recent studies is due to the interaction of ejected particles/spatter with the laser and meltpool [78]. Usually when Large spatter are formed and ejected during the powder fusion process, they may not be fully melted during subsequent laser interaction, thus becoming potential sites for pore formation. Hence, to mitigate these types of porosity, process parameters like hatch spacing, layer thickness, and scanning speed must be optimized. Examples of balling and lack-of-fusion porosity are presented in Figure 1.4 (a) [79] and Figure 1.4 (b) (this current work) respectively. In contrast, the keyhole porosity results from abnormalities in the meltpool dynamics such as a combination of fluid flow patterns and capillary instability, creating deep keyholes which may get cut-off, leaving behind large unfilled pores [80].

Another type of pore origin that warrants mentioning is gas porosity which results from the evaporation or sublimation of constituent elements or compounds that make up the melt composition due to excessively high processing temperatures [81]. Another reason for the

formation of gas porosity is entrapment of gases and other volatile matter within the melt pool and are characterized by their highly spherical shapes [40, 62].

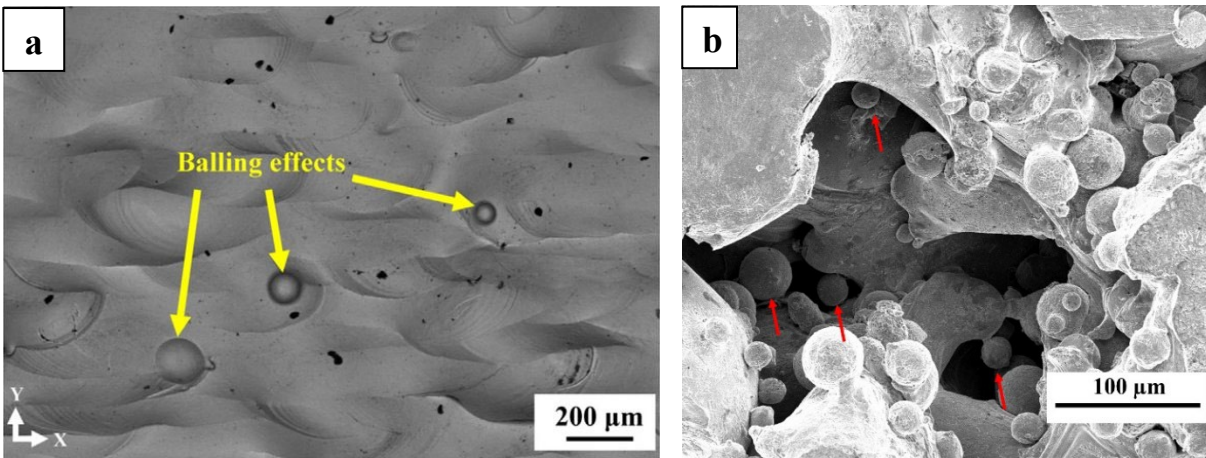


Figure 1.4 Scanning electron microscopy image showing (a) balling effect in SLM-processed commercial pure titanium [79] and (b) lack of fusion porosity in SLM-processed SS316L (current work), with the red arrows indicating unmelted SS316L particles.

1.4.2 Part distortion in laser powder bed Fusion AM

Part distortion is the bending or deformation of a part usually as a result of residual stresses due to the layered nature of LPBF [82]. The layering effect imposes compressive stresses on the top segments of the AM part, while imposing tensile stresses on the lower segments of the AM parts. With large enough stresses and improper or insufficient support structures, the part breaks off from the support structure and is distorted [83].

It has been estimated that about 70% of all metal AM failures result from physical distortion of the part during the printing process, leading to interrupted printing process [84]. Thermal stress has been attributed as the cause of these distortions. When these distortions are large enough, the distorted parts interfere with the recoater. When the recoater is made of a soft material such as silicone or rubber, the raised part of the distorted part interferes with the recoater, leading to damage to the recoater or even jamming of the recoater, resulting in printing of defective

parts (Figure 1.5) or even complete interruption of the printing process. Another cause of part distortion is insufficient support structure. When the support structures are insufficient, they detach from the part or build plate causing the part being printed to interfere with the recoater, leading to a failed printing process [82].

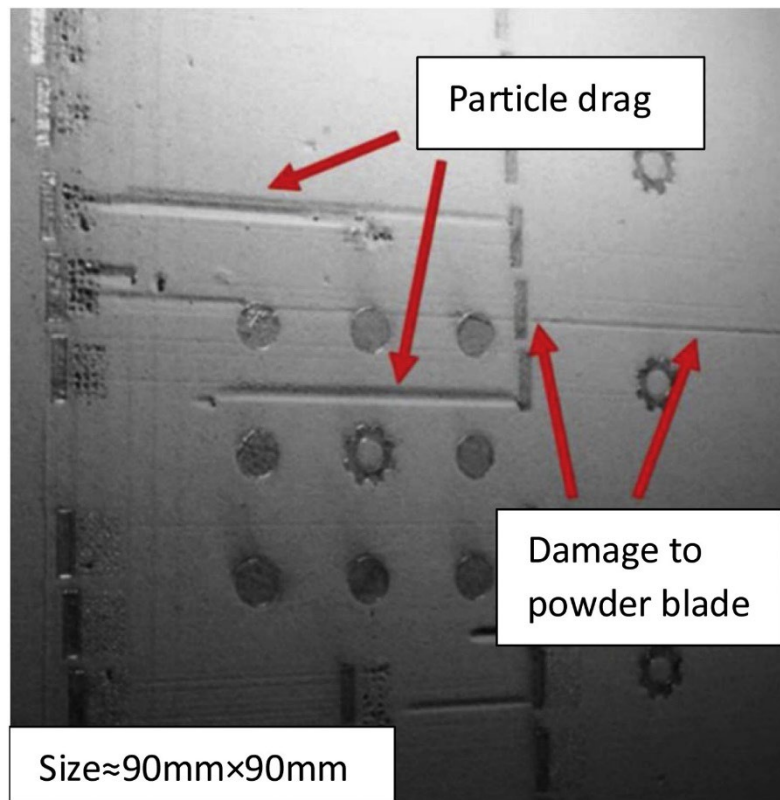


Figure 1.5 A typical powder bed highlighting the various possible defects [85]

During PBF AM, a situation known as powder short-feed may arise either as a result of depleted powder in the supply chamber or printer set to dispense too little powder from the powder supply unto the build platform [85]. In either case, the powder feeding mechanism delivers insufficient powder to completely fill the entire build platform. When this arises, regions towards the end of the build platform are left with little or no powder for the laser beam to melt, resulting in defective parts. Other causes of part distortion include distortions due to issues with inert gas

supply, leading to oxidation of printed part; unexpected power outage leading to inconsistencies in physical and mechanical properties of printed parts.

One way to minimize part distortion is to minimize residual stresses by either optimizing printing parameters or carrying out stress relieving thermal treatments either in situ by carrying out re-scanning operations [86] or via ex situ stress relief annealing [87].

1.4.3 Cracks in laser powder bed fusion AM

Cracks occur due to the segregation of solute or impurity elements within a melt pool as it solidifies. Two commonly attributed origins of crack formation in LPBF are solidification cracking and hot cracking [88]. Solidification cracking occurs due to thermal strain associated with non-equilibrium solidification conditions resulting when a liquid portion in a melt pool is trapped between already solidified material [89]. This becomes particularly pronounced in composite systems where rigid inclusions are intentionally added as in the case of metal-matrix-ceramics composites. Here, the ceramic inclusions serve as rigid pinning points for the liquid, resulting in large enough strains to cause cracking [90]. On the other hand, hot cracking occurs due to excessive strain from the thermal stresses resulting from reduced ductility of the solidified material [91]. Impurity oxide inclusions such as SiO_2 or intermetallic precipitates are other reasons for hot cracking to occur since they serve as potential sites for stress concentration.

Recent studies have also attributed observed cracks on PBF parts to coarse, elongated grain structure which is characteristic of PBF parts [92]. To ensure crack free parts, undesired inclusions must be avoided. Moreover, post processing operations like hot isostatic pressing can be carried out. Another approach to eliminating cracks is to carry out stress relieve heat treatment procedures on AM parts in order to eliminate the residual stresses which are the root causes of cracks.

1.5 Defects in binder/solvent jetting AM

1.5.1 Porosity in binder jetting AM

Binder jetting is a multi-step AM process involving steps such as printing, curing, depowdering, debinding and sintering. Of these process steps, the two that play the most role in determining the level of porosity in the final part are printing and sintering steps. During the printing step, just as in the case of PBF AM, the powder spreading parameters influence the powder packing efficiency and thus the porosity of the printed part. Printing parameters such as layer thickness, binder saturation level, speed of powder spreading, etc. have been shown to influence the level of porosity of the green parts [11, 23, 65, 93]. The porosity of the green part is usually transferred to the sintering step, thus it is important that printing parameters are chosen in such a way as to minimize the porosity of the green parts.

1.5.2 Part distortion in binder/solvent jetting AM

Part distortions in binder jetting are a major concern because the B/SJ parts are loosely held together during printing. Even though modeling investigations have shown that the roller or blade recoater motion over the powder bed affects the previously spread layers [94, 95], and even the previously printed parts, [96], there exists very limited experimental work to validate or disprove these model predictions. In the past, there has been very little interest in the AM community on the effect of powder spreading on the distortion of green parts because it is typically only experienced during B/SJ and absent in fusion-based AM technologies which are more predominant technologies compared to the more nascent B/SJ. However, as BJ begins to attract more attention in the AM research community, there is now the need to properly investigate and account for this phenomenon.

It has been reported that the motion of the spreading mechanism induces some level of dilation on the powder particles that are within the vicinity of the spreading mechanism [97, 98]. This localized dilation affects the packing density of the powder, and thus it therefore follows that different final layer heights of the spread powder will affect the packing of that layer. Indeed, both experimental and modeling results have shown that decreasing final layer height results in increasing layer packing and thus high printed part density which eventually translates to higher sintered part [99]. It follows therefore that with low packing density of printed green parts, larger part distortion and shrinkage will be experienced during sintering [26, 27].

In experiments conducted by Lee et al., [67] on 3D printing of alumina, results show that printing layers with a thickness greater than 2.5 of the average particle diameter results in poor dimensional accuracy after debinding and sintering. At the same time, it appears that the lower the final height of the deposition layer, the higher the impact of powder spreading on the distortion of previously deposited layers, thus a compromise must be reached by optimizing the printing parameters. Recent publications on binder jetting indicate that the optimal layer thickness for best part dimensional accuracy and minimal part distortion in previously printed layers is about 3.0 particle diameters [100].

Other than final layer thickness, other printing parameters that affects part distortion during green body printing in B/SJ AM includes translational speed of the recoater roller or blade, rotational speed of the recoater roller, adhesive strength of the binding medium and the mechanical stability of the powder bed, amongst others [11, 32].

1.5.3 Cracks in binder jetting AM

Cracks in binder jetting occur during the printing process and is transferred to the finished product. During printing, mechanical instability in the powder bed resulting from unwanted motion

may disturb the powder bed, leading to crack formation [100]. Another way cracks are introduced to printed parts during binder jetting is associated with the binder-powder particle interaction. When a binder is jetted onto a powder bed, capillary action aids the binder in filling the spaces between powder particles. As the binder dries or solvent evaporates with heating, powder particles attract and adhere to each other, as a result, stresses develop across the powder bed. These stresses can lead to cracks formation on the printed part [100]. Therefore, in order to prevent cracking due to capillary and thermal stress/strain effects, binder composition and chemistry along with printing parameters must be carefully chosen. Furthermore, because of the fragile nature of green printed parts, there is the possibility of cracks formation due to handling as material is transferred from the printer to the curing chamber, debinding chamber or the sintering furnace.

1.6 Post-processing-related defects

Post-process-related defects are more common to B/SJ processed components, as this AM technique requires post printing operations before they can be useful for engineering applications. Defects can be introduced to printed B/SJ parts during the curing, debinding and sintering post processes. Most of these defects come in the form of cracks and the introduction of impurities.

In the sintering step, inappropriate sintering parameters can lead to low final density or even cracks in processed samples. For example, on one hand, over sintering, i.e., sintering at higher than necessary temperatures and holding times, can cause the appearance of pores filled with gases and other volatile materials to expand, causing an increase in the pore sizes, and thus an increase in the overall porosity of the part. On the other hand, insufficient sintering i.e., sintering at low temperatures and/or holding times also leads to excessive porosity in finished parts.

German [101] have shown that sintering of a bimodal powder results in poor sintering as the small particles are constrained at regions close to the large particles, resulting in sintering

anisotropy or even introduction of cracks as illustrated in Figure 1.6 below. It thus follows that even though the use of bimodal powder leads to higher green densities, it also leads to poor sintering of the green part. Thus, a careful balance for the appropriate powder particle size distribution must be sought after to ensure that both high printed-green and final-sintered densities can be reached for B/SJ processed parts.

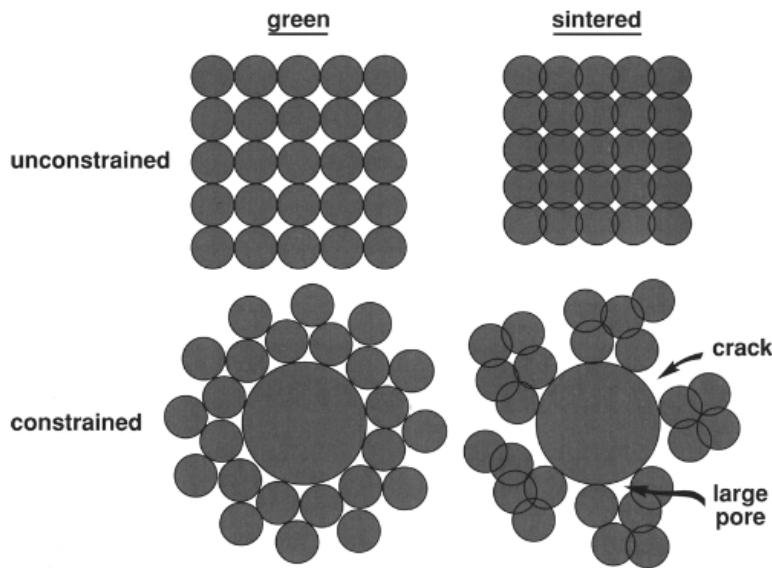


Figure 1.6 Schematic of the sintering behavior of monomodal and bimodal powder mixtures showing the mechanism of sintering anisotropy and crack introduction in a bimodal powder mixture [101].

SLM processes also experience some level of introduction of post-process-defects when post process exercises such as heat treatment and surface finishes are carried out. For example, in an attempt to mitigate residual stresses by stress relief annealing heat treatments, if care is not taken, parts could be subjected to oxidation.

1.7 Defects characterization

To fully understand and predict the behavior of parts during service, the part's physical and mechanical properties must be known, and correlated to its microstructure. To this end, several

research in recent times have been dedicated to the study of the macro and microstructural characterization of AM parts and how these are influenced by the AM processing parameters. Also, optimizations of AM process parameters have been carried out with the aim of minimizing part defects for better part performance in service [10].

Of the various forms of defects in AM processes, the ones that have gained considerable interests among researchers include excessive porosity and dimensional anomaly. These two types of defects can be found in both high and low energy AM techniques, while others of interest such as residual stresses and strains are more associated with high energy AM processes [87]. To fully understand these defects, one must be able to visualize/monitor and develop means of quantifying them by characterization.

There are several destructive and non-destructive ways of characterizing defects in AM. Characterization of defects can be done during the manufacturing process, known as the in-situ characterization [102] or after the manufacturing process has been completed, otherwise known as the ex-situ characterization [85]. The advantage of the in-situ characterization techniques is that defects formation is captured in real-time, and as such, steps can be taken to either correct it or stop the process, thereby saving time, energy and material.

There are three broad defects monitoring or visualization methods viz; Optical, thermal/infra-red, and x-ray computed tomography (x-ray/CT) scan, based monitoring methods. Optical methods are employed in either in-situ or ex-situ monitoring to visualize the powder bed during AM. Spectral analysis from spectral emissions during powder spreading may contain information that can be related to powder spreading defects such as recoater streaking, super elevation and incomplete spreading [103, 104]. The two major setbacks to optical based defect monitoring in AM are associated with non-optimal lighting of the build stage during in-situ

monitoring, resulting in poor visibility and the use of low-resolution cameras, resulting in low resolution images [105].

In the conventional ex-situ thermal/infra-red evaluation techniques, a stationary heat source such as quartz lamp or flash is employed to induce a temperature rise. Defects such as cracks, delamination damage, or voids obstruct the flow of heat causing a change in the transient heat flow response. In in-situ thermal/infra-red monitoring in such AM process as SLM, heat sensors such as an infra-red (IR) camera are used to monitor the temperature distribution across the powder bed as the laser melting process proceeds [102, 106]. An abnormal temperature reading usually indicates anomaly in the AM process which could be because of a defect formation.

Thermal imaging methods yield better resolutions in comparison to optical methods, thereby providing useful information on the fundamental correlation between process parameters, the melt pool temperature, and the part properties. There are drawbacks to these methods however, resulting from limited camera's angle of view, poor camera focusing, extreme temperature gradients and fast transient responses [107].

Synchrotrons have the ability to generate very high-energy x-rays (in the order of 100 keV), allowing for deep penetration into AM processed components, and when combined with efficient x-ray detectors, provides milli- to micro-second time resolution providing information on the melt pool dynamics and phase transformations occurring during and after solidification in SLM processing [108, 109]. For example, researchers at the Argonne national laboratory [110] successfully used in-situ high speed resolution synchrotron x-ray imaging experiments to study the dynamics and mechanism of pore motion and elimination during SLM. They find that the high thermocapillary force, induced by the high temperature gradient in the laser interaction region, rapidly eliminates pores from the melt pool.

Neutrons possess an even greater capability to penetrate metallic materials than high-energy x-rays because they do not possess any charges and thus only interact with atomic nuclei via the strong force. This has led researchers in more recent times to attempt with great success, to use neutrons to measure voids, phases, and residual stresses in AM parts, thus providing a better understanding of the processing-structure-properties relationships in AM parts [111].

To further underscore the importance of defect characterization in AM processes, the Minerals, Metals, and Materials Society (TMS) Advanced Characterization, Testing, and Simulation Committee in collaboration with the Additive Manufacturing Committee, sponsored a 4-day symposium for scientific discourse between AM researchers and synchrotron/neutron scientists at the 149th TMS Annual Meeting and Exhibition (San Diego, CA, February 2020). During this period, a broad range of scientific and engineering topics such as defects visualization, evaluation and quantification, microstructural evolution, etc. were discussed.

1.8 Defects mitigation

There is a growing body of work that is focused on developing effective AM process windows that are defined by parameters that dictate the presence or absence of LOF, balling and keyhole porosities in manufactured parts [104, 112]. When parts are printed using parameters within certain process window, there is a higher chance of mitigating porosities from these processes, and the only pores that would be present would be those transferred from the starting powder. Hence, making a right choice in selecting the appropriate process parameters, coupled with a careful selection of defect free starting powder, greatly increases the chances of manufacturing defect free parts [9, 74, 76].

To this end, special focus on eliminating LOF, balling and keyhole porosities in alloy systems will be placed on this thesis, along with examination of the role of laser dwell time in pore

elimination in laser melting of metal matrix composites. The aim is to manufacture parts with full density. By full density, we mean parts whose relative density can be quantified as $> 99\%$. The aim is to optimize processing parameters, reduce unwanted defects in SLM and B/SJ AM processed materials, and ultimately compare the microstructure and mechanical properties of parts processed within the developed process window defined by minimized defect microstructures.

Of particular interest in the current work are such defects as excessive porosity, part distortion or warping and cracking and how they are affected by the AM process techniques. To mitigate these defects, process parameters must be very carefully optimized as recent studies have shown that optimizing process parameters in order to mitigate a certain defect may inadvertently exacerbate another defect. As an example, in order to mitigate excessive porosity, residual stresses may be introduced into a finished part [36]. To this end, a thorough understanding of the process parameters and how they influence the integrity of finished parts must be investigated to ensure defects free parts. It must be mentioned that porosity in an AM part can sometimes be desirable if the application warrants a porous structure as in the case of certain biomedical applications [67]. But when it is not desirable, necessary steps must be taken during the AM process to reduce it to the barest minimum. In both instances, the pores must be quantified or characterized in order to properly predict the mechanical properties of the AM part. In this work, we have considered the pores as unwanted defects, and means to minimize them explored.

1.8.1 Pre-printing defect mitigation strategies

Most pre-printing defects mitigation strategies center on ensuring that the initial starting powder meets the requirements for AM, as such steps are taken to ensure that the powder has the right morphology and particle size distribution that will ensure optimal powder packing during powder spreading. Results have shown that the use of bimodal powder as opposed to unimodal

powder size distribution yields better packing of spread layers, resulting in higher green density of binder jetted parts and final part density of sintered binder jetted parts [70, 113]. Also results involving selective laser melting of components have also shown that the use of bimodal powders results in higher density of finished parts [48, 49].

When dealing with bimodal powders, consideration must be given to the particle size ratio of the large and small powders. German [114] and McGeary [115] have shown that for optimal powder packing, the size ratio of the large to small powder particles must be greater than 5 and the volume fraction of the small particles must be about 0.3 as is illustrated in Figure 1.7 where, f^* is the maximum packing of a bimodal powder mixture composed of two unimodal powders with initial packing fraction of f_s and f_L for the small and large powders respectively. The maximum packing occurs at an optimal volume fraction X^* . For typical size ratio range for AM, the relative apparent density of the bimodal powder goes up by about 15% from an apparent density of 55% for a unimodal powder size distribution to about 63% apparent density for bimodal powder size distribution [116].

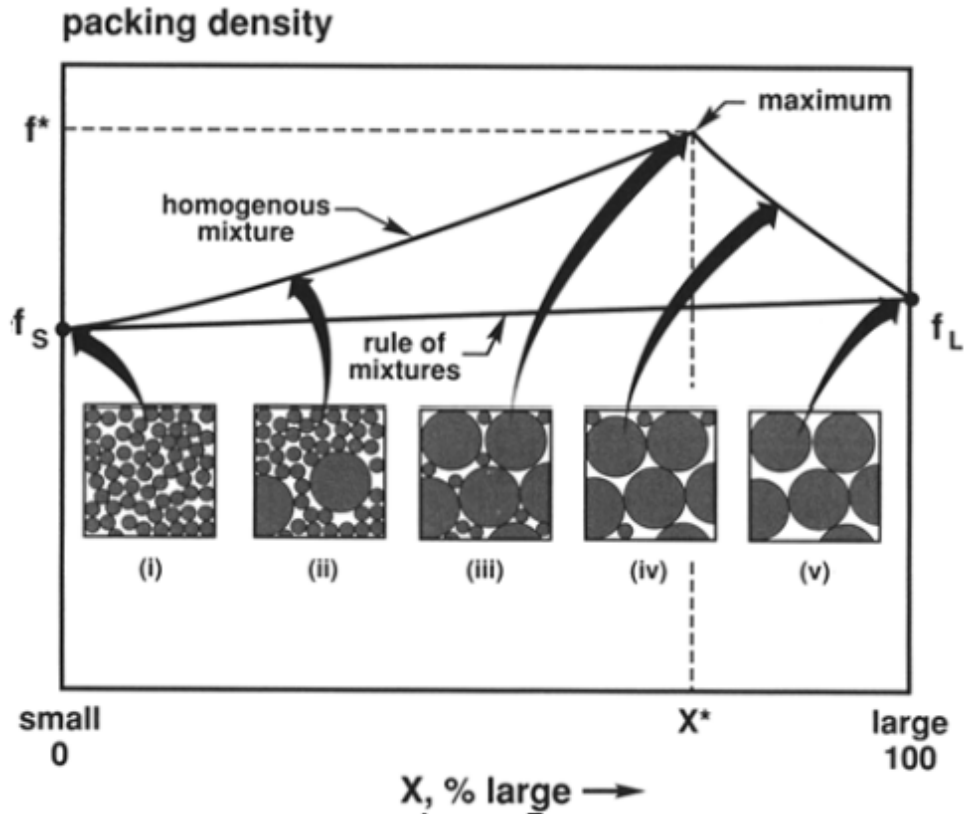


Figure 1.7 Packing density variation with composition for a bimodal powder mixture [101]

Particle size distribution inhomogeneity and segregation must be taken care of during the pre-printing process of powder spreading. Particle segregation is highly influenced by particle size distribution and powder spreading speed. To mitigate this phenomenon, the starting powder with the right particle size distribution, ratio and mixing volume fractions must be carefully selected to ensure a homogeneously spread powder layer.

1.8.2 In-printing defect mitigation strategies

Once the appropriate powder has been selected, powder spreading parameters and printing parameters must be optimized during the printing process to minimize defects in the printed parts. Increasing packing density of spread layer for both SLM and B/SJ and optimizing powder spreading parameters such as roller rotational speed and roller/blade translational speed must be fine-tuned to ensure a homogeneously spread powder layer.

1.8.3 Defects mitigation in selective laser melting

During SLM, printing parameters such as layer height, laser power, laser diameter, laser speed, and hatch spacing must be carefully selected to yield the right energy density unto the powder bed. Gong et al [117] showed that with the right energy density, fully dense parts can be processed. They presented a set of parameters (zone I in Figure 1.8) within which fully dense parts can be produced. Printing outside of these parameters could result in over melting or incomplete melting as presented in the set of parameters represented by zones II and III respectively in Figure 1.8.

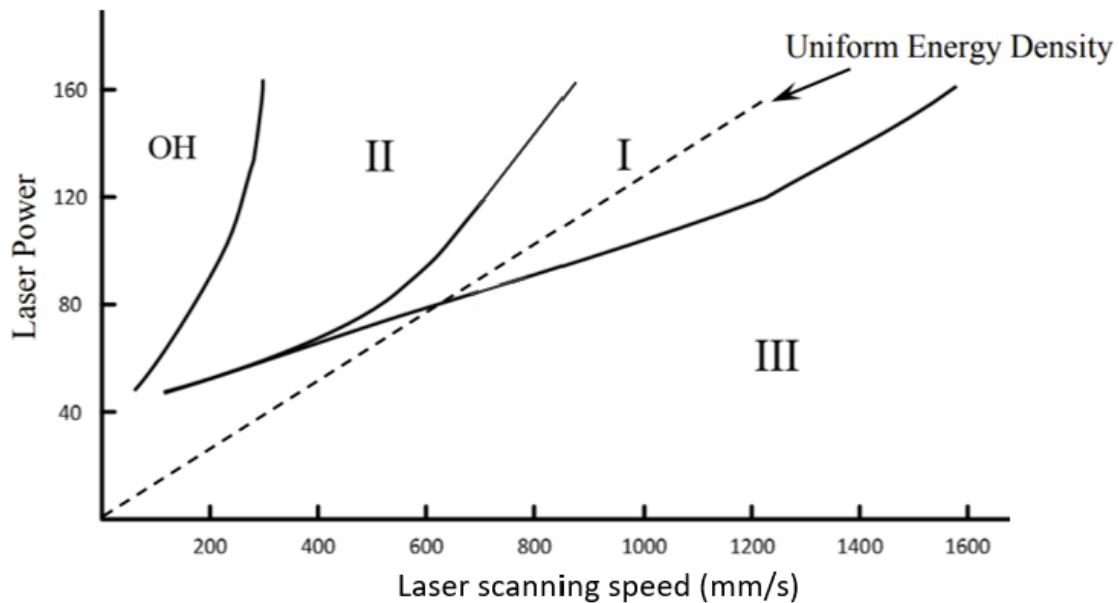


Figure 1.8 SLM processing map developed by Gong and his co-workers [117]

For example, relative density of 99.98 % was achieved for Ti-6Al-4V by manipulating the processing parameters during SLM i.e. using a high energy density input [18]. Also, increasing the laser heat input has been shown to reduce the formation of gas pores by decreasing the solidification rate, allowing gaseous phase to escape before the melt pool solidifies. Furthermore, Kobryn et al [118] found that both LOF and gas porosity decreased with increasing scan speed and

laser power. It has been shown that large hatch spacing, especially when greater than the laser beam diameter leads to insufficient overlapping of the melted tracks resulting in LOF porosity. Also, low laser power, high scanning speed and large layer thickness must be avoided as they lead to the so called balling effects which deteriorate the spreading of a new layer and may result in LOF porosity [16].

Scanning strategy means any specific scan pattern or exposure method that is used to influence a dependent variable during the LPBF process. This includes, but is not limited to, different vector, segment, or layer scanning methods. The scanning strategy which describes the laser scan pattern plays a significant role in residual stress formation and surface quality prints. Care must be taken when selecting the laser scan strategy in order to mitigate such defects as part distortion, delamination, and balling [82, 119].

Melt pool dynamics have a large influence on dimensional accuracy of finished parts, as such, there is the need to ensure a stable melt pool during SLM in order to minimize dimensional anomaly and other defects [120]. Several attempts have been made to correct defects just as they are formed by remelting the previously melted layer. In this defect mitigation method, in-situ monitoring combined with machine learning is employed to detect, classify and remedy defects just as they are formed during SLM [121, 122]

1.8.4 Defects mitigation in binder and solvent jetting

To achieve defect free B/SJ, printing parameters must be optimized. Such parameters include initial and final layer height, binder saturation, spreader rotational and translational speed. Unlike the SLM process where printed parts are fully dense, in the case of B/SJ, the printed parts are quite fragile, thus the amount of powder deposited and spread over the previously printed layer becomes very important. As such the amount of deposited powder must be such that distortion of

previously printed layers does not occur. The height of the initially deposited powder is referred to as the initial layer height, while the final height of the spread layer is called the final layer thickness.

To ensure optimal compaction of the spread layer, resulting in less porosity defect of the printed part, a final layer height of about 3 times the particle diameter is recommended [123-125]. Ensuring a powder bed with high packing density results in lower part distortion during post printing operations and must be encouraged. Furthermore, to produce defect free B/SJ, the speed of the spreader must be optimized. Results have shown that the rotational and more importantly translational speed of the spreader significantly affects the integrity of the printed part [23].

Improper binder saturation levels may result in dimensional inaccuracy and part distortion. For instance, excessive binder saturation results in slumping of the printed part, while insufficient binder saturation may lead to layer delamination, thus the optimal binder saturation must be used during B/SJ AM. Several works [126-128] have been done on optimizing the binder saturation amongst other parameters. For example, Wang et al [129] showed that two materials properties, powder bed porosity and the particle contact angles influences the binder penetration level, and thus the integrity of the printed part.

Just as in the case of the SLM AM process, there have been attempts to develop real time in-situ monitoring capabilities for the B/SJ AM technique. For example, Gaikwad et al. [130] developed a machine learning algorithm to monitor in-process binder droplet quality during binder jetting AM.

Other important factors like drying/curing temperature and time, and depowdering must be carefully selected to ensure that parts do not crack or distort during printing, handling, and transfer

to the next processing stage such as a sintering furnace. Results have shown that excessive in-process drying could result in insufficient inter layer adhesion and should thus be avoided [124].

1.9 Post-printing defect mitigation strategies

Post-printing defect mitigation strategies becomes particularly important in B/SJ because parts produced by these techniques require post printing operations such as depowdering, debinding, sintering, liquid phase infiltration, cold isostatic pressing and compaction amongst others before parts are fit for use. As such, during these post printing operations, necessary steps are taken to eradicate defects incurred during the printing stage and additional care should be taken to ensure that new defects are not introduced into the parts.

After printing B/SJ components, the green body should be handled with care during depowdering such as not to cause part deformation. Also, curing, debinding and sintering parameters such as heating rates, holding temperatures and time should be fully optimized to ensure defect free part. The curing, debinding and sintering atmospheres should also be carefully selected in order to mitigate defects resulting from part oxidation.

For SLM processed parts, one major post printing operation that is employed in mitigating defects such as residual stress is stress relief annealing [131]. For example, heat treatment procedures are routinely employed to homogenize the microstructure processed SLS and B/SJ AM components [83]. Results have shown that post annealing of AM part is capable of reducing residual stresses in AM processed components by about 70% [87].

Also, in order to mitigate defects associated with surface irregularities that impact surface integrity of both SLM and consolidated B/SJ part such as poor surface finishing and surface anisotropy, post-processing operations such as grinding, sand blasting, chemical polishing, shot peening and electropolishing are carried out [132-134].

1.10 Simulation and modeling of powder spreading in AM processes

Defects like excessive porosity in the starting powder bed and distortion in printed layers (particularly in the case of B/S J) get inherited by the final product. There is therefore the need to closely examine the influence of powder spreading on powder packing and distortion of previously printed layers during AM, hence the need for modeling of the powder bed. The complexity of the AM processes and wide range of length scale dictates the modeling techniques. In modeling AM processes, there are usually 3 modeling techniques based on the length scales involved [135]. Firstly, there is the micro-scale modeling technique which involves modeling of components with dimensions in the micro-meter length scale, i.e with dimensions in the range 100 nm to 100 μm [136]. Secondly, there is the meso-scale modeling technique which considers components with dimensions in the range of about 0.1 mm to 5 mm length scale [137]. And thirdly, there is the Macro-scale modeling technique that is employed during the modeling of components with dimensions greater than 0.5 mm [138]. The meso-scale modeling technique fills the gap between micro and macro modeling and has a length scale that overlaps both.

A few other reasons why modeling is useful in the AM process include the need to reduce the cost and time associated with optimization experiments and to provide an insight into the underlining physics of the various aspects of the AM process [33]. Several aspects of the SLM have been modeled and include i) powder deposition and spreading, and ii) laser-powder interaction [139]. In the case of the B/SJ, aspects modelled include i) powder deposition and spreading ii) binder-particle interaction and iii) sintering [100]. In both SLM and B/SJ cases, it is evident that powder deposition and spreading is unique and very crucial as the success of the process heavily depends on it, to this end, several modeling techniques have been employed in

modeling powder spreading in SLM and B/SJ. One such modeling technique is the Discrete Element Modeling (DEM) technique [94].

DEM has been widely used to investigate particle-spreader and particle-particle interactions. In the DEM models, the effects of various contact forces are estimated and used to estimate the motion and position of particles. For example, the instantaneous translational and rotational accelerations of particles could be determined using the following expressions:

$$m \frac{d^2x}{dt^2} = \sum F_i + F_G \quad (1.6)$$

$$I \frac{dw}{dt} = \sum M_i \quad (1.7)$$

where $\sum F_i$ is the sum of all particle-particle interaction forces, F_G is the gravitation force, $\sum M_i$ is the sum of all the torques, x is the position of the particle center, w is the angular velocity of the particle, m is the mass of the particle, and I is the momentum of inertia of the particle.

Solving for the translational/rotational acceleration for each particle yields the translational/rotational speed and hence the position. The relative position of each particle is then used in computing the particle parking density. In solving the translational/rotational acceleration of each particle, the attractive and non-attractive contact forces between particles and between particle and spreader, where the spreader is considered a particle with an infinite mass and radius, are taken into consideration. To calculate the non-attractive forces, several models including soft particle model, continuous potential model, linear viscoelastic model, and non-linear viscoelastic model can be used [140, 141]. While to estimate the attractive forces, models like the Hertz-JKR or the Hertz-mindlin models are used [142].

During powder spreading modeling/simulation, spreading parameters such as rotational and translational speed, geometry of the spreader, initial and final layer thickness, amongst others are taken into account. The effects of these parameters on the spread layer quality when factored in with the particles-laser interaction, as in the case of SLM or with the particles-binder interaction, as in the case of the B/SJ gives an insight into the quality of the printed part.

Miao and coworkers [71] have investigated the effects of roller diameter and layer thickness on the packing fraction of a spread powder layer. Their result shows that increasing the roller diameter increases the powder bed packing fraction for a fixed layer thickness, while decreasing the layer height for a fixed roller diameter also led to an increased powder bed packing fraction. Also, several works have shown that increasing the rotational and translational spread of the spreader leads to poorly packed powder bed with high surface non-uniformity. Furthermore, results have shown that spreading with a roller produces better spreading results as opposed to spreading with a blade [95, 96].

CHAPTER 2

Research Incentives and Objectives

2.0 Research motivation/justification

Currently, the service life of additively manufactured metals and alloys is considerably low compared to their wrought counterparts and exhibits significant defects in terms of excessive porosity, part distortion and property anisotropy, limiting their wide scale industrial application. There is therefore the need for additional research efforts towards developing novel approaches to mitigating and eliminating unintentional defects in additively manufactured parts. It is hoped that this research work will help to improve on the current understanding of the defect mitigation strategies in AM parts and contribute towards accelerating new discoveries of innovative approaches in eliminating detrimental defects in high and low energy AM processes, with particular emphasis on selective laser melting and binder/solvent jetting.

2.1 Research objectives and scope

The previous sections have presented a general outlook on past studies and current questions on SLM and B/SJ AM that need answers. Answering these questions are very important for developing effective defect mitigation strategies, particularly for excessive porosity and parts distortion in high and low energy AM processes. To the best of the author's understanding, there is no current work from literature that has been conducted to directly compare the properties of parts processed via SLM and B/SJ.

With the above in mind, the primary objective of this body of research work is to investigate ways for defect mitigation in low and high energy AM processes, while the secondary objective is to carry out comparative studies on these two AM processes in terms of the microstructure and mechanical properties of parts manufactured via these processes. The overall

goal of the research work is the optimization of high and low energy AM of selected alloys and composites.

The scope of the research will be limited to the binder jetting and solvent jetting techniques in the case of low energy AM process and selective laser melting in the case of high energy AM process. Materials of choice include SS316L alloy, WC reinforced SS316L matrix composite, and functionally graded SS316L / WC system. The investigations are primarily fundamental in nature, and a natural starting point for the thesis work are the studies conducted previously by Maximenko and Olevsky [73], Olevsky [143], Olevsky et al. [24] and Lee et al. [67].

The research topic has been approached experimentally from both a macroscopic and microscopic point of view. For example, part dimensions and Archimedes' density measurements, which are essential macroscopic techniques have been employed to probe part distortion and density respectively. On the other hand, scanning electron microscopy, x-ray diffraction and micro indentation techniques have been utilized for microstructural analysis.

Here, it should be mentioned that a new selective laser melting machine, the Xact Metal XM200C printer (Xact Metal, Inc. Pennsylvania, USA); the Anton Paar PSA 1090 (Graz Australia) particle size analyzer; and the Anton Paar Ultrapyc 5000 pycnometer (Graz Australia), were all recently acquired by the San Diego state university powder technology lab for this work. Moreso, the binder jetting ZPrinter 450 machine (Z-Corporation, now 3Dsystems Inc., South Carolina, USA) has been modified to print metal powders and fitted with a special structure to allow for pressure and heat application on the powder bed. Combining pressure and heating makes the binder jetting printing unique and an integral part of this Ph.D. work.

2.2 Major research tasks

In order to achieve the formulated research objectives, the following main tasks have been carried out:

1. **Discrete Element Modeling (DEM) of powder bed:** discrete element modeling has been employed to simulate and model part distortion due to powder spreading during B/SJ AM, optimal powder particle size distribution for low porosity defects and pressure assisted B/SJ for low porosity defects and maximum inclusion packing in composite systems in SLM melt pool.
2. **BJ Printing Optimization:** Optimization experiments using the Taguchi optimization method has been carried out to determine optimal printing process for low porosity defects and minimal part distortion. A novel B/SJ process involving the application of pressure for powder bed compaction has been explored for possibility of improved green body packing without significant part distortion.
3. **Sintering Optimization:** Optimization of debinding and sintering temperature, time and atmosphere has been carried out with the aim of mitigating oxidation and high porosity defects of final parts processed by B/SJ AM.
4. **SLM optimization:** This has included single-track/layer and multiple-tracks/layers experiments involving selected alloy and composite systems. The Taguchi optimization method has also been employed for process optimization. Experiments have been conducted to validate/improve on existing model put forward by Maximenko and Olevsky for predicting the pore filling time for a pore free composite system processed via SLM.

5. **Comparative studies:** This has involved microstructural characterization and mechanical properties tests and comparison between B/SJ and SLM processed samples. To add more context to the comparison study, a powder-based non-additive manufacturing technique, the spark plasma sintering, is also considered in comparison to the other two additive manufacturing techniques.

A schematic of the structure of the conducted research is presented in Figure 2.1.

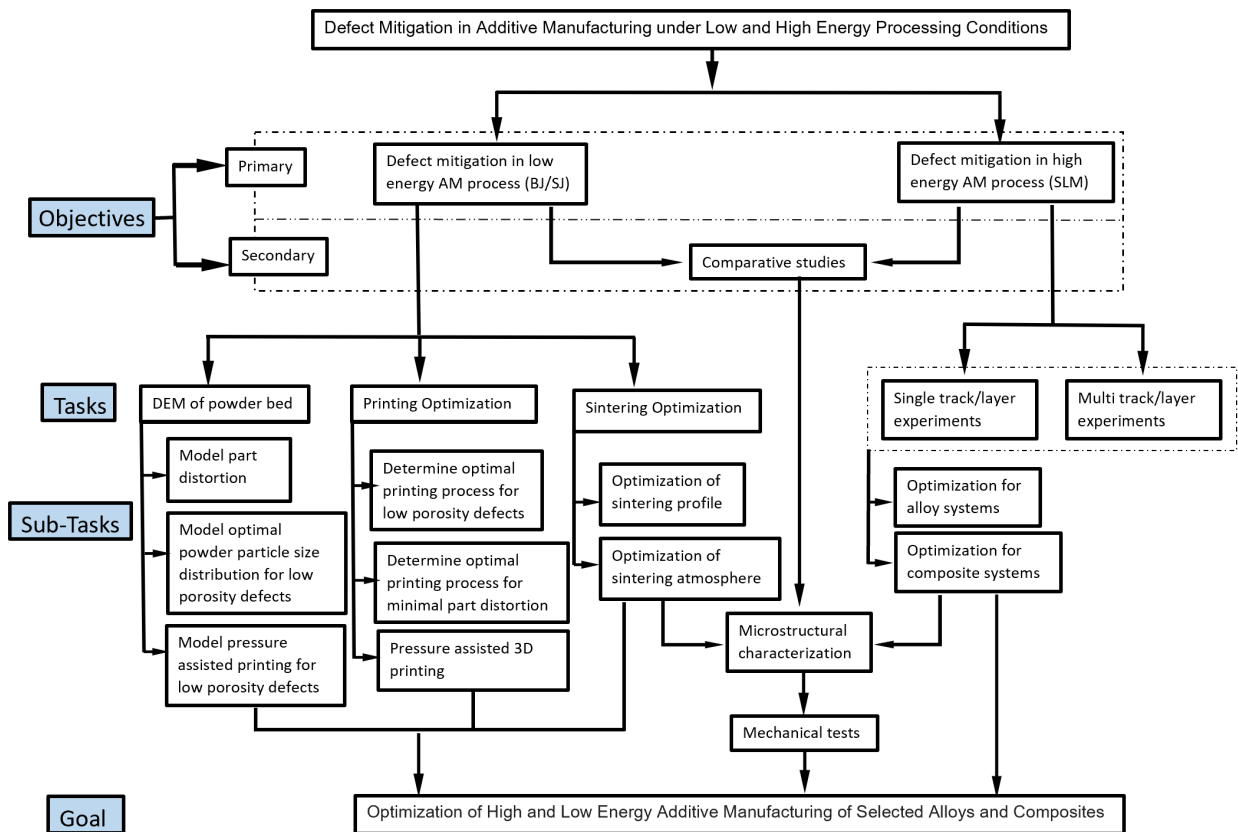


Figure 2.1 Schematic of the structure of the research

2.3 Dissertation format

This dissertation is prepared using a multiple-paper format. Three published papers, one submitted paper and two papers in preparation for publication are employed to describe the research results, discussions and conclusions based on the research goals and objectives mentioned in the previous section.

Chapter 1 is a literature review on the current trends in defects mitigation strategies in additive manufacturing, with an emphasis in selective laser melting and binder/solvent jetting additive manufacturing techniques.

Chapter 2 details the overall research goals, objectives, and scope of the dissertation. The major research tasks undertaken to achieve these research objectives are highlighted.

Chapter 3 presents research results on the optimization of the binder/solvent jetting additive manufacturing technique for defects free manufacturing of stainless-steel parts. Parts of Chapter 3 have been published in the Rapid Prototyping Journal (I.D., Olumor, L. Geuntak, and E. Olevsky, (2021), "Effect of process route on powder three-dimensional-printing of metal powders", Rapid Prototyping Journal, Vol. 27 No. 2, pp. 399-406). The dissertation author is the primary investigator and author of this paper.

Parts of Chapter 3 have also been published in the Powder Technology Journal (A.L. Maximenko, I.D. Olumor, A.P. Maidaniuk, and E.A. Olevsky, (2021), "Modeling of effect of powder spreading on green body dimensional accuracy in additive manufacturing by binder jetting", Powder Technology, Vol. 385, pp 60-68). The dissertation author is the primary experimentalist and co-author of this paper. Other parts of Chapter 3 are being prepared for publication (I.D. Olumor, E. Torresani, A.L. Maximenko, E.A. Olevsky, (2023) "Pressure assisted

binder jetting”. Prepared for publication). The dissertation author is the primary investigator and author of this paper.

Chapter 4 presents research results on the optimization of the selective laser melting additive manufacturing technique for defects free manufacturing of stainless-steel and stainless-steel-Tungsten carbide metal-matrix-ceramic components. Parts of Chapter 4 have been published in the Journal of Materials Research and Technology, (I.D. Olumor, A.L. Maximenko, E.A. Olevsky, (2018), “Effect of laser dwell time on pore elimination in powder bed fusion of metal matrix composites: experimentally validated modeling”, Journal of Materials Research and Technology, Vol 21, 2022, pp 4994-5003). The dissertation author is the primary investigator and author of this paper.

Chapter 5 is a comparative study of the two additive manufacturing techniques investigated. To add more context to the comparison study, a non-additive manufacturing technique, the spark plasma sintering, is also considered in comparison to the other two additive manufacturing techniques. Parts of Chapter 5 have been submitted for publication in the Journal of Materials Science and Engineering: A (I.D. Olumor, M. Wiśniewska, E. Torresani, and E.A. Olevsky, (2023), “Additive manufacturing and spark plasma sintering as effective routes for manufacturing of AISI 316L austenitic stainless steel -WC composites”. Journal of Materials Science and Engineering: A, submitted for publication). The dissertation author is the primary investigator and author of this paper. Parts of Chapter 5 are also being prepared for publication (I.D. Olumor, E. Torresani, A.L. Maximenko and E.A. Olevsky, (2023), “Property anisotropy in SLM and SJ processed SS316L”. Prepared for publication). The dissertation author was the primary investigator and author of this paper.

Chapter 6 discusses major conclusions from this work and identifies future work.

Chapter 3

Optimization of Low Energy Based AM for Defects Free Parts

In this chapter of the dissertation, we carry out optimization of the low energy AM process. But first, experiments are conducted to determine the best choice of the processing route between the SJ and the BJ. Once the right processing route is determined, the effects of materials properties such as powder particle size/size distribution and morphology, followed by the effects of process parameters such as layer heights, powder spreading speed etc. on the density and integrity of processed parts are investigated.

3.1 Binder jetting vs solvent jetting: Determining the best processing route

As previously mentioned in chapter 2, there are several 3D printing techniques used in fabricating parts, some of which include selective laser sintering (SLS), selective laser melting (SLM), powder 3D printing (P-3DP), stereolithography, amongst others [73, 144-146]. Recently, the P-3DP technique has attracted the interests of researchers due to the advantages it provides over other methods. In particular, the P-3DP technique has the advantage of producing parts faster and more cost-effectively. The downside with this technique, however, is the inability to produce fully dense parts after sintering [147].

The P-3DP technique is categorized into two methods known as Binder jetting (BJ) and solvent jetting (SJ) techniques [148]. The BJ and SJ techniques are two similar methods that involve building parts layer by layer, and often the terms have been erroneously used interchangeably. The difference between them, however, is in how the binder is applied to the powder bed, with details already provided in section 1.2 of chapter 1. The SJ technique can further be sub-divided into three approaches depending on the mode of powder-binder mixing. There is

the Solvent Jetting on Dry (SJD) [149], Solvent Jetting on Granulated (SJG) [150], and Solvent Jetting on Coated (SJC) feedstock powder[151].

The primary challenge faced with the BJ and SJ techniques is the inability to produce fully dense, homogeneous parts without employing liquid phase sintering, infiltration, or other post sintering operations. This has led current focus on achieving high green densities of printed parts to be a priority for researchers, as printed green (pre-sintering) density has been shown to influence the final density in conventional powder processing [152]. Attempts to influence the green density of printed parts have been made by several authors [11, 70, 153-155]; to this end, the effect of several printing parameters on the green density of printed alumina parts has been investigated. The role of the initial green density of copper parts printed via BJ on the final density has been investigated by Kumar et al., where they were able to achieve different initial green porosity by utilizing powders with different sizes and size distribution. Further, they were able to obtain a final density of 90.5% after sintering of a bimodal powder mixture, and a further 97.3% density was achieved after hot isostatic pressing (HIP) [156]. Other methods have been employed to achieve high final density including liquid phase sintering. For example, Mostafaei et al. investigated the effect of powder size distribution on densification and microstructural evolution of binder-jet 3D-printed Inconel 625 subjected to super-solidus liquid phase sintering [157]. Hence, the issue with low final density is not peculiar to ceramics materials alone but seems to be observed for all material systems subjected to P-3DP.

There have been several attempts to additively manufacture stainless steel parts. The major challenge faced has been, however, the inability to achieve full density of final parts. Several attempts have been made to enhance the final part density by other post sintering operations like infiltration with copper and subjecting final parts to HIP [153, 156, 158].

In this aspect of the dissertation, we investigate the influence of two process routes for P-3DP (i.e., binder jetting versus solvent jetting process routes) on the green density of two different powder systems with different chemistry and particle morphology. AISI 316L austenitic stainless steel (SS316L) powder, with irregular shape and approximate particle size of 22 μm , and Nickel (Ni) powder, with spherical shape and approximate particle size of 7 μm were chosen for this study. The choice of these powder systems with different chemical composition and particle morphology was to show if results obtained can be generalized, irrespective of powder chemistry and morphology. The influence of printing parameters such as layer height, shaker speed, and nozzle temperature on the green density of printed parts for each process route was investigated in an effort to better understand the process-property relationships in BJ and SJ of SS316L and Ni components.

For the SJ technique in this work, we have employed the Solvent Jetting on Dry (SJD) method which involves simply mixing a water-soluble polymeric binder and metal powder in a dry condition. This mixture is then fed into the print bed, followed by jetting a liquid solvent to activate the dry binder. P-3DP was carried out in a lab-assembled powder solvent jetting printer which consisted of an Ultimaker 2+ extended printer (manufactured by Ultimaker, Geldermalsen, Netherlands), reconfigured to work synergistically with an attached colorpod-run setup (designed by Spitstec, Noordwijk, Netherlands) as shown in Figure 3.1.

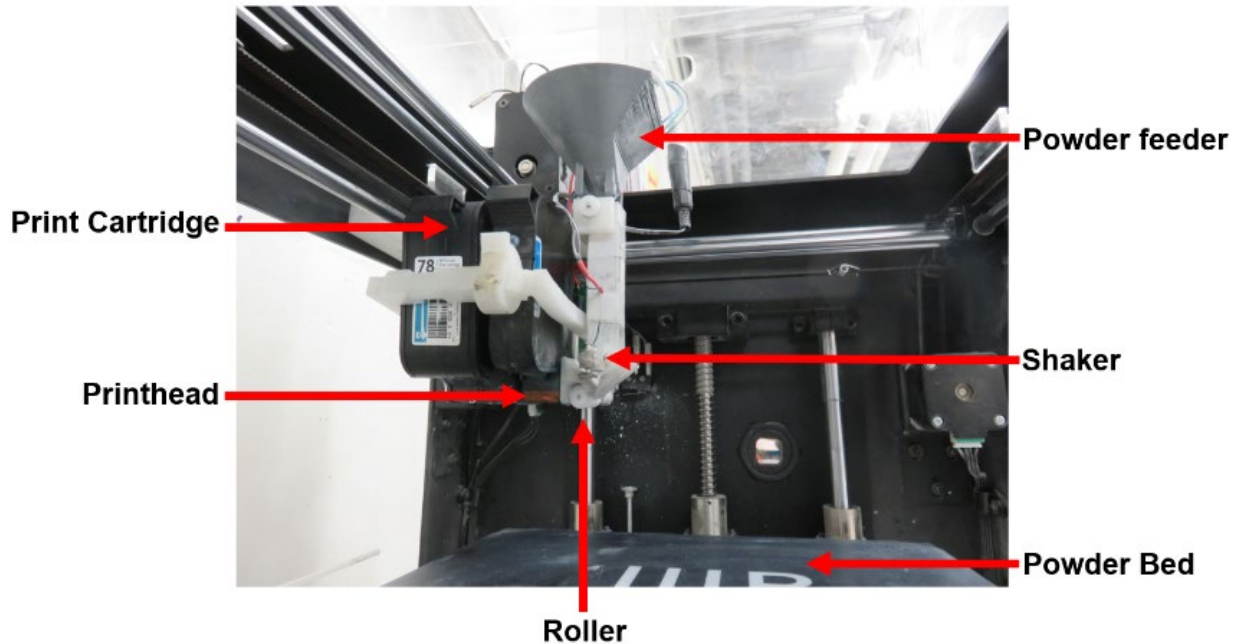


Figure 3.1 Printer set up for showing the attached colorpod run set up

The colorpod set-up is a do-it-yourself add-on that converts FDM 3D printers into powder printers. The set-up is run by a software of the same name designed to process 3D models (both STL and OBJ formats) into printable G-code. The G-code is then sent to both the Ultimaker 2+ extended printer and the colorpod set-up, thereby allowing the software to synergistically synchronize both hardware.

Colorpod has the same work schematics like other conventional binder jetting printers with slight variation in terms of how the powder is fed to the build plate. In the case of the colorpod set-up, the powder is deposited on the build plate from the powder feeder (with the help of a shaker), while at the same time, a rotating roller evens the deposited powder into a uniform layer. The printing process uses liquid droplets, dispensed from an inkjet print head. This printhead includes a powder dispensing mechanism and HP inkjet cartridges. For the purpose of this research, we have used the colorpod as a means to dispense droplets of solvent (in the case of the SJ technique) or liquid binder (in the case of the BJ technique) on a layer of metal powder. For the BJ technique

however, the binder is jetted by the ink cartridge onto a layer of pure powder, just as done with other conventional binder jetting printers.

3.1.1 Materials and experimental methods

3.1.1.1 Powder pre-processing for BJ/SJ

SS316L powders from OzoMetal LLC New Jersey, USA, were used for this study. The average particle size of powder particles was approximately 22 μm . The particle size distribution and shape are generally inhomogeneous as can be seen in the micrograph presented in Figure 3.2(a). Ni powders used were commercially sourced from Cerac incorporated - Specialty Inorganic Chemicals, Milwaukee, WI - USA, and had an average particle diameter of 7 μm . The Ni powders are more spherical and have a more homogeneous size and shape distribution when compared to the SS316L powders Figure 3.2(b). The choice of these powders was such as to be able to carry out our analysis on two different powder systems to see if a general trend can be observed irrespective of powder chemistry and morphology.

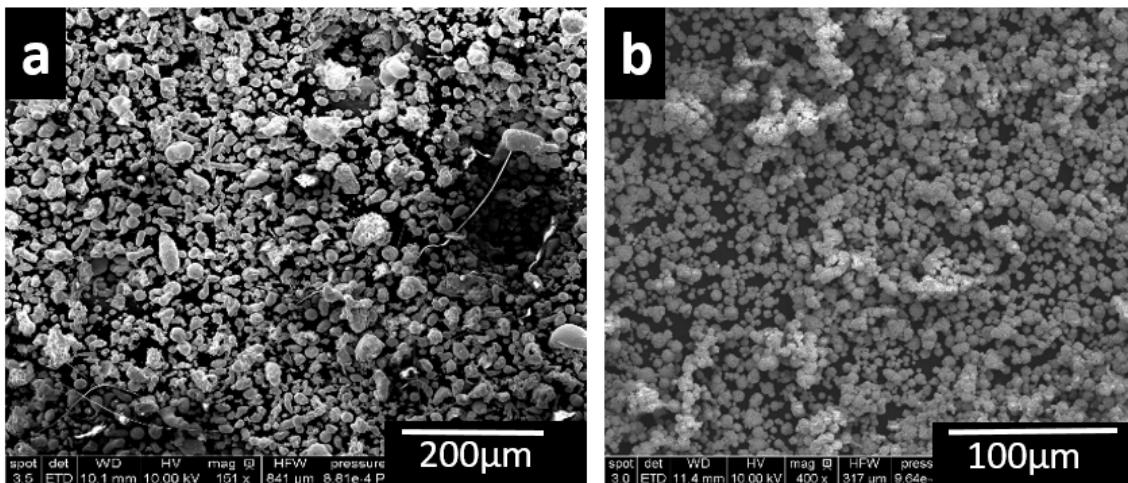


Figure 3.2 SEM images of as received (a) SS316L powders and (b) Nickel powders.

The binder used was a mixture of water-soluble maltodextrin and sugar in a 1:1 ratio, which is activated in contact with a water-based solvent. The water-based solvent or binder activator was composed of 8.3 vol% of Isopropyl alcohol (IPA), 8.3 vol% of diethylene-glycol and 83.4 vol% of deionized (DI) water. For the case of BJ, 5g of sugar and 5g of maltodextrin were dissolved in the water-based solvent and the mixture homogenized by an SH-3 magnetic stirrer (Fristaden Lab, Chicago, USA) for 2hrs at 22 °C. The choice of this composition for the binder/solvent mixture was to have a solution that will easily be jetted from the printhead nozzles and at the same time yield a satisfactory bonding of powder particles during printing. For the case of SJ on the other hand, 90%, 95% and 99% weight percent of powder samples were mixed with 10%, 5% and 1% weight percent of binder respectively and subsequently fed into the print bed through the hopper, after thorough mixing. Thereafter, the solvent was jetted from the printhead to activate the binder during printing.

3.1.1.2 BJ and SJ 3D printing processes

3D printing was carried out in a lab-assembled solvent jetting printer which is made up of an Ultimaker 2+ printer (manufactured by Ultimaker, Geldermalsen, Netherlands) reconfigured to work synergistically with an attached colorpod-controlled setup. The colorpod-controlled setup controls the amount of solvent by determining the nozzle temperature of a HP 45 ink cartridge. Increased nozzle temperature leads to increased quantity of the solvent that is jetted onto the powder bed during printing. The colorpod-controlled set up also controls the quantity of the powder deposited on to the print bed from the hopper by determining the speed of the shaker. Once the powders were deposited, the roller spread the powder to a height determined by the layer height chosen, and the HP inkjet cartridge sprayed the water-based solvent on the areas corresponding to the cross section of the part being printed, as determined by the STL file that has been imported

into the colorpod software. The process was repeated layer by layer until the printed component was completed.

Several printing parameters can be manipulated during printing, amongst which parameters of importance include roller speed, shaker speed, layer height, and nozzle temperature. The roller speed determines the speed of the rotor that controls the roller, which in turn determines the uniformity of each layer. The roller speed and shaker speed are expressed as percentages in the colorpod software and were set at 60 and 50, respectively. Layer height determines the thickness of each layer and this was varied from 100 μm to 250 μm , while the nozzle temperature was varied from 50 $^{\circ}\text{C}$ to 90 $^{\circ}\text{C}$. The proper shaker and roller settings were determined first, followed by the layer height and finally the adequate nozzle temperature. The effects of layer height and nozzle temperature on the density of the printed sample are determined in this work for both the BJ and SJ processing routes. Cube-shaped samples were printed with nominal dimensions of 10 mm x 10 mm x 10 mm using SS316L and Ni powders.

To demonstrate the ability to print complex shapes, gears and other complex shaped objects were also printed from SS316L powders. After printing, printed samples were left in the powder bed at room temperature for a minimum of 30 min before being transferred to an oven for curing. The cured green parts were used for post printing analysis, debinding and sintering.

3.1.1.3 Post-BJ/SJ debinding and sintering

SS316L-based components were selected for further post printing operations which included debinding and sintering; hence, the thermogravimetric analyses (TGA) of the SS316L powder samples, binder and cured components were carried out using the SDT Q600 (TA Instruments, USA), with heating up to 1400 $^{\circ}\text{C}$ at a heating rate of 5 $^{\circ}\text{C}/\text{min}$, in order to ascertain the cycle of debinding. The mass loss is shown as plotted in Figure 3.5. The debinding and sintering

were achieved in two separate steps. The debinding was carried out in air using a conventional muffle furnace (KSL-1200X-J-UL, MTI, Richmond, CA), while the sintering operation was carried out in vacuum using the conventional tube furnace (GSL-1700X-KS-UL-60, MTI, Richmond, CA). The specimens were held at the sintering temperatures for various holding times (5hrs, 10hrs, and 24hrs), and the cooling rate to room temperature was 5 °C/min.

3.1.1.4 Characterization of BJ/SJ-ed sintered components

The particle size of the powder, the fractured green samples, etched and unetched surfaces of sintered parts were analyzed using a scanning electron microscopy (SEM), (FEI Quanta 450, USA). The green densities of the cube-shaped printed samples and the bulk densities of the sintered samples were estimated using the Archimedes' immersion method following ASTM standard C373-18.

3.1.2 Results and Discussions

3.1.2.1 Powder characterization/ BJ/SJ printing

The as received SS316L powders have an average particle size of 22 μm, while the average particle size of the Nickel powders was approximately 7 μm of spherical agglomerates, as can be seen in the SEM images in Figures 3.2 (a) and (b), respectively. The SS316L powders have non-uniform shape and size distribution, while the Ni powders have a more uniform shape of approximately spherical agglomerates and a narrower size distribution.

Figure 3.3 shows various geometries that were successfully printed from SS316L and Ni powders using both the BJ and SJ processing routes. The complex shapes (gear and “wristwatch case”) were printed via the SJ processing route with a 10%wt binder and 90%wt SS316L powder. It was observed that due to the thin sections of the wristwatch case, higher binder amount was

necessary to achieve the final printed components that can be firmly handled without crushing during post printing operations.

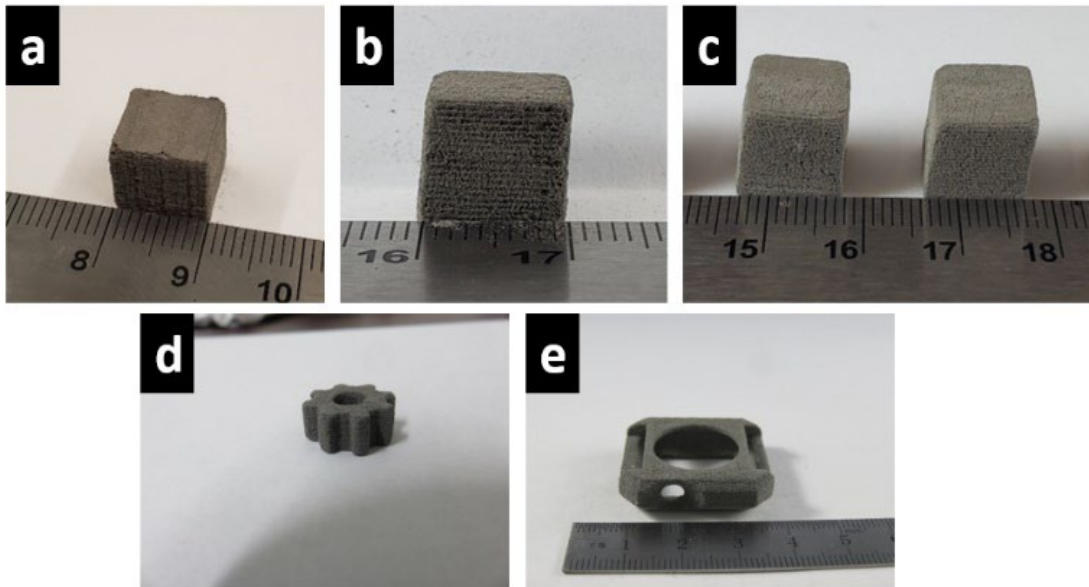


Figure 3.3 Images of printed samples (a) binder jetted SS316L cube, (b) solvent jetted SS316L cube, (c) solvent jetted Ni cubes, (d) solvent jetted SS316L gear and (e) solvent jetted SS316L wristwatch case

3.1.2.2 Curing of BJ/SJ printed samples

One crucial step in P-3DP, particularly the SJ method, that has often been taken for granted, is the curing of printed samples. With the right curing step, minimal binder can be used, resulting in green parts with increased green density. For parts to be firm enough to withstand post printing operations, there has to be enough binder to hold powder particles together, but too much binder could leave behind a residual binder amount or excessive burn-out products like carbon, which could alter the sintering behavior of components after debinding. Also, an excessive binder amount could lead to swelling/distortion of green compacts during debinding.

With the right curing regime, however, the minimal amount of binder can be used. Figure 3.4 shows SEM micrographs of samples with varying amounts of the binder after curing. We were

able to develop a curing regime that allowed the use of 99 %wt SS316L powders in our powder-binder mixture during SJ.

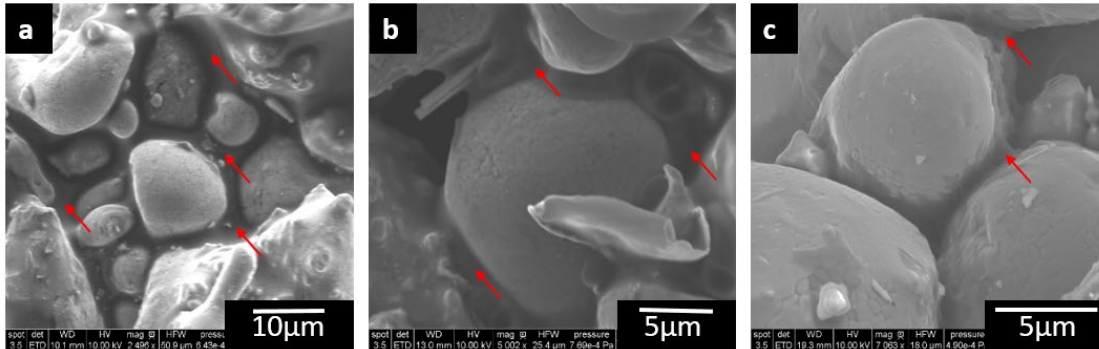


Figure 3.4 SEM micrographs of solvent jetted SS316L samples after curing (a) 90%SS316L, (b) 95% SS316L and (c) 99% SS316L

As can be seen from Figure 3.4(a), when using an excessive amount of binder, the binder, indicated by the red arrows, dissolves to form a matrix around the powder particles. During debinding, the binder decomposes, creating voids causing the powder particles to re-arrange and this could lead to the distortion of printed parts. But with a minimal binder amount, as shown in Figure 3.4(c), the binder decomposition will not create any appreciable additional voids, and hence, there will be less distortion observed after debinding.

3.1.2.3 Debinding analysis of BJ/SJ printed samples

For a successful sintering procedure to be conducted on SS316L parts, a very robust debinding regime has to be developed. This is to ensure the complete binder removal and also, importantly, to carry out debinding without exposing samples to oxidation. To ascertain the right debinding regime, the binder mixture (maltodextrin and sugar), the as received SS316L powder, and the solvent jetted cubes of SS316L were subjected to thermo-gravimetric analysis (TGA). Figure 3.5(a) shows the mass loss profile for the binder mixture. From the profile, it is evident that at approximately 560 °C, we have the total binder decomposition. Figure 3.5(b) shows the mass

profile for as received SS316L, from which we determine the onset of powder oxidation as approximately 600 °C. With this information, we were able to develop a debinding time profile for the complete binder removal without powder oxidation. Figure 3.5(c) shows a typical debinding time profile used for a 90% SS316L and 10% binder mixture after SJ.

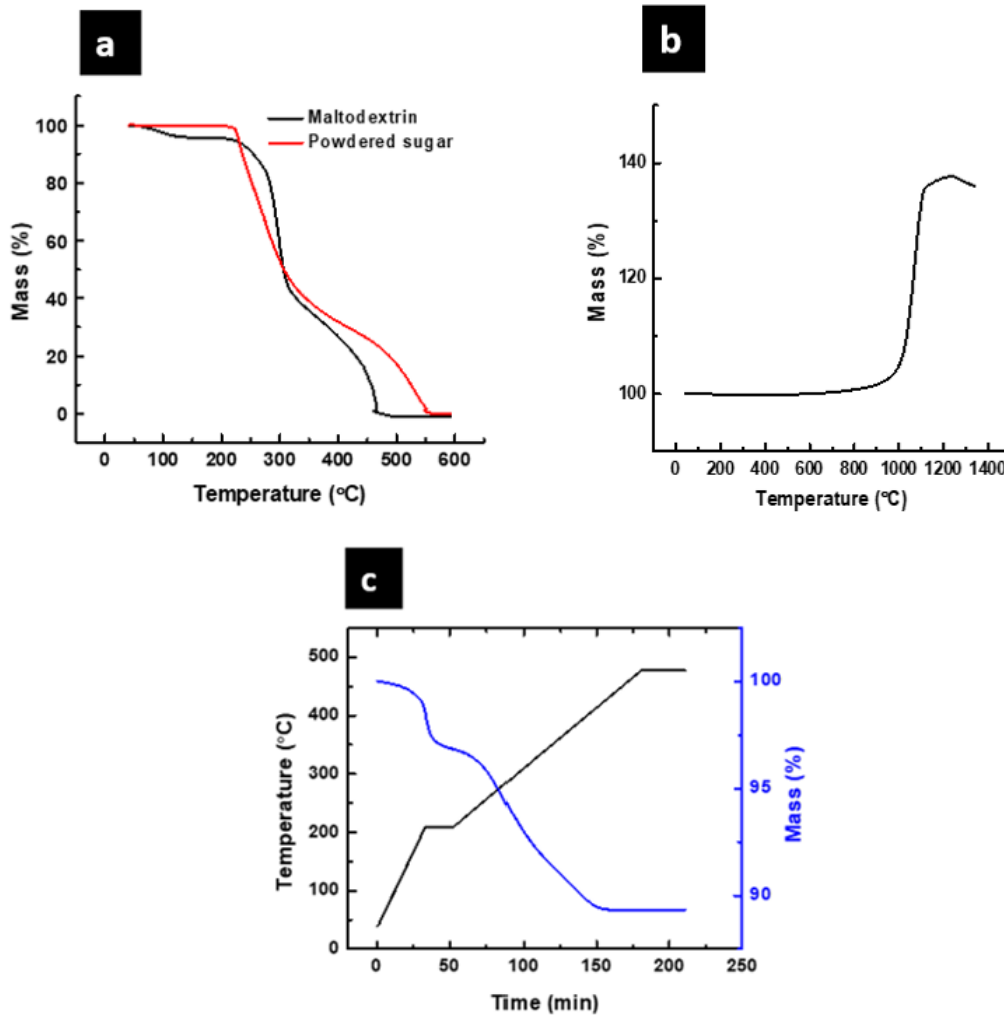


Figure 3.5 Mass loss profile of (a) binder mixture, (b) SS316L powder and (c) printed SS316L cube

It can be observed that after debinding there is a mass drop of approximately 10% which corresponds to the mass percent of the binder, hence the total removal of the binder was achieved.

Figure 3.6 includes micrographs of SS316L samples before debinding optimization showing

evidence of oxidation (Figure 3.6b), and after debinding optimization showing no signs of oxidation (Figure 3.6c).

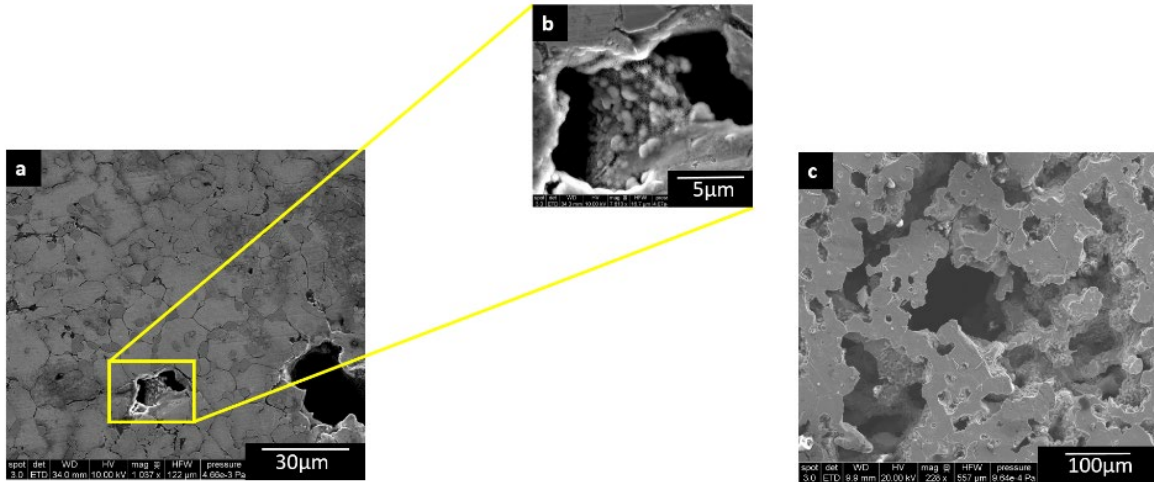


Figure 3.6 SEM micrographs of sintered SS316L showing evidence of oxidation before debinding optimization.

3.1.2.4 Effect of printing parameters and processing route on the green density of BJ/SJ printed parts

In this work, the printing parameters investigated are layer height and nozzle temperature for the BJ and SJ routes. For the printer used in this work, the roller and shaker speed are given as a percentage of the power sent to the drive the roller, and not actual speed values. Thus, the roller speed and shaker speed were set constant at 60% and 50%, respectively, which correspond to the values that yielded the optimal spreading of powder layers. We noticed a general decrease in the green printed density with increasing the layer height for both processing routes in both material systems (Figure 3.7). However, we see a slightly higher green printed density for all material systems and at all layer heights for solvent jetted samples as compared to binder jetted samples.

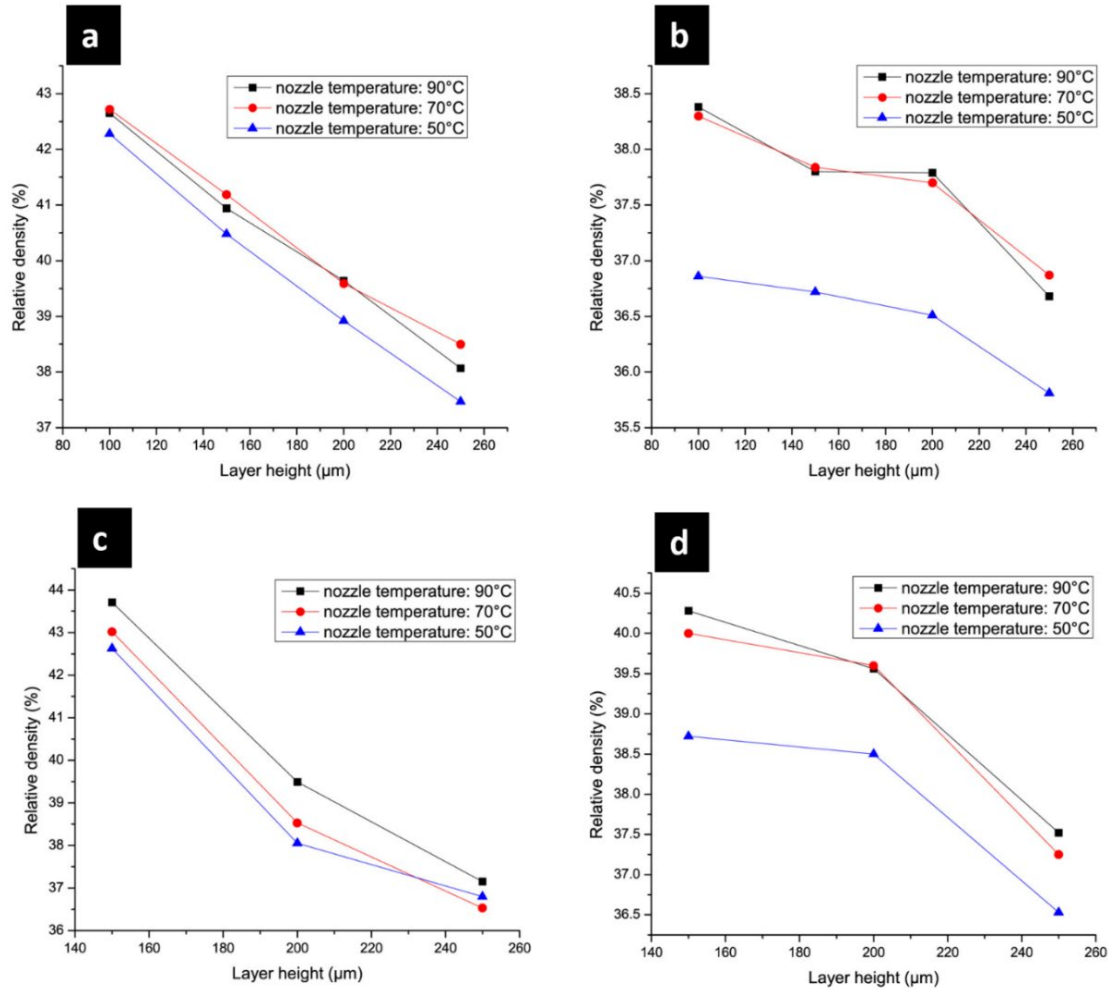


Figure 3.7 Effect of printing parameters on green density of printed parts (a) Solvent jetted SS316L, (b) Binder jetted SS316L, (c) Solvent jetted Ni and (d) Binder jetted Ni

The BJ route shows more contrast in the green printed density when the nozzle temperature is changed from 50 °C to 70 °C for both material systems. This is to be expected since for the BJ route, the print head deposits the actual binder, and with a higher nozzle temperature, more binder is jetted onto the print bed, leading to better adhesion of powder particles and, hence, higher green printed density. Whereas for the SJ route, the binder composition is constant, but the amount of the solvent jetted to activate the binder varies with the nozzle temperature, hence a slight change in the relative density of green compacts with change in nozzle temperature is observed.

3.1.2.5 Relative density of BJ/SJ-ed sintered SS316L components

The highest sintered relative density for SS316L was achieved at sintering temperature of 1220 °C in a vacuum atmosphere and holding time of 24hrs. For the solvent jetted samples investigated for sintering behavior, we noticed that for samples with higher binder percentage i.e. 10% and 15% binder concentration, melting occurred before the sintering temperature of 1220 °C was reached, Figure 3.8(b). This can be attributed to the presence of high concentration of residual carbon after debinding because of the high concentration of the binder.



Figure 3.8 Sintered SS316L after SJ and debinding (a) 99% SS316L cube, (b) 90% SS316L cube and (c) gear

The residual carbon is suspected to have been the cause of the reduced melting temperature as dictated by the Fe-C phase diagram. For samples with 99% SS316L, 87.2% relative density was achieved with the stated sintering conditions. To achieve this final sintered density, printing was carried out at 100 μ m layer height and 70% nozzle temperature, resulting in a relative green density of 42.7%.

Table 3.1 presents results of the sintering of solvent jetted components with 99%wt SS316L. We observe that increasing relative green density results in increasing sintered relative density of SS316L parts. It therefore follows that to achieve very high final part densities, the printing process should be optimized to yield the highest possible green density.

Table 3.1 Effect of relative green density on final relative density of sintered part

Layer height (μm)	Nozzle temperature ($^{\circ}\text{C}$)	Green density (%)	Sintered density (%)
250	50	37.47	83.76
200	90	39.64	86.62
100	70	42.72	87.21

3.2 Influence of powder morphology on BJ/SJ-ed green and BJ/SJ-ed sintered part density

To investigate the influence of powder morphology on the density of green and sintered parts, two different powder types were used, the water atomized SS316L powders used in the previous set of experiments and the gas atomized SS316L powder from from Praixair S.T technology, Inc., Indiana, USA. The morphology of the powders is presented in Figure 3.9. The Table 3.2 presents the properties of both powder types.

Table 3.2 Properties of water and gas atomized powders.

Property	Powder type	
	Water atomized	Gas atomized
Chemical composition	Fe-16Cr-10Ni-2Mo	Fe-17Cr-12Ni-3Mo
shape	irregular	spherical
Apparent density	38%	50%
Tapped density	51%	60%

The printing machine used for this experiment was a lab-modified ZPrinter 350 printer (Z-Corporation, USA), originally designed to print parts using gypsum powder but modified to allow printing parts from metallic powders. In the solvent jetting technique employed, the procedure was similar to the one described in section 3.1. However, the pure SS316L powders were premixed with a 1% similar water-soluble granular binder mixture instead of 5%.

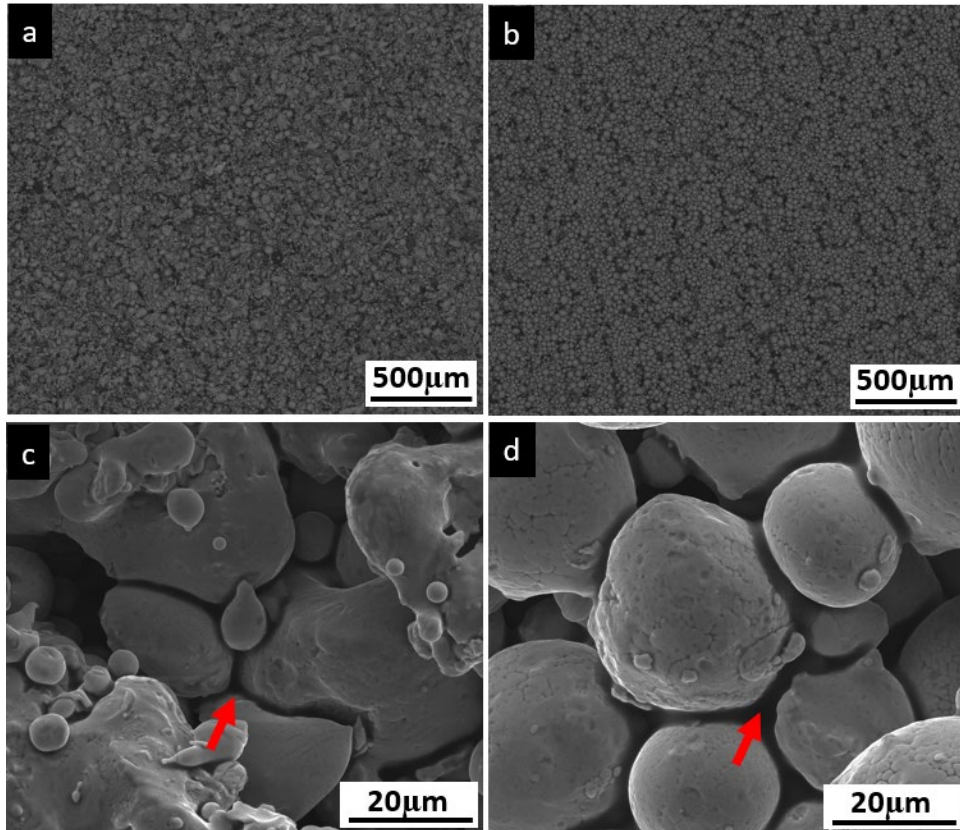


Figure 3.9 SEM micrographs after spreading a single layer of the (a) water atomized powder (b) gas atomized powder (c) magnified image of the water atomized powder within the spread layer (d) magnified image of the gas atomized powder within the spread layer. Red arrows indicate binder.

It is evident that the powder composition is quite similar. Both powders were used to print simple cubes using the SJ technique. After printing, the densities of the parts were estimated. Furthermore, samples were sintered at several temperatures and sintered densities were estimated for all temperatures sintered.

From Figure 3.10 it is clear that the water atomized samples experience larger volume shrinkage after sintering. This can be attributed to the lower density of the printed green part. It therefore becomes evident that for volume shrinkage to be minimized after sintering, the starting powder should be such that the printed density has a high enough density.

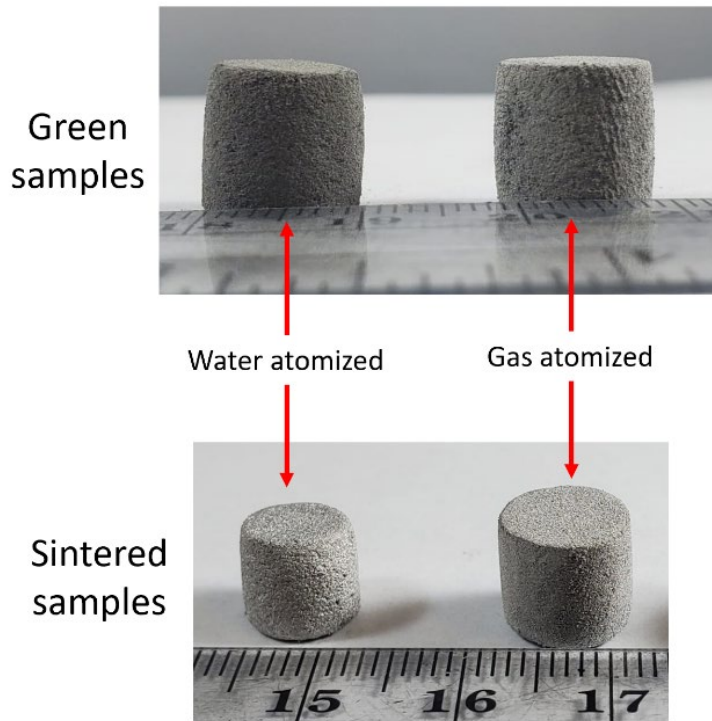


Figure 3.10 Water and gas atomized samples after printing and sintering at 1350 °C

Table 3.3 Green and sintered relative density of processed samples.

	Green relative density	CIPed relative density	Sintered relative density			
			1250 (°C)	1300 (°C)	1350 (°C)	1380 (°C)
Water atomized	38.40%	-	88.73%	89.97%	90.15%	90.48%
Water atomized (CIPed)	38.40%	48.93%	88.90%	90.24%	91.88%	94.88%
Gas atomized	48.60%	-	70.24%	70.96%	85.56%	96.25%

Parts processed with the irregularly shaped water atomized powders showed higher relative densities when sintered at lower temperatures, but as the sintering temperature was increased to 1380 °C, which is the general temperature of sintering binder jetted SS316L parts, the gas atomized powder exhibited higher densification. This trend is presented in Table 3.3.

It is assumed that the irregular shape of the water atomized powder aided sintering at the intermediate sintering stage because of the larger fraction of contacting area of the particles. But as the sintering progresses to the final sintering stage, the pores in the water atomized powder become closed and sintering becomes more difficult. For the parts processed by the spherical gas atomized powder on the other hand, it is suggested that the initial low fraction of contacting area wasn't favorable for sintering in the intermediate sintering stage, but as the temperature reached the final sintering stage, sintering progresses as the pores are still open at this stage, and as such the pores could be easily eradicated. Figure 3.11 presents SEM micrographs of the sintered parts

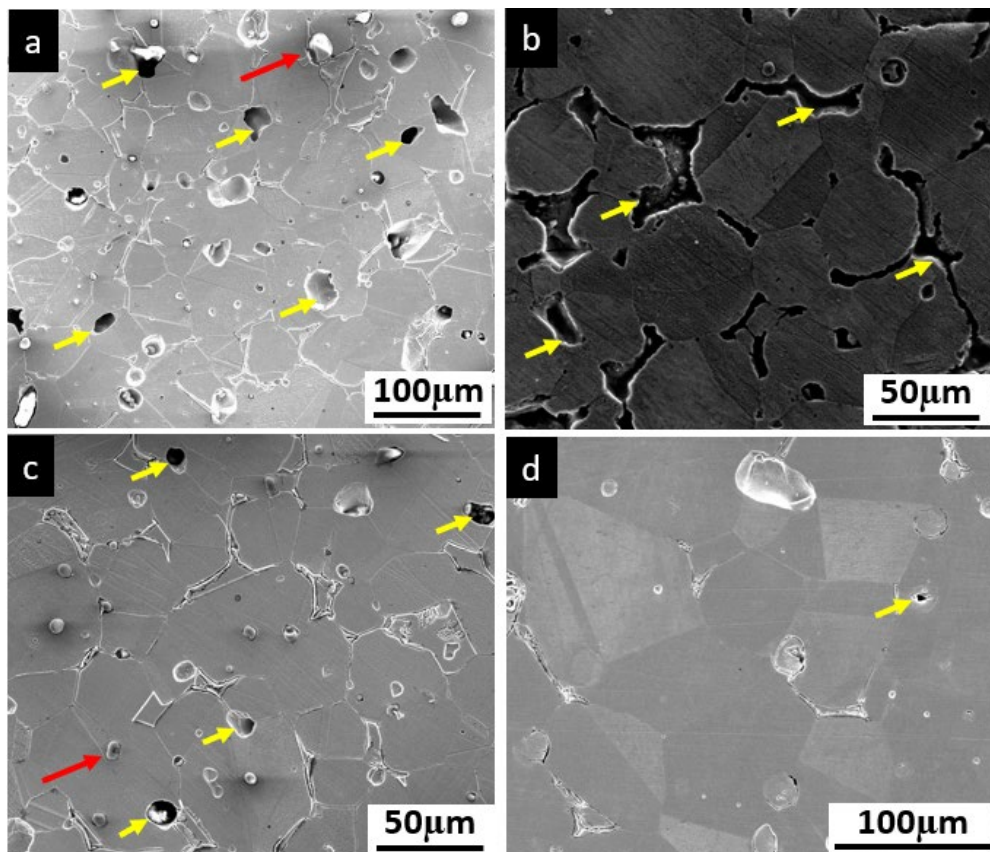


Figure 3.11 SEM micrograph of etched (a) water atomized powder at 1250 °C (b) gas atomized powder at 1250 °C (c) water atomized powder at 1380 °C (d) gas atomized powder at 1380 °C. The red arrows indicate SiO₂ impurities and yellow arrows indicate pores.

3.3 Optimizing powder bed spreading in BJ AM: Experimentally validated modeling

3.3.1 Selection of deposited powder layer thickness in binder jetting

From the BJ experiments and results from section 3.1, it is known that the thickness of all the deposited layers should be sufficiently small. Several reasons for this thickness selection can be found in literature. First, the application of thin powder layers provides means for the close buildup of the desired shape of the green body, because the layer thickness constrains the possible design feature size [159]. Another important reason is that BJ relies on the uniform binder distribution in the deposited layer, and thin layers are better controlled and, as a result, they provide a better integrity of green bodies [160].

Experimental observations show that when a green body is deposited by thin powder layers, it has better strength and higher elastic moduli [127, 161]. The question then arises as to what exactly the optimum value of the deposited layer thickness is. It is empirically established that this thickness depends on the powder particle size. In our experiments on 3D printing of stainless steel, nickel and even alumina, it was found that printing layers with a thickness greater than 2.5 particle diameters does not provide the necessary dimensional accuracy after debinding and sintering. The recently published data on binder jetting indicates that the optimum layer thickness is about three particle diameters [162]. At the same time, it appears that the thinner deposition layer assumes the higher impact of powder spreading on the distortion of previously deposited layers.

3.3.2 Powder spreading during binder jetting

The behavior of granular materials under different types of loading has been actively investigated during the last decade. During powder spreading in all powder-bed AM technologies, a blade or a roller passage through the powder bed levels its surface. Considerable modeling and

experimental efforts have been devoted to the optimization of powder spreading approaches for obtaining dense and uniform powder bed with smooth surface.

Discrete Element modeling (DEM) efforts have been aimed at the analysis of the particle size and shape distribution influence on surface roughness and particle segregation in a powder bed. Spreading of rod-shaped particles in realistic AM settings has been simulated by Haeri et al., who used DEM to investigate the effects of particle shape and operating conditions on the bed quality [163]. They discovered that larger particle aspect ratios, or higher spreader translational velocities resulted in a lower bed quality. They also compared the performance of a roller versus a blade spreader and reported that a roller outperforms a blade spreader in terms of the quality of the prepared bed under the same operating conditions. They further carried out the micro-structural analysis of the powder bed and showed particle alignment in response to the induced flow.

Furthermore, Eric et al., [96] developed a numerical tool and used it to investigate the characteristics of the powder layer deposited onto printed parts using a roller as the coating system. Their simulations considered the complex geometric shapes of the powder particles. Their results showed that increasing the coating speed led to an increase in the surface roughness of the powder bed. They also reported that powders with broader size distributions led to larger values of surface roughness as the smaller particles formed large agglomerates, resulting in increased porosity. They attributed inhomogeneity of inter-particle forces in the granular packing to a non-uniform load/stress distribution in the part during the coating process.

A body of works on DEM have also been aimed at the description of the powder bed density evolution and pore formation for different recoating speeds. Quanquan et al., [164] employed DEM to optimize powder layer thickness in laser-assisted additive manufacturing. Their work was based on a theoretical model of the interactions between the particles, the coater blade,

and the build plate during the powder deposition. Their focus was on a systematic theoretical and experimental investigation of the effect of the powder layer thickness on various powder bed characteristics during a single-layer and multi-layer powder deposition. Their theoretical model predicted a uniform powder bed deposition when employing a 40 μm layer thickness value. Lower and higher values of layer thickness resulted in large voids and short-feed defects, respectively. Their theoretical results were tested and validated experimentally using Hastelloy X with an average particle size of 34.4 μm .

Discrete Element Method, using the soft sphere model, has been used to model particles with mono-size, bimodal, and Gaussian size distributions, for different layer thicknesses and applied compression. The results showed that the packing density and coordination number increased with the layer thickness. Increasing the initial packing, and subsequently applying compressive force on the powder bed effectively increase the density and coordination number of a powder bed [165].

Previously, a number of authors have also focused on using DEM capabilities to study the contribution of adhesion between particles in all these phenomena. One of such recent studies is the work of Lee et al. [166]. In their study, they presented a multi-layer powder spreading DEM simulation model and experimentally validated their results. They calibrated their model experimentally using static angle of repose measurements. The model results showed that interaction between particle and the powder spreading blade led to variation in packing density, surface roughness, dynamic angle of repose, particle size distribution, and particle segregation.

Optimization of blade spreader shape for improvement of powder bed quality has been modeled using DEM tools. In particular, a set of DEM simulations have been performed at device-scale to optimize the geometry/profile of blade spreaders to yield the lowest powder bed porosity,

with qualities comparable to a roller, using simple rod-shaped grains to control the computational costs [95]. Furthermore, optimization of roller size and speed on bed quality has been modeled using DEM tools [167].

The research direction in this aspect of the dissertation work is different and specific to BJ technology in the sense that in our work, we have not only studied the influence of powder spreading on the spread layer, but have moved a step further in studying the effect of the powder spreading on distortion of the previously printed layer. Both modeling and experimental observations confirm that powder spreading in BJ generates some displacements not only in the upper spread layer of the powder but also in the bottom layer where particles have already been glued during the previous step. This is why we concentrate not only on the analysis of the powder bed preparation but on another type of problem: evaluation of the interaction between the powder bed flow and green body produced by BJ.

As a rule, in BJ practice it was always implicitly assumed that powder flow due to spreading was completely localized near the blade, and it could not distort previous deposited layers. Indeed, the localized flow is a typical regime for granular materials behavior [168]. However, experimental observations show that the width of the localized flow cannot be less than 6-10 particle diameters.

In modeling analyses, as long as we move down this width, we move off the applicability of granular mechanics concepts and, probably, even off the applicability of the continuum mechanics postulates [169]. For example, experiments show that the flowability of thin powder layers is significantly reduced due to the formation of the large amount of stress chains under loading [170]. Therefore, the present investigation is dedicated to the analysis of powder spreading during BJ via a Discrete Element Method (DEM) approach.

3.3.3 Discrete element modeling of powder spreading in BJ

Bullet Physics SDK (Software Development Kit) is open-source collision detection, rigid and soft body dynamics library written in portable C++. It provides a solver for rigid body dynamics. For the case of the blade spreader particle simulation, the workflow Maxon Cinema 4D package was used, while for the case of the roller spreader, the ALTAIR EDEM software package was used for the simulation. In both cases, the modeling included such problems as filling a container with layers of particles, the blade or roller movement over time, the simulation dynamics of powder bed and green body distortion and rendering the modeling results. For the case of simulation using the workflow Maxon Cinema 4D, C4D Python tags and Python plugins were developed to implement some tasks that could not be resolved by conventional modeling techniques.

3.3.3.1 Parameters of particle interaction in BJ

Our DEM analysis is based on the modeling of sphere-sphere (also known as particle-particle) collision dynamics of identical particles taking into account energy dissipation through the inelastic restitution, friction, and central forces between particles. In our modeling, the restitution coefficient, which is the ratio of final to initial velocity between two colliding spheres, was taken equal to 0.4. This value was chosen empirically to prevent excessive particle scattering along the powder bed during spreading. Higher restitution coefficient led to unphysical particle dispersion along a powder bed.

Another important parameter in the model is a friction coefficient between particles. It was fitted to provide experimental repose angle of our powder. In our modeling results, the static repose angle is clearly visible at the ends of the powder beds (Figure 3.12). Inter-particle forces are different for different types of particles: green free particles and blue glued ones. Binding forces

in the blue elements are defined as center-to-center forces. These forces in the Bullet Physics SDK have to be defined as functions of a distance between particles. In our calculations we used force inversely proportional to the second degree of the distance between particles.

$$F = \frac{A}{r^2} \quad (3.1)$$

where coefficient A was found from experimental assessments of the external energy supply required to fully break a contact between particles:

$$\int_{d/2}^{\infty} F dx = V_c S \varepsilon_f \quad (3.2)$$

$$V_c = \frac{d^3}{Z} \quad (3.3)$$

Where;

S is the strength of green bodies with maltodextrin equal to 1.5 MPa,

ε_f is the fracture strain equal to 0.0,

V_c is the volume per single contact between particles,

d is the particle diameter,

Z is the coordination number of a packing in the powder bed equal to 6.

This strength value of green body roughly corresponds to the tensile strength of maltodextrin in a wide range of water content [171], and it is a typical strength of green bodies with other binder formulations [127].

Lack of the reliable experimental information on the behavior of the composite powder bed under loading limits us primarily to qualitative analysis of the interplay between different problem parameters. We have assumed the presence of two vertical walls in our model. The optimum distance between the walls was found by a trial-and-error approach through computing the variances in the modeling results with distance change. Results for the distance of 15d were close to the results for higher distances, and thus, 15d was used as the distance between the walls.

3.3.3.2 Schematics of virtual experiments on BJ

The schematic of the virtual experiments is shown in Figure 3.12. In our investigation the blade powder spreading of the upper deposited powder layer from the initial height H_i to the final height H_f was modeled in order to estimate the concomitant distortion of the glued elements in the previous layers of the powder bed. To create the DEM powder bed unit cell for the investigation, 28500, 31000 or 34000 spherical particles of the same size filled the space between two rigid walls standing on a rigid base (Figure 3.13). The distance between the walls was taken equal to $15d$ where d was the particle diameter.

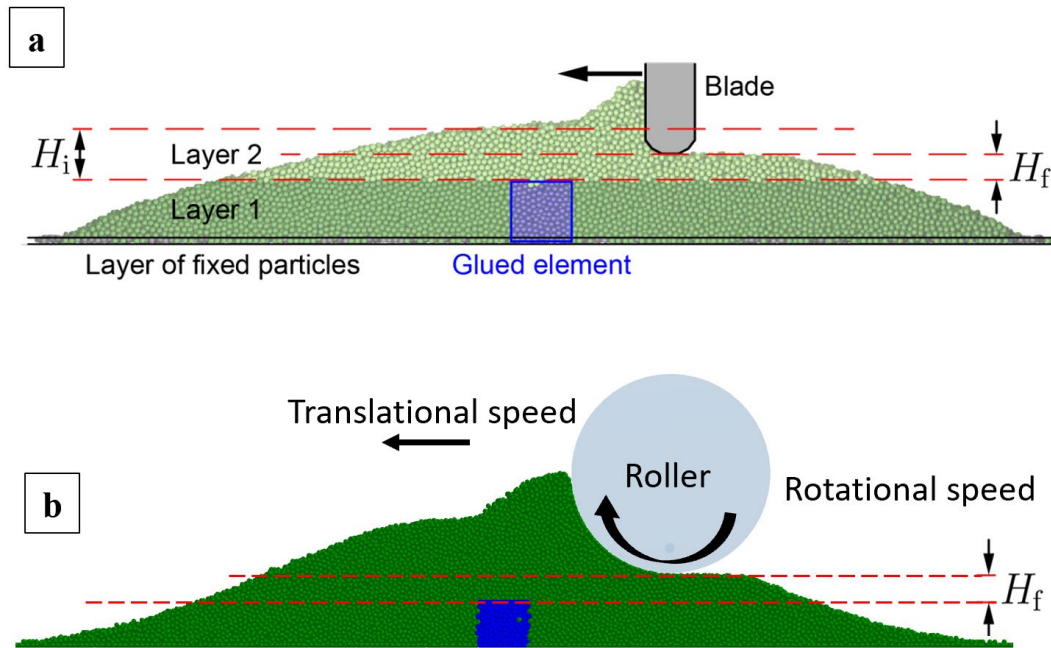


Figure 3.12 Schematic of virtual experiment with powder spreading during binder jetting (a) blade spreader (b) roller spreader.

The powder bed consisted of three layers (Figure 3.12a). The very bottom layer included a fixed layer of particles at the base to provide a realistic value for the powder layers coefficient of friction with the base. Above this fixed layer, the next group of particles formed the bottom layer of the powder bed. It was assumed that some elements of this layer can be glued during the

previous BJ steps. They are shown in blue color in Figure 3.13. If some particle volumes were considered as glued, tensile strength was introduced in the model through the particle-to-particle attraction force.

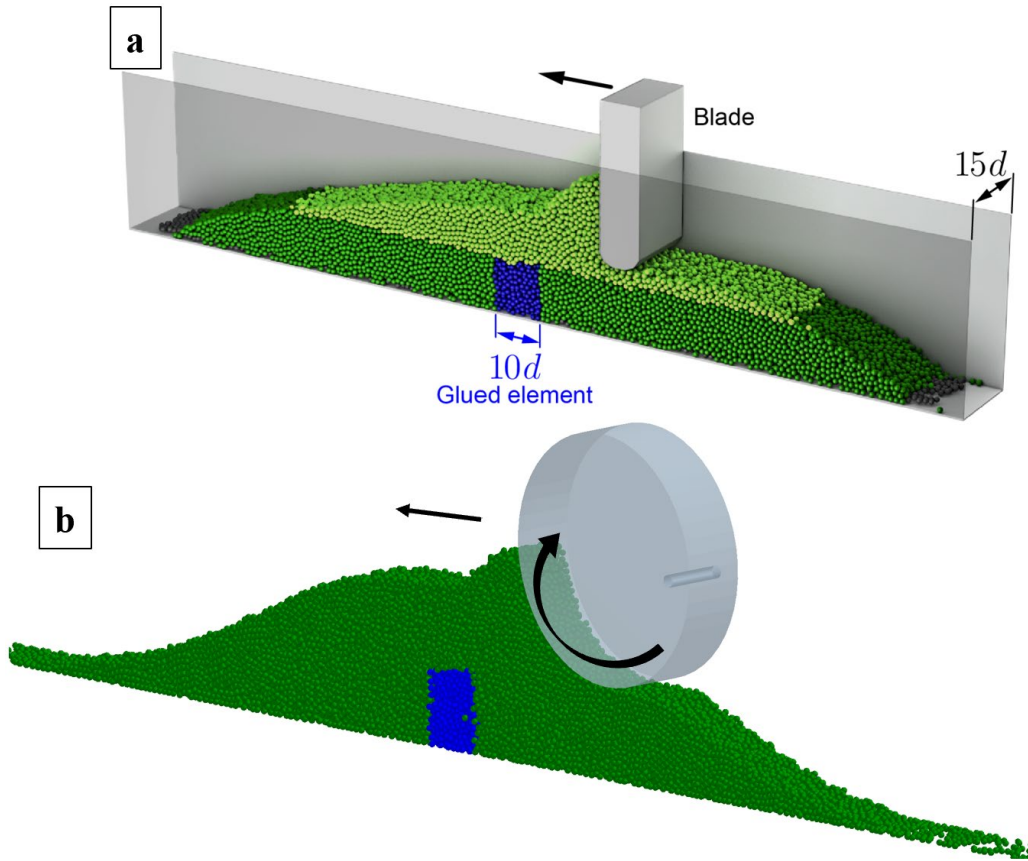


Figure 3.13. Discrete Element model of powder bed and (a) blade (b) roller powder spreading

The height of Layer 1 was about $9.5d$. Finally, the height H_i of Layer 2 varied depending on the pre-set thickness of this layer. The restitution coefficient for all free particles was taken equal to 0.4, and the particle-to-particle friction coefficient during modeling was estimated from the repose angle at Figure 2.12 as 0.15 – 0.2.

In the case of the blade spreader, two types of spreading blades were investigated: the narrow one with the thickness $8d$ and the wide one with the thickness $40d$. For the case of the roller, rotational and translational speeds were varied from 250 to 1000 rpm and 250 to 2000 mm/min respectively.

3.3.4 Density evolution during powder spreading in BJ

For the case of simulation using the workflow Maxon Cinema 4D, C4D, special plugin in Python has been developed for density evaluation of a powder bed. For simulations with the EDEM software package, density evaluation was done by implementing the voidage estimation capability embedded in the software. For both cases, relative density in an element of the powder bed after spreading was estimated as an average density in the box with dimensions $[25d, 2.5d, 13.5d]$ around this element.

Density variations of the upper part of the Layer 2 along powder bed after spreading with narrow and wide blades for the different H_f values and fixed $H_i = 8.25d$ are shown in Figure 3.13. for the case of the roller spreading the density variations of the upper part of layer 2 are shown in Figure 3.14. It is clear from both figures that the final thickness of the deposited layer significantly influences its dilation during spreading.

The density values in the conducted modeling also correspond to the range of values 0.54-0.64 reported by previous authors [98]. Although these changes in density seem to be small, they are important because they can contribute to considerable local changes in coordination numbers during powder packing. Dilation can be estimated as a difference between density at the ends of a powder bed and local powder bed density.

Our simulation results for the roller spreading shows that the dilation increases with increasing roller rotational speed (Figure 3.15), while for the case of the blade spreading, the dilation rapidly decreases with the increase of the layer thickness from $2.75d$ to $5.5d$ (Figure 13.14). This corresponds to the experimental and modeling results of other authors [97].

The high strain rate in the thin layers during spreader passage has been suggested to be the main reason for the high dilation of a thin powder layer. The dilation increases porosity in the powder

bed, decreases the strength of the green body and worsens its dimensional accuracy due to the possible non-uniform powder return to the initial more stable state.

For the case of the blade spreader, it follows from the modeling results that the narrow blade produces less dilation than the wide one. It is a general trend for all modeling results: a wide blade always produces much more disturbances (distortion and dilation, resulting from shear strain) in the powder bed than a narrow blade. Thus, we may also conclude that a larger roller diameter would produce larger dilation and distortion.

Overall, the use of a blade spreader appears to yield a better compacted powder layer when compared to a roller. Density changes observed in Figure 3.14 and Figure 3.15 can be attributed to the redistribution of particles in the powder bed, resulting from shear forces imposed by the blade and roller motion respectively. This redistribution of particles is often manifested as dilation, hence, the density changes observed are evidence of changes in dilation.

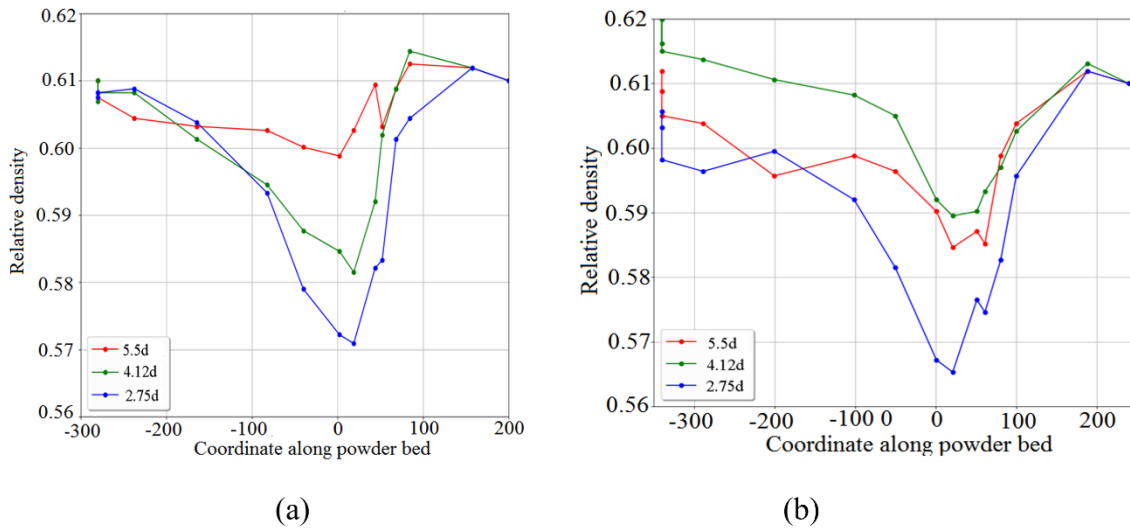


Figure 3.14 Relative density distribution along powder bed in Layer 1 after spreading with different H_f for the fixed $H_i=8.25d$: a) narrow $8d$ blade; b) wide $40d$ blade.

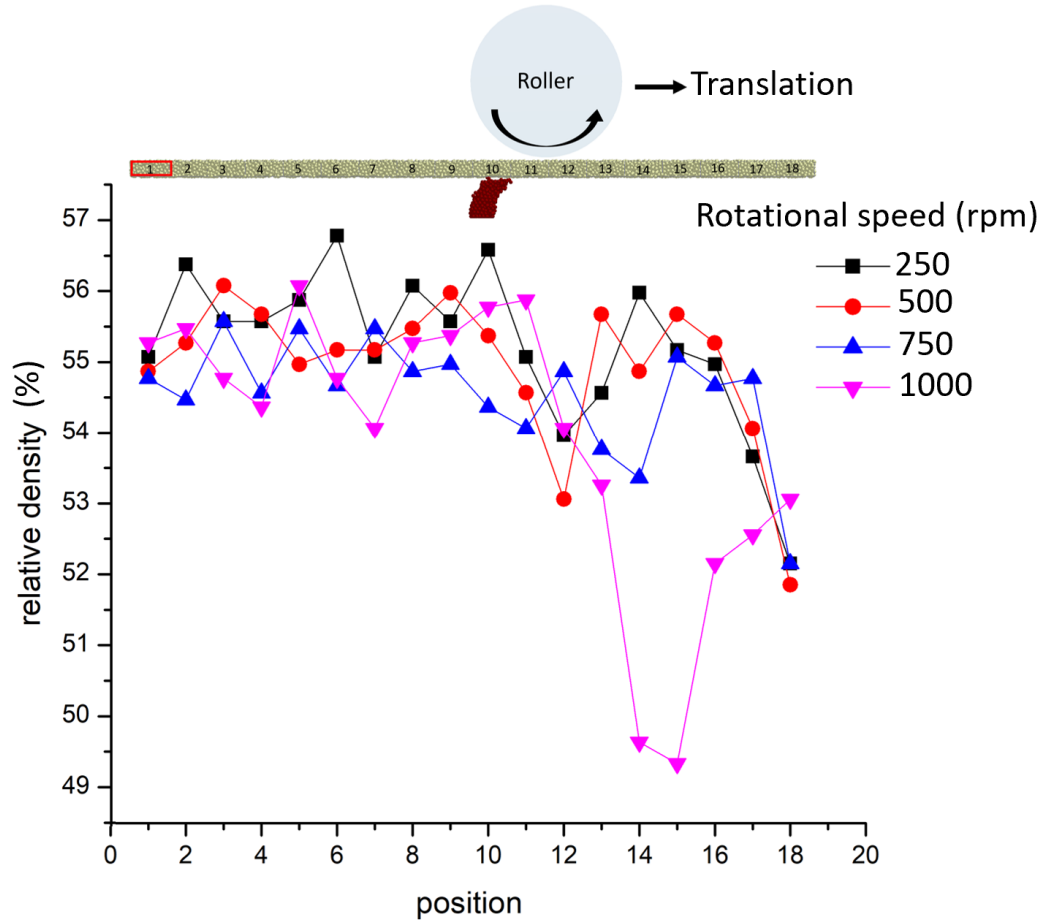


Figure 3.15 Effect of roller speed on packing density across spread layer

Figure 3.14 shows that for the case of a blade spreader, the shear strains and dilation in the powder bed depend on the thickness of a spreading layer. Additionally, Figure 3.15 shows that the shear strains and dilations in the newly spread layer are affected by the rotational speed when a roller is used instead of a blade. These results will also be confirmed in the next section. This means that the spreading of a large amount of powder with large heap in front of the spreader increases dilatancy and, therefore, deteriorates properties of the powder bed. This dilatancy and deterioration of the powder bed is exacerbated when a roller is used at a high rotational speed.

It is clear from the conducted modeling that the uniformity of the powder bed can be significantly improved if more advanced powder spreading methods like spray deposition or

moving hopper deposition with controlled dispenser in combination with blade-spreading are used [172].

3.3.5 Shape distortion during powder spreading with a blade

Because of the small thickness of the deposited layer, the blade moves just several particle diameters apart of the glued elements of the previous layer, and it can provoke their distortion. In the conducted modeling, this shape change becomes clearly visible if the thickness of the manufactured components is small enough. The results of the blade passage during powder spreading from $H_i = 8.25d$ to $H_i = 2.75d$ above the blue glued elements in the Layer 1 with the $10d$ thickness are shown in Figure 3.16. For comparison, there are two red unglued volumes in this picture to demonstrate the specific features of the free powder flow around the glued volume. Figure 3.16b also shows angle ϕ used as the quantitative measure of the element distortion.

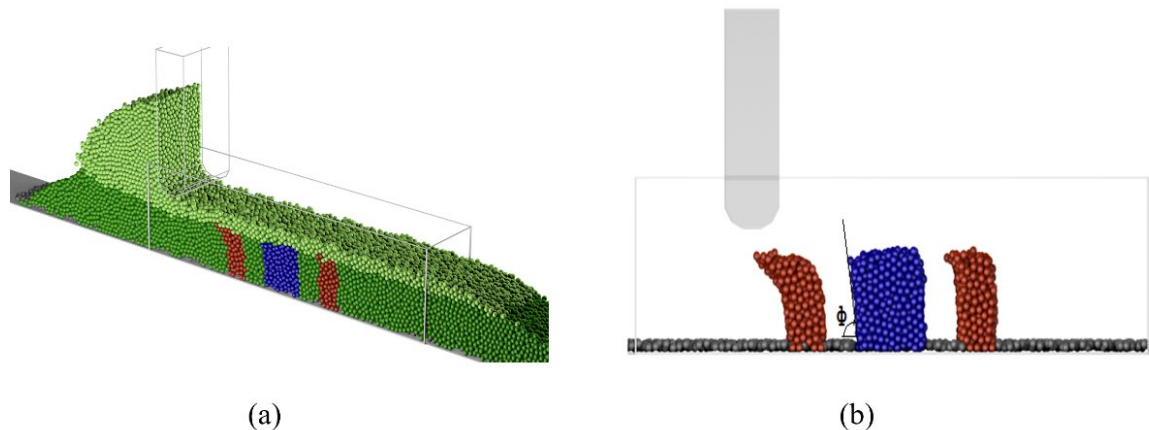


Figure 3.16 Shape distortion of previously glued powder elements:(a) general view of powder bed; (b) blue glued powder element and red free powder elements are shown.

It is clear from this picture, that the distortion angle was defined as the deviation from the initial straight angles in the glued powder elements after the blade passage. Again, like in the case involving dilatancy, the wide blade produces much more distortion than the narrow one (See Figure 3.17).

As it is shown in Figure 3.18, the distortion angle increases with the decrease of the deposited layer thickness H_f , and it becomes the largest distortion angle for the smallest considered layer thickness of $2.75d$.

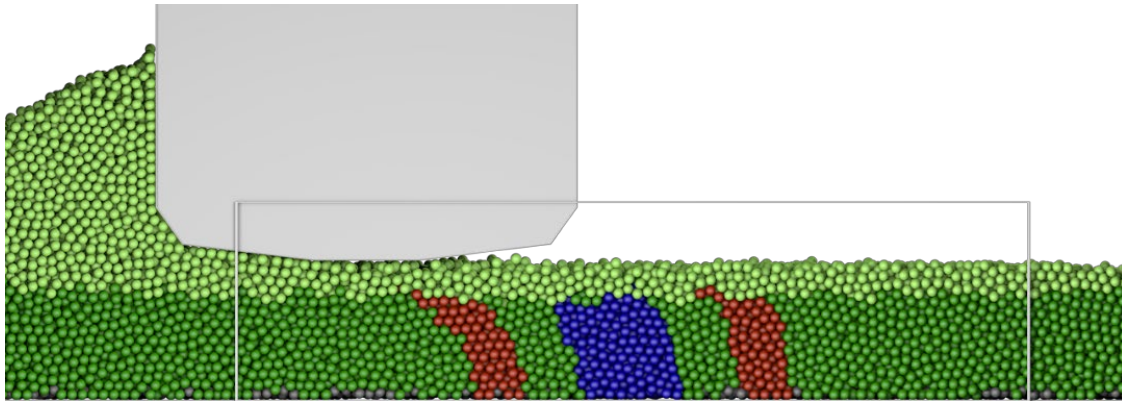


Figure 3.17 Distortion of bound powder elements after passage of wide blade

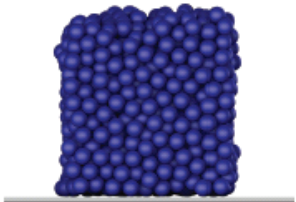
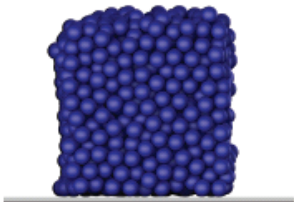
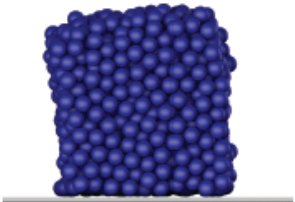
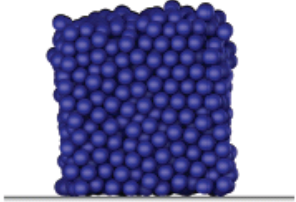
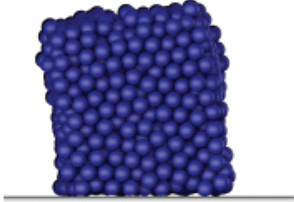
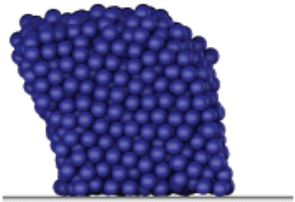
	Layer thickness		
	5.5d	4.125d	2.75d
Narrow blade	 1.5°	 3°	 6°
Wide blade	 5°	 8.5°	 14°

Figure 3.18 Distortion of the glued 12d-wide element after blade passage.

In order to elucidate and separate the contributions of the H_i and H_f parameters into the distortion, we also estimated the distortion of the same blue element for the fixed H_f and different H_i values. Figure 3.19 shows the plots of the distortion angle variation with H_i and H_f . Figure 3.19a demonstrates the distortion angle as a function of H_i for the fixed $H_f = 2.75d$, and Figure 3.19b shows a similar plot for the fixed $H_i = 8.25d$ and different H_f .

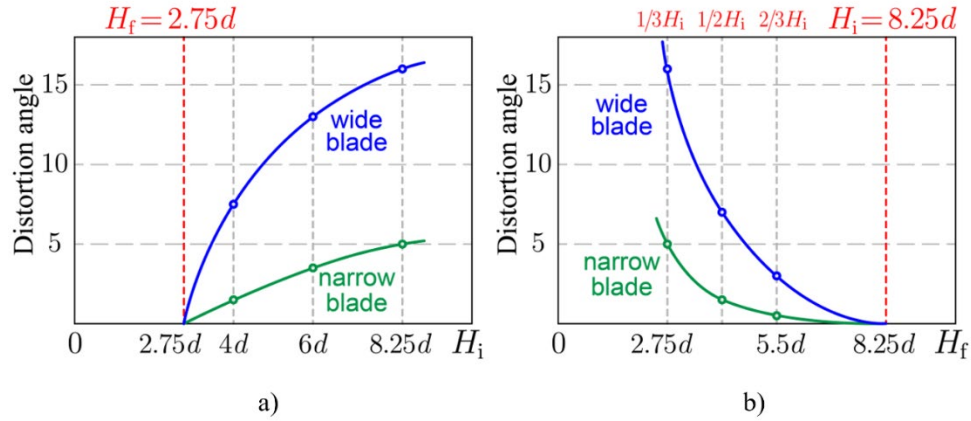


Figure 3.19 Distortion angle as a function of parameters of deposited layer: a) distortion angle as a function of H_i for the fixed $H_f = 2.75d$; b) distortion angle as a function of H_f for the fixed $H_i = 8.25d$.

The modeling results indicate that the distortion angle for the wide blade spreading and can be approximated as:

$$\varnothing = \text{const} \left(\frac{d}{H_f} \right) \sqrt{\frac{H_i - H_f}{d}} \quad (3.4)$$

The constant in Eq. (3.4), in turn, is a function of the blade width W , thickness of the glued volume L , velocity of spreading, and other parameters. For example, approximation of our modeling results gives

$$\varnothing = (2.7 + 4.28U) \left(\frac{d}{H_f} \right) \sqrt{\frac{H_i - H_f}{d}} \quad (3.5)$$

where;

$$U = \frac{W}{L} \quad (3.6)$$

3.3.6 Shape distortion during powder spreading with a roller

The results of the roller passage during powder spreading from $H_i = 8.25d$ to $H_f = 2.75d$ above the glued elements in the Layer 1 with the $10d$ thickness are shown in Figure 3.20 for the various rotational speeds at constant translational speed (dash-lines indicate line of distortion measurement). Figure 3.21 shows the distortion angle as a function of roller rotation speed for the fixed $H_f = 2.75d$ and translation speed = 250 mm/min. Also, Figure 3.21 shows results of the distortion as a function of the roller translational speed for a fixed roller rotational speed = 250 rpm. It is evident that the distortion increases with increasing translational and rotational speed of the roller, with the translational speed having a greater impact.

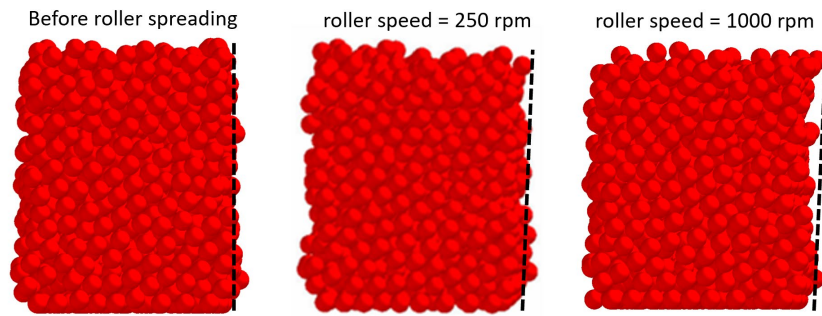


Figure 3.20 Distortion of previously printed part resulting from various rotational speeds

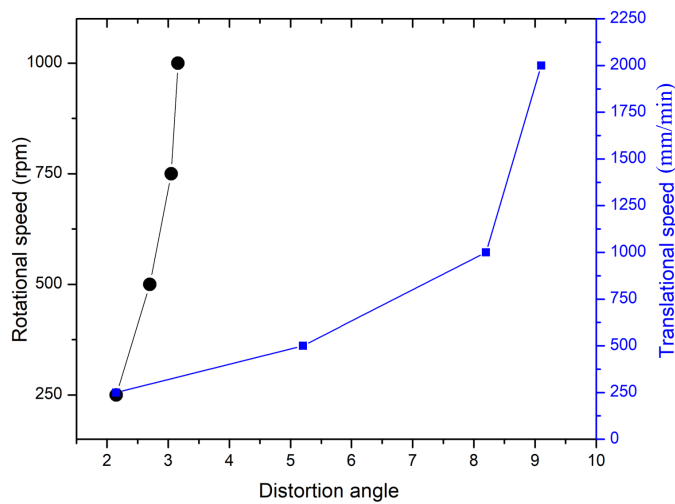


Figure 3.21 Effect of roller rotational and translation speeds on the distortion of the previously printed layer for a fixed $H_f = 2.75d$

3.3.7 DEM simulation of bimodal powder packing for improved packing density in BJ

We set out to do this by using the EDEM software package. The same particle properties used previously were maintained. However, we have assumed a spherical unimodal particle system for simplicity. Particles sizes of coarse and fine particles were chosen in such a way that a size ratio of coarse to fine of 5:1 was achieved. Particles were randomly populated inside a container and allowed to settle. After settling, the porosity of the powder bed was estimated. The coarse to fine particle weight ratio was varied and the effect on the final porosity after settling was estimated. Figure 3.22 presents the results from the bimodal powder packing. In agreement with most literature, our simulations show that at about 70% weight fraction of coarse particles, a powder bed with a porosity decrease of about 12% was achieved.

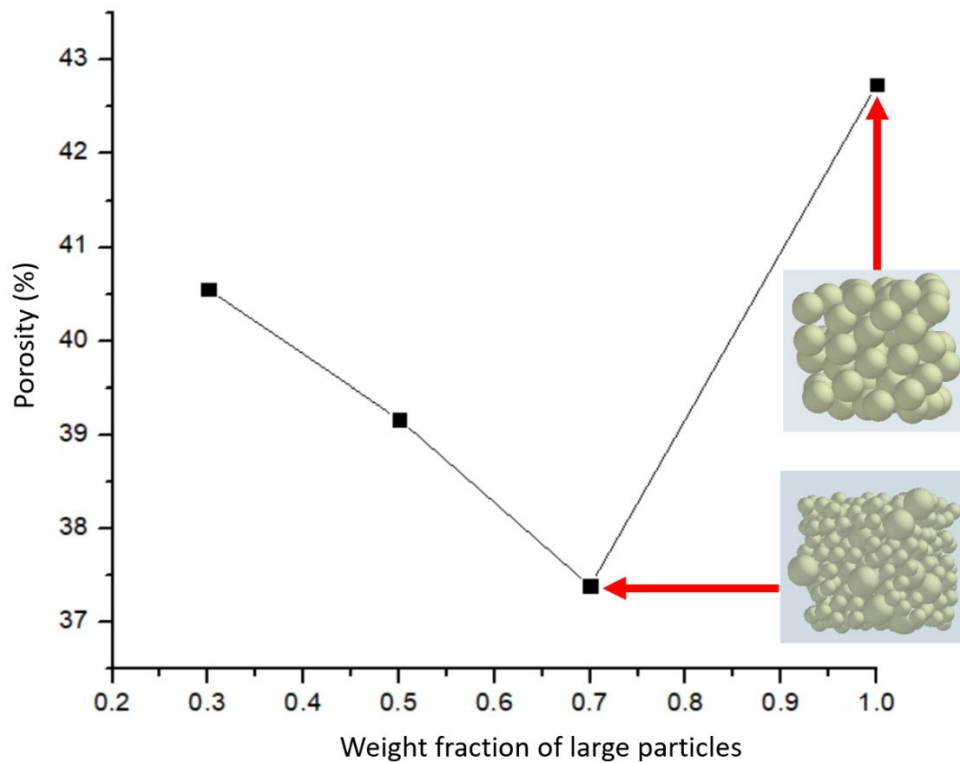


Figure 3.22 DEM modeling result of bimodal powder packing

3.3.8 Experimental verification of DEM simulation of BJ

Due to the constraint imposed by our lab assembled printer, experimental validation of the effects of the roller on the part distortion of previously printed layers is beyond the scope of the current dissertation work, even though there is currently an ongoing effort for the experimental validations. Experiments were however aimed at the analysis of basic features of the distortion of glued elements under the influence of blade spreaders with different sizes.

Samples with geometry as shown in Figure 3.23 (a) were printed using a lab-assembled 3D printer which was based on an Ultimaker 2+ (manufactured by Ultimaker, Geldermalsen, Netherlands) reconfigured to work synergistically with an attached Colorpod-controlled setup [23]. After printing, curing and depowdering, deformation angle is measured as shown in Figure 3.22 (b).

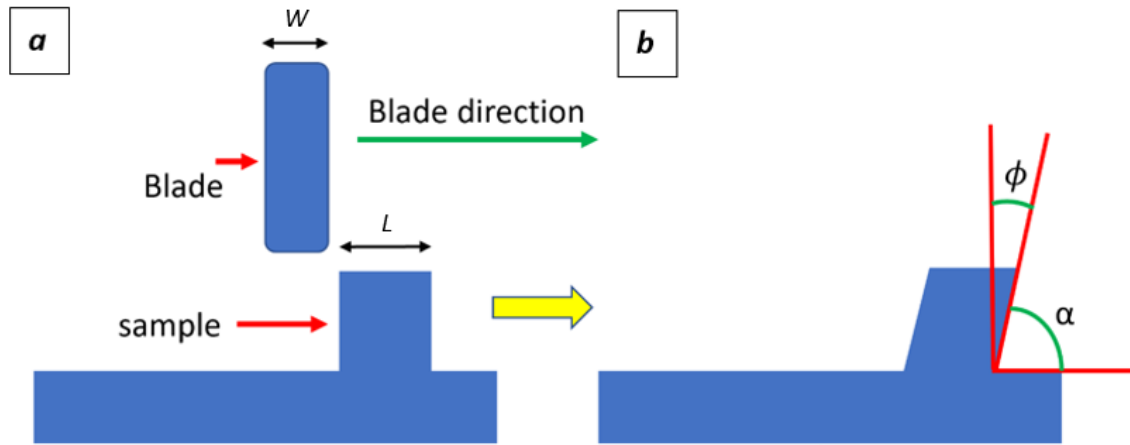


Figure 3.23 Schematics of experimental set up (a) designed shape for printing (b) after printing, curing and depowdering.

The colorpod-controlled setup controls the amount of binder ejected onto the spread powder bed by dictating the nozzle temperature of the printer cartridge. Increased nozzle temperature leads to increased amount of binder that is jetted onto the powder bed during printing. Once the powders were deposited, the blade spreads and levels the powder to a predetermined

layer height, and the printer cartridge sprays the water-based binder on the areas corresponding to the cross section of the part being printed, as determined by the STL file that has been imported into the colorpod software.

Different U value configurations, i.e., blade-thickness/sample-thickness values, as shown in Figure 3.24, were investigated in order to study the effects of the blade size viz-a-viz sample thickness on the distortion of printed samples.

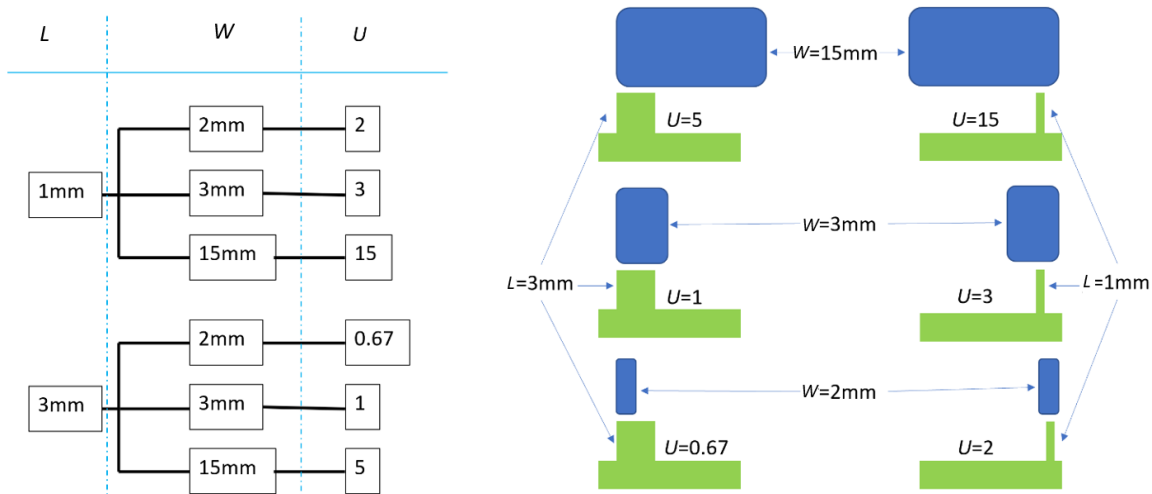


Figure 3.24 Different configurations of blade/sample thickness.

SS316L powder of approximately 22 μm average particle size, with sieve analysis of 7.8% and 92.2% retention and passing-through respectively on 45 μm (-325 mesh), was used for an initial attempt to print at a final layer height of 100 μm and blade speed of 5000 mm/min. This attempt was, however, unsuccessful as shown in Figure 3.25. The printed part experienced layer shifting, which can be attributed to the poor adhesion of the printed layers to the base powder and due to the excessive high speed of the blade. TNZT powders with composition Ti-35%Nb-7%Zr-5%Ta, and average particle size of 278 μm (mesh size -500+300) (TOSOH, USA), were therefore used for the experimental part of this study.

The printing method employed was the Binder Jetting technique. The binder was a solution of 5g maltodextrin and 5g sugar in 4ml of solvent. The water-based solvent was composed of 8.3 vol% of Isopropyl alcohol (IPA), 8.3 vol% of diethylene-glycol, and 83.4 vol% of deionized (DI) water. The attempts to print with higher concentrations of maltodextrin and sugar were not successful due to the high viscosity of the solution resulting in inability of the binder to be jetted from the printer cartridge nozzle.

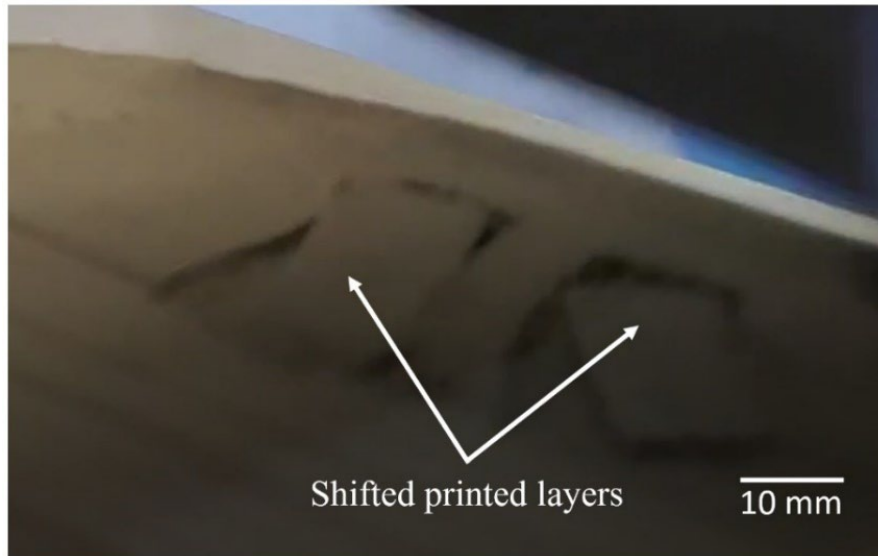


Figure 3.25 Distortion (Layer shifting) of printed base for SS316L.

The speed of the blade during printing was set at 2000 mm/min. The initial layer height (which corresponds to H_i) was set at 1.24mm, while the final layer height (corresponding to H_f) was varied between 450, 550, 650 and 750 μm .

After printing, the printed samples were left in the powder bed at room temperature for a minimum of 30 minutes before being transferred to an oven (AccuTemp-09, Across International) and cured for 30 mins at 120 °C. Thereafter, samples were depowdered using a jet of pressurized air and pictures were taken. The pictures were subsequently imported into the image-j software and the angle α was measured. The deformation angle ϕ was thereafter calculated.

Using the TNZT powder, and the blade speed of 2000 mm/min, the successful printing was achieved. The distortion angles were measured and plotted against the final layer thickness in Figure 3.26. Figure 3.27 shows representative printed samples and lines drawn for angle measurements for various printing parameters.

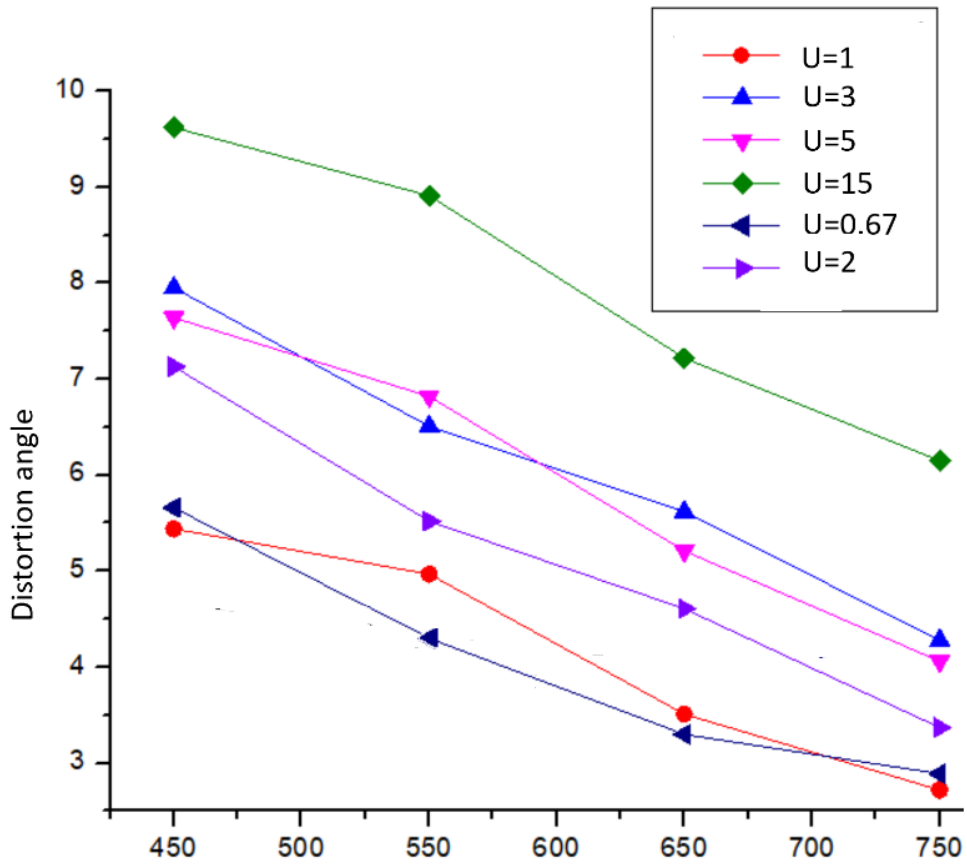


Figure 3.26 Distortion angle vs final layer height for printed TNZT samples at different values

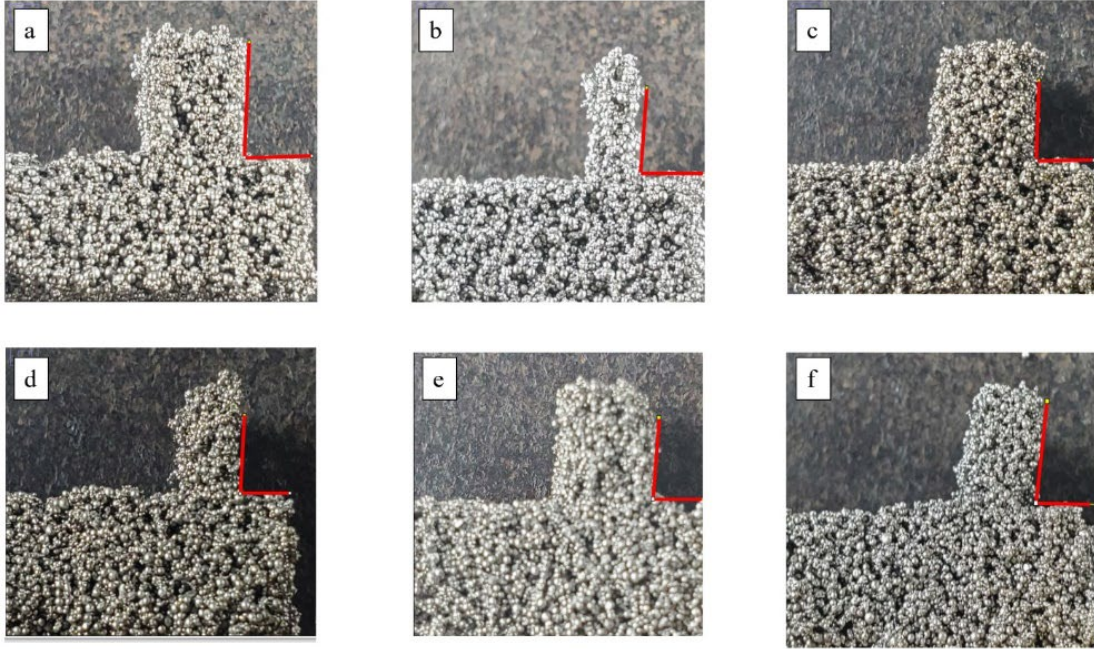


Figure 3.27 Samples printed with; (a) $U = 5$ at $H_f = 750 \mu\text{m}$ (b) $U = 15$ at $H_f = 750 \mu\text{m}$, (c) $U = 1$ at $H_f = 750 \mu\text{m}$ (d) $U = 3$ at $H_f = 750 \mu\text{m}$ (e) $U = 1$ at $H_f = 550 \mu\text{m}$ (f) $U = 3$ at $H_f = 550 \mu\text{m}$.

Both experiments and modeling confirm considerable distortion of the thin-wall (approximately equal to $10d$) green body elements under the influence of active powder spreading along the surface of a powder bed. It was theoretically predicted and verified by the experiments that the distortion angle of the glued elements is inversely proportional to the thickness of the depositing layer and directly proportional to the square root of the thickness of the powder layer removing during spreading. It was found that distortion increased with increase in spreader width. Results show that distortion angle was a function of blade-thickness/sample-thickness ratio, $U=W/L$ and it did not depend separately on the blade width W and the element width L .

Experimental data from Figure 3.26 are almost parallel lines with constant slope that can be readily approximated analytically. The final approximation is

$$\phi = (5.15 + 0.33U) \frac{d}{H_f} \sqrt{\frac{H_i - H_f}{d}} \quad (3.7)$$

For the comparison, recall equation (3.5) obtained in our modeling. It is clear that our modeling significantly overestimates the influence of the blade width. The experimental and modeling results for $L = 3\text{mm}$ are shown in Figure 3.28. At the same time, the uncertainty with many constitutive parameters of the powder bed warrants mostly qualitative interpretation of the modeling results. Several important parameters are still beyond the scope of the conducted analysis, including the real strength of the glued green body, spreading velocity, friction coefficients between blade and powder, non-uniform particle size/distribution in experimental powder, and agglomeration of particles amongst others.

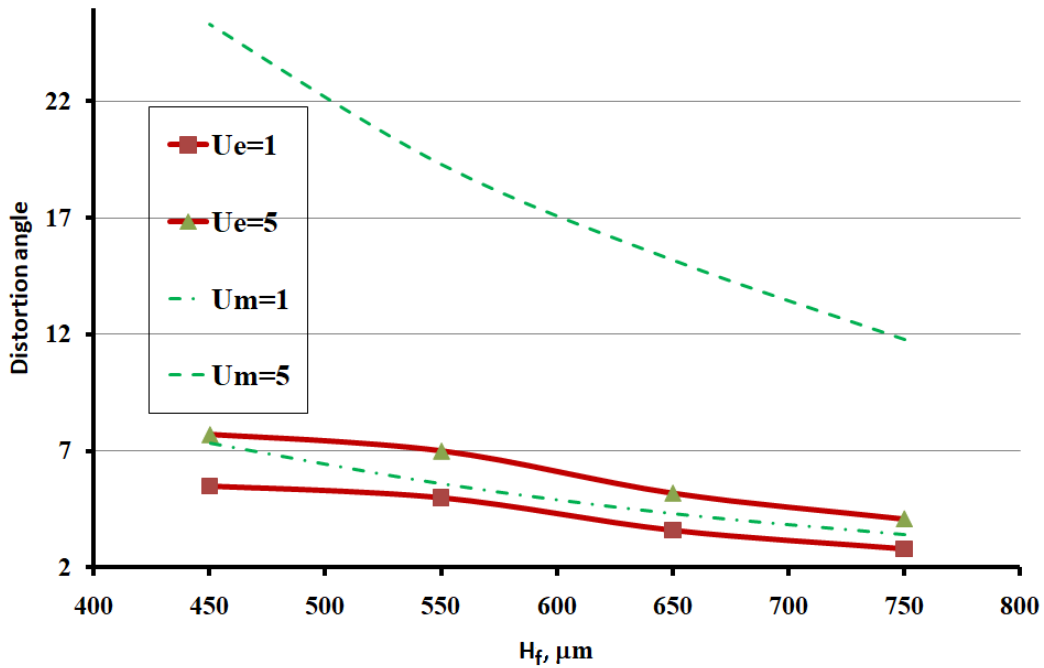


Figure 3.28 Experimental and theoretical results for different U values for $L = 3\text{ mm}$. Index e and m indicates experimental and modeling values respectively.

Another important factor to note is the fact that in the simulation we assumed a fixed initial powder layer as the substrate upon which a subsequent layer is glued to, but in the actual experiment, the substrate was a loose powder layer. This, we believe, also contributed in the disparity observed between the experimentally measured and simulated distortions. Nevertheless,

for the fixed spreading velocity, empirical Eq. 3.4 in combination with several simple experiments for detection of appropriate parameters, provides a useful tool for the estimation of the dimensional accuracy of a BJ green body. According to the derivation of this equation, it is primarily applied to powders with narrow particle size distributions.

3.4 Influence of powder size distribution on BJ/SJ-ed green and BJ/SJ-ed sintered parts density

In order to achieve improved green and sintered density of solvent jetted water atomized powder based on our results from sections 3.1, 3.2 and 3.3, we set out to reprocess the powder to achieve bimodality. To do this, the original (as received) powder was sieved into several powder size groups. Particle analysis of the various size groups was conducted. Based on literature and our DEM simulation results in the previous sections, a coarse:fine particle size ratio of 3:1 to 5:1 with a corresponding weight ratio of 7:3 is ideal for improved bed packing, thus, various size groups were combined with the aim of achieving the required size and weight ratios to yield bimodality. Due to the limitation placed on the available particle size groups by the starting powder, the highest particle size ratio achievable was 3.53 which corresponds to the mixture of the 15 and 53 μm particle size groups (Figure 3.29).

From Figure 3.29, it is clear that, in agreement with our powder packing simulation results and literature, bimodality was achieved with a particle size ratio of 3.53. Also, packing density evaluation of the various powder mixtures shows an increase in the apparent and tapped relative densities with the bimodal powders as against the original powder feed stock (Table 3.4)

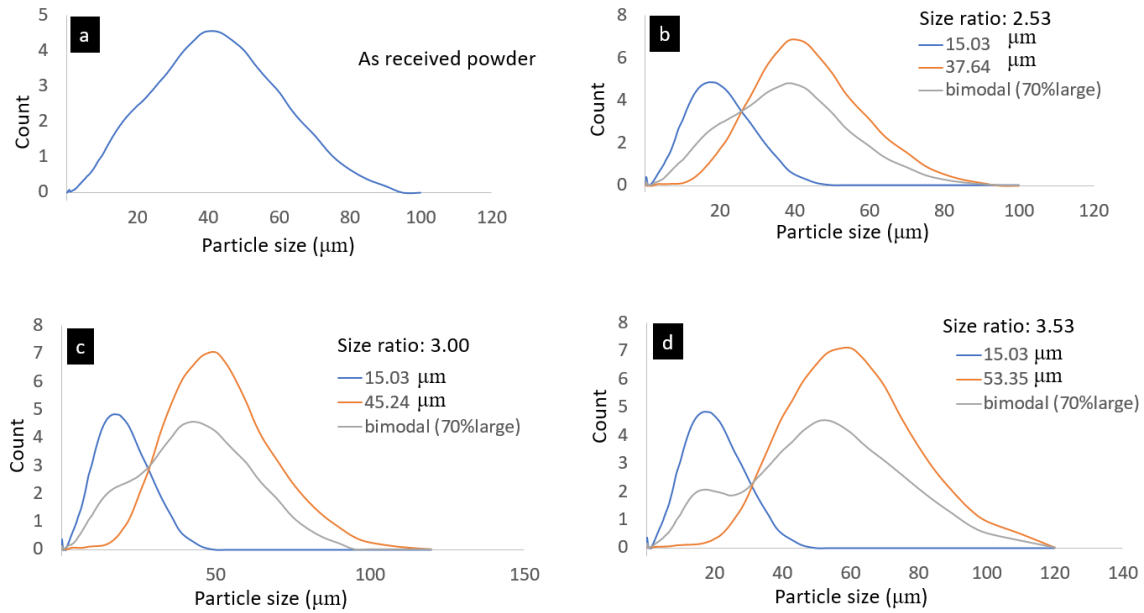


Figure 3.29 particle size distribution of (a) unprocessed powder, and processed powder for the size ratios (b) 2.53 (c) 3.00 (d) 3.53

Table 3.4 Estimated relative densities for the processed and unprocessed powders.

	Size group (μm)	Relative density (%)	
		Apparent	Tapped
Unimodal distribution	As received	38.66	50.70
	15	37.45	53.46
	27	33.87	47.45
	31	34.71	47.22
	38	37.72	49.66
	45	39.43	51.56
	53	38.85	48.68
Bimodal distribution	15+38 (70%)	42.14	54.15
	15+45 (70%)	46.42	55.02
	15+53 (70%)	46.45	55.38

In fact, an increase in apparent density and tapped density of about 20% and 9% respectively was achieved by the 15+53 μm size group. The processed powders were used to print simple cubes and relative density estimations of printed cubes showed an increased value when

using the processed powders (Figure 3.30). It is estimated that an increase in density of about 22% was observed with the 15+53 μm size group after printing. Furthermore, density of the processed samples after sintering was measured. Results also showed that the processed bimodal powders sintered better at the sintering temperature of 1380 $^{\circ}\text{C}$ investigated, with an average increase of about 7% for the 15+53 μm size group (Figure 3.30).

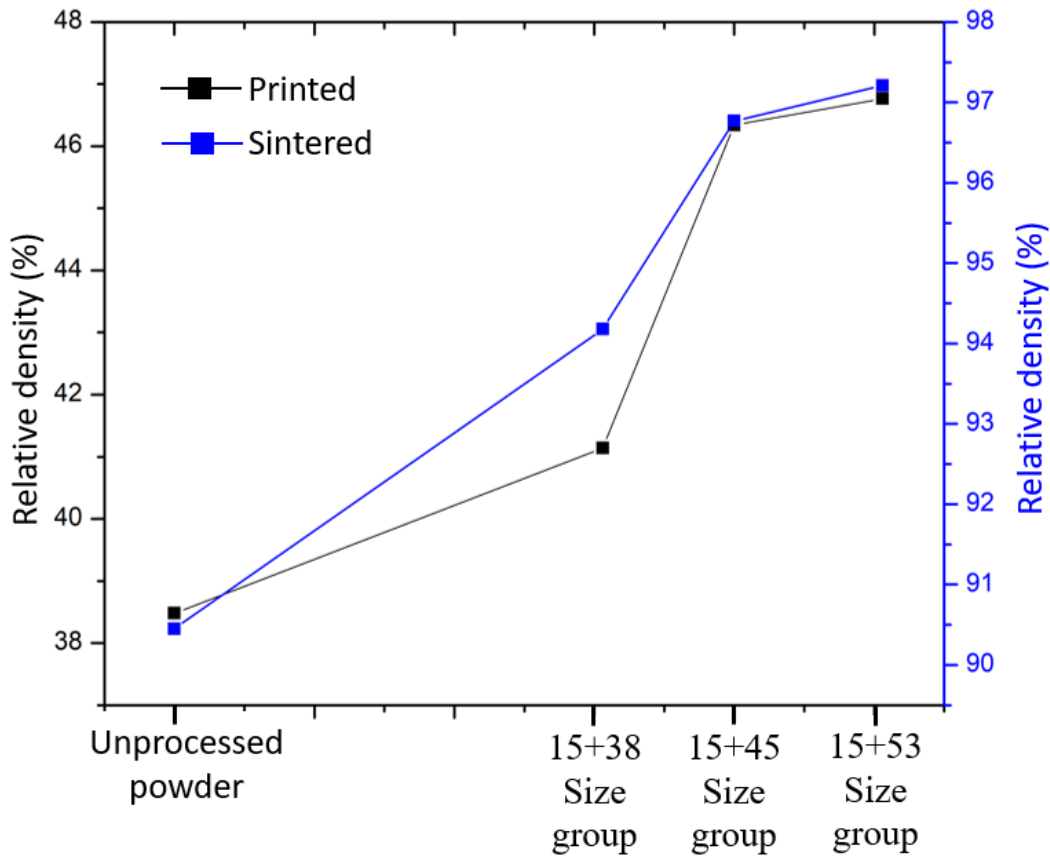


Figure 3.30 Effect of powder processing on green and relative densities of processed samples

Microstructural analysis of the sintered samples processed by the original and bimodal powders shows less porosity in the 15+53 μm size group bimodal powders when compared with the original unprocessed powder (Figure 3.31), in agreement with density measurements. EDS analysis of the microstructure revealed the presence of SiO_2 impurities as indicated by the red arrows in Figure 3.31.

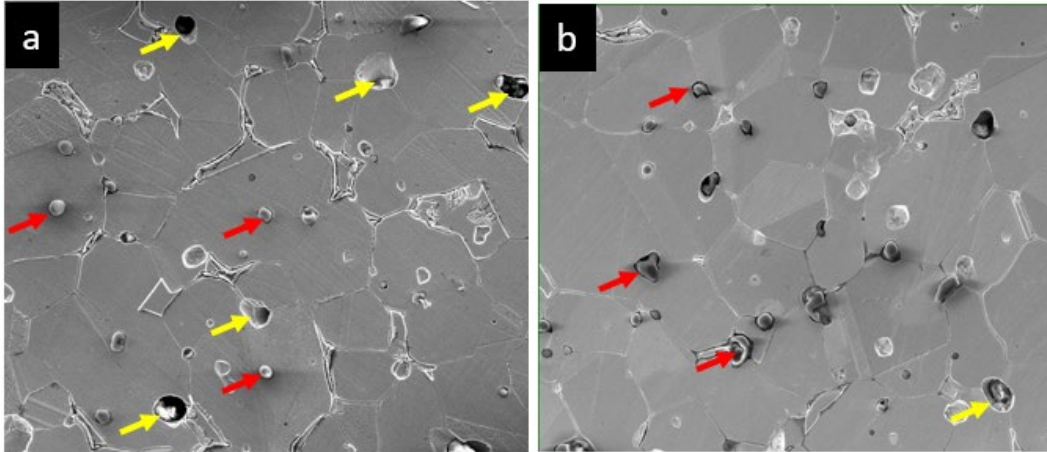


Figure 3.31 SEM micrograph of samples processed with (a) unprocessed water atomized powder (b) processed with 15+53 μm size group bimodal powder. Red arrows indicate SiO_2 impurities and yellow arrows indicate pores.

3.5 Process optimization for the SJ process

Even though the SLM and the BJ are both powder-based AM techniques, the BJ is very distinct in that it does not require the elaborate design for support structures [100]. Also, the BJ AM technique does not involve the fusion of powder layers during the BJ process, rather, a subsequent heat treatment step is required to fully consolidate the parts. Because the BJ does not require particle fusion, the process can be done at ambient conditions allowing for reduced energy consumption during the printing process [173]. To further improve on the final sintered density of the gas atomized SS316L powder, an optimization was carried out.

3.5.1 SJ Materials and Method

For the SJ, the optimization was done using the Taguchi method. As with previous works [25, 65, 67, 174], the granular binder is a 1:1 mixture of sugar and maltodextrin premixed with the gas atomized SS316L powder prior to printing. A Taguchi orthogonal array design, comprising of 2 factors and 3 levels, was implemented in the Minitab 17 statistical software. The design factors

and levels are presented in Table 3.5. The roller speed and binder saturation levels were kept constant at 300 mm/min and 100 % respectively.

Table 3.5 Factors and levels implemented in Minitab 17 for the SJ optimization.

Factors	Level 1	Level 2	Level 3
Layer thickness (μm)	100	125	150
Binder content (%)	1	2	3

The various weight ratios of the gas atomized SS316L powder and the binder mixture were thoroughly mixed using a turbular mixer (WAB US Corp, New Jersey, USA) for 1 hour to ensure a homogeneous mixture. The water-based solvent or binder activator was composed of 8.3 vol% of Isopropyl alcohol (IPA), 8.3 vol% of diethylene-glycol and 83.4 vol% of deionized (DI) water. After printing, the green specimens were cured, depowdered and the relative densities of printed parts estimated using the Archimedes method.

In this study, the relative density of the SJ processed green part was the response criterion and the goal is to obtain the highest relative density values, requiring that “higher is better” characteristic-form is used during the statistical analysis. The analysis of the effects of the variable process parameters on the relative density of printed green parts for the SJ process was conducted using signal to noise (S/N) ratio and ANOVA analyses which are statistical procedures embedded in Minitab 17. Subsequently, a simple linear regression was carried out and the result was used to predict the optimal parameters to achieve high density for SJ processed green parts. With these predicted parameters, SJ was conducted and printed part characterized to confirm the prediction.

Microstructural analysis was conducted on polished and etched samples by scanning electron microscopy (SEM) (FEI Quanta 450, USA). The V2A solution with a composition of

20%, 5% and 75% volume concentration of HCl, HNO₃ and H₂O respectively was the etching solution. Etching time was approximately 60s. Final densities of SJ processed and Sintered parts were measured using the Archimedes' immersion method following ASTM standard C373-18 and the PSA 1090 gas pycnometer (Anton Paar, Graz Australia), and the average relative densities estimated by assuming a bulk density of 7.89 g/cm³.

Table 3.6 presents the S/N ratio and relative densities of green bodies obtained from our Taguchi's L₉ Orthogonal Array which highlights the influence of the SJ parameters (layer thickness and binder content) on the relative density values of the green samples processed at a constant roller speed during SJ.

Table 3.6 S/N ratio and relative densities of green parts obtained from Taguchi's L₉ Orthogonal Array for the SJ AM processing technique.

Layer thickness (μm)	Binder content (%)	relative density (%)	S/N
100	1	55	34.807
100	2	50	33.979
100	3	47	33.442
125	1	53	34.486
125	2	49	33.804
125	3	48	33.625
150	1	52	34.320
150	2	48	33.625
150	3	46	33.255

3.5.2 S/N analysis from Taguchi DOE for the SJ optimization

The influence of the various parameters on the relative density at all levels is shown in Figure 3.32a. It is evident from the difference between the maximum and minimum values of the mean of S/N ratios for the investigated SJ parameters, as can be deduced from Figure 3.32b, that

for the SJ AM technique, the more crucial factor that influences the density of processed green parts is the amount of the binder premixed with the metal powder.

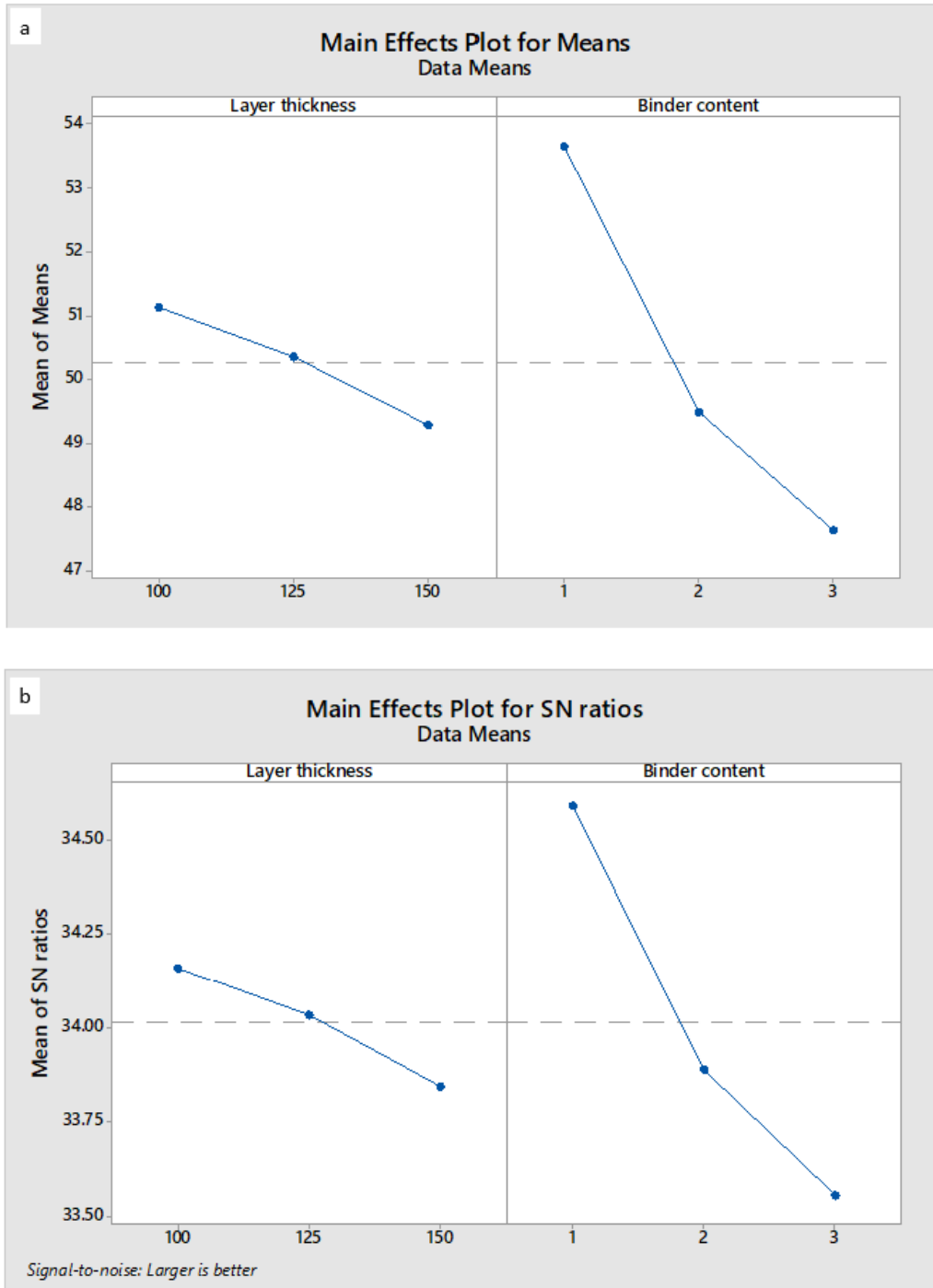


Figure 3.32 The main effects plots for the mean values of (a) relative density and (b) S/N ratio on the parameters investigated.

3.5.3 Regression analysis of SJ

A linear regression was also carried out using Minitab 17 statistical software package to develop an equation which models the relationship between the layer thickness, binder content and the relative density. The regression equation is as follows:

$$\rho = 60.91 - 0.0371l - 3.01c \quad (3.8)$$

where;

ρ is relative density of the printed green part,

l is layer thickness, and

c is binder content.

From the regression equation, optimized layer thickness, and binder content were estimated as 100 μm and 1%, respectively. Printing with these parameters yielded green parts with an average relative density of 52.57% even though the predicted optimal value was 54.19%.

SEM microscopy results of optimized samples sintered at 1380 °C show a remarked improvement in the microstructure of the samples as can be seen in Figure 3.33. Estimated relative density was about 98.76%. A more detailed microstructural analysis of the fully sintered part from the optimized SJ process will be discussed in chapter 5 along with a comparison with the microstructure of the optimized SLM processed part.

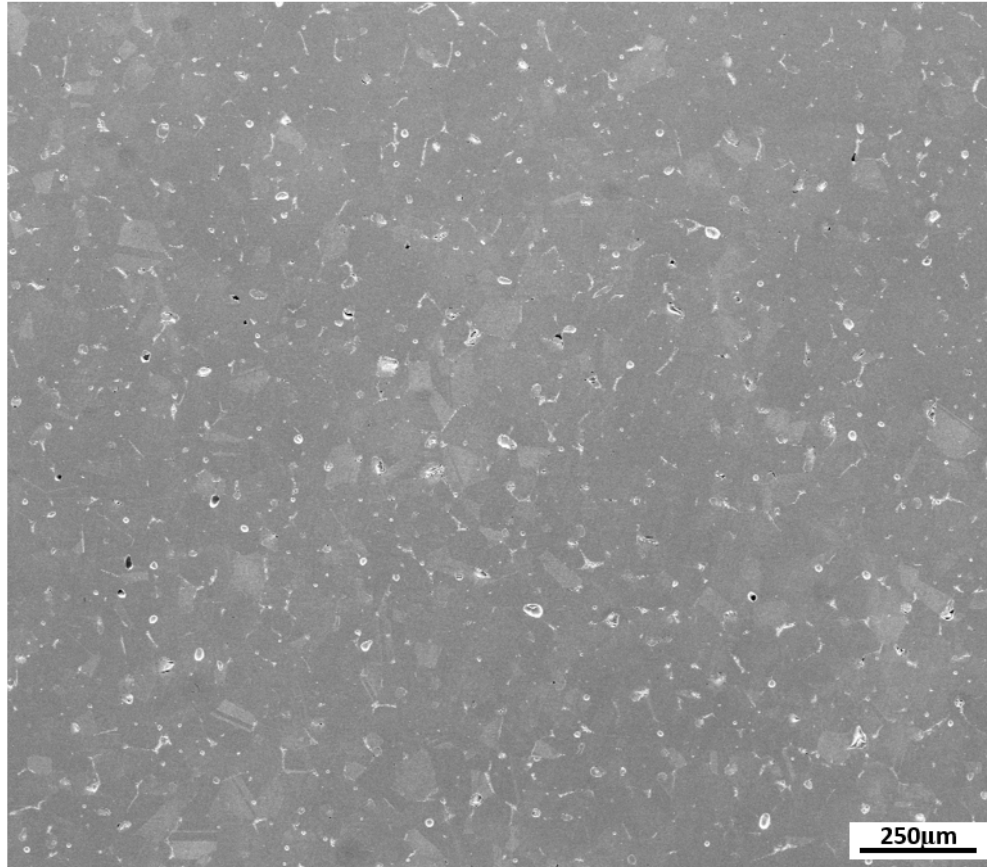


Figure 3.33 SEM micrograph of fully sintered part after optimization.

3.6 Pressure assisted solvent jetting

To further increase the density of the printed part, a novel means to apply pressure on the powder bed was developed. Following the previous work conducted by Olevsky and coworkers [143] on quasi-isostatic pressing (QIP), particularly the work on densification of porous bodies in a granular pressure-transmitting medium, we developed a novel and unique way of applying a quasi-isostatic pressure on the printed green sample by applying a uni-axial pressure onto the powder bed. The schematics for this process is presented in Figure 3.34 following [143].

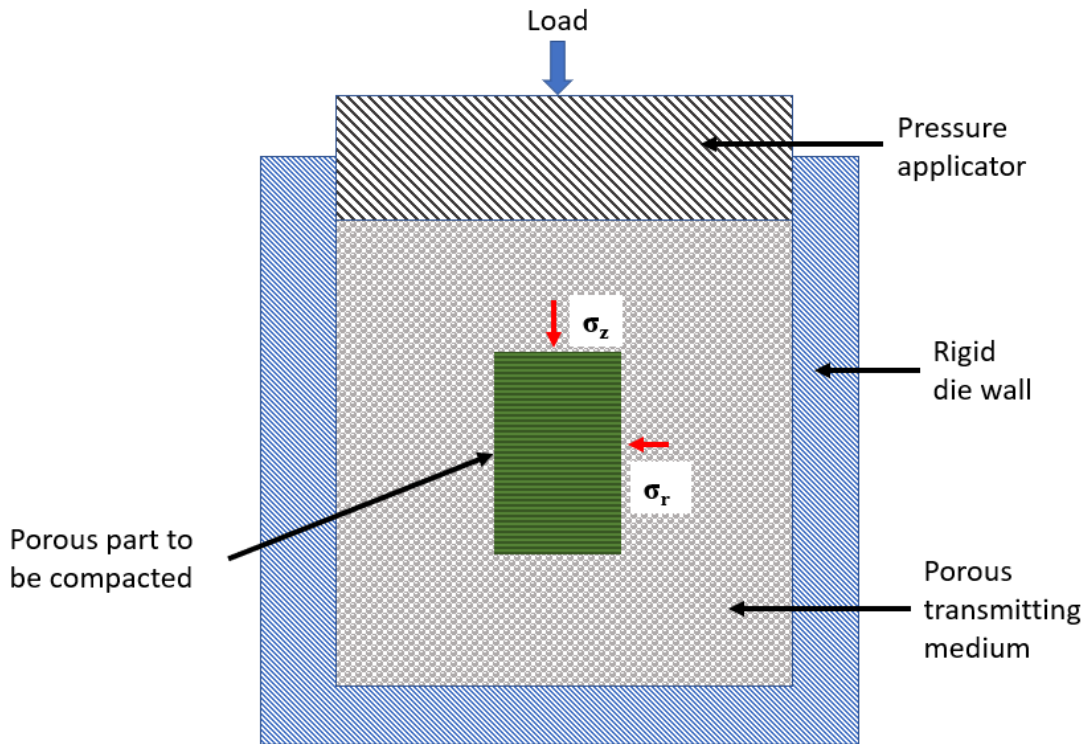


Figure 3.34 Schematics of the QIP process following [143]

Because of the nature of the SJ and BJ techniques, the QIP seems to be a way to compact the printed part by applying a pressure onto the powder layer that is spread over the printed layer. The pressure can be applied to the powder bed either in-situ or ex-situ. The in-situ powder bed pressing entails applying the pressure onto the powder bed during the printing process, either after each layer is printed or at the end of the final print. Although considerable work has been done and is still ongoing on this novel approach, it is outside the scope of this dissertation. In the ex-situ pressure application on the other hand, the entire build platform is transferred to an hydraulic press where the entire powder bed is compacted by a uni-axial load followed by curing and depowdering (Figure 3.35).

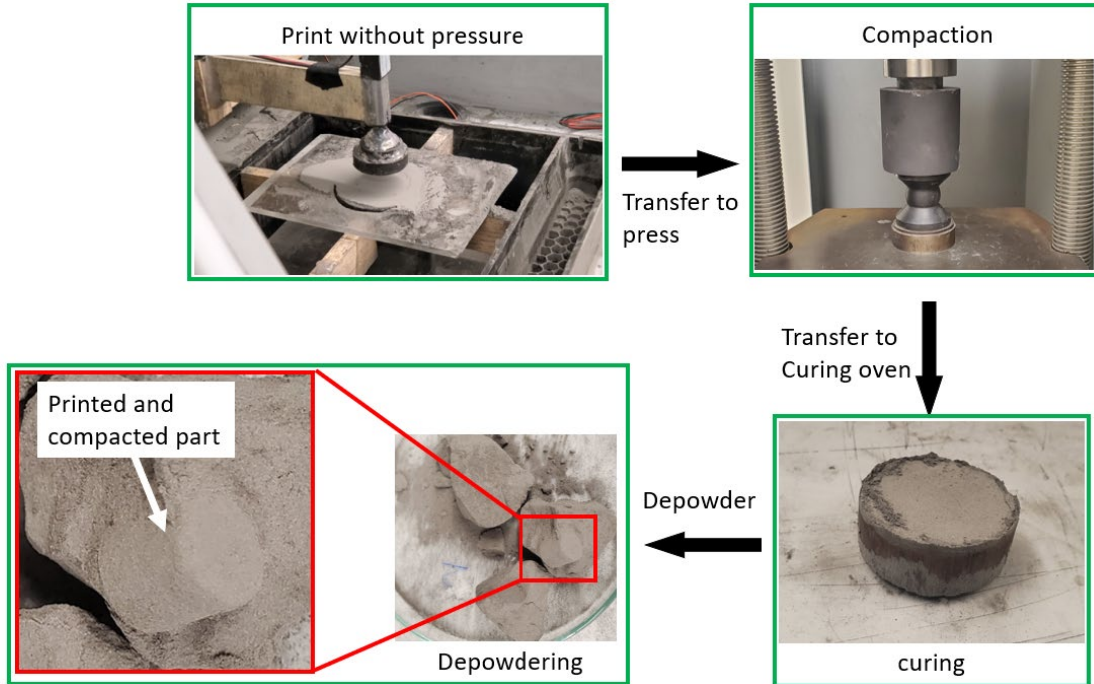


Figure 3.35 Steps involved in the ex-situ pressure assisted solvent jetting

During the powder compaction, the applied load is transferred from the surrounding powder unto the printed part, compacting it in the process. As depicted in Figure 3.34, the applied load is transmitted both axially (σ_z) and radially, (σ_r) onto the printed part.

The expected shape change after pressing, given as the ratio between the resulting axial and radial strains has been formulated and expressed as a function of the porosities of the part and the surrounding porous media as follows [143];

$$\frac{\dot{\epsilon}_{rr}}{\dot{\epsilon}_{zz}} = \frac{\theta - \theta_p}{2\theta_p + (1 - 3\theta_p)\theta} \quad (3.9)$$

Where;

$\dot{\epsilon}_{rr}$ = radial strain rate

$\dot{\epsilon}_{zz}$ = axial strain rate

θ_p = porosity of the transmitting medium and;

θ = porosity of the printed part.

From equation (3.9), it follows that when the density of the porous transmitting medium is equal to the density of the printed part, the radial strain rate equals 0, resulting in no shape change in the radial direction. Thus, to minimize shape change in the radial direction during powder compaction, the density of the printed part should be as close as possible to the density of the surrounding powder. This means that the properties of the printed part should be very similar to those of the surrounding powder. One way to achieve this is to use a very minimal binder amount in the printing process. To achieve this, instead of printing solid parts, attempts were made to print only the outlines of the part.

Due to the limitation imposed by the binder available for our experiments, printing very thin outlines of parts was not successful, thus, solid cylindrical parts were printed and thereafter the powder bed was transferred to a press and compacted.

Results showed that the relative density of the printed and compacted part increased to 52.6% from an initial value of 31.98%, indicating an increase of 64.5%. This increase in relative density was accompanied by an increase in the diameter of the cylindrical part of about 30%, however, this change in shape was almost uniform across the length of the cylinder as can be observed in Figure 3.36(c).

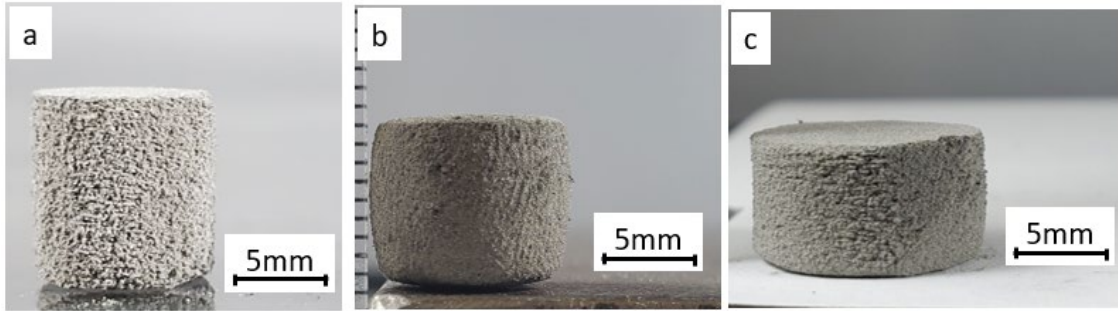


Figure 3.36 Samples (a) before compaction (b) after compaction with a single layer of powder above and below the sample during compaction (c) after compaction with several layer of powder above and below the sample during compaction.

It is clear from Figure 3.36(b) that when compaction is done with a very fine layer of powder above and below the printed part, barreling of the printed part occurs. This has been attributed to the adhesion of the top and bottom parts of the printed part unto the punch surface. This hinders the particles in the vicinity of the punches from moving with the rest of the part, thus resulting in a barreled part. On the other hand, when there is sufficient powder layer surrounding the entire printed part, barreling of the part does not occur (Figure 3.36(c)) as all the particles within the printed part are allowed to freely move in line with the forces acting on them.

3.7 Chapter conclusions

This work has shown that during B/SJ AM, processing route has an impact on the green density of printed metal powders irrespective of powder chemistry and morphology. For all powder systems investigated, decreasing layer height results in increased relative density of printed samples for both the BJ and SJ processing routes. More so, it has been shown that the binder content has a more pronounced effect on the density of printed green parts during solvent jetting.

Even though experiments were conducted using unique lab assembled 3D printers, it is safe to assume that results obtained are also obtainable with other 3D printing systems because the printers have similar work schematics with other conventional printers. Pursuing this, however, is

beyond the scope of the present study. Furthermore, it has also been shown that there is the need for debinding optimization to ensure total binder removal during debinding and good oxidation control during debinding and sintering.

Bullet Physics, Cinema 4D and EDEM packages have been used to model powder spreading during BJ additive manufacturing. Dimensional accuracy in this type of additive manufacturing necessitates the application of very thin powder layers at every additive step. The modeling of spreading of these layers with the thickness 2-3 particle diameters is questionable within continuous medium postulates. Discrete Element Modeling allows the prediction of the density evolution of the powder layer during spreading and the influence of the narrow and wide blade passage on the distortion of glued elements in the previously deposited layers. For the case of the powder spreading using a blade, it has been shown that all these effects are directly proportional to the square root of the difference between initial and final height of powder layers during spreading and inversely proportional to the thickness of the deposited layer. Results of powder spreading with a roller have additionally shown that the degree of part distortion increases with the roller rotational speed.

Taking into account all the relevant processing parameters, optimization of the solvent jetting process of the water atomized SS316L powder was successfully carried out with a net result of samples processed with a relative density of about 98.76%.

Finally, pressure assisted ex-situ compaction of the powder bed after printing was carried out with the aim of improving the relative density of the green part. Increase in the relative density of the green body after compaction was achieved, but at the expense of a slight change in the dimension of the printed part.

Parts of Chapter 3 have been published in the Rapid Prototyping Journal (I.D., Olumor, L. Geuntak, and E. Olevsky, (2021), "Effect of process route on powder three-dimensional-printing of metal powders", Rapid Prototyping Journal, Vol. 27 No. 2, pp. 399-406). The dissertation author is the primary investigator and author of this paper.

Parts of Chapter 3 have also been published in the Powder Technology Journal (A.L. Maximenko, I.D. Olumor, A.P. Maidaniuk, and E.A. Olevsky, (2021), "Modeling of effect of powder spreading on green body dimensional accuracy in additive manufacturing by binder jetting", Powder Technology, Vol. 385, pp 60-68). The dissertation author is the primary experimentalist and co-author of this paper.

Other parts of Chapter 3 are being prepared for publication (I.D. Olumor, E. Torresani, A.L. Maximenko, E.A. Olevsky, (2023) "Pressure assisted binder jetting". Prepared for publication). The dissertation author is the primary investigator and author of this paper.

Chapter 4

Optimization of High Energy Based AM for Defects Free Parts.

Just like all other conventional manufacturing techniques, AM techniques are associated with manufacturing defects which can lead to potential part failure during service. To fully understand and predict the behavior of parts during service, the part's physical and mechanical properties should be known and correlated to its microstructure. To this end, several research in recent times have been dedicated to the study of the microstructural characterization of AM parts and how the microstructure is influenced by the AM processing parameters. Also, optimization of AM process parameters has been carried out with the aim of minimizing part defects for better part performance in service [10]. Of the various forms of defects in AM processes, the ones that have gained considerable interest among researchers include excessive porosity and dimensional anomaly.

It should be mentioned that porosity in an AM part can sometimes be desirable if the application warrants a porous structure as in the case of certain biomedical applications [67]. But when it is not desirable, necessary steps should be taken during the AM process to reduce it to the barest minimum. In both instances, the pores should be quantified or characterized in order to properly predict the mechanical properties of the AM part. In this work, the pores are considered as unwanted defects, and means to minimize them by optimizing the laser dwell time are explored.

During SLM process, several defects are encountered including excessive porosity, part distortion, and residual stresses [[65, 83, 118, 175]. Of particular interest in the current work are the defects associated with excessive porosity. A type of porosity known as lack of fusion porosity have been shown to correlate with gaps in-between the melt tracks known as hatch spacing [76]. Hence, to mitigate these types of porosity, process parameters like hatch spacing, layer thickness,

and scanning speed should be optimized. To this end, a thorough understanding of the process parameters and how they influence the integrity of finished parts should be analyzed to ensure defects free parts.

There are several types and origins of porosity in SLM processed parts and thus require different strategies to be mitigated. Several works have been done to investigate pores resulting from melting mode of the melt track. With the improper melting mode, phenomenon such as lack of fusion, balling and keyhole formation may result in lack of fusion porosity, balling pores, and keyhole pores respectively. The origin for the formation of these pores has been given as: (i) melt instabilities due to hydrodynamic factors [74], (ii) insufficient dwell time allowing melt spreading [75], and (iii) poor wettability resulting from oxidation [76]. In this work, we will focus on pores resulting from insufficient pore filling time in dealing with AISI 316L austenitic stainless steel (SS316L)-WC composite system.

To fully understand the various modes of defects formation in AM parts, several techniques of monitoring and quantifying defects have been explored including in-situ and ex-situ techniques [105, 176, 177]. Of particular interest are the in-situ defects monitoring and measuring techniques as these allow for real time defects observation, measurements and possible mitigation steps as the process is underway. Recent works have shown some success in the ability to monitor and quantify defects in real time. For example, Jamison et al [176] have developed and demonstrated the capabilities of an in-situ monitoring system using full-field infrared thermography to monitor AlSi10Mg specimens during SLM production. Their system was able to effectively detect lack of fusion (LOF) defects with detection success improving as the defect size increases.

For the analysis of metal and alloy systems manufactured through the SLM process, Ferro et al. [175] used a modified volumetric energy density (VED) that takes into account printing

parameters such as hatch spacing, scan speed, laser size and laser power and materials properties such as thermal diffusivity and absorptivity factors in assessing porosity during SLM.

In the quest to minimize part defects in powder bed AM, several works have been focused on understanding the process-property relationships in AM parts with the aim of improving on the predictability of the process. Jamison et al [178] reviewed existing relationships between material properties and processing variables on residual stresses and observed that residual stresses are more heavily dependent on process variables, with a slight linear dependence on materials properties such as thermal diffusivity and conductivity.

In this chapter of the dissertation, results from optimization of the SLM for porosity defects free parts are presented. First, single track experiments were conducted to get an insight to the effects of the various processing parameters on the melting of the powder particles. Once the single-track experiments were concluded, a full optimization of the SLM process part for pore free 3D part was conducted by printing multiple tracks and layers.

4.1 Qualitative examination of SLM printed SS316L single tracks.

4.1.1 Effects of SLM process parameters on printed SS316L single tracks.

This section deals with purely qualitative examination of printed single tracks. Here, single tracks were printed using pure gas atomized SS316L as the powder feedstock. For a successful print, the printed part should firmly adhere to the build plate, also referred to as the substrate in order to ensure that the printed part does not move out of position and also to ensure adequate heat transfer from the printed part unto the build plate. Therefore, in order to select the right substrate, single tracks were printed on copper and steel substrates. A visual examination was conducted to ascertain the best substrate that provides the optimum SS316L wettability. Secondly, once the right substrate or build plate material is determined, single-track-multiple-layer experiments were

conducted to investigate the influence of process parameters on the porosity of a thin layer of printed SS316L.

4.1.2 SLM Materials and Methods

Single track experiments were conducted using the Xact Metal XM200C SLM printer (Xact Metal, Inc. Pennsylvania, USA). Unimodal spherical gas atomized SS316L powders, with average D10, D50 and D90 values of 15, 35, and 50 μm respectively with a mean diameter of 38 μm , from Praixair S.T technology, Inc., Indiana, USA was the powder of choice. The Anton Paar PSA 1090 (Graz Australia) particle size analyzer was used for particle size analysis.

After printing, single-track samples were prepared for metallography, and thereafter the scanning electron microscope (SEM), (FEI Quanta 450, USA) was used to examine the microstructure of the printed samples. Printing parameters were chosen by trial-and-error method, but with guidance from reported work in the literature. Laser power and diameter were kept constant at 120 W and 100 μm respectively, while the laser speed was varied between 200, 600 and 1000 mm/s. Figure 4.1 presents the schematic of the single track, highlighting the process parameters, where d represents the laser diameter and v is the laser speed. The length L of all single tracks was 10 mm.

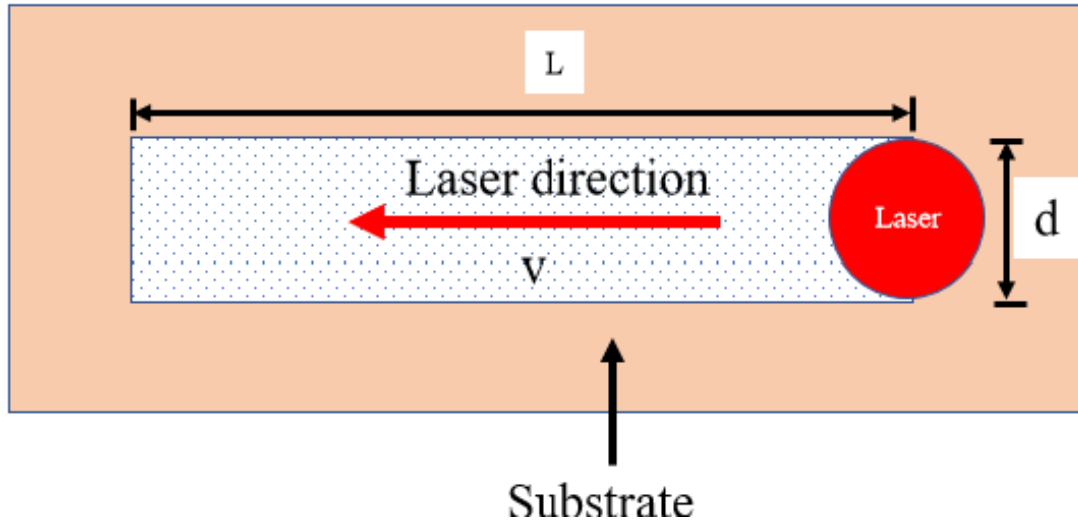


Figure 4.1 Schematic of single-track printing process

4.1.3 Results and Discussion

SEM analysis of printed single-tracks (Figure 4.2) showed that as the scanning speed increases, the printed tracks become more disjointed or discontinuous, a phenomenon known as sputtering. Also, using a copper plate as the substrate exacerbated the sputtering phenomenon and also showed poor attachment of the printed track onto the substrate when compared to using a steel plate as the substrate. It is evident from Figure 4.2 that a quite uniform track was formed at a laser speed of 200 mm/s when a steel substrate was used. The observed increased sputtering when using a copper plate as the substrate can be attributed to the poor wettability of SS316L on copper.

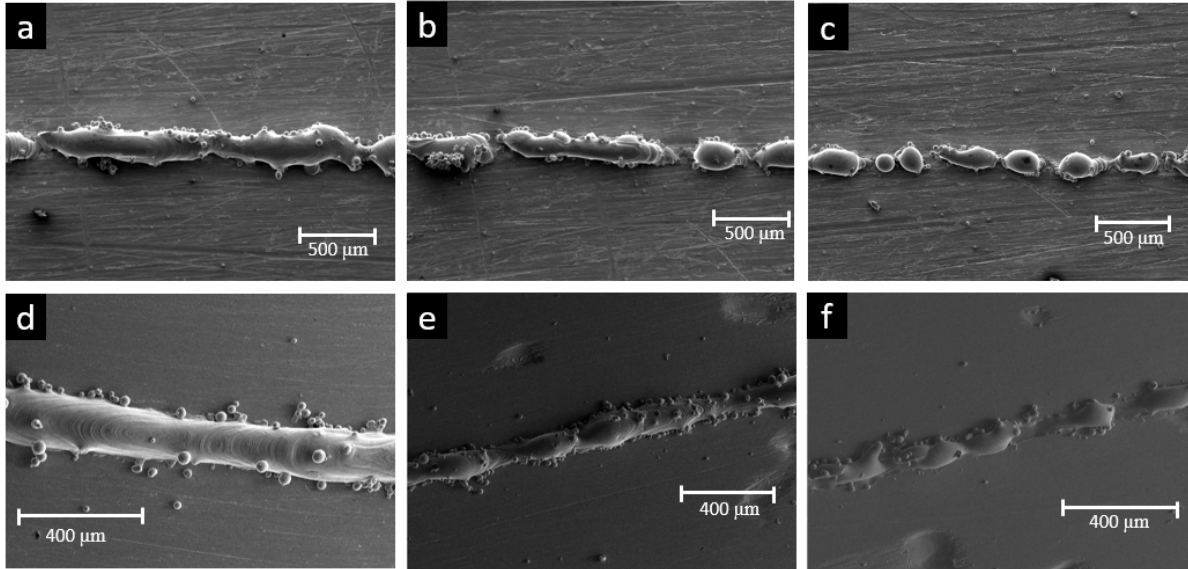


Figure 4.2 SEM images of Single-track specimens processed on a copper substrate at (a) 200 mm/s (b) 600 mm/s (c) 1000 mm/s; and processed on a steel plate at (d) 200 mm/s (e) 600 mm/s (f) 1000 mm/s.

SEM results of polished and etched single-track samples processed on a steel substrate showed that with increasing laser speed, the amount of partially or unmelted SS316L particles within the melt pool increases as shown in Figure 4.3. It was observed that samples processed at 200 mm/s (Figure 4.3(a)) had very little to no unmelted particles within the melt track. It is believed that due to the low speed, there is sufficient time for all particles to melt before the passage of the laser beam.

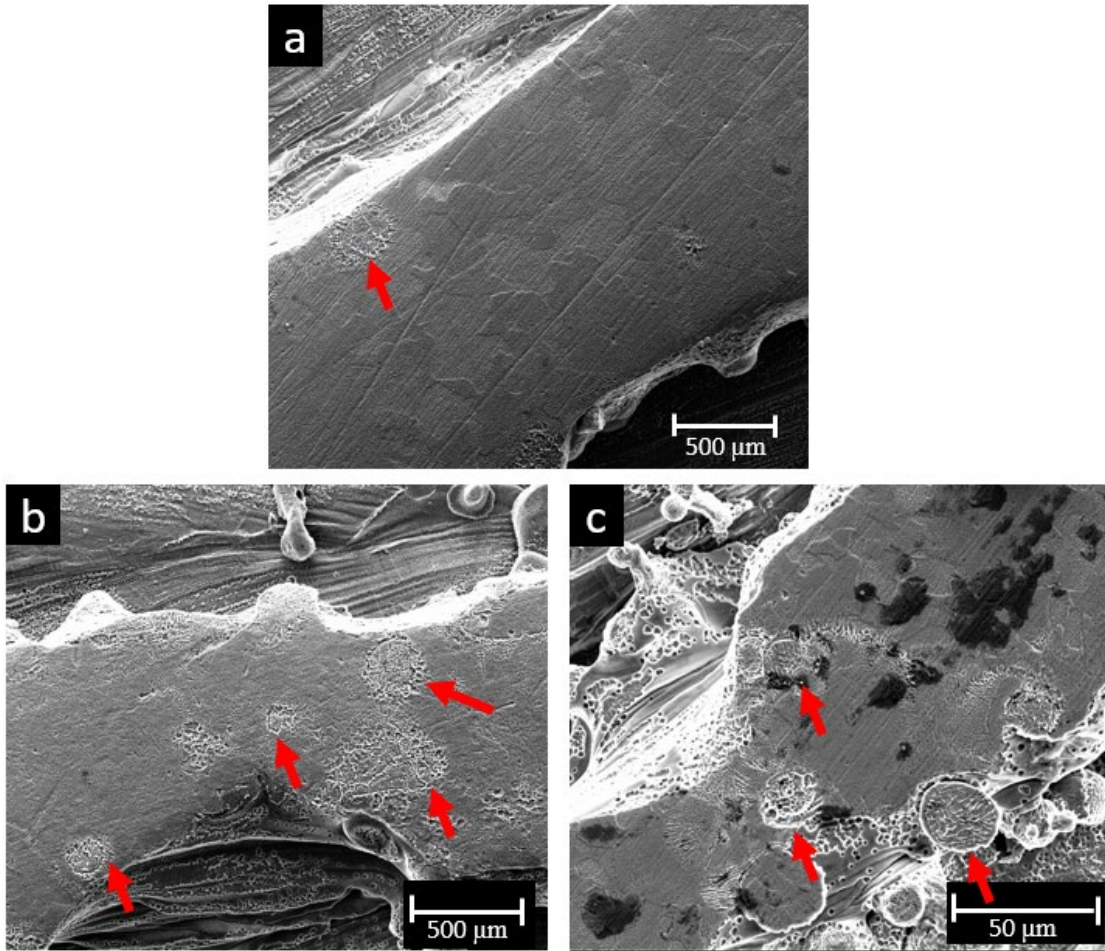


Figure 4.3 SEM micrographs of polished and etched single track specimens on a steel substrate processed at (a) 200 mm/s (b) 600 mm/s (c) 1000 mm/s. Red arrows indicating partially or unmelted SS316 particles within the molten track.

For single-track-multi-layered samples, SEM images showed that as the laser speed increases, the regions of unfused particles increase significantly (Figure 4.4). It is therefore quite clear that printing parameters that produce sputtering during the printing of a single track are not right for the printing of the bulk part as the defects in the tracks are carried on as the printing progresses.

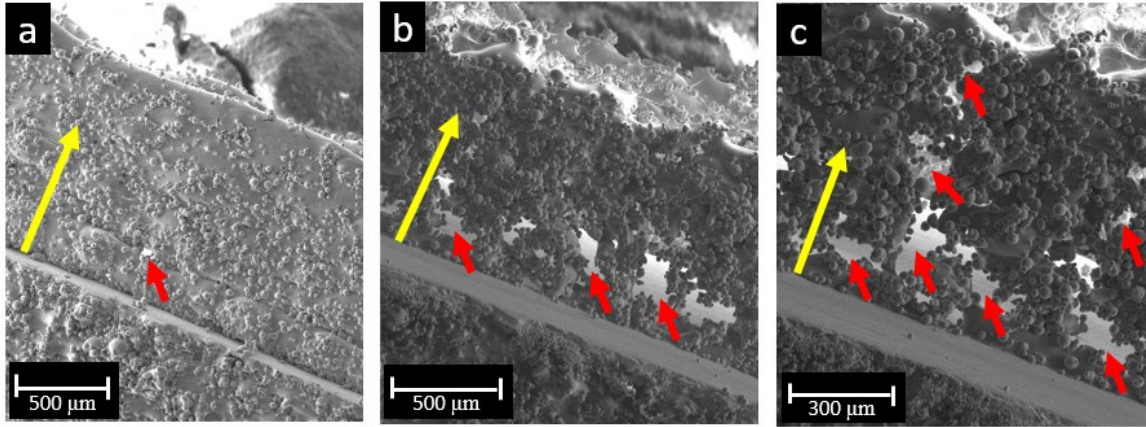


Figure 4.4 Printed single track, single layer specimens printed at (a) 200 mm/s (b) 600 mm/s (c) 1000 mm/s. Red arrows indicating areas with lack of fusion, and yellow arrow indicating the build direction.

4.2 Effect of laser dwell time on pore elimination in SLM of WC reinforced SS316L matrix composite: Experimentally validated modeling

4.2.1 Background to the study

The rate of application of particle reinforced metal matrix composites (MMCs) in the aerospace, automotive and defense industry has been on the rise in recent times. This can be attributed to their excellent mechanical and thermal properties such as high strength, good thermal stability, reasonable ductility, and their isotropy. A ready example of the application of MMC in the automotive industry is in the manufacture of brake disks [179]. The complexity involved in shaping MMCs by post-subtractive processes like machining has however stalled its wider adaptation [180].

MMCs also provide a unique class of materials for use in biomedical and space environments where extreme conditions dictate the use of materials with excellent biocompatibility, high specific stiffness, high thermal conductivity, extremely low coefficient of thermal expansion and superior thermal stability [181-183]. One such composite system for space

application is the aluminum based Al6061 MMC with boron particle reinforcements which has found use in certain parts of space shuttles [184].

The difficulty and prohibitive high cost of manufacturing MMCs have, however, hindered their widespread use, despite their numerous advantages. One such manufacturing difficulty is associated with the problem of non-uniform dispersion of reinforcing particles within the matrix, resulting in microstructural inhomogeneity. Another challenge faced during processing of MMCs is the poor wettability between the matrix and reinforcement particles. To mitigate the poor wettability, attempts have been made by various researchers to either coat the reinforcing particles with the metal or alloy system or to carryout heat treatment of the reinforcing particles prior to dispersing in the melt [185-187].

Despite the excellent properties of MMCs when compared to conventional materials, the complexity involved in shaping MMCs by post-subtractive processes like machining and prohibitive high cost associated with their manufacturing have stalled its wide industrial adaptation. This has led current research efforts towards focusing on alternative ways of manufacturing MMCs, one of such being additive manufacturing (AM).

There is currently a wide range of AM process techniques that are being used to manufacture parts made of polymers, metals, ceramics, and composites [14, 188-191]. These AM process techniques differ from the other conventional processing techniques in that parts are manufactured in a layer-by-layer fashion. One of such AM process techniques is the powder bed fusion technique (PBF) which allows the production of very complex shapes directly from a powder feed stock without the need for time consuming mold design or machining operations [192].

There are several forms of PBF, one of which being the selective laser melting (SLM). The SLM process technique involves the deposition of a powder layer on a build platform or previously processed layers, followed by selectively melting the deposited powder with a high energy laser beam in accordance with a cross section that corresponds to an input computer-aided design (CAD) file. Next, the build plate is lowered based on a predefined layer thickness, followed by spreading of a fresh layer of powder bed. This new powder bed is then selectively melted again in accordance with the next layer cross section as defined by the CAD file. The process is repeated until the manufactured process is completed [67, 93, 193]. With the use of the SLM technique, near net shape manufacturing is easily achieved, therefore post-subtractive operations are not required, making it ideal for manufacturing MMCs.

Porosity defects in MMC made by the SLM process are not well studied. To minimize porosity in MMCs during SLM, process parameters should be fine-tuned. Two of such parameters are the energy density and the laser dwell time.

Maximenko and Olevsky [73] have proposed a condition for minimum dwell time in order to achieve pore free composites. They analytically developed their criterion from the well-known Reileigh-Plesset equation and arrived at the following expressions:

$$t_p = \frac{2R_0\mu_0}{\gamma\left(1-\frac{\phi}{\phi_c}\right)^2} \quad (4.1)$$

$$t_p < \frac{L}{V} \quad (4.2)$$

where t_p is pore filling time (minimum time for melt to completely fill pores between ceramic particles within a melt pool); L is size of melt pool; V is speed of laser; R_0 is initial pore size between ceramic particles; μ_0 is viscosity of the liquid melt; γ is surface energy of liquid melt; ϕ is volume fraction of ceramic particles; ϕ_c is maximum packing fraction of ceramic particles within the melt pool.

From this condition, the ratio of the laser diameter to the laser speed, which is essentially the laser dwell time, should be greater than the pore filling time in order to print a pore free composite part. Hence, once the materials properties of the starting powder in Equation (4.1) are known, the printing parameters like laser diameter and speed in Equation (4.2) can be carefully selected for a pore free composite system.

In recent times, research efforts have been geared towards understanding the behavior of powder materials under different spreading modes during AM. The most common powder spreading techniques employed in powder-bed AM technologies include the use of a blade or a roller to level the powder bed surface [65]. This has necessitated the need to focus both experimental and modeling efforts towards the optimization of powder spreading to obtain optimal powder packing of the powder bed.

Zok et al. [194] used a statistical approach in their work on packing density of composite powder mixture to develop a model of particle packing in binary composite systems. Their results show that the effects of inclusions on the packing density suggests that the packing efficiency is governed by the volume fraction of the inclusions and the size ratio of particles and inclusions.

DEM efforts have been employed in the analysis of particle size distribution and morphology and how they affect particle packing in a powder bed. Haeri [95] used DEM to investigate the effects of particle shape and operating conditions on the bed quality of a powder bed and realized that larger particle aspect ratios, or higher spreader translational velocities resulted in a lower bed quality. Experimental and numerical analysis of void structure in random packed beds of spheres have shown the so-called wall-effect in powder packing. If particle sizes are of the same order as a powder volume, powder packing density decreases due to rearrangement

constraints of the particles. For example, maximum relative powder packing density ϕ_c evolves from 0.3 to 0.6 depending on the volume-to-particle diameter ratio [195].

It is evident from Equation (4.1) that, for the pore filling time to be calculated, the maximum ceramic particle packing within the powder bed prior to melting of the metallic/alloy particles should be correctly estimated. Hence, DEM analysis of powder packing to estimate maximum ceramic packing fraction within a melt pool is necessary.

The research direction of this work is therefore to experimentally determine the relationship between porosity and SLM process parameters such as laser size and speed, and in essence, the laser dwell time, in processing SS316L-WC MMC and compare our experimental results with model prediction put forward by Maximenko and Olevsky [73] with special consideration of inertia effects.

4.2.2 SLM Materials and Methods

Single experiments were conducted using the Xact Metal XM200C SLM printer (Xact Metal, Inc. Pennsylvania, USA). Unimodal spherical gas-atomized SS316L powders, with average D10, D50 and D90 values of 15, 35, and 50 μm respectively with a mean diameter of 38 μm , from Praixair S.T technology, Inc., Indiana, USA (Figure 4.5(a)), and unimodal irregular shaped WC powders, with average D10, D50 and D90 values of 50, 95, and 140 μm respectively with a mean diameter of 105 μm , from Atlantic Equipment Engineers Inc., New Jersey, USA (Figure 4.5(b)), were used for this study. The Anton Paar PSA 1090 (Graz Australia) particle size analyzer was used for particle size analysis. After printing, samples were prepared for metallography, and thereafter the scanning electron microscope (SEM), (FEI Quanta 450, USA) was used to examine the microstructure of the printed samples.

SS316L and WC powders were mixed in varying volume fractions of WC ranging from 0.3, 0.35 and 0.4. By taking into account the bulk densities of WC and SS316L, appropriate mass fractions were mixed to correspond to the desired volume fractions. Volume fractions have been calculated by assuming that the SS316L particles have a bulk density of 7.98 g/cm³, and WC particles have a bulk density of 15.63 g/cm³.

Samples were mixed thoroughly for 1 H to ensure homogeneous mixture using the Turbular mixer (WAB US Corp, New Jersey, USA). For single-track, single-layer experiments of the composite system, printing parameters were chosen such that the planar energy density for all prints was kept constant, while varying the dwell time (Table 4.1). Due to the power limit of our SLM printer, the maximum power output of 200W could not be exceeded for sample S7, hence the planar energy density for these samples was slightly lower than for all other samples.

Table 4.1 Printing parameters for single track experiments of WC-SS316L MMC

sample ID	laser power (W)	laser diameter (μm)	laser speed (mm/s)	dwell time (s)	planar energy density (J/mm ²)
S1	30	50	10	5.0E-3	60
S2	60	50	20	2.5E-03	60
S3	90	50	30	1.65E-03	60
S4	120	50	40	1.25E-03	60
S5	150	50	50	1.0E-03	60
S6	180	50	60	8.5E-04	60
S7	200	50	70	7.0E-04	57.14

The planar energy density, E_p , was estimated as follows [4].

$$E_p = \frac{P}{v * L} \quad (4.3)$$

While the dwell time, t_d , was estimated as;

$$t_d = \frac{L}{V} \quad (4.4)$$

where: P = laser power; V = laser speed; L = laser diameter.

During printing, a steady flow of ultra-high purity Argon gas (Airgas, California, USA) was allowed to flow through the build chamber in order to maintain an oxygen level within the build chamber that is below 0.3%. After printing single tracks on a single layer, samples were prepared for metallographic examination across both vertical and horizontal cross sections of the single tracks using the SEM. Pore sizes within the single tracks were estimated thereafter for all dwell times and WC content with the image-j software. The laser beam diameter was estimated taking into account size variation due to uncertainty that is normally associated with the laser beam diameter. To this end, an effective beam size, in accordance with the printer manufacturers recommendation was estimated as 50 μm and used in our analysis.

To estimate the dwell time, the laser speed and spot size as shown in the schematic in Figure 4.1 in the preceding section 4.1 were considered. Figure 4.5(c) presents a representative single track of the composite system after printing.

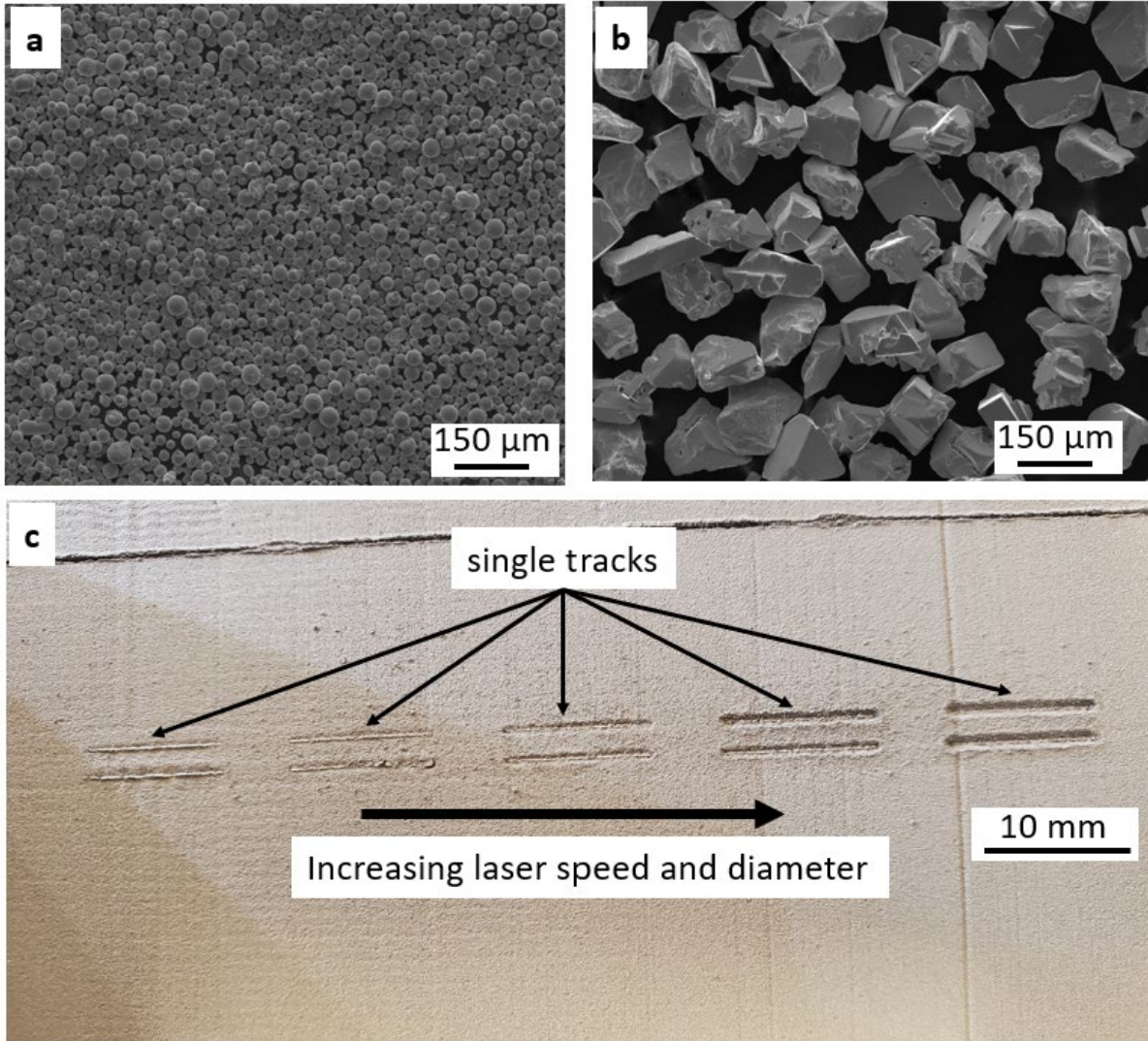


Figure 4.5 SEM micrographs of (a) SS316L powder (b) WC powder and (c) photograph of presentative composite single tracks after laser passage.

4.2.3 Setup of virtual experiment on SLM of WC reinforced SS316L

Our DEM analysis is based on the modeling of particle-particle collision dynamics using the EDEM simulation package (Altair Engineering, Michigan, USA). In order to simplify the simulation of powder bed process, which involves solving highly complex problems involving contact forces, there is the need for approximations. Thus, SS316L and WC were modeled as single-spherical particles with fixed diameters equal to average particle sizes of actual powders

used in the experiments. We assumed no adhesion between particles, hence the Hertz–Mindlin (no slip) contact mechanics model was selected for the simulation process. Material property data were obtained by referencing existing parameters and are presented in Table 4.2.

Table 4.2 Discrete element method parameters for the simulations

Property	SS316L	WC
Poison’s ratio	0.26	0.2
Bulk density	7.89g/cm ³	15.63g/cm ³
Shear modulus	74GPa	274GPa
Particle diameter	37.8μm	105μm

For the simulations, calibration was done using a combination of both real and virtual experiments in estimating the repose angle of the powders following [196-198]. Once calibration was done, the property values presented in Table 4.2, are then used in the model implantation. Based on our calibration, coefficient of restitution and static friction for all contacts were taken as 0.4 and 0.5 respectively, while coefficient of rolling friction was taken as 0.01 for all contacts. To account for the wall effect, powder packing was done in a hollow cylinder, with one end closed. The diameter and length of the cylinder was set equal the width and length of the single tracks so as to mirror the experimentally observed melt pool geometry.

Particles were randomly generated automatically within the cylinder by a static factory and allowed to settle under the influence of gravity with initial particle velocity set equal to zero. The number of each particle type was determined from the particle volumes to accurately yield the

volume fraction of each particle type. In our model implementation, the particle sizes were fixed for each particle type for simplicity.

4.2.4 Results and Discussion

For pore size estimation during microstructural analysis, an initial average pore size in the powder bed has been assumed equal to 150 μm which is well within the range of observed pore sizes between rigid inclusions in a metal matrix composite system with comparable particle size of rigid inclusions [199]. When, during analysis of micrographs, pores that are interconnected are encountered, we have assumed that these are a result of large pores with insufficient melt between ceramic particles, and therefore during sample preparation for metallography, loosely held WC particles fall out of position. This presents difficulty in estimating actual pore sizes for these single tracks. Therefore, when such a case arises, we assigned the initial average pore size to these pores.

Analysis of micrographs obtained using the SEM shows that for samples with 0.3 volume fraction WC particles, there are no observed pores when the samples were printed at dwell times of 5, 2.5, 1.65 and 1.25 ms. However, at dwell times below 1.25 ms, pores begin to appear, and increases in size as the dwell time is further decreased. Figure 4.6 shows representative SEM micrographs of single-track samples showing the presence or lack of pores at various dwell times for 0.3 volume fraction of WC.

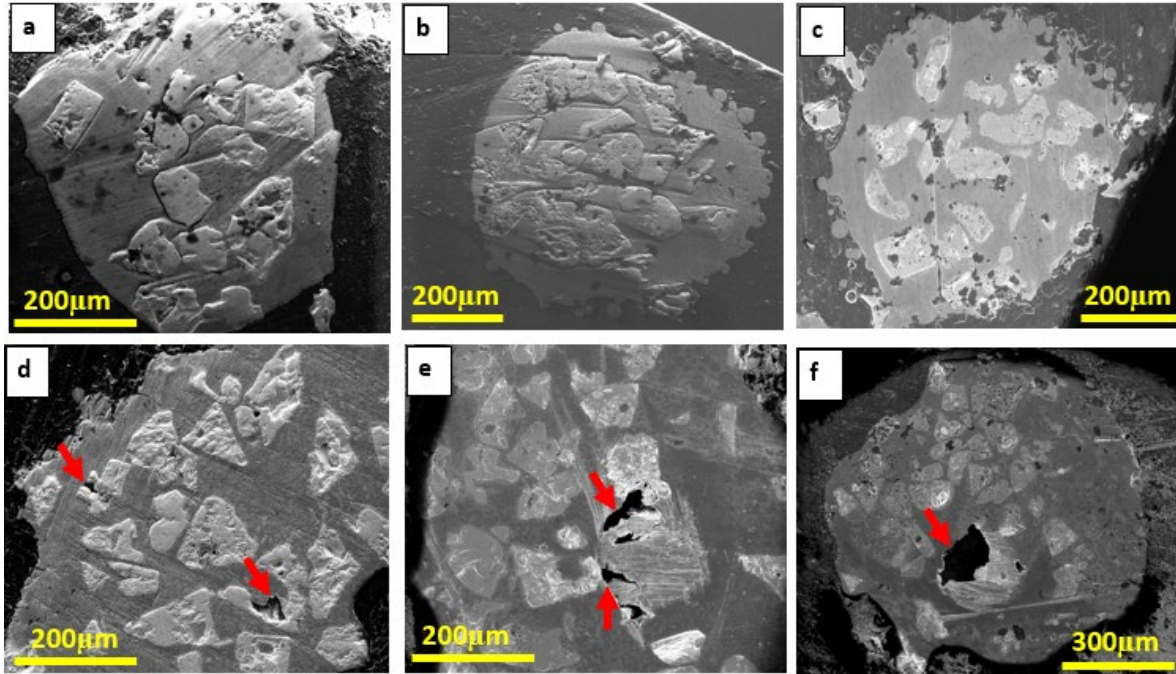


Figure 4.6 SEM micrographs of single-track samples printed with 0.3 volume fraction WC for dwell times of (a) 2.5 ms (b) 1.65 ms (c) 1.25 ms (d) 1 ms (e,f) 0.85 ms. Red arrows indicate pores. The direction of the laser beam is into the plane.

Regarding the analysis of micrographs for samples with 0.35 volume fraction WC particles, there are no observed pores when the samples were printed at dwell times of 5 and 2.5 ms. However, at dwell times below 2.5 ms, pores begin to appear, and increase in size as the dwell time is further decreased. Figure 4.7 shows representative SEM micrographs of single-track samples showing the presence or lack of pores at various dwell times for 0.35 volume fraction of WC.

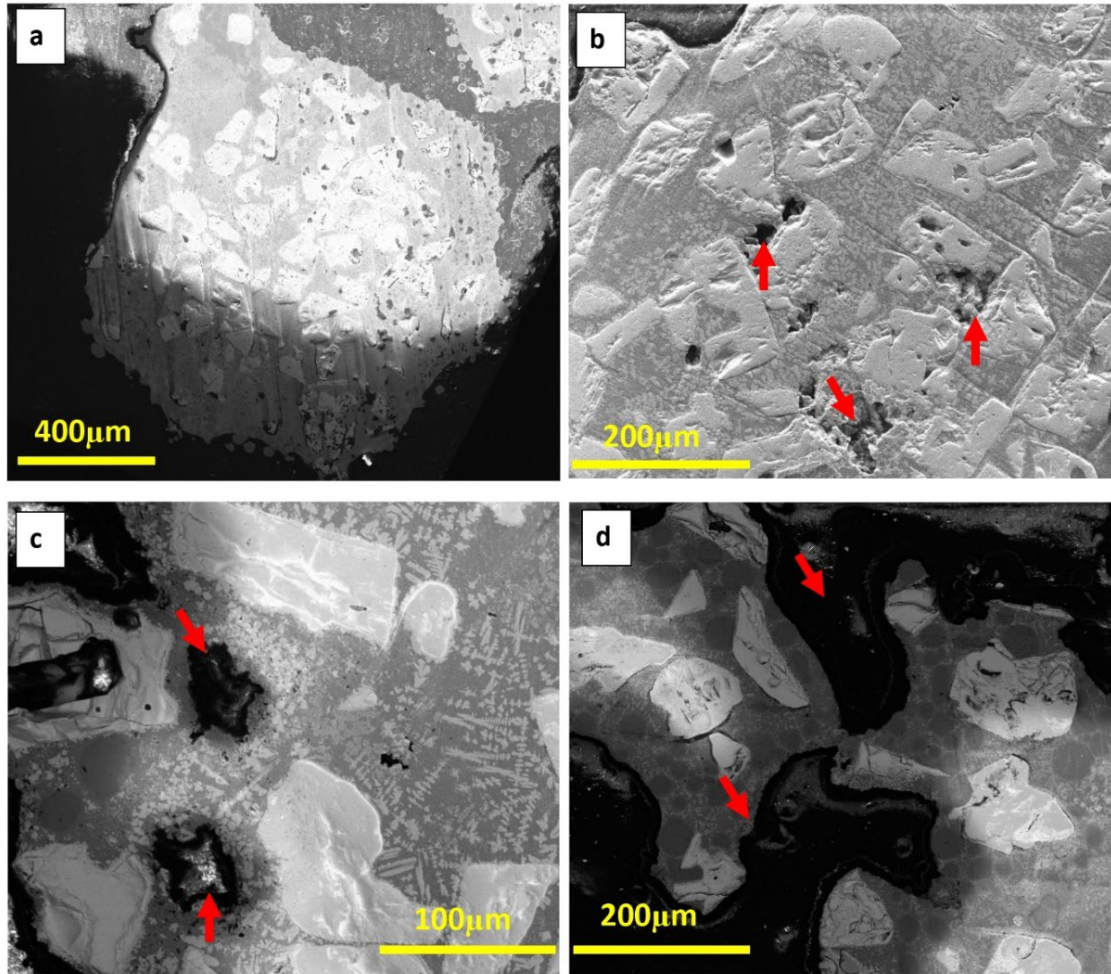


Figure 4.7 SEM micrographs of single-track samples printed with 0.35 volume fraction WC for dwell times of (a) 2.5 ms, (b) 1.65 ms, (c) 1.25 ms (d) 0.85 ms. Red arrows indicate pores. The direction of the laser beam is into the plane.

For 0.4 volume fraction WC particles, pores begin to appear quite early in the samples printed at 2.5 ms. Figure 4.8 shows representative SEM micrographs of single-track samples indicating the presence or lack of pores at various dwell times for 0.4 volume fraction of WC.

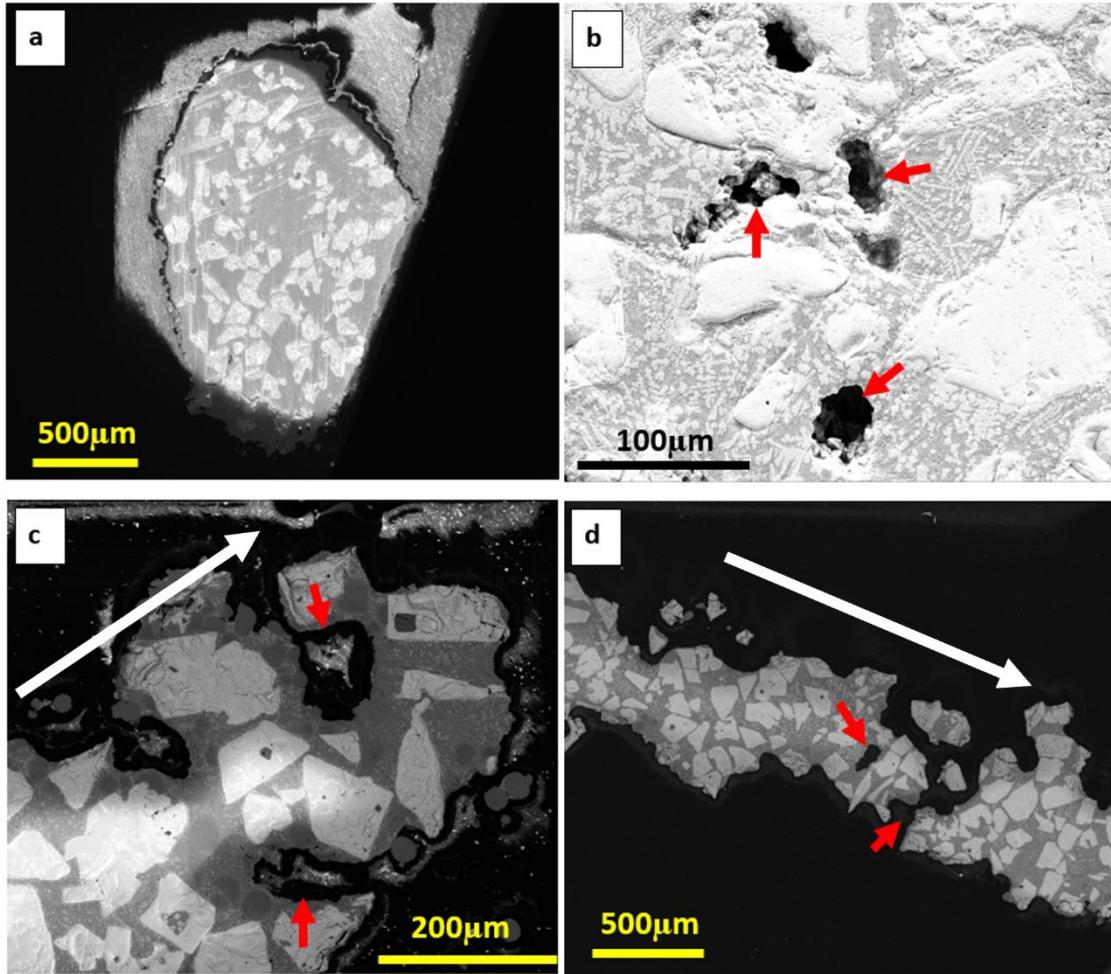


Figure 4.8 SEM micrographs of single-track samples printed with 0.4 volume fraction WC for dwell times of (a) 5 ms, (b) 2.5 ms, (c) 1.25 ms (d) 0.85 ms. Red arrows indicate pores. The direction of the laser beam is into the plane for (a) and (b), and as indicated by the white arrows in (c) and (d).

Results show that for all WC volume fractions, pore sizes increase with decreasing dwell time, as shown in Figure 4.9. Results also show that for 0.3 volume fraction of WC, we notice the absence of pores in the melt pool at dwell times greater than 1 ms. On the other hand, for 0.35 and 0.4 volume fractions WC, the time at which we begin to notice the absence of pores are significantly higher at dwell times greater than 1.65 and 2.5 ms respectively as is shown in Figure 4.9. The observed increase in dwell times for complete pore filling with increasing volume fraction of WC can be attributed to an increase in the effective viscosity of the melt pool as the fraction of

rigid inclusions increases, necessitating a longer time requirement for the melt pool to completely fill the voids between rigid inclusions in agreement with [200].

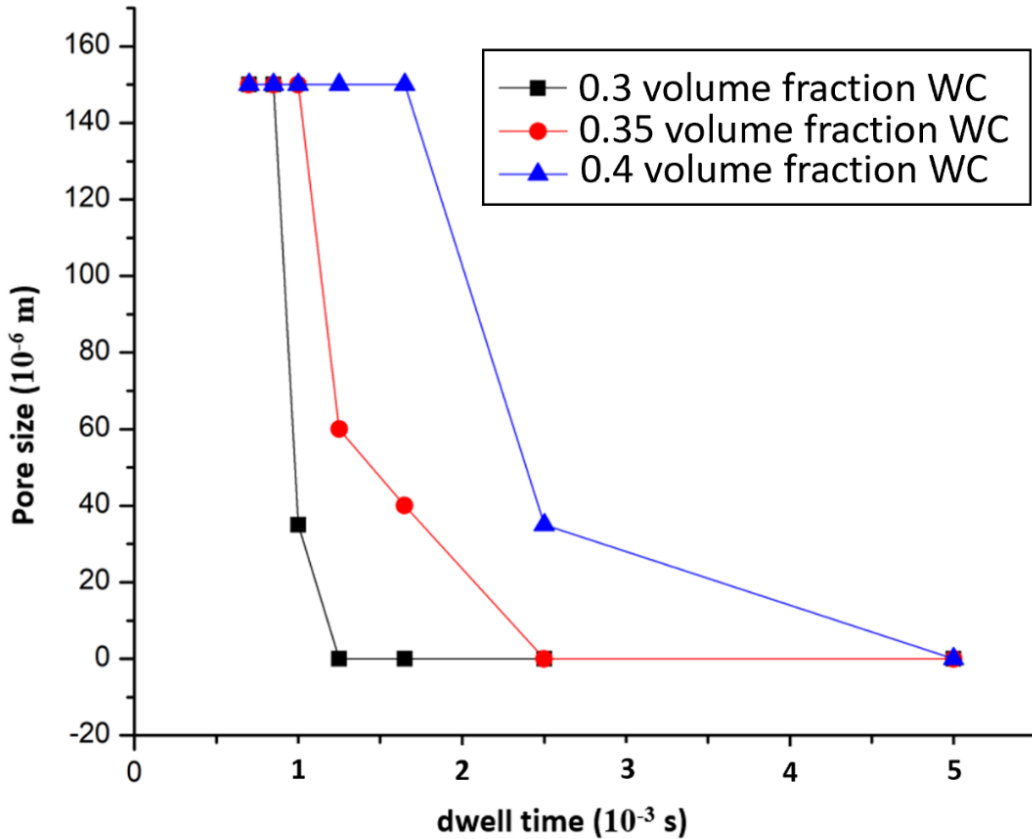


Figure 4.9 Effect of dwell time on pore sizes of single tracks with different vol fraction of WC

In order to compare our experimental results with the model criterion developed by Maximenko and Olevsky [73], we had to consider inertia effects when using the expression in Equation (4.1) to estimate the pore filling time, since for our case, the viscosity of the SS316L melt pool is very low and the WC rigid inclusions are large. To this end, for the various volume fractions of WC, we estimate the pore filling time, t_p , and compare with the corresponding dwell times, t_d , from our experimental results.

The surface energy and viscosity of SS316L were taken as 1.943 N/m and 6.45 mPa.s respectively, while the mean WC particle diameter was estimated as 105 μm . Experimental results (Figure 4.6-4.8) show the presence of the residual pores mainly between WC particles.

For composite powder packing with ceramic particle volume concentration more than 0.3, there are always pores surrounded only by ceramic particles without any steel particles. According to German [199], pore sizes in powder packing ranges from 0.225D for tetrahedral pores to 0.414D for octahedral pores can be as large as 1.9D for random packing, where D is the particle diameter.

Our modeling of powder packing during spreading of composite powder shows that pores between ceramic particles can be larger than 2D, particularly at regions close to the start of the build plate and their size reduces as the spreading proceeds towards the end of the build plate. This non-uniform spreading of the composite powder is due to the well-known phenomenon of particle-size-difference induced segregation effect [199]. This poses a problem in correctly estimating the actual initial pore sizes between WC particles and volume fraction of the WC particles within the melt pool. Hence, in our analysis, we have estimated pore filling time with consideration of 2 special cases viz; a case with very large pores, with pore size assumed to be equal to 2D, and the case for small pores with pore size assumed to be equal to D, where D is the WC particle diameter. These pores in our case are the largest ones in the powder bed and most difficult to fill because liquid metal should permeate between ceramic particles to get into the pore. We have also estimated and used effective volume fraction of WC within the melt pool from micrograph analysis of the melt pool for the various single tracks printed.

Evolution of the pore radius is described by the Rayleigh-Plesset equation given as:

$$\rho \left(R \frac{d^2R}{dt^2} + \frac{3}{2} \left(\frac{dR}{dt} \right)^2 \right) = P_g - P_\infty - \frac{2\gamma}{R} - 4 \frac{\mu}{R} \left(\frac{dR}{dt} \right) \quad (4.5)$$

But, unlike the case considered in [73], viscosity of the liquid metal is too small to dominate the pore collapse. In the case of our experiments, pore filling time t_p depends, mainly, on the maximum pore size in the powder packing, which can be quite large if one considers particle segregation effect during powder spreading due to the large difference between the WC and steel particle sizes. The left-hand term of Equation (4.5) takes into account inertia effect. Calculations of t_p were based on the finite-difference approximation of the Rayleigh-Plesset equation:

$$1.375\bar{R}_{i+1}^3 + \bar{R}_{i+1}^2(-2\bar{R}_i + 0.25\bar{R}_{i-1}) + \bar{R}_{i+1}\left(0.375\bar{R}_i^2 + \frac{2\mu}{\rho R_0^2}\Delta t\right) - \frac{2\mu}{\rho R_0^2}\Delta t\bar{R}_{i-1} + \frac{2\gamma}{\rho R_0^3}(\Delta t)^2 = 0 \quad (4.6)$$

Here, \bar{R}_i is the value of the dimensionless pore radius R/R_0 at the moment i , R_0 is the initial pore radius, and Δt is the time step, ρ is the liquid density, and γ is its specific surface energy. Viscosity of the liquid metal with ceramic particles was estimated as:

$$\mu = \frac{\mu_0}{\left(1 - \frac{\varphi}{\varphi_c}\right)^2} \quad (4.7)$$

where μ_0 is the viscosity of the liquid, φ is the volume concentration of ceramic particles, and φ_c is the maximum volume concentration of spherical particles in the melt.

In the step-by-step procedure, the relative pore radius at the moment $i+1$ was found as a solution of the cubic equation with coefficients depending on the radiuses from the previous moments and physical parameters of the problem. Initial maximum pore size depends on the homogeneity of a powder packing and in the bimodal packing it could reach values above two diameters of larger particles [199]. Because of uncertainty with the maximum pore size, we consider the interval of possible maximum pore sizes between $2D$ and D , where D is the diameter of the larger ceramic particles in the bimodal steel-ceramic powder bed mixture. In our case, ceramic WC particles had average diameter D equal to $105 \mu\text{m}$. Kinetics of the pore collapse for the $R_0 = D$ and $R_0 = D/2$ is shown in Figure 4.10.

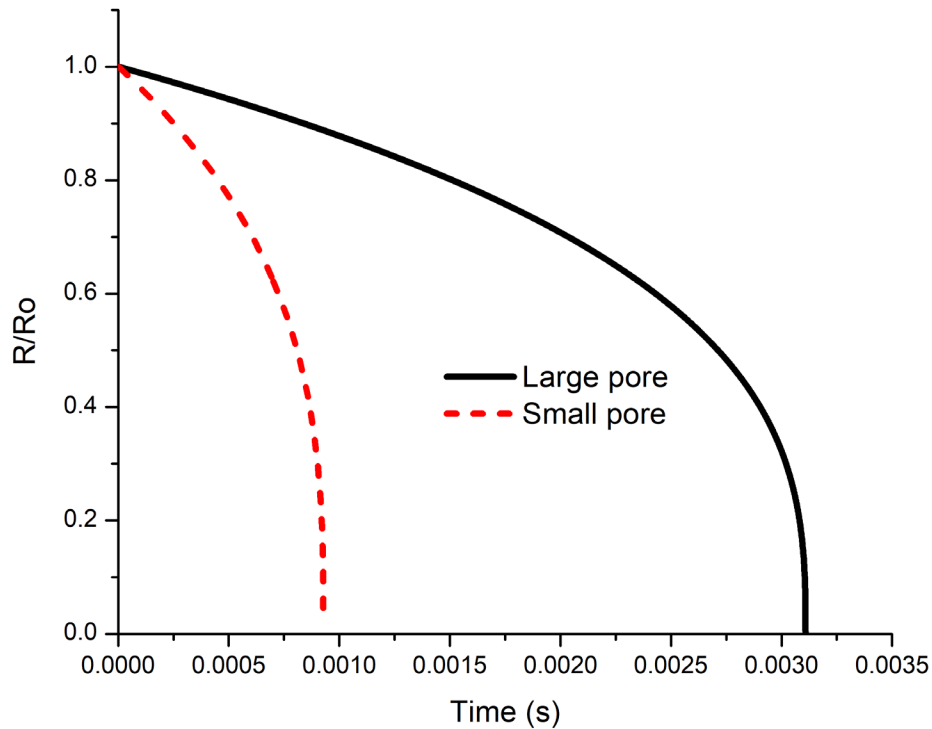


Figure 4.10 Kinetics of pore collapse for the various pore sizes considered.

To estimate the critical value ϕ_c , DEM simulations were carried out to estimate maximum packing fraction of WC. To determine maximum packing of WC particles, and to properly account for the so-called wall-effect, particles of SS316L and WC were randomly generated automatically within a cylinder by a static factory and allowed to settle under the influence of gravity. Thereafter, the steel particles are removed, and the WC particles are allowed to freely settle. After complete settling under gravity, WC packing is then estimated. Figure 4.11(a) shows packing of the composite powder mixture after freely settling, where the magenta-colored spheres represent SS316L alloy particles, and the green spheres represent WC particles. Figure 4.11(b), (c) and (d) presents the simulated packing for WC after the removal of the steel particles, the final state after freely settling to maximum possible packing, and the packing evolution, respectively.

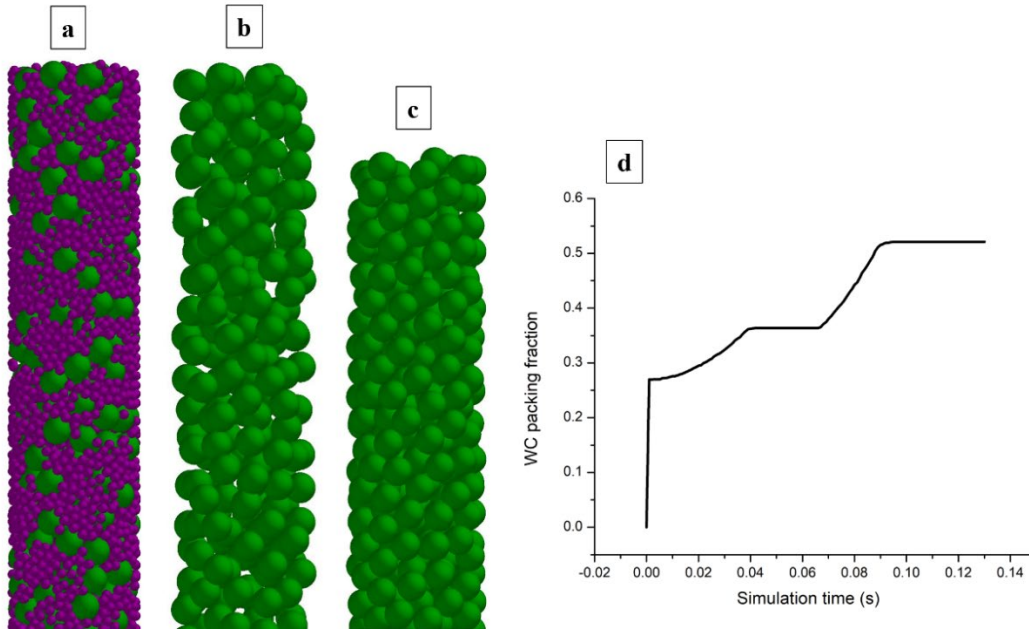


Figure 4.11 DEM simulation of powder packing (a) Powder packing of small and large particles (b) results with small particles removed (c) large particles allowed to settle freely (d) evolution of WC packing fraction over time.

Our DEM results, in agreement with [195], showed that, for our case with melt-pool to ceramic-particle size ratio being equal approximately to 5, critical concentration ϕ_c of ceramic particles is equal to about 5.2. Viscosity of the liquid steel was taken equal to 6.45 mPa.s. Viscosity increases with the increase of the ceramic particle volume concentration in agreement with [200]. Larger viscosity means lengthy pore collapse time. Estimation of the pore filling time t_p considering the interval of the pore collapse times for different relative volume concentrations of the ceramic particles is shown in Figure 4.12 for the different pore sizes considered.

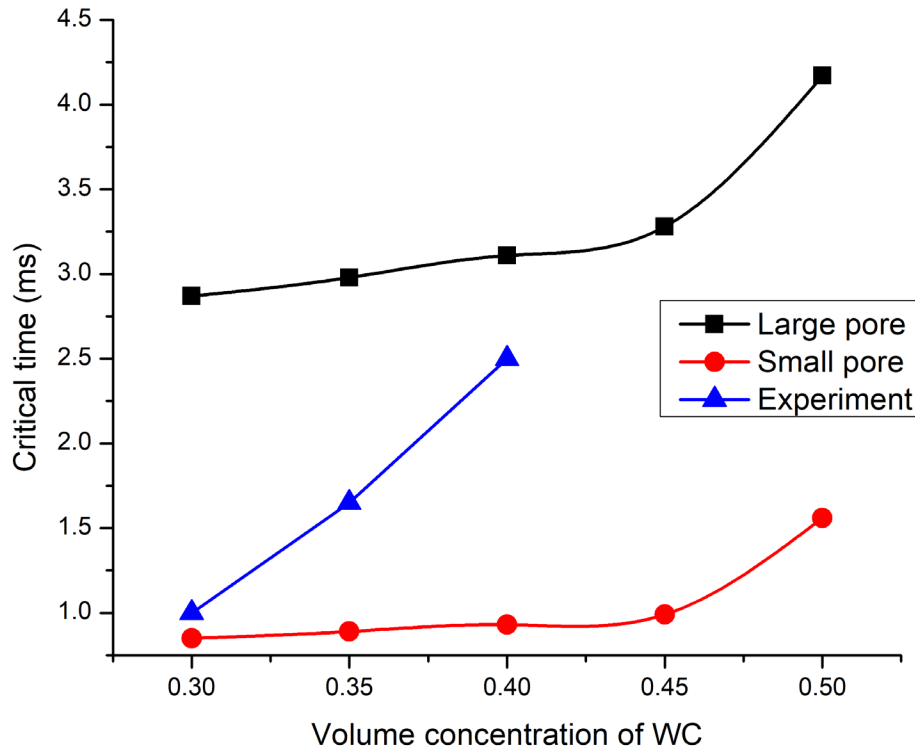


Figure 4.12 Effect of volume fraction of WC on critical time interval for pore-free laser treatment for the various initial pore sizes considered in model estimate and comparison with experimental observations.

The condition put forward in Equation (4.1), with the consideration of the effects of inertia, predicts that for a pore free composite with 0.3, 0.35 and 0.4 volume fraction of WC particles, pore filling time should be in the range of 0.89 to 3.11 ms for the initial pore sizes considered, otherwise, there will be no sufficient time for pore filling. When compared to the experimentally observed dwell times values of 1.0, 1.65 and 2.5 ms for 0.3, 0.35 and 0.4 volume fraction of WC respectively, as shown in Figure 4.12, we note that the experimentally observed dwell times for complete pore elimination falls within the model predicted values.

4.3 Effect of volumetric energy density and laser dwell time on relative density of SLM processed bulk SS316L parts

4.3.1 Background to the SLM of bulk SS316L study

In the processing of bulk components via SLM, we have to consider other parameters such as layer thickness and hatch spacing which do not come into play when dealing with single-tracks but are very important in the successful printing of bulk parts. To this end, it is usually not sufficient to define the energy density in terms of the planar energy density of equation (4.3). Usually, the energy density is defined as a volumetric term expressed in either two forms viz;

$$E_{VH} = \frac{P}{V*H*t} \quad (4.7)$$

$$E_{VL} = \frac{P}{V*L*t} \quad (4.8)$$

where E_{VH} and E_{VL} are the volumetric energy density defined by considering the hatch spacing and laser diameter respectively with units of J/mm^3 . Here,

P = Laser power

V = laser speed

H = hatch spacing

L = Laser diameter

t = layer thickness.

Most research, when considering the effect of the volumetric energy density of the SLM process on the density of processed parts have always taken into account only one of Equations (4.7) and (4.8). Results from these studies have always shown inconsistencies in the relationships between the energy density and the observed relative densities of processed parts, and as such the energy density has been said to be an unreliable metrics in predicting the outcome of the SLM process. In our work, we have sort to study the influence of the different energy densities defined

above and the laser dwell time defined by equation (4.7) on the relative density of SLM process parts.

4.3.2 SLM of bulk SS316L experimental procedure

Bulk processing of simple cubes with dimensions 10 mm x 10mm x 10 mm were carried out using the Xact Metal XM200C SLM printer (Xact Metal, Inc. Pennsylvania, USA). Unimodal spherical gas-atomized SS316L powders, with average D10, D50 and D90 values of 15, 35, and 50 μm respectively with a mean diameter of 31 μm , from Praixair S.T technology, Inc., Indiana, USA. After printing, the relative densities of processed samples were estimated by the Archimedes method. Samples were also prepared for metallography, and thereafter the scanning electron microscope (SEM), (FEI Quanta 450, USA) was used to examine the microstructure of the printed samples.

In order to study the effect of the various SLM processing parameters on the density of bulk SS316L, we set up a series of experiments with varying printing parameters as given in Table 4.3 with the aim of printing at different conditions of energy densities and laser dwell times. For example, we wanted to see the relationship between the relative density of processed parts and the laser dwell time when both E_{VH} and E_{VL} were kept constant, but not equal to each other, and when it is kept constant but equal to each other, etc.

Table 4.3 SLM parameters for processing bulk SS316L

Sample ID	Laser Power (W)	Hatch spacing (mm)	Scan Speed (mm/s)	Spot Size (mm)	Layer thickness (mm)	Dwell Time (10E-4s)	E_{VH} J/mm ³	E_{VL} J/mm ³
A1	120	0.08	200	0.05	0.05	2.50	150	240
A2	120	0.08	400	0.075	0.05	1.88	75	80
A3	120	0.08	600	0.1	0.05	1.67	50	40
A4	120	0.08	800	0.125	0.05	1.56	37.5	24
A5	120	0.08	1000	0.15	0.05	1.50	30	16
F1	120	0.08	200	0.05	0.05	2.50	150	240
F2	120	0.08	200	0.075	0.05	3.75	150	160
F3	120	0.08	200	0.1	0.05	5.00	150	120
F4	120	0.08	200	0.125	0.05	6.25	150	96
F5	120	0.08	200	0.15	0.05	7.50	150	80
G1	120	0.08	200	0.05	0.05	2.50	150	240
G2	150	0.096	250	0.05	0.05	2.00	125	240
G3	180	0.12	300	0.05	0.05	1.67	100	240
G4	210	0.16	350	0.05	0.05	1.43	75	240
H1	120	0.08	200	0.05	0.05	2.50	150	240
H2	100	0.08	200	0.05	0.05	2.50	125	200
H3	80	0.08	200	0.05	0.05	2.50	100	160
H4	60	0.08	200	0.05	0.05	2.50	75	120
H5	40	0.08	200	0.05	0.05	2.50	50	80
J1	120	0.08	200	0.05	0.05	2.50	150	240
J2	150	0.08	250	0.05	0.05	2.00	150	240
J3	180	0.08	300	0.05	0.05	1.67	150	240
J4	210	0.08	350	0.05	0.05	1.43	150	240
J5	200	0.08	400	0.05	0.05	1.25	125	200
K1	90	0.08	150	0.08	0.05	5.33	150	150
K2	120	0.08	200	0.08	0.05	4.00	150	150
K3	150	0.08	250	0.08	0.05	3.20	150	150
K4	180	0.08	300	0.08	0.05	2.67	150	150
K5	200	0.08	333.29	0.08	0.05	2.40	150	150

4.3.3 Results and Discussion

Results show that the laser energies and dwell time all have an effect on the relative density of the processed SLM parts, thus should be taken into consideration collectively, and not be dealt with in isolation from one another. For specimens processed at varying E_{VH} , E_{VL} and dwell times (sample A1 to A5), the relative density is seen to increase with increasing E_{VH} , E_{VL} and dwell time (Figure 4.13).

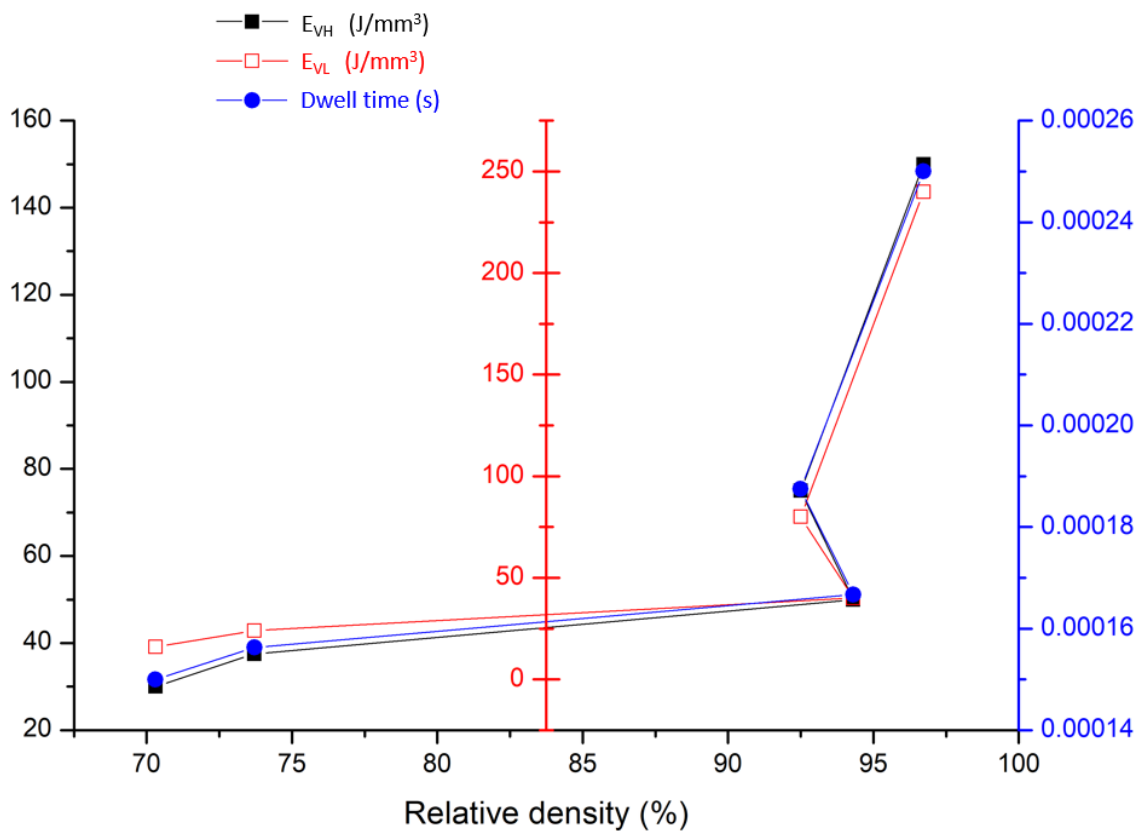


Figure 4.13 Effect of simultaneously varying E_{VH} , E_{VL} and dwell time on relative density of processed parts.

When one processes parts with a constant E_{VH} , resulting from constant laser speed, hatch spacing and power, one expects that there should be no change in the relative density. Our results have shown this to not be the case when the E_{VL} is changing due to changing laser diameter. For

example, Figure 4.14 shows results of samples (samples F1 to F5) processed at a constant E_{VH} of 150 J/mm^3 and constant laser scan speed and power of 200 mm/s and 120 W respectively but increasing laser diameter resulting in increasing E_{VL} and decreasing dwell time. It can be seen that the relative densities of processed parts increased with increasing E_{VL} and decreasing dwell time. Here, the E_{VL} had a more impact on the relative density than the dwell time.

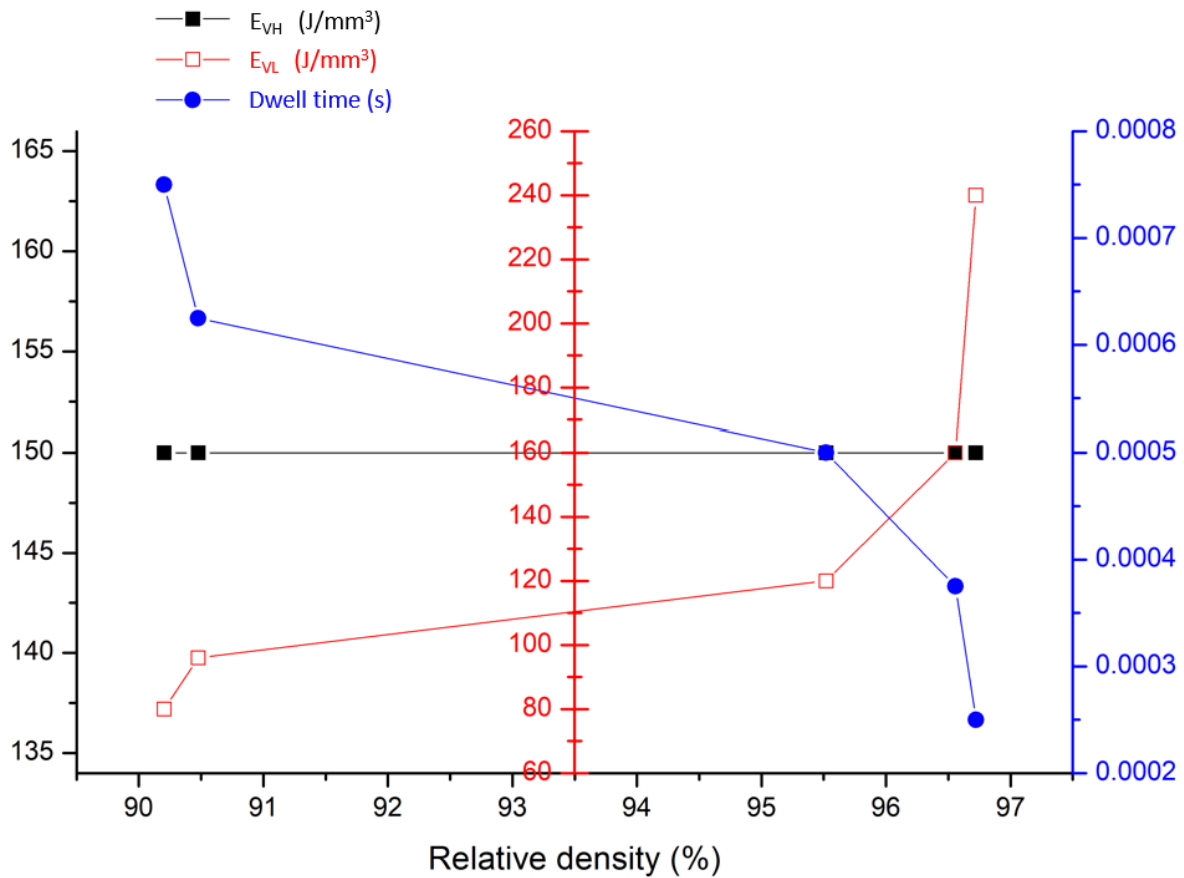


Figure 4.14 Effect of varying E_{VL} at a constant E_{VH} , on relative density of processed parts

When on the other hand E_{VL} is kept constant, but varying E_{VH} and dwell time (samples G1 to G4), we observed an increase in the relative density of processed parts with increasing E_{VH} and dwell time (Figure 4.15).

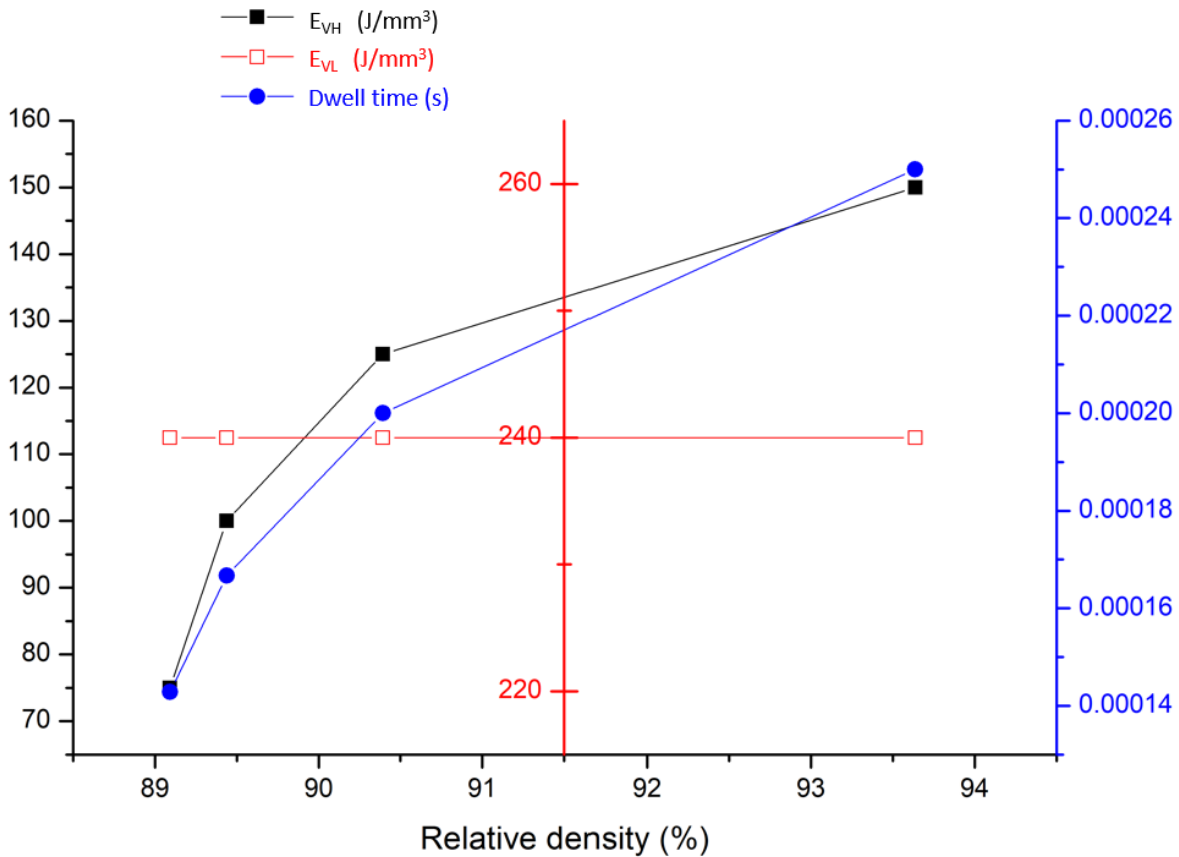


Figure 4.15 Effect of varying E_{VH} at a constant E_{VL} , on relative density of processed parts.

When the processing parameters were such that the dwell time was constant but increasing E_{VH} and E_{VL} as with samples H1 to H5, we observe an increase in relative density (Figure 4.16) with increasing energy densities. For samples (samples J1 to J5) processed at a constant E_{VH} and E_{VL} , but in which E_{VH} is not equal to E_{VL} due to differences between the hatch spacing and laser diameter, we observe an increasing relative density with increasing dwell time (Figure 4.17). When however, the constant E_{VH} and E_{VL} are made equal, as with the case of samples K1 to K5, we do not see any significant change in the relative density with change in the dwell time (Figure 4.18).

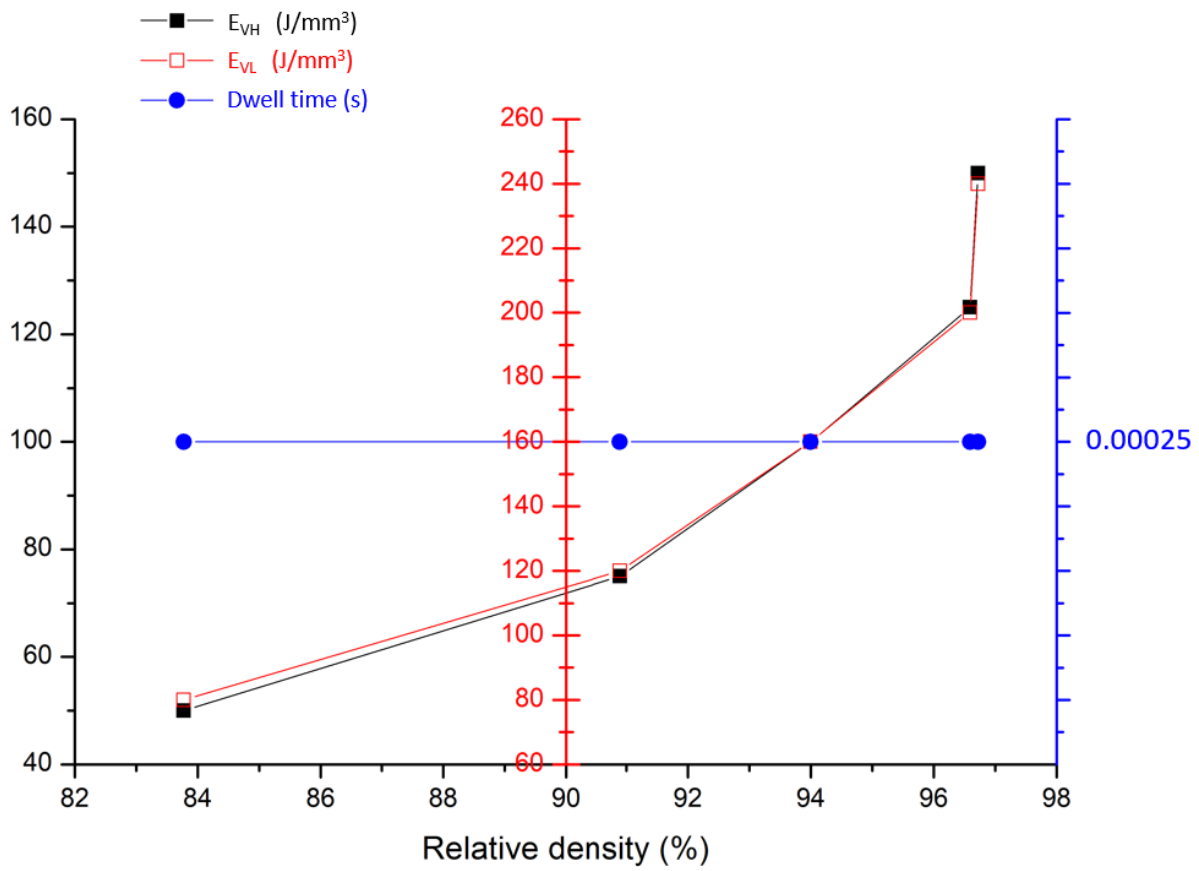


Figure 4.16 Effect of varying E_{VL} and E_{VH} , at a constant dwell time on relative density of processed parts.

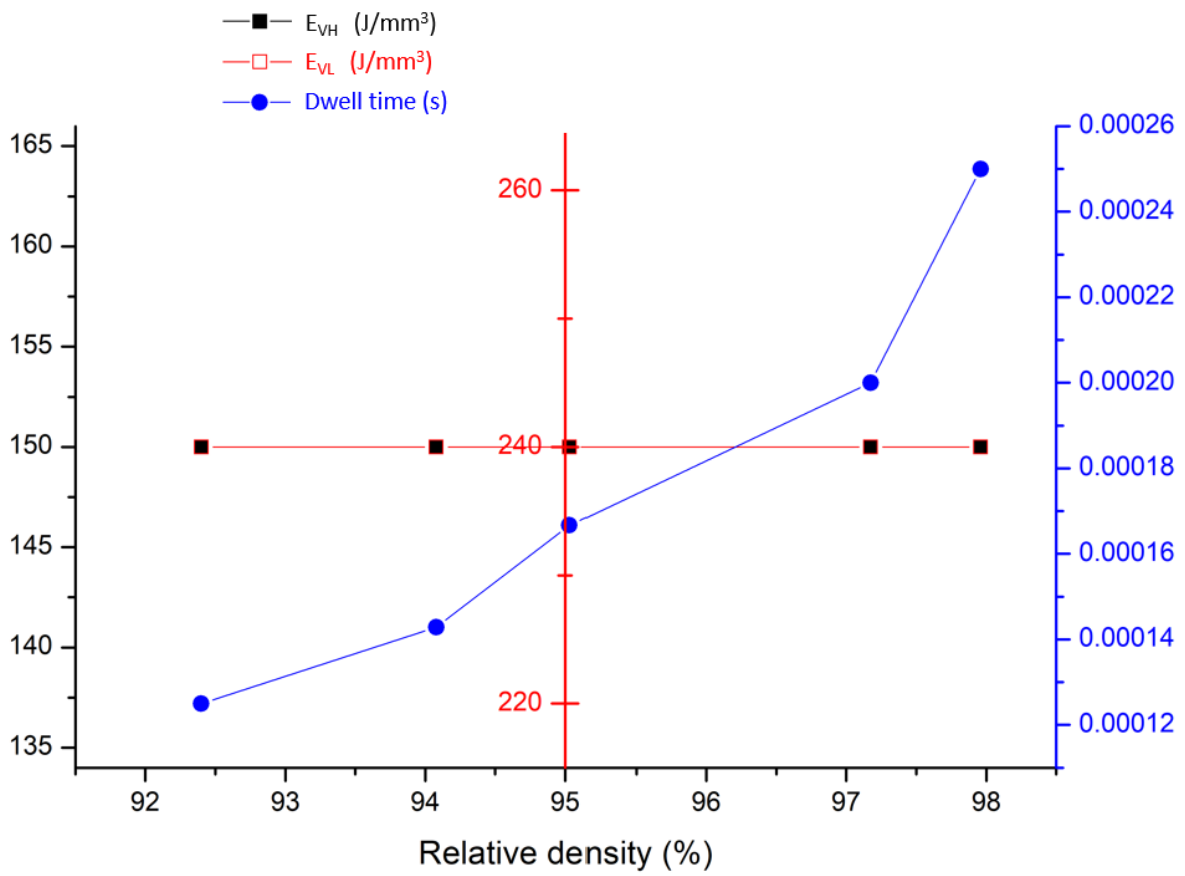


Figure 4.17 Effect of a constant E_{VL} and E_{VH} , and varying dwell time on relative density of processed parts when hatch spacing is not set equal to the laser diameter.

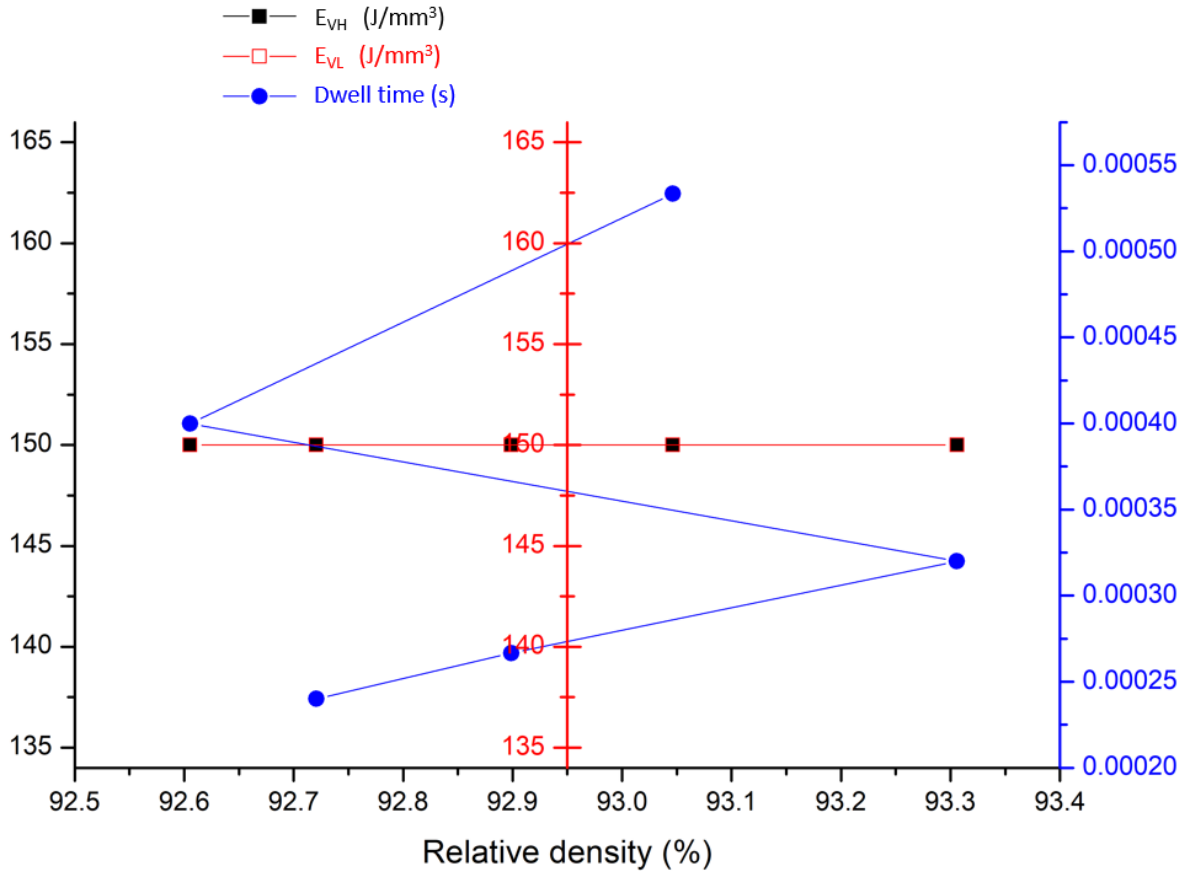


Figure 4.18 Effect of a constant E_{VL} and E_{VH} , and varying dwell time on relative density of processed parts when hatch spacing is set equal to the laser diameter.

From the foregoing, it follows that the SLM process involves very complex physics that cannot be adequately described by estimation of energy densities alone. However, our results have shown that varying process parameters such as laser power, speed, diameter, hatch spacing, and layer thickness affect the final density of the SLM processed part. To obtain fully dense parts therefore, these process parameters should be optimized.

4.4 Process optimization for the SLM processing of pure SS316L parts

Based on the results from the previous section, we were able to understand the critical roles of the various SLM parameters such as laser power, diameter, hatch spacing, speed and layer thickness. Next, we set out to fully optimize the printing process for pore free additive

manufacturing of SS316L parts. To this end, printing parameters were optimized by carefully selecting the various print parameters ranging from laser power, layer thickness, laser speed, laser diameter and hatch spacing. Optimization of the SLM process was conducted by employing the Taguchi Design of Experiment (DOE).

4.4.1 SLM Materials and Methods

During SLM processing, a bulb-shaped piece of silicon spreads the powder from the feed platform onto the build platform. Thereafter, a 200 W Ytterbium fiber laser, with a wavelength of 1070 nm, was used to selectively melt the powder bed in accordance with the cross-section area of the part to be printed as defined by the sliced 3D model of the part created using the magics software. After the passage of the laser beam, the build platform is lowered to a predefined height corresponding to the set layer thickness, while the feed platform is raised accordingly, and the spreader then spreads a fresh powder layer over the printed layer. The process repeats itself until the entire part is produced. Both the build plate and the feed platform move linearly in opposite directions and in accordance with the set layer thickness of the part to be printed.

A Taguchi orthogonal array design, comprising of 3 factors and 5 levels, was implemented in the Minitab 17 statistical software. The design factors and levels are presented in Table 4.4. The result of the Taguchi DOE is presented in Table 4.5

Table 4.4 Factors and levels implemented in Minitab 17 for the SLM optimization.

Factors	Level 1	Level 2	Level 3	Level 4	Level 5
Scan speed (mm/s)	200	400	600	800	1000
Layer thickness (μm)	50	75	100	125	150
Laser diameter (μm)	50	75	100	125	150

Table 4.5 Result of the Taguchi DOE

Group ID	Sample ID	Layer thickness (μm)	Scan speed (mm/s)	Spot size (μm)
Group A	A1	50	200	50
	A2	50	400	75
	A3	50	600	100
	A4	50	800	125
	A5	50	1000	150
Group B	B1	75	200	75
	B2	75	400	100
	B3	75	600	125
	B4	75	800	150
	B5	75	1000	50
Group C	C1	100	200	100
	C2	100	400	125
	C3	100	600	150
	C4	100	800	50
	C5	100	1000	75
Group D	D1	125	200	125
	D2	125	400	150
	D3	125	600	50
	D4	125	800	75
	D5	125	1000	100
Group E	E1	150	200	150
	E2	150	400	50
	E3	150	600	75
	E4	150	800	100
	E5	150	1000	125

To simplify our experimental runs, the laser power and hatch spacing were kept constant at 120 W and 50 μm respectively. Equipment, powder feedstock and processed cube dimensions were consistent with the previous section. Samples were printed in groups based on their layer thickness. As such, all samples with same layer thickness were printed in a single batch. In all, 5 groups were printed ranging from group A, B, C, D, and E corresponding to layer thicknesses of 50, 75, 100, 125 and 150 μm respectively (Table 4.5).

In this study, the relative density of the final processed SLM part was the response criterion and the goal is to obtain the highest relative density values, requiring that “higher is better” characteristic-form is used during the statistical analysis. The analysis of the effects of the variable process parameters, on the relative density of printed parts for the SLM process was conducted using signal to noise (S/N) ratio and ANOVA analyses which are statistical procedures embedded in Minitab 17. Subsequently, a multiple regression was carried out and the result was used to predict the optimal parameters to achieve full density for SLM processed parts. With these predicted parameters, SLM was conducted, and printed part characterized to confirm the prediction.

Microstructural analysis was conducted on polished and etched samples by scanning electron microscopy (SEM) (FEI Quanta 450, USA). The V2A solution with a composition of 20%, 5% and 75% volume concentration of HCl, HNO₃ and H₂O respectively was the etching solution. The Etching time was approximately 60s. Final densities of SLM processed parts were measured using the Archimedes’ immersion method following ASTM standard C373-18 and the PSA 1090 gas pycnometer (Anton Paar, Graz Australia), the average of these values was used in estimating the relative densities of the processed parts by assuming a bulk density of 7.89 g/cm³ for SS316L.

4.4.2 Results and Discussion

Photographs (Figure 4.19) of the final printed layer of the printed samples showed remarkable difference from one sample to the other, showing the influence of the varying process parameters on the melting and solidification of the powder particles. Visual examination of samples shows evidence of excessive energy input on some samples like E1, D1, C1 to name just a few. On the other hand, it is also evident that some samples were printed with insufficient energy, leading to insufficient melting of the powder particles resulting in layer detachment as is evident on examination of sample B5.

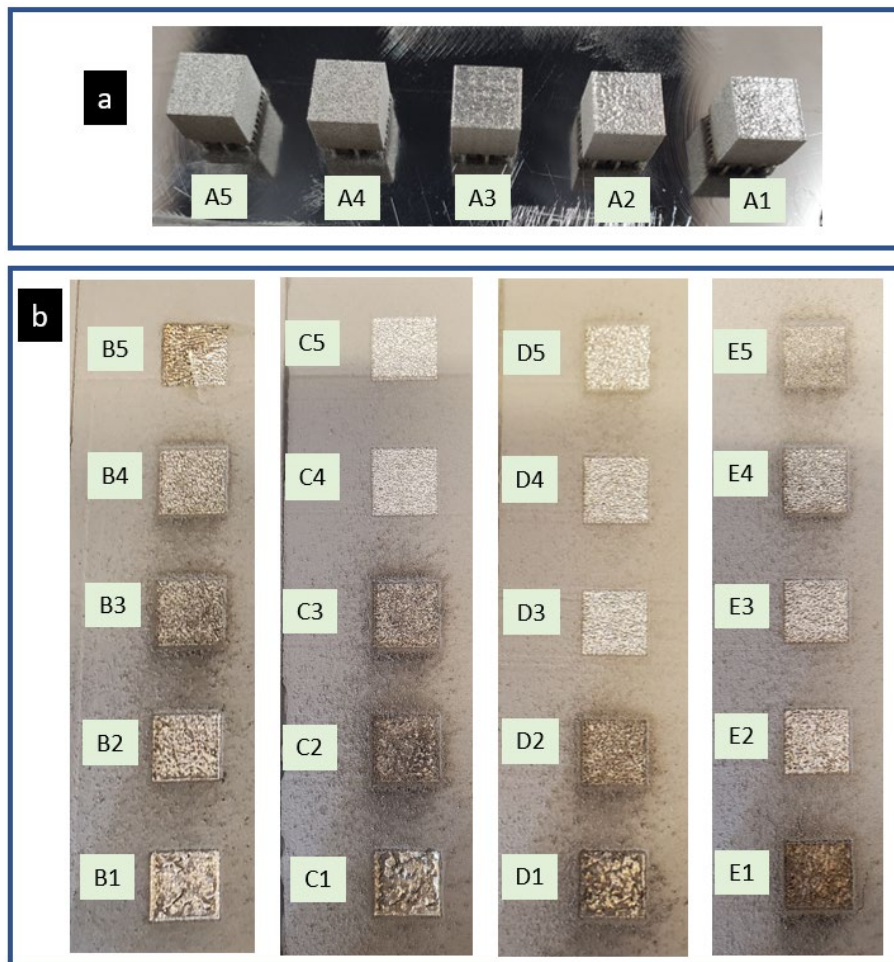


Figure 4.19 Printed samples (a) Group A after depowdering
(b) Groups B, C, D and E before depowdering

4.4.2.1 Relative density variation and S/N analysis from Taguchi DOE

Relative density estimation for the processed parts showed significant variation with the various processing parameters investigated. In order to estimate the influence of the various factors on the relative density of processed SLM parts, the means and signal-to-noise ratios (S/N) were estimated for each process factor. The signals are an indication of the effects of the various factors on the density output, while the noise is a measure of the deviations from the average density output, accounting for the sensitivity of the experiment output to the noise factors. To correctly estimate the S/N ratio, one should choose either of three categories of the quality characteristics in the analysis of the S/N ratio which includes 1) smaller-is-better 2) larger-is-better and 3) nominal-is-better. In our study, we have chosen larger-is-better as the criterion for our analysis of the S/N ratio since the higher the density output of our SLM process, the better the process is considered.

Table 4.6 presents the S/N ratio and relative densities obtained from our Taguchi's L₂₅ Orthogonal Array which highlights the influence of the SLM parameters (scan speed, layer thickness and spot size) on the relative density values of the processed samples processed at a constant laser power and hatch spacing.

Table 4.6 S/N ratio and relative densities obtained from Taguchi's L₂₅ Orthogonal Array

Sample ID	Layer thickness (μm)	Scan speed (mm/s)	Spot size (μm)	Relative density (%)	S/N
A1	50	200	50	96.72	39.710
A2	50	400	75	92.55	39.323
A3	50	600	100	94.31	39.491
A4	50	800	125	73.71	37.351
A5	50	1000	150	70.36	36.939

Table 4.6 S/N ratio and relative densities obtained from Taguchi's L₂₅ Orthogonal Array
(Cont'd)

Sample ID	Layer thickness (μm)	Scan speed (mm/s)	Spot size (μm)	Relative density (%)	S/N
B1	75	200	75	90.74	39.156
B2	75	400	100	89.10	38.998
B3	75	600	125	75.57	37.567
B4	75	800	150	72.34	37.188
B5	75	1000	50	60.15	35.563
C1	100	200	100	85.68	38.658
C2	100	400	125	81.81	38.256
C3	100	600	150	72.98	37.264
C4	100	800	50	75.54	37.564
C5	100	1000	75	71.68	37.108
D1	125	200	125	81.79	38.254
D2	125	400	150	71.59	37.097
D3	125	600	50	76.54	37.678
D4	125	800	75	70.17	36.923
D5	125	1000	100	66.39	36.442
E1	150	200	150	85.46	38.629
E2	150	400	50	67.82	36.627
E3	150	600	75	65.04	36.264
E4	150	800	100	62.59	35.930
E5	150	1000	125	58.45	35.269

The influence of the various parameters on the relative density at all levels is shown in Figure 4.20 (a). It is evident from Figure 4.20 (a) and (b) that the first level for layer thickness (50 μm) and scan speed (200 mm/s) provided the highest relative densities and S/N ratios, while the third level for laser spot size (100 μm) provided the highest relative density values and S/N ratios.

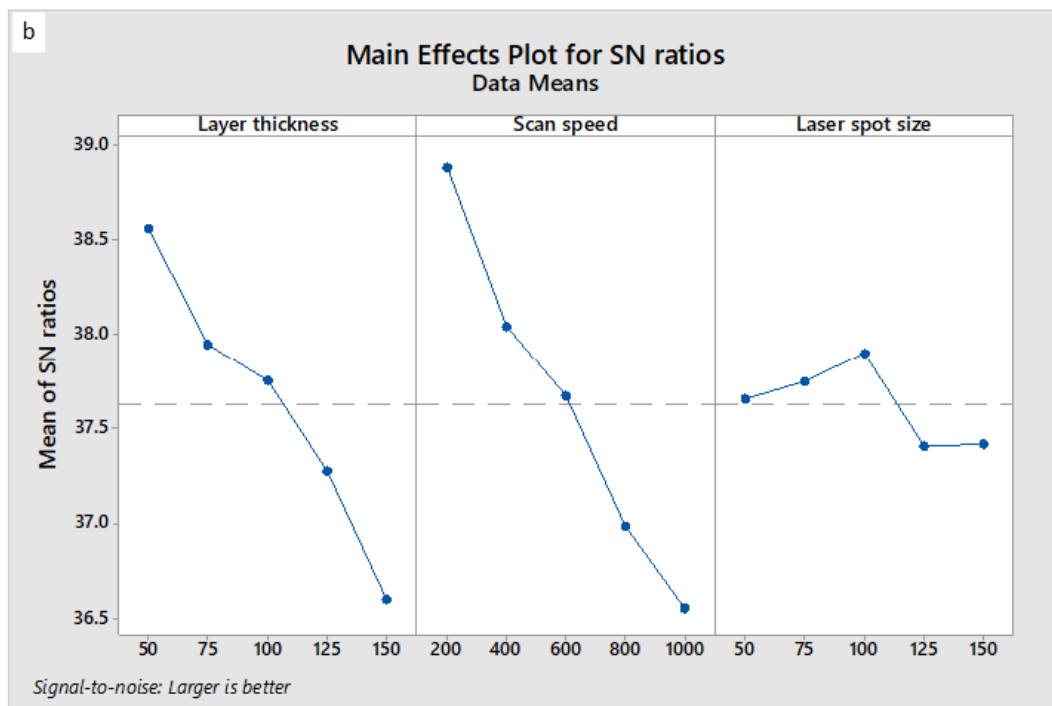
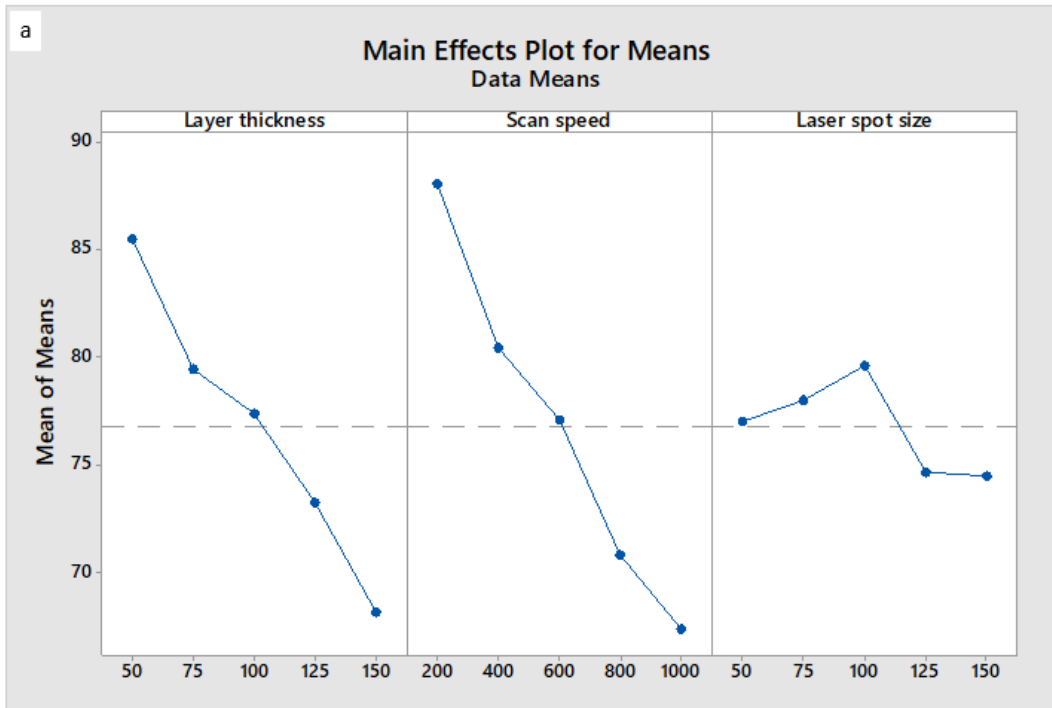


Figure 4.20 The main effects plots for the mean values of (a) relative density and (b) S/N ratio on the Parameters investigated.

The difference between the maximum and minimum values of the mean of S/N ratios for the investigated parameters was estimated and used to determine the parameter with the strongest influence following [201, 202]. The larger the difference between the minimum and maximum of the S/N ratio indicates the parameter with the most influence on the relative density of processed parts. From our analysis, it is evidence from Table 4.6 and Figure 4.20 that the scan speed and the laser spot size have the highest and least influence on the relative density respectively.

4.4.2.2 Microstructural analysis of SLM processed parts

Results of the microstructural analysis from the SEM micrographs of processed parts show agreement with the measured relative densities. It is evident from observing the micrographs presented in Figure 4.21 to Figure 4.25 that the presence of pores increases with increasing layer thickness and increasing scan speed.

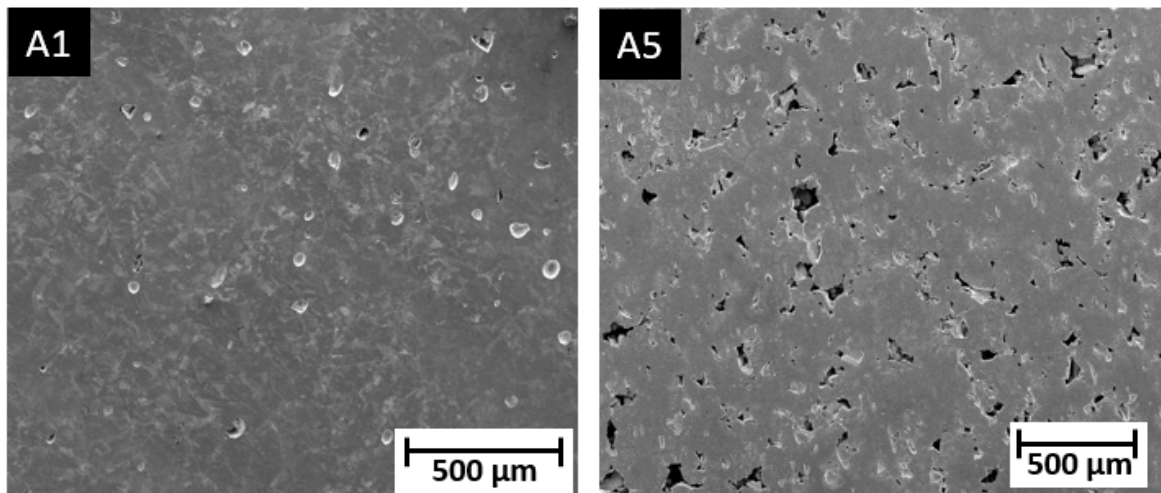


Figure 4.21 Select SEM micrographs of samples processed at 50 μm layer thickness.

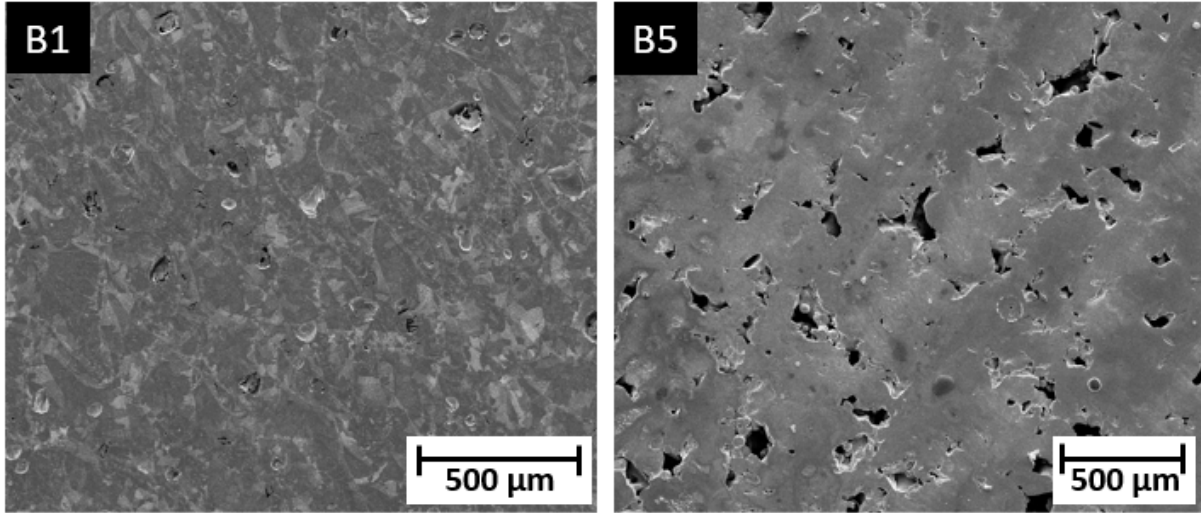


Figure 4.22 Select SEM micrographs of samples processed at 75 μm layer thickness.

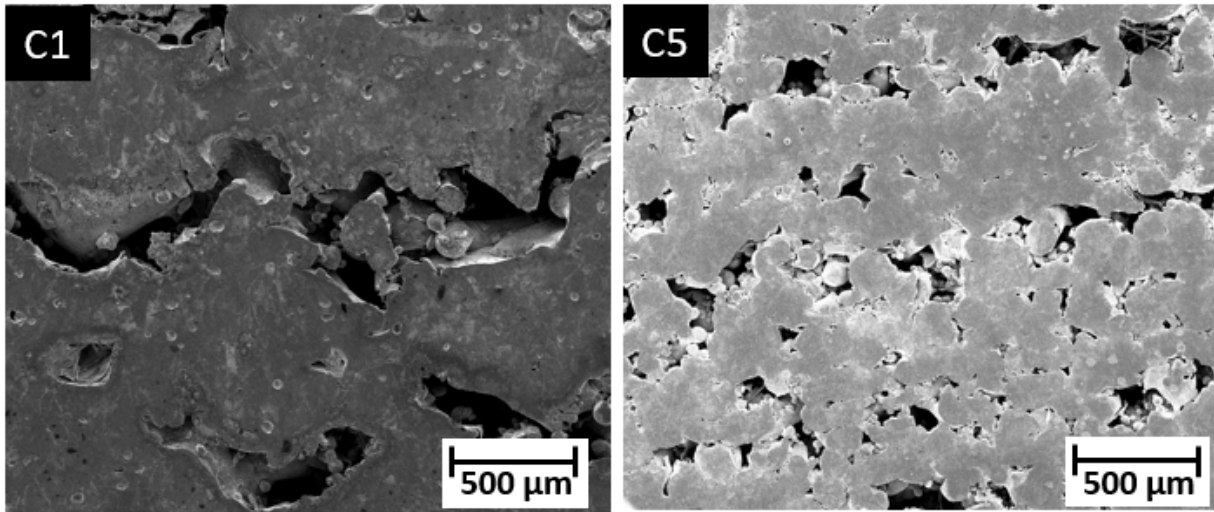


Figure 4.23 Select SEM micrographs of samples processed at 100 μm layer thickness.

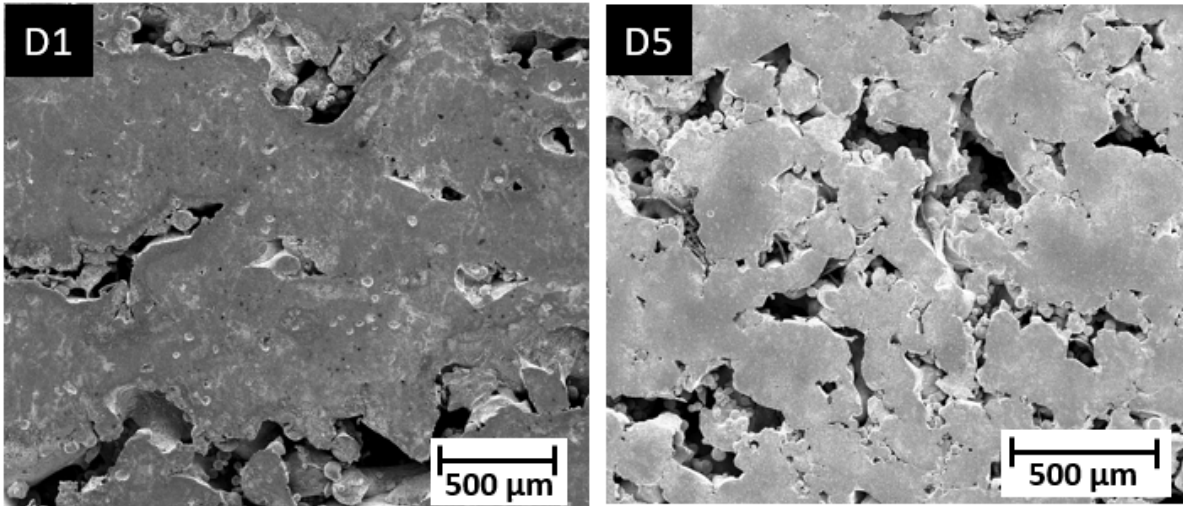


Figure 4.24 Select SEM micrographs of samples processed at 125 μm layer thickness.

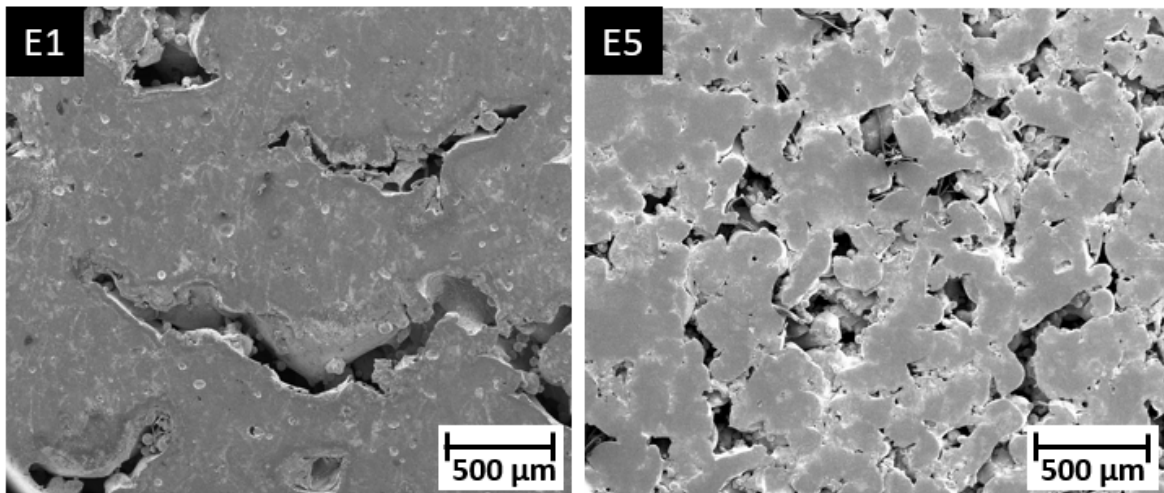


Figure 4.25 Select SEM micrographs of samples processed at 150 μm layer thickness.

4.4.2.3 Regression analysis of SLM processing

A multiple regression was carried out using Minitab 17 statistical software package to develop an equation which models the relationship between the laser speed, spot size, layer thickness and the relative density. The target goal was a relative density of 100 %. The regression equation is as follows:

$$\rho = 125.81 - 318.7l - 0.023s - 189d + 1544ld \quad (4.9)$$

Where ρ is relative density, l is layer thickness in μm , s is laser scan speed in mm/s and d is laser diameter in μm . From the regression equation, optimized scan speed, laser diameter and layer thickness were estimated and the final SLM parameters presented in Table 4.7 was used to produce parts with >99% relative density.

Table 4.7 Optimized SLM process parameters at a constant laser power and hatch spacing

Laser Power (W)	Hatch Spacing (μm)	Laser Speed (mm/s)	Laser Diameter (μm)	Layer Thickness (μm)
120	50	200	50	50

Figure 4.26 is an SEM micrograph of parts processed with the optimized processing parameters obtained from Equation (4.9) and given in Table 4.7. A more detailed microstructural analysis of the optimized SLM processed part will be discussed in chapter 5 along with a comparison with the microstructure of the fully sintered part processed from the optimized SJ process and the spark plasma sintering (SPS), a non-additive manufacturing process that is also of interest to many researchers.

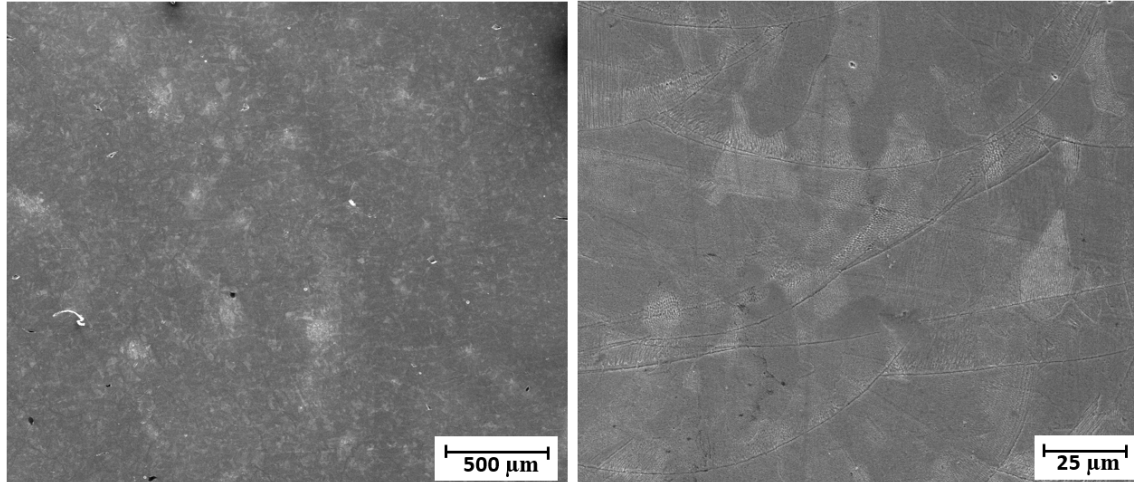


Figure 4.26 SEM micrograph of sample processed using the optimized processing Parameters.

Analysis of our results so far shows that one major factor to consider during SLM processing is to ensure that the laser diameter and hatch spacing are set equal to each other. With this, a uniform energy density across the entire build area is ensured.

4.5 SLM processing of WC-SS316L composite and functionally graded WC-SS316L system

Just as with the processing of pure SS316L by SLM, the processing of MMCs also faces the need to fully optimize the process for pore free parts. Because of the limitless possibilities of parts composition in MMC, resulting from the various volume composition of the reinforcing particles possible, optimization becomes only possible within a defined MMC composition. Our approach in processing MMC is to employ the already optimized parameters for processing the pure alloy and determine how much rigid inclusions can be added to the matrix without any significant pore formation. Furthermore, an attempt to additively manufacture a functionally graded material (FGM) consisting of SS316L with gradually varying WC content was carried out.

4.5.1 SLM Materials and Methods

MMC consisting of SS316L and WC with varying WC volume composition ranging from 5, 10 and 15% were printed using the optimized set of parameters to ascertain if or not the optimized parameters for the alloy system was sufficient to successfully print a composite system. The WC powder used in this case was a finer powder with an average particle size less than 10 microns (Figure 4.27(b)), while the SS316L powder was consistent with the previous section (Figure 4.27(a)). Powder samples consisting of the appropriate fractions of SS316L and WC were thoroughly mixed to ensure a homogeneous powder feed stock.

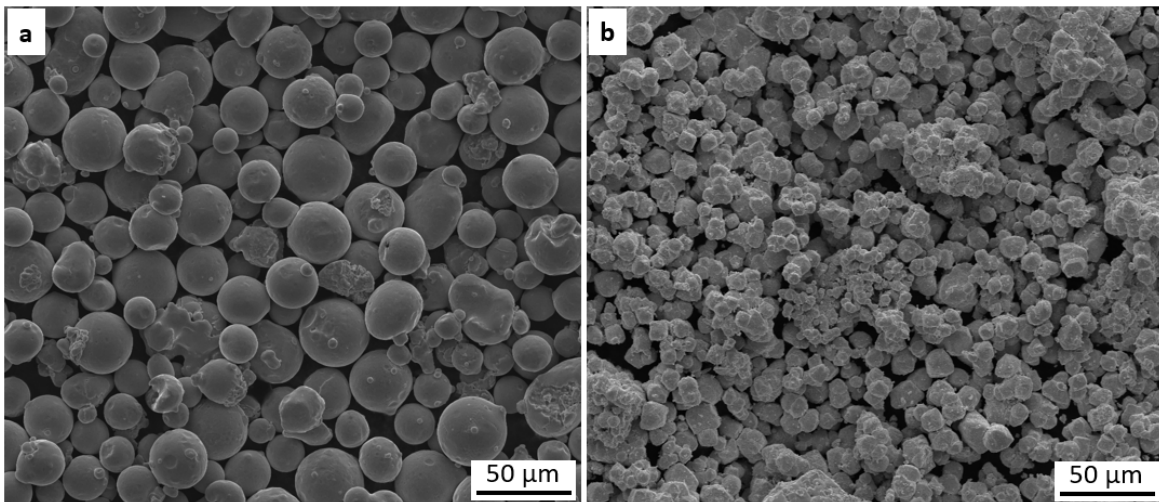


Figure 4.27 SEM micrographs of the (a) SS316L powder (b) WC powder.

For the processing of the FGM, mixtures of SS316L with varying WC concentration, ranging from 5, 10, 15 and 40% were fed into the powder feed chamber in stacking consecutive layers as depicted in Figure 4.27. During printing, these powders are spread unto the build bed and selectively melted.

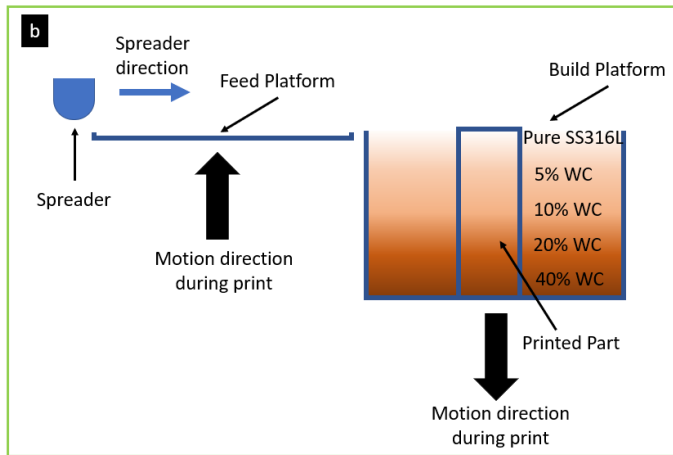
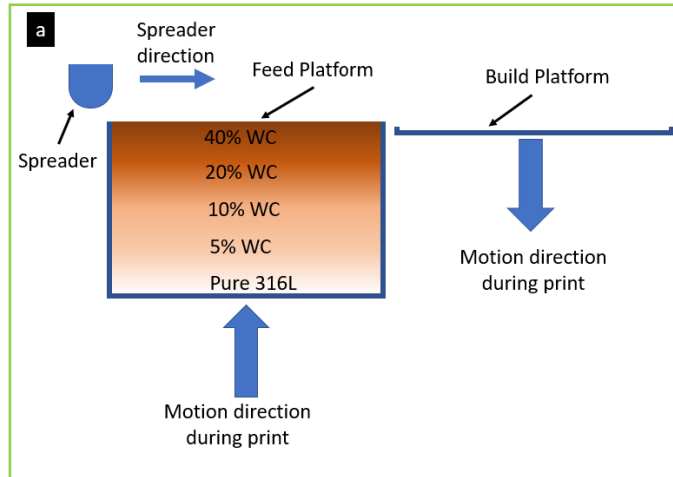


Figure 4.28 Schematic describing the SLM setup for the processing of functionally graded SS316L-WC (a) at start of printing (b) at the end of printing (c) actual powder bed in the build platform after sample removal

4.5.2 Results and Discussions

SEM analysis (Figure 4.29 (a)) and density measurements of the various SS316L-WC composites processed confirmed that for the samples processed with the optimized processing parameters, relative densities >99% were attained. Samples processed with WC content up to 15% showed no signs of cracking. For samples with WC content greater than 15% however, we noticed cracks within the microstructure which increases with increasing WC content. It appears that the cracks result from the thermal stresses imposed by the presence of the rigid WC inclusions within the SS316L matrix.

For the functionally grade SS316L-WC system, examination of the spreading of the powder from the feed platform to the build platform after the print process showed that the powder layers with the different WC compositions were properly and evenly distributed over each other as can be seen in Figure 4.29(a). Samples processed using the unoptimized processing parameters produced highly porous structures, unlike those processed with the optimized parameters (Figure 4.29 (b) and (c)). Just as in the case of the composite system, the FGM samples show evidence of cracks at WC concentration greater than 15%.

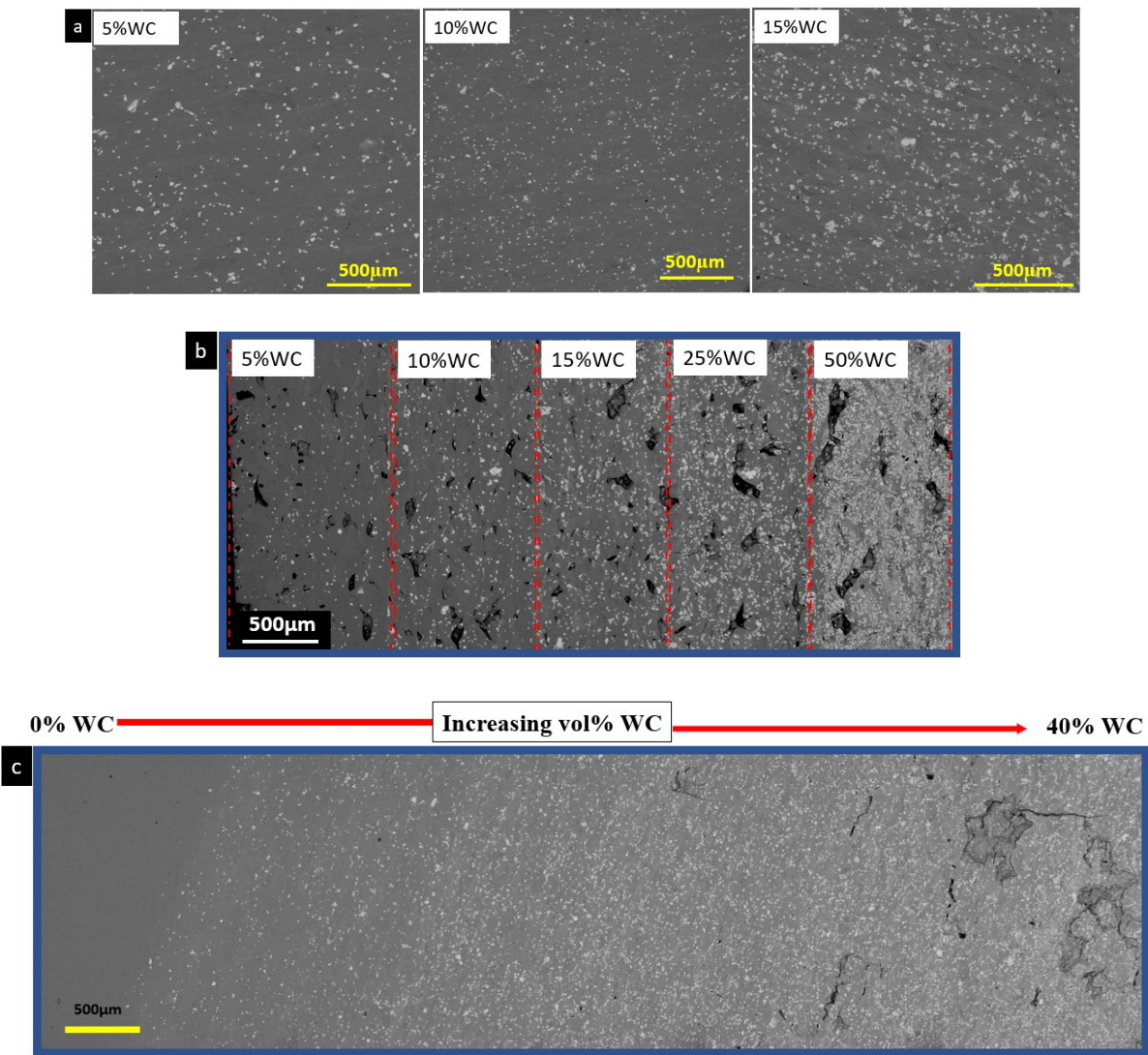


Figure 4.29 SEM micrographs of the processed (a) composites and functionally graded SS316L-WC (b) with un-optimized parameters (c) with optimized parameters

4.6 Chapter conclusions

Our single-track experiments of pure SS316L show that for a successful SLM printing, the substrate or build plate should be considered to ensure that there is adequate attachment between the substrate and the printed part. With the appropriate selection of the substrate, a continuous and uniform melt pool is ensured, mitigating the formation of sputtering defects.

Also, our single-track experimental results on selective laser melting of WC reinforced SS316L, with the help of DEM results, show that the filling of the pores between WC ceramic particles by the molten SS316L is dependent on the laser dwell time. Both experiment and finite difference modeling of pore filling, with the help of DEM results, confirm that higher volume fraction of WC particles in the melt pool needs longer laser dwell time for the composite densification for the given laser planar energy density investigated. The values of the minimum dwell times necessary for complete pore elimination for the various volume fractions of WC are within the range of the minimum pore filling times found from the solutions of the Rayleigh-Plesset equation. However, analysis of the quantitative modeling results underscores the importance of correctly estimating initial pore size range in the powder bed.

In general, our experiments show that with the knowledge of the materials properties of the metal phase such as viscosity, surface energy and particle fraction of the ceramic inclusions in a composite system, the printing parameters during SLM can be predicted from the modeling results to yield pore free composites.

Furthermore, our results on full part processing of SLM parts show the need to adequately account for the different energy density estimation to ensure proper predictability of the SLM process. Our results also show the need to ensure that the laser diameter and hatch spacing be kept

approximately equal to each other to ensure a uniform energy density across the build bed, thereby mitigating lack of fusion porosity.

Full optimization of the SLM process has yielded SLM processed SS316L parts with greater than 99% relative density. With the optimized parameters, we have been able to process defects free SS316L-WC composites and functionally graded materials with WC composition up to 20%.

Parts of Chapter 4 have been published in the Journal of Materials Research and Technology, (I.D. Olumor, A.L. Maximenko, E.A. Olevsky, (2018), “Effect of laser dwell time on pore elimination in powder bed fusion of metal matrix composites: experimentally validated modeling”, Journal of Materials Research and Technology, Vol 21, 2022, pp 4994-5003). The dissertation author is the primary investigator and author of this paper.

Chapter 5

Additive Manufacturing and Spark Plasma Sintering as Effective

Routes for Manufacturing of SS316L and SS316L-WC Composites: A Comparative Study

5.1 Introduction to comparative study

The idea of making engineering components with highly complex shapes has preoccupied the minds of many researchers. This idea is however being realized, thanks to the advent of additive manufacturing. As a result, a lot of excitement has been generated in the area of Metal Matrix Composites (MMCs) manufacturing, as this has been seen as a sign to successfully manufacture highly complex-shaped parts made of MMCs, which hitherto has been very challenging using the more conventional manufacturing processes like machining.

Selective Laser Melting (SLM), Spark Plasma Sintering (SPS) and Solvent Jetting (SJ) are three powder-based manufacturing techniques that show great potential in the manufacture of complex shaped MMCs [1, 203, 204]. The SLM and the SJ techniques are two additive manufacturing techniques that use a powder-bed based technique in building parts layer by layer, whereas the SPS is usually not considered an additive manufacturing process because parts are not manufactured in a layer-wise manner.

The SLM process uses a laser source to selectively melt the powder bed in accordance with a 3D file sliced into layers by a computer program [205-208]. On the other hand, the SJ technique jets a solvent unto the powder bed which selectively binds the powder bed in accordance with a 3D file sliced into layers by a computer program [93]. The solvent is usually a water-based solution that activates a granular polymeric binder that is premixed with the powder material that is to be manufactured [67, 93]. The part produced by this technique is usually fragile and possesses high porosity, necessitating the need for sintering for final part consolidation. The spark plasma

sintering (SPS) technique on the other hand is a powder-based manufacturing technique that, although, not considered an AM technique, has been used to manufacture complex shapes without the need of post operations such as machining. For example, Torresani et al., [25] and Charles et al., [204] have used the SPS technique in producing complex shapes.

When dealing with complex-shaped MMC components with particulate reinforcements, the powder-based additive manufacturing techniques have shown great promise [205]. All powder-based manufacturing processes, be it additive or not, are faced with peculiar issues and challenges during the fabrication of Metal Matrix Composites (MMCs) reinforced by ceramic particles. In the case of the Selective Laser Melting (SLM) process, these challenges are related to interactions between the laser beam and reinforcing ceramic particles on the one hand, and the interaction between the ceramic reinforcing particles and the metal matrix melt pool on the other hand [209]. For example, melting, evaporation or decomposition of the ceramic inclusion may result from the laser beam interacting with the reinforcing ceramic particles [210, 211]. Also, previous works have shown that ceramic inclusions tend to be dissolved in the molten metal matrix during the processing of MMCs via selective laser melting due to the interaction between the molten matrix and the ceramic inclusions [205, 212-214]. For example, Lo et al., have shown the dissolution of WC in the molten SS316L matrix during SLM resulting in the formation and precipitation of new phases [215]. Results have also shown that due to the very fast thermal cycles involved in the SLM process, these new phases generally exhibit ultra-fine structures often resulting in improved hardness and wear properties [213, 215, 216].

When considering the processing of MMCs processed via SJ, the crucial step is the sintering of the green solvent-jetted components. Depending on the sintering temperature of

MMCs, several carbides are precipitated, some of which impart undesirable properties to the MMC system [217].

Tungsten carbides (WC) have been widely used as reinforcement in steels. They however tend to dissolve in the ferrous matrix [218, 219], resulting in formation of finely dispersed secondary precipitates of mixed carbide phases such as, M_6C , $M_{23}C_6$ or M_7C_3 where M could be Fe, W or Cr depending on the kinetics and chemistry at play [209]. This secondary phase formation and solid solution strengthening of W dissolved in the steel matrix have been attributed to the increase in the hardness and wear resistance of steel matrix composites manufactured by SLM [220, 221]. Despite these increases in hardness and wear properties of steel-WC MMCs, attention should be given to the precipitation of chromium at the grain boundaries, as if not arrested, leads to the depleting of essential chromium in the matrix resulting in reduced corrosion resistance of the MMC system [221].

This current work therefore aims to investigate the influence of three different manufacturing routes, the SJ, SPS and SLM, on the microstructure and hardness property of processed AISI 316L austenitic stainless steel - Tungsten Carbide (SS316L-WC) MMC.

5.2 Materials and Methodology utilized in comparative study

5.2.1 Powders and powder preparation

Spherical gas-atomized AISI 316L austenitic stainless steel (SS316L) powders (Figure 5.1 a) with a mean diameter of 38 μm (Praixair S.T technology, Inc., Indiana, USA), and irregular shaped Tungsten Carbide (WC) powders (Figure 5.1 b) with a mean diameter of 32 μm (Atlantic Equipment Engineers Inc., New Jersey, USA), were employed for this study. The Anton Paar PSA 1090 (Graz Australia) particle size analyzer was used for particle size analysis.

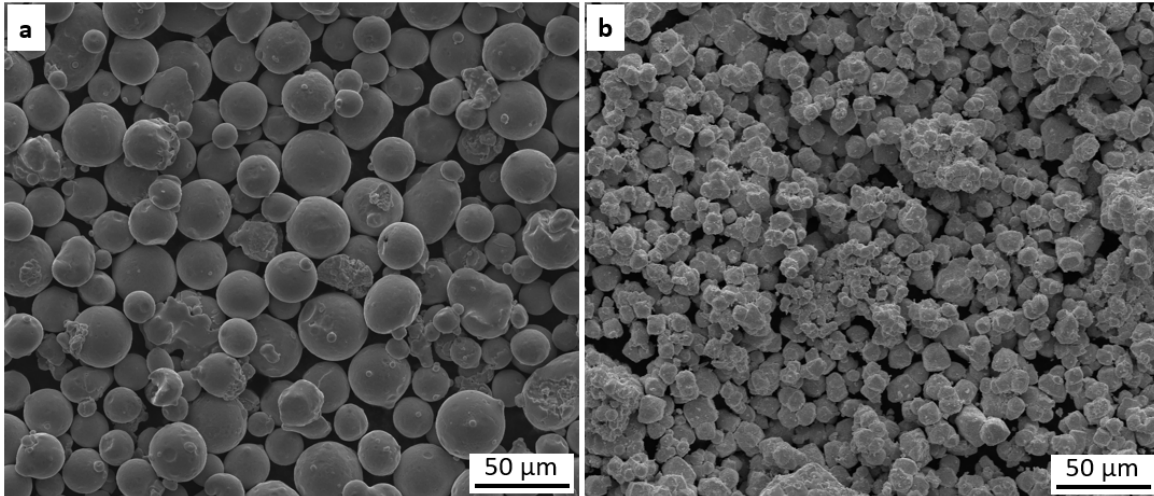


Figure 5.1 SEM micrographs of powders (a) SS316L (b) WC.

For the case of the composite systems, SS316L and WC powders were mixed in varying volume percent of WC ranging from 5%, 10% and 15%. By taking into account the bulk densities of WC and SS316L, appropriate mass fractions were mixed to correspond to the desired volume fractions. Volume fractions have been estimated by assuming that the SS316L particles have a theoretical density of 7.98 g/cm^3 , and WC particles have a theoretical density of 15.63 g/cm^3 . Samples were mixed thoroughly for 1hr to ensure homogeneous mixture using the Turbula® mixer (WAB US Corp, New Jersey, USA) and some samples were subsequently milled using the Pulverisette 6 planetary mono mill milling machine (Fritsch, Germany) for times ranging from 1, 2, 3 and 4 Hs with rotational speed of 500 rpm. After milling, powder samples for selective laser melting and solvent jetting were tested for flowability by estimating the angle of repose and spreadability by visually inspecting a finely spread layer for spreading defects and non uniformity.

5.2.2 Selective laser melting

Laser powder bed fusion experiments were conducted using the Xact Metal XM200C printer (Xact Metal, Inc. Pennsylvania, USA), a laboratory-scale selective laser melting machine at the San Diego State University Powder Technology Laboratory, USA. A 200 W Ytterbium fiber

laser, with a wavelength of 1070 nm, is used as the beam source. A steady flow of Argon gas is used as inert gas to purge the build chamber and maintain an oxygen level below 0.3% during printing. A bulb shaped piece of silicon rubber serves as a recoater and spreads the powder from the feed platform onto the build platform. Both the build plate and the feed platform move linearly in opposite directions and in accordance with the set layer thickness of the part to be printed. Printing parameters optimized in the previous study and presented in chapter 4 were used for processing 10mm x 10mm x 10mm cubes of pure SS316L and SS316L-WC composite parts. By setting the hatch spacing equal to the laser diameter and employing the right energy density, we ensured that the formation of lack of fusion porosity (LOF) is mitigated, resulting in parts with greater than 99% relative densities.

5.2.3 Solvent jetting

3D printing was carried out in a lab-modified ZPrinter 350 printer (Z-Corporation, USA), originally designed to print parts using gypsum powder but modified to allow printing parts from metallic powders. In the solvent jetting technique employed, the pure SS316L and SS316L-WC powders were premixed with a 1% water-soluble granular binder mixture. The granular binder mixture comprises of maltodextrin and sugar in a 1:1 weight percent ratio. Upon powder spreading, an inkjet cartridge deposits a water-based solvent or binder activator over the spread powder layer in accordance with a 3D cad model corresponding to the cross section of the part to be printed.

The water-based solvent or binder activator was composed of 8.3 vol% of Isopropyl alcohol (IPA), 8.3 vol% of diethylene-glycol and 83.4 vol% of deionized (DI) water. Upon deposition, the deposited solvent binder activator then activates the granular binder within the powder bed, thereby gluing the powder particles together. The build bed is lowered in accordance with the predefined layer thickness, a fresh powder layer is spread over this printed layer and the

process repeats itself layer by layer until the entire part is printed. The layer height was set at 88 μm and the binder saturation level was set at 100%. Cube-shaped samples were printed with nominal dimensions of 10mm x 10mm x 10mm using pure SS316L and SS316L-WC powders.

After printing, printed samples were left in the powder bed at room temperature for a minimum of 60 min before being transferred to an oven (AccuTemp-09, Across International) for curing at 120 °C, thereafter, cured samples were subjected to thermogravimetric analyses (TGA) using the SDT Q600 (TA Instruments, USA), with heating up to 1400 °C at a heating rate of 5 °C/min, in order to ascertain the melting temperature of the pure SS316L samples and the various WC vol % composite systems. With the information from the TGA results, samples were debinded and sintered in a single step using the conventional horizontal tube furnace (GSL-1700X-KS-UL-60, MTI, Richmond, CA) in a slightly reducing atmosphere consisting of 5% H₂ and 95% Ar. The specimens were held at sintering temperatures for 5hrs, and the cooling rate to room temperature was 5 °C/min.

5.2.4 Spark plasma sintering

Spark plasma sintering process was conducted using a SPS furnace from DR. SINTER LAB Series (Fuji Electronic Industrial Co, Japan). The pure SS316L and SS316L-WC powders were placed into a graphite mold with an internal diameter of 15 mm and were closed from both sides with two symmetrical graphite punches. Mold's wall was surrounded with graphite felt to limit heat loss. All samples were at the beginning uniaxially compressed with a pressure of 50 MPa, then were heated with a heating rate of 100 °C/min. In order to optimize the sintering temperature and dwell time, tests were performed for 1000, 1050, 1100 °C, and 5 and 10 minutes, respectively.

Analysis of the sintering curves (temperature and punch displacement in time) and densification behavior allows deciding the sintering temperature of 1100 °C and dwelling time of 5 min as the most optimized parameters (Figure 5.2). The sintering process was conducted in a low vacuum, the temperature was controlled by an external thermometer, which measured the temperature on the half height of the mold's wall. After sintering, the mold and punches were disassembled with a hydraulic press, and then graphite foil from the specimen's surface was removed with sandpaper (grade 80).

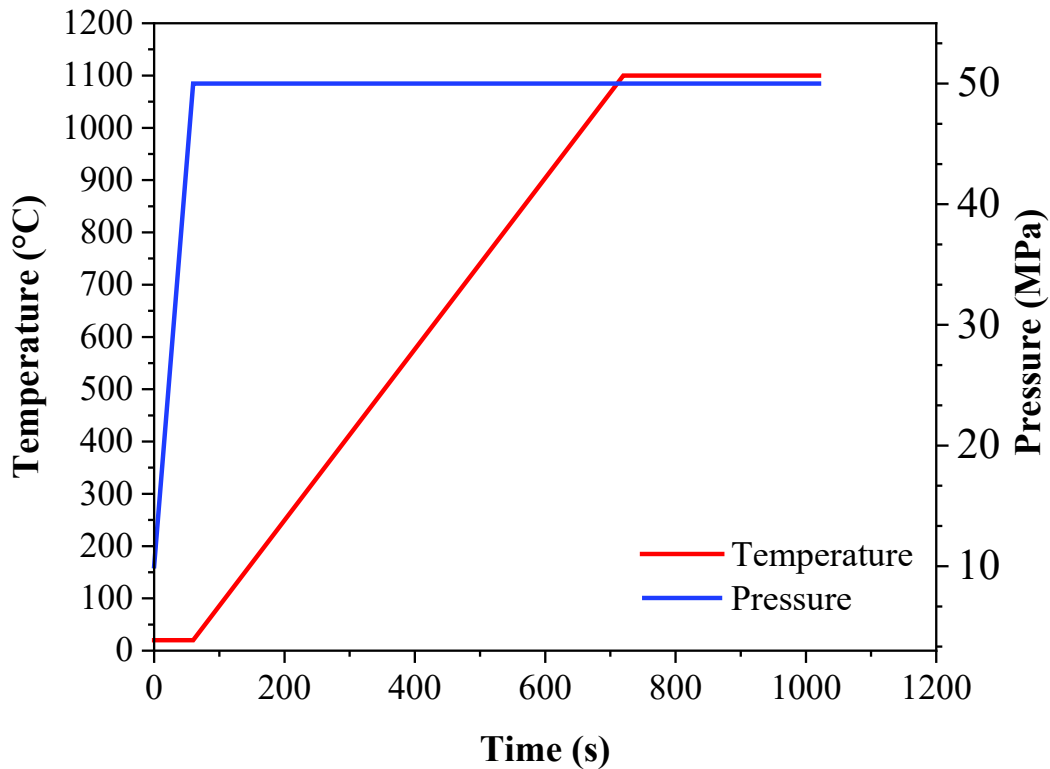


Figure 5.2 Optimized parameters of the spark plasma sintering process.

5.2.5 Characterization

At the end of solvent jetting processes, the green body densities of samples were estimated using the Archimedes' immersion method following ASTM standard C373-18. Final densities for sintered solvent jetted parts and parts manufactured by selective laser melting and spark plasma sintering were estimated using the Anton Paar PSA 1090 (Graz Australia) gas pycnometer and Archimedes method and average values noted.

Samples processed by the SLM process were further subjected to recrystallization annealing by heating to a temperature of 1100 °C, at a heating rate of 5 °C/min and held for 1 H. Subsequently, all samples were prepared for metallography, and etched samples along cross-sections parallel and perpendicular to the build direction were subjected to scanning electron microscopy (SEM) and energy dispersive spectroscopy (EDS) analysis using the scanning electron microscope (FEI Quanta 450, USA) to examine the microstructure of the manufactured samples.

The Image-J software was used to estimate the average grain sizes of samples from SEM micrographs. The etching solution was the V2A solution with a composition of 20%, 5% and 75% volume concentration of HCl, HNO₃ and H₂O respectively. The Etching time was approximately 60s. Polished samples were also subjected to x-ray diffraction analysis, micro indentation and tensile tests.

XRD analyses were performed on a Phillips X'Pert Pro X-ray diffractometer (PANalytical-Philips, Slovak Republic) with a K α wavelength of 1.54060 Å. Samples were analyzed across a range of 30.02°–59.98° 2 θ with a step width of 0.04°, and the X'pert Highscore software was used for peak identification.

Micro hardness was conducted on polished samples. The Vickers micro hardness method was employed for the micro hardness measurement using the Vickers hardness tester of the

Armstrong Pedestal type (Vickers-Armstrongs Ltd, UK) with a load of 10 kg, and a dwell time of 15 s. Indentation dimensions were measured and expression 1 below was used to estimate the Vickers hardness values.

$$HV=0.1891F/d^2 [N/mm^2] \quad (5.1)$$

Where F is the load, and d is the average length of the indentation diagonal.

Tensile tests were conducted on samples with the tensile pull parallel and perpendicular to the build direction.

5.3 Results and Discussions

5.3.1 Powder milling and flowability test

Figure 5.3(a) shows the micrograph after mixing the SS316L-WC composite system. Results of powder samples milled for 4 h show a very robust blend of the SS316L and WC powders, with the WC particles completely embedded within the matrix powders (Figure 5.3(b)). Measured values of the repose angle before and after milling are respectively 29.8° and 33.59°, indicating that the milled powder samples exhibited good flowability. However, spreadability was hampered due to the presence of very large, agglomerated particles resulting from the milling operation as can be seen by the visible streaks on the powder bed during spreading a fine layer over the build platform during SLM and SJ (Figure 5.3(c)). As a result of the spreading defect observed, the milled powders were unsuitable to be processed by both SLM and SJ. However, the milled powders were still able to be processed by spark plasma sintering as this process does not require powder spreading.

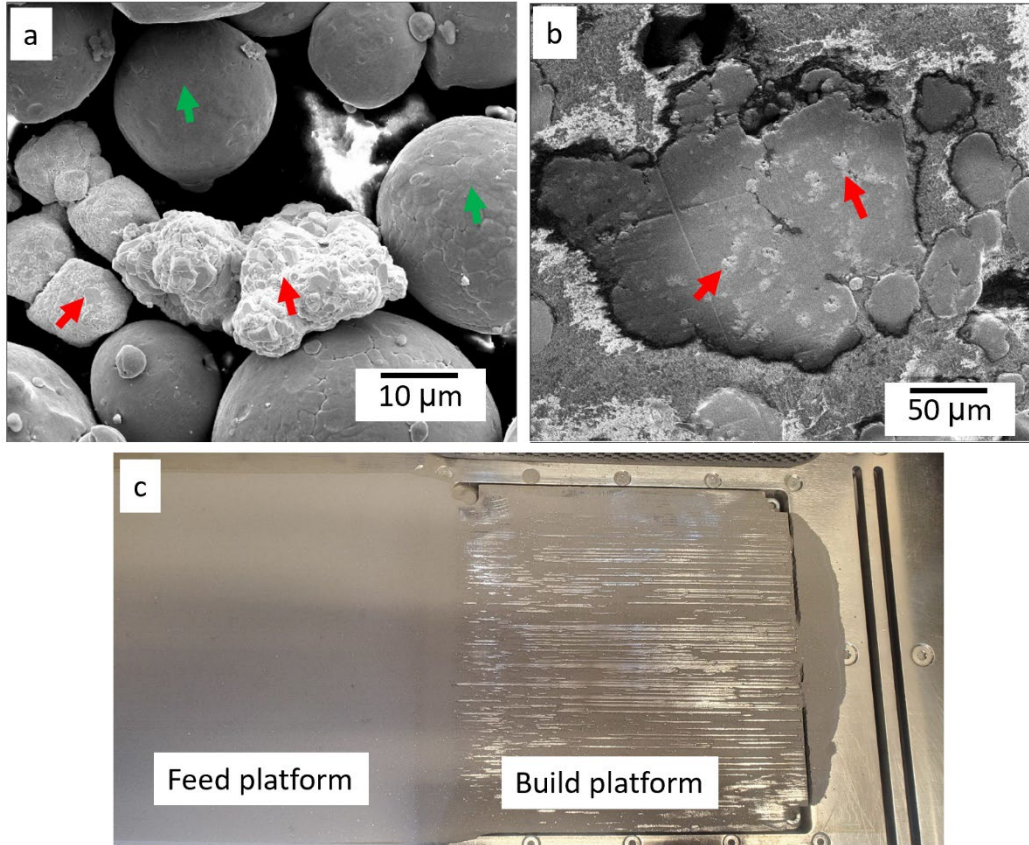


Figure 5.3 Composite powder mixture (a) before milling (b) after milling (c) during SLM powder spreading. Green and red arrows indicate SS316L and WC particles respectively.

5.3.2 Sintering of solvent jetted samples

Sintering at the conventional sintering temperature of 1380 °C for solvent jetted SS316L was not successful for the composite systems as all samples experienced melting (Figure 5.4(a)). Sintering at a lower temperature of 1300 °C yielded melting for the 10% and 15% volume concentration of WC additions, but highly porous specimen for the 5% volume concentration of WC addition (Figure 5.4(b)). Hence TGA analysis was carried out to provide an insight to the appropriate sintering temperatures for the various WC volume fraction additions by ascertaining the melting points.

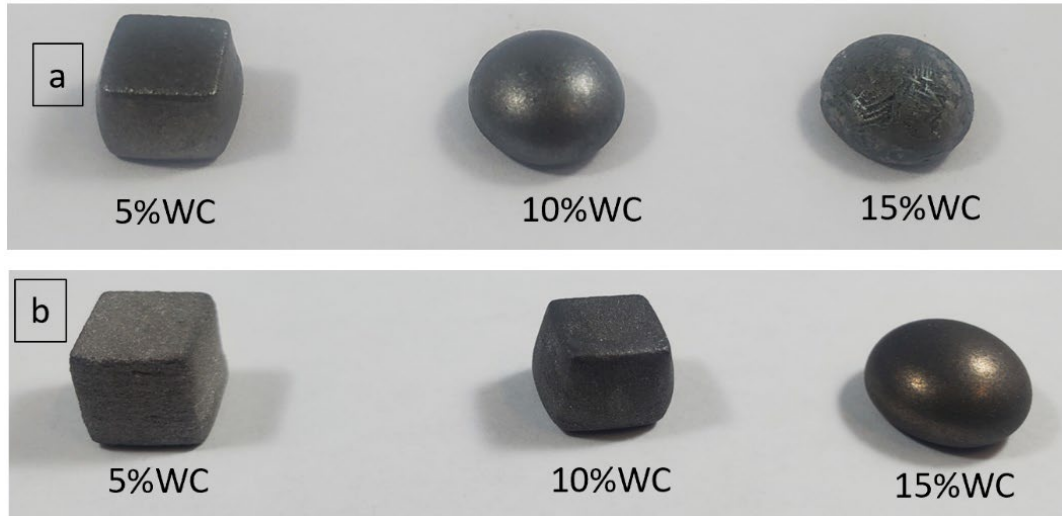


Figure 5.4 Sintered composite samples (a) sintering at 1380 °C for 4 H
(b) sintering at 1300 °C for 4 H.

TGA results (Figure 5.5) show that as the WC content increases for the composite systems, the temperature at which melting occurs is significantly reduced. This can be attributed to the diffusion of carbon atoms from the WC into the SS316L matrix, thereby increasing the carbon contents in localized areas, resulting in localized melting. With the information from the TGA analysis (Figure 5.5), we were able to determine the appropriate sintering temperatures for the various WC volume concentrations of the composite system as 1320, 1260 and 1220 °C for 5, 10 and 15 %vol concentration of WC respectively. Pure SS316L was sintered at 1380 °C. Sintering at these temperatures yielded composite systems with high density without melting.

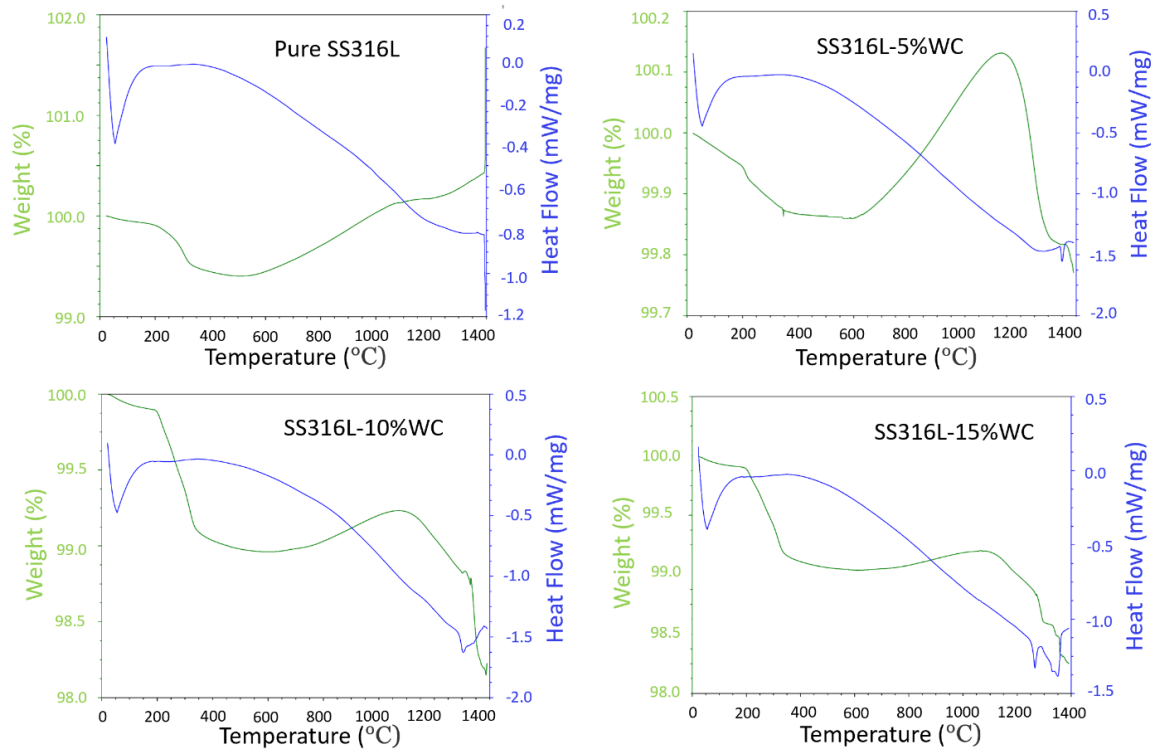


Figure 5.5 Representative TGA data for pure SS316L and samples with various WC volume fraction additions.

5.3.3 Relative density of SJ, SLM and SPS processed samples

The relative density of the green solvent jetted SS316L was estimated to be about 52.8% while that of the green binder jetted composite systems were 53.8%, 53.5% and 53.3% for the 5, 10 and 15 vol% WC composites respectively. Relative densities of the sintered solvent jetted parts and the SLM and SPS processed samples produced with pure SS316L powder and for the various WC additions are presented in Figure 5.6. Generally speaking, as the amount of WC addition increases, the relative density of all processed samples gradually decreases irrespective of the processing technique. It is however evident that higher relative densities were achieved for samples processed by SPS and SLM compared to samples processed by solvent jetting.

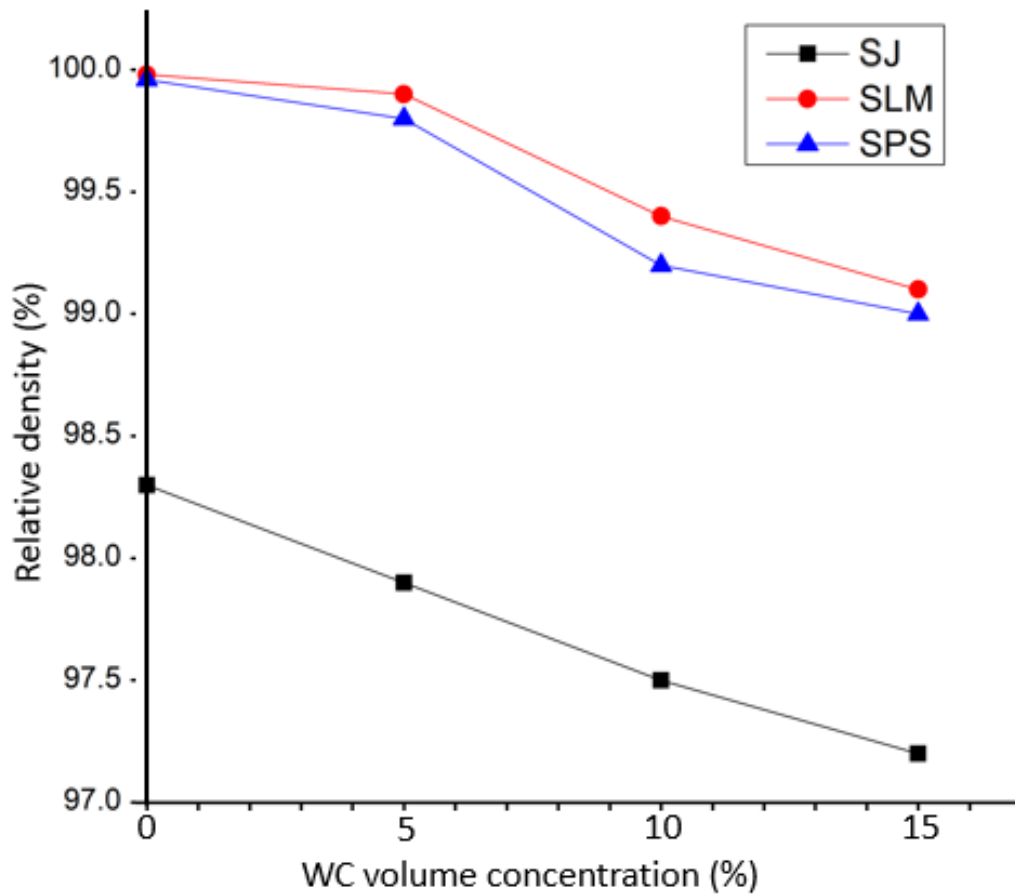


Figure 5.6 Final relative densities of processed samples.

5.3.4 Microstructure of samples

The etched microstructure of pure SS316L samples, from cross section parallel to the build direction for SLM and SJ, and parallel to the load direction for SPS are shown in Figure 5.7. Figure 5.7 (a) presents the microstructure of the pure SS316L processed via the solvent jetting technique sintered at 1380 °C for 5 H to a relative density of 97.3%, while Figure 5.7 (b) and (c) show SEM micrographs of pure SS316L processed by SLM and SPS respectively.

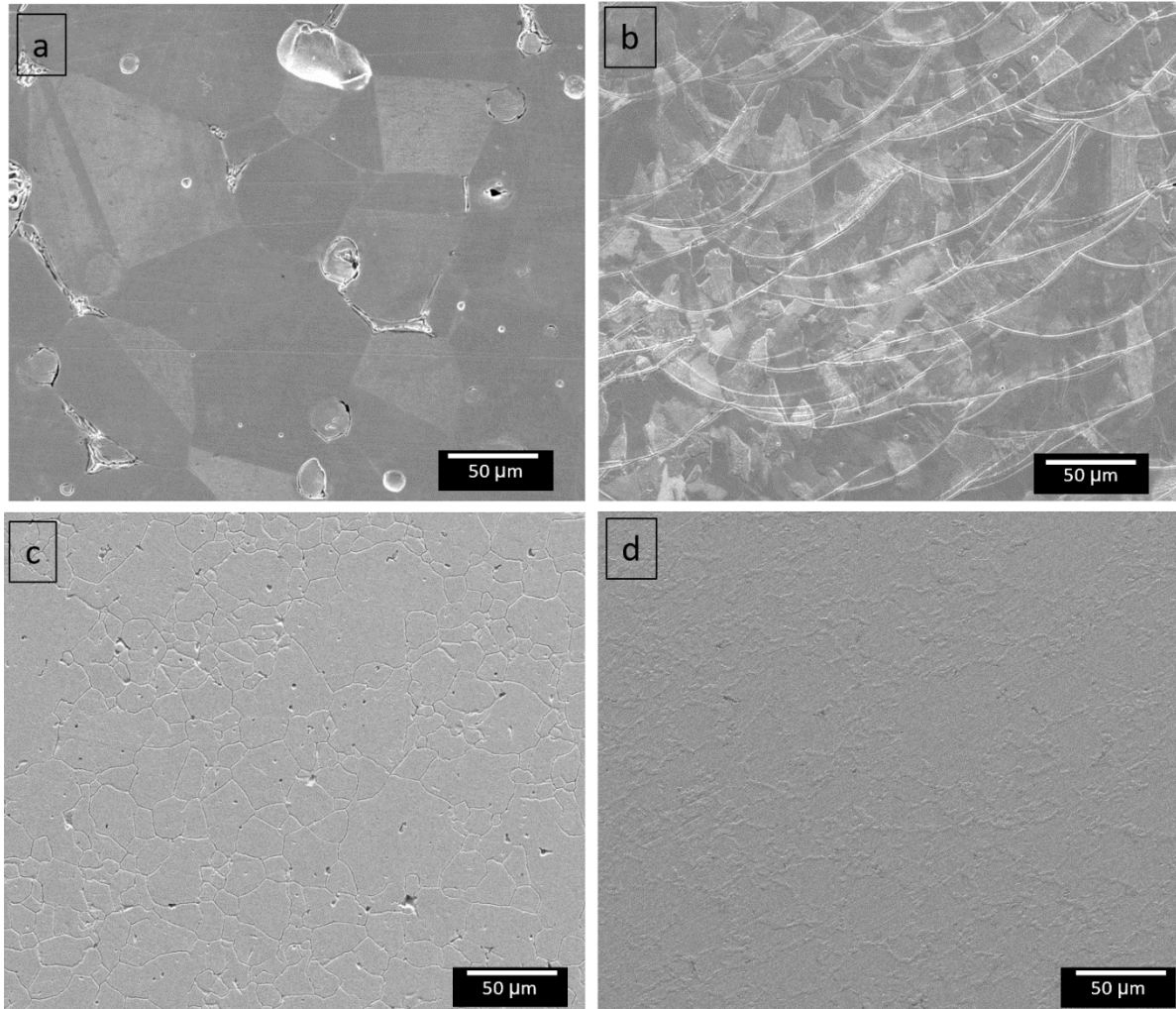


Figure 5.7 Micrographs of etched pure SS316L samples processed by (a) solvent jetting (b) selective laser melting (c) spark plasma sintering (d) spark plasma sintering for regions close to the graphite tooling.

Both SLM and SPS processed samples have densities greater than 99% and about 98% respectively as can be inferred from the micrographs and confirmed by both Archimedes and pycnometer density measurements. The microstructure of the solvent jetted SS316L samples exhibit large equiaxed grains, while the microstructure of the SPS samples show finer equiaxed grains. On the other hand, the microstructure of the SLM samples show fine columnar grains elongated in the direction of the build. In the case of the SLM processed microstructure, the melt

pool boundary is clearly visible in the micrograph. For the SPS processed sample, the micrograph of processed samples in the region of the graphite tooling shows a network of a precipitated phase along the grain boundaries. EDS analysis shows the precipitated phase to be very likely a chromium carbide phase. It is assumed that the reason for this is the diffusion of the carbon atoms from the graphite tooling into the SS316L, causing the precipitation of the chromium carbide.

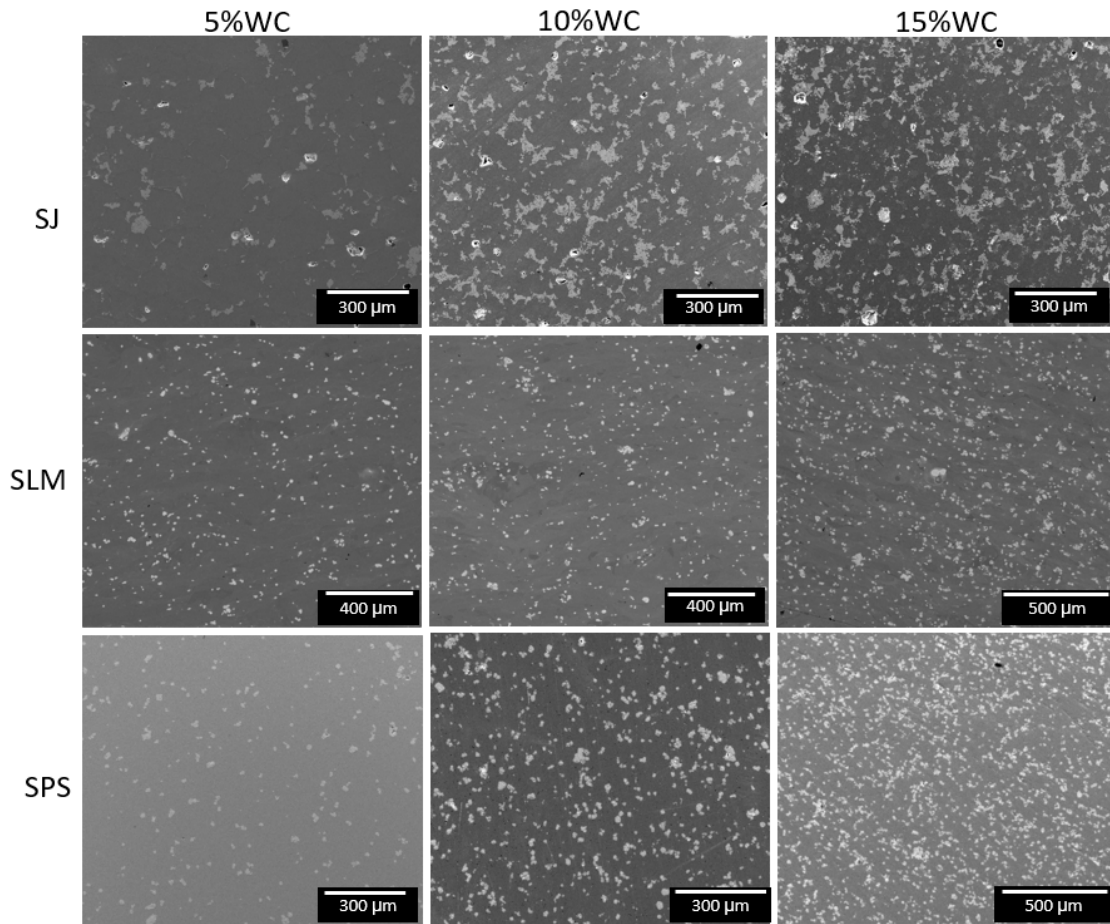


Figure 5.8 Micrographs of the various composite samples processed.

For the processed composite systems, Figure 5.8 presents the SEM micrographs for the various volume percent WC additions for all processing techniques investigated. From the micrographs, it is evident that a more homogeneous distribution of the WC reinforcing particles is achieved for the SLM and SPS techniques compared to the SJ technique. It is also evident that for

the SJ processed samples, the WC particles tend to cluster around the grain boundaries, particularly within the triple junctions.

EDS analysis shows that for samples processed by all three techniques, to some extent, there is diffusion of the SS316L into the WC and likewise the diffusion of WC particles into the SS316L matrix. The extent of these diffusions is dependent on the kinetics of the process. As can be observed from the data from the EDS mapping of samples processed by SJ (Figure 5.9), it is evident that there is the precipitation of a chromium carbide phase.

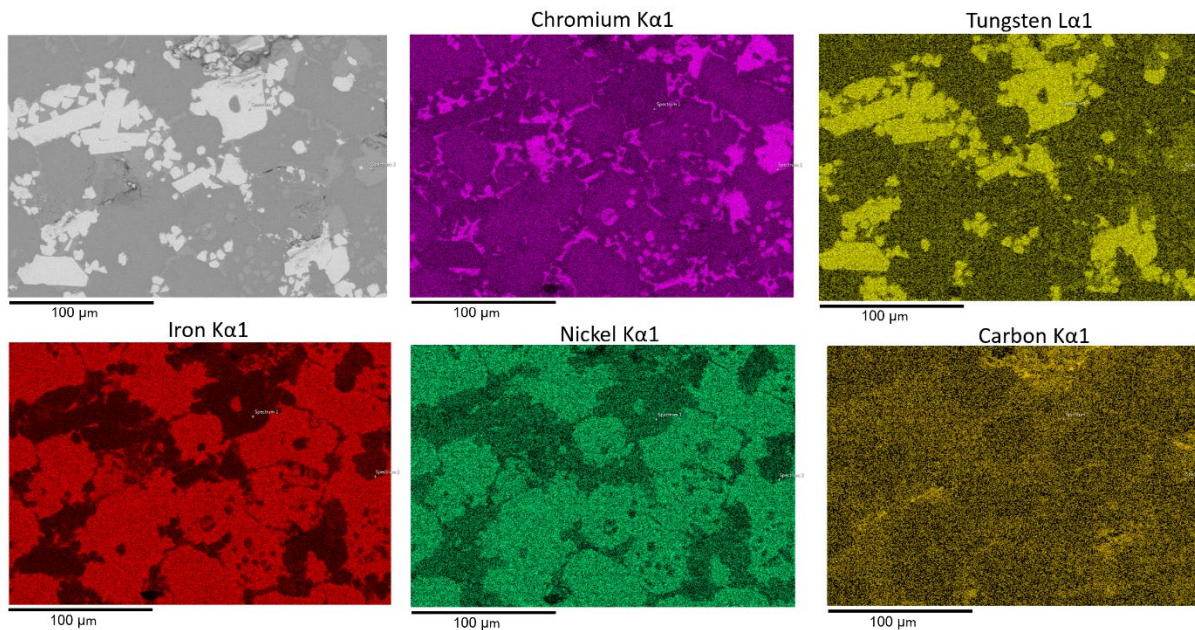


Figure 5.9 SEM micrographs of 15%WC composite composition processed by SJ and corresponding EDS mapping data

This phase seems to precipitate along grain boundaries and between the matrix-inclusion interface. Because of the abundant time involved in the SJ process, there is enough time for the carbide phase to grow, thereby depleting the matrix phase of chromium as is evident from the EDS maps. This precipitate tends to grow with increasing WC content. EDS quantitative analysis

suggests that this chromium phase is likely Cr_{23}C_6 . The presence of this phase in the SJ processed composites was further confirmed by XRD analysis (Figure 5.11).

On the other hand, for pure SS316L samples processed via SPS, EDS analysis confirms that chromium carbide (Cr_{23}C_6) precipitates along grain boundaries in regions close to the graphite tooling (Figure 5.10 (a)), but this is not the case at regions away from the graphite tooling. In the case of the composite systems processed by SPS, there is a formation of a Fe-Cr-W rich layer at the matrix-inclusion interface, which can be seen as the dark grey region in the micrograph and confirmed by EDS line scan (Figure 5.10 (b)). The abundance of Cr in the Fe-Cr-W rich phase results in the stabilization of the ferrite phase, as Cr is known to be a ferrite stabilizer [222]. Hence, as more Fe-Cr-W rich phase is formed at the matrix-inclusion interface, ferrite phase grows at the expense of the austenitic phase as can be inferred from the XRD data in Figure 5.11. One possible phase present in this matrix-inclusion interface is W_2C as confirmed by the XRD analysis. It is believed that dissociated C atoms react with diffusing Cr atoms, yielding Chromium carbide (Cr_{23}C_6), while the regions depleted of carbon transforms to W_2C .

The EDS line scan data of the MMC processed via SLM is shown in Figure 5.10 (c). It is evident from the microstructure that partially dissolved WC particles are finely distributed within the austenitic matrix. Analysis also shows that a network of reaction carbides is also well distributed within the austenite matrix. It's been reported by several authors [206, 216, 223, 224] that the formation of carbides results from partial or total dissolution of the original WC particles within the metal matrix. Dash and Nayak have suggested that this dissociation reaction likely occurs at 1250–1300 °C [225]. Anne and Jacqueline [209] have suggested that the partially dissolved WC in the molten SS316L matrix forms dendritic structures which include lamellar mixtures resulting from eutectic reactions during solidification of the melt pool.

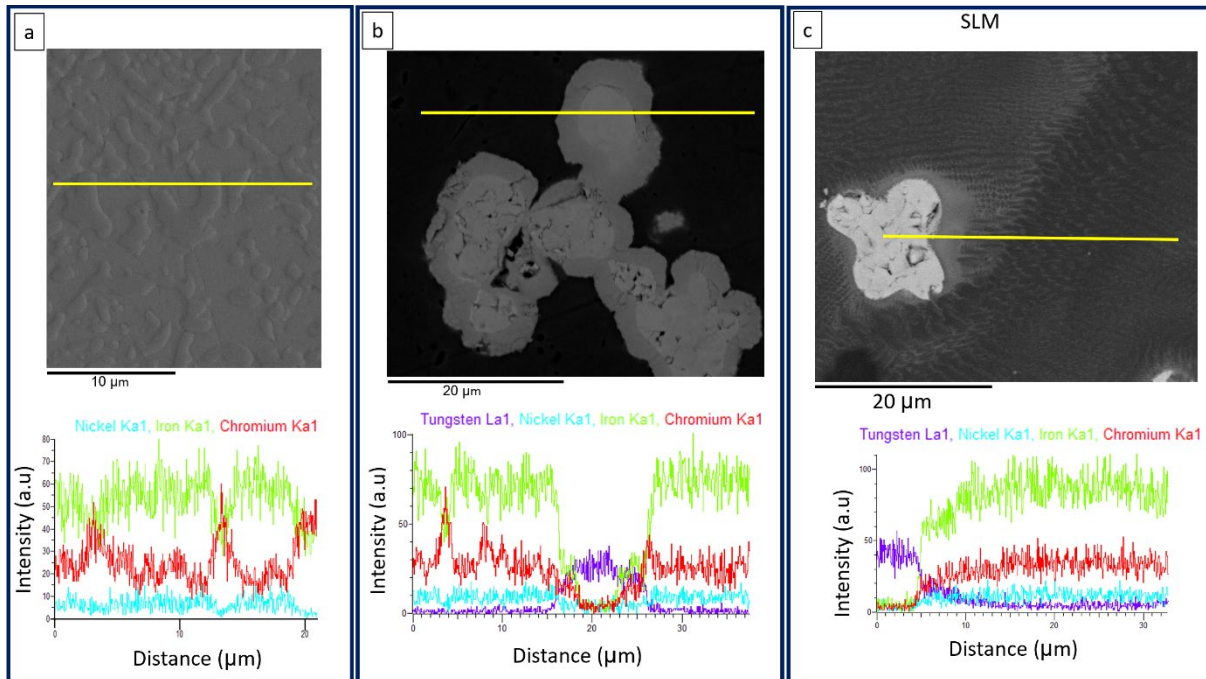


Figure 5.10 SEM micrographs with the yellow lines representing lines across which EDS line scans were conducted for (a) the edge of the SPS processed pure SS316L samples (b) the center of the SPS processed samples with 15% WC composition (c) SLM with 15% WC composition.

5.3.5 XRD analysis

Results from XRD shows that for SLM processed samples, the BCC phase becomes more stabilized with increasing WC volume concentration. However, even with the maximum volume concentration of WC addition investigated, there is still the presence of the FCC (γ -Fe) phase. It is also clear from XRD data of samples processed by SLM that the peak of the austenitic phase broadens and shifts towards lower angles with increasing WC addition, indicating that the austenitic lattices are deformed (expanded) and strained, resulting from increasing atomic diffusion with increasing WC addition. Also, for the SLM processed samples, XRD data shows the absence of the we observe the presence of the W_2C phase. It is suggested that due to the transient nature of the SLM process, the kinetics of the process does not favor the formation of the W_2C phase.

On the other hand, in the case of the samples processed via SPS, we observe that with increasing WC addition, the more stable phase of the matrix is the BCC (α -Fe) phase. At the maximum WC addition investigated, there is almost a complete replacement of the FCC by the BCC phase. Also, we notice that with the SPS processed samples, there is the formation of the W_2C phase with increasing intensity as the WC volume concentration increases as is evident from the XRD peaks in Figure 5.11. Both XRD data and EDS analysis confirm the kinetics involved in the SPS process favor the precipitation of the $Cr_{23}C_6$ carbide. Finally, XRD analysis of samples processed by the SJ method shows the presence of Fe_3W_3C in addition to $Cr_{23}C_6$ carbide (Figure 5.11).

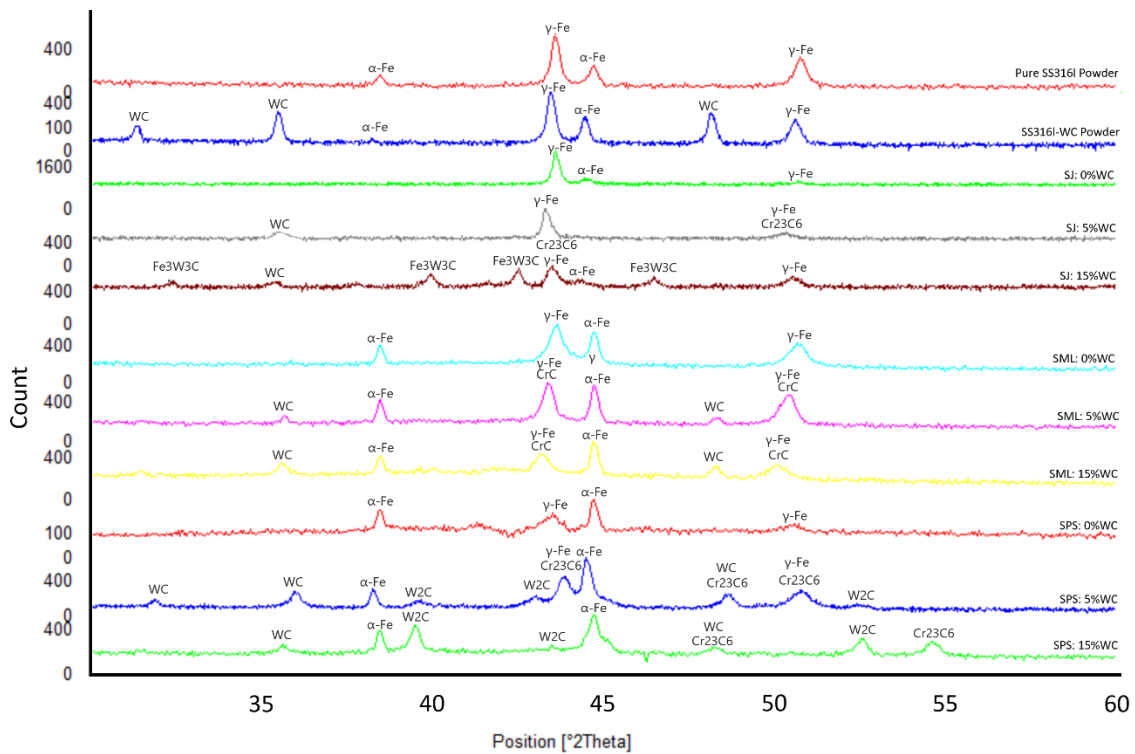


Figure 5.11 Selected XRD patterns of processed samples showing formation and growth of new phases for the different processing techniques.

5.3.6 Micro hardness of processed composite samples

The comparison of the micro hardness properties for all processed samples is presented in Figure 5.12. It can be observed that generally, for all techniques investigated, the Vickers hardness values increases with increasing WC volume addition. It can however be seen that the SLM processed samples showed overall higher Vickers hardness values than those processed by solvent jetting and SPS for all WC volume addition. Of the various chromium carbide encountered in this work, the Cr_{23}C_6 has been reported to exhibit the least hardness [226].

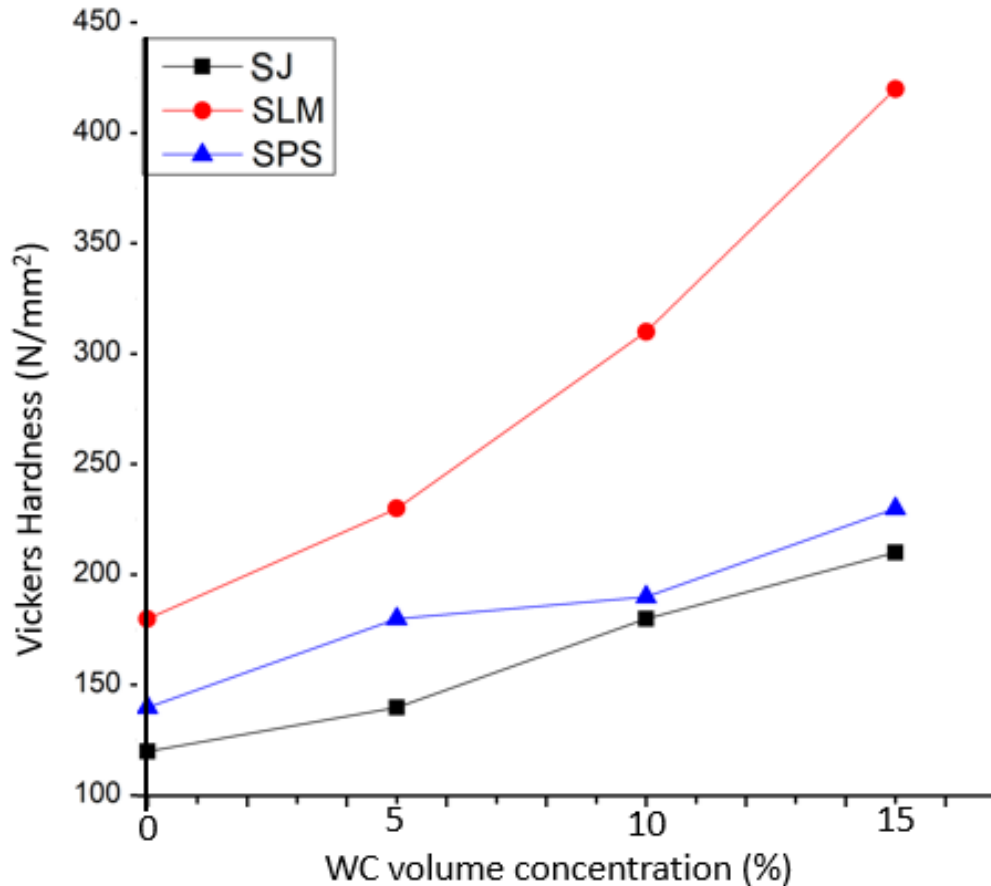


Figure 5.12 Effect of WC content on the micro hardness values of the processed samples for all manufacturing techniques investigated.

According to recent results by Ayorinde et al., [227], the BCC α -Fe phase is softer than the FCC γ -Fe phase. Also, Fernando et al [228] have suggested that the Vicker's hardness of W₂C phase is slightly inferior to that of WC phase. Considering the above, we can safely assume that the samples processed by the SJ and the SPS techniques, have shown lower Vickers hardness when compared to the samples processed by SLM due to the formation of the more inferior Cr₂₃C₆, BCC α -Fe and W₂C phases by samples processed by these techniques.

5.3.7 Property anisotropy in the SLM and SJ processed samples.

5.3.7.1 Microstructural anisotropy

Microstructural analysis of the SJ processed samples show that the grains are randomly oriented. Grain size analysis of samples shows the presence of coarse grains with an average diameter of 50 μ m irrespective of cross section relative to the build direction (Figure 5.13).

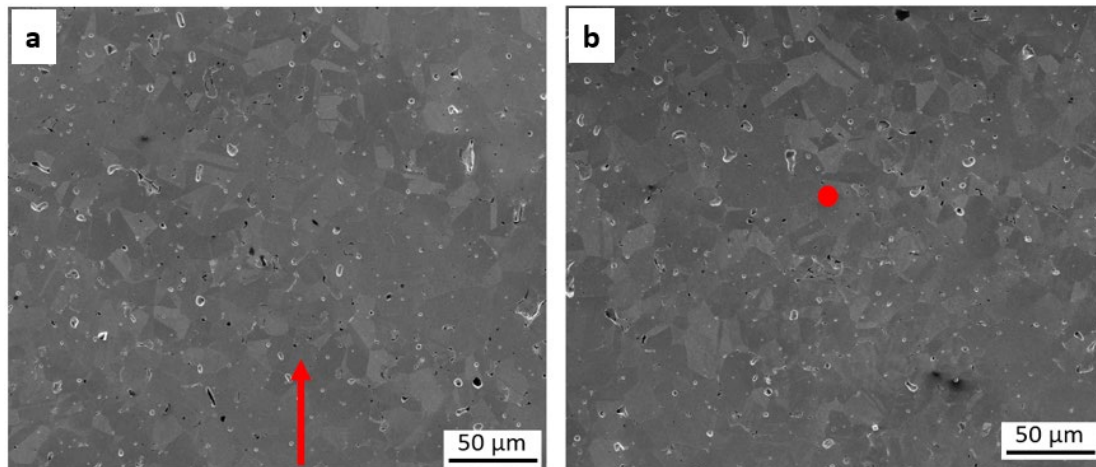


Figure 5.13 SEM micrograph of SJ processed SS316L sample along cross-sections (a) parallel (b) perpendicular to the build direction of. Red arrow and dot indicate the build direction.

The microstructure of the SLM processed SS316L without any subsequent heat treatment on the other hand shows the presence of overlapping melt pool tracks boundaries. Within the melt pool boundaries, there is the presence of columnar grains which sometimes extend across the melt pool boundaries. This behavior has been attributed to epitaxial growth of the grains [229, 230]. The grains are oriented in the direction of build. The reason for this has been suggested to be resulting from the orientation of the surface of the previously processed layer, which is the energetically favored surface for crystallization [231].

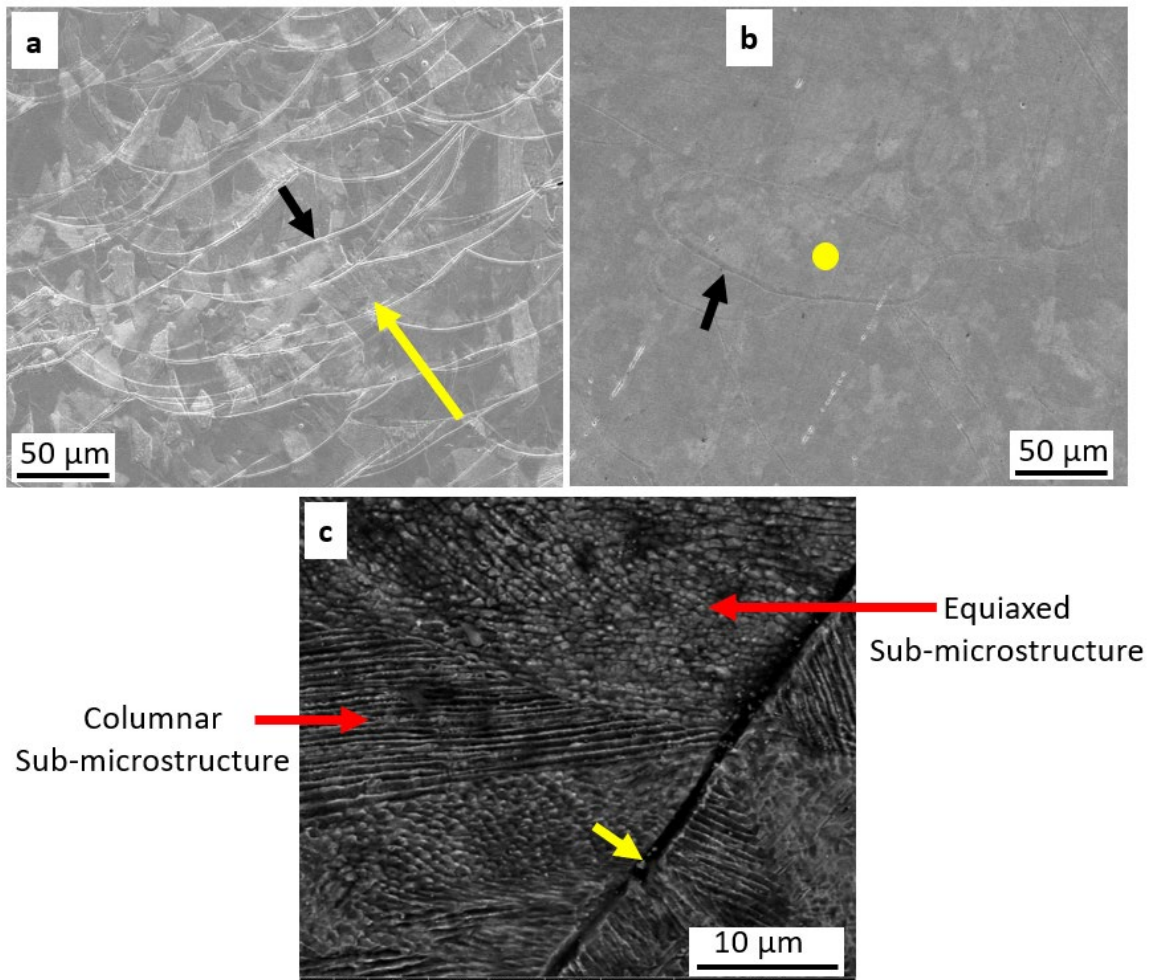


Figure 5.14 Microstructural details of the SLM processed SS316L (a) parallel to build direction. The yellow arrow indicates the build direction and black arrow indicates the melt pool boundary. (b) perpendicular to build direction. The yellow dot indicates the build direction and black arrow indicates the melt pool boundary (c) high magnification image from (a). The yellow arrow indicates the melt pool boundary.

Apart from the presence of these columnar grains, there is also the presence of equiaxed cellular grains as is evident from Figure 5.14(c). These cellular grains are perpendicular to the columnar grains. Thus, the microstructure of the unannealed, SLM processed samples exhibit a cellular-columnar microstructure which is typical for stainless steels that undergo very rapid solidification under fast cooling rates.

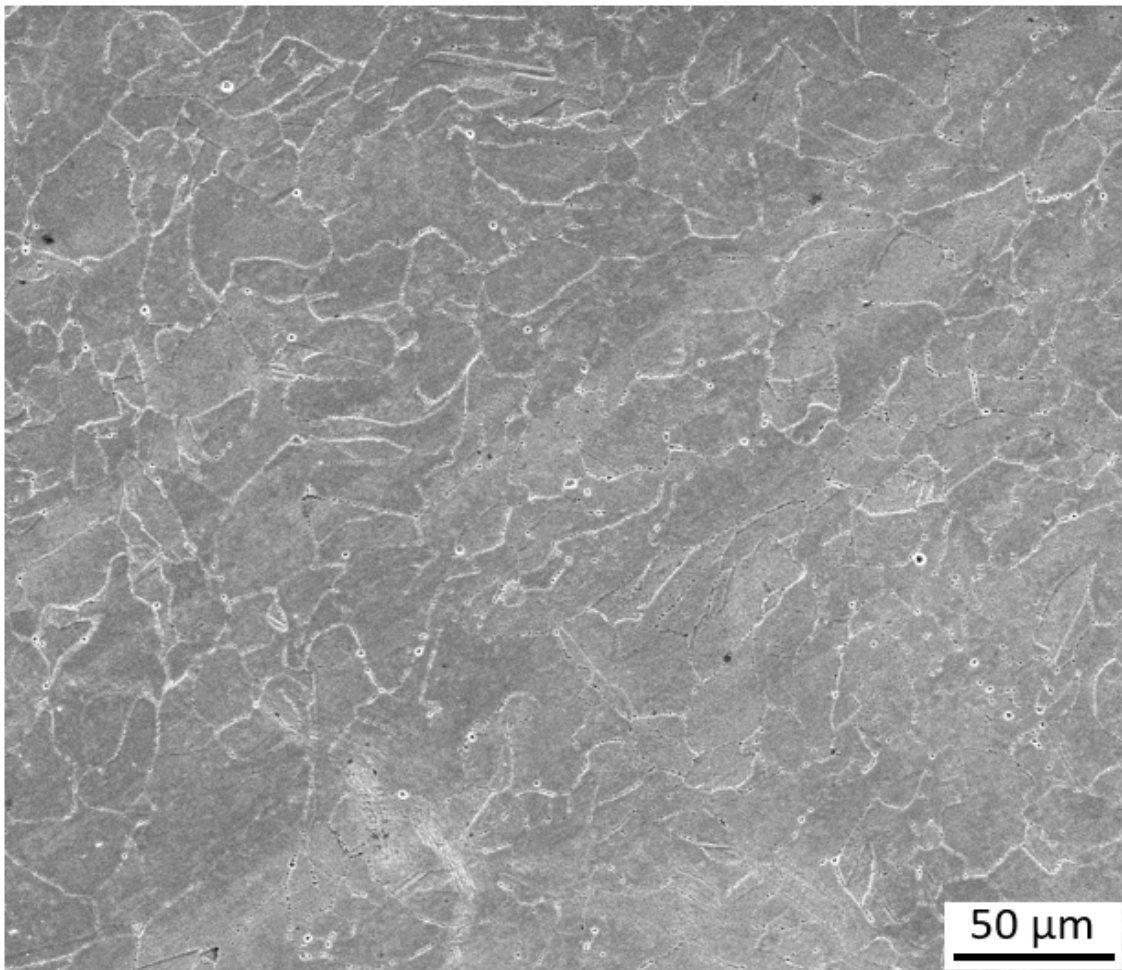


Figure 5.15 Microstructure of the annealed SLM processed SS316L.

Recrystallization annealing at 1100 °C for 1 H of the SLM processed SS316L samples resulted in a remarkably different microstructure from the unannealed SLM processed samples as is evident from the micrograph in Figure 5.15. It is clear that the annealing operation resulted in the removal of the melt pool boundaries and the coarsening of the grains. After annealing, the cellular substructure produced by the SLM process was no longer present in the microstructure. Also, after annealing, microhardness value dropped to about 151 ± 3 HV from a value of 185 ± 4 HV observed in the SLM processed SS316L.

5.3.7.2 Tensile strength anisotropy

For SLM processed SS316L samples with tensile strength perpendicular and parallel to the build direction, average tensile test at failure was estimated as approximately 720 MPa and 526 MPa respectively, resulting in about 27 % variation in the observed tensile strength. On the other hand, samples processed via SJ showed an approximate variation of only 1%, corresponding to tensile strength perpendicular and parallel to the build direction of approximately 630 MPa and 622 MPa respectively.

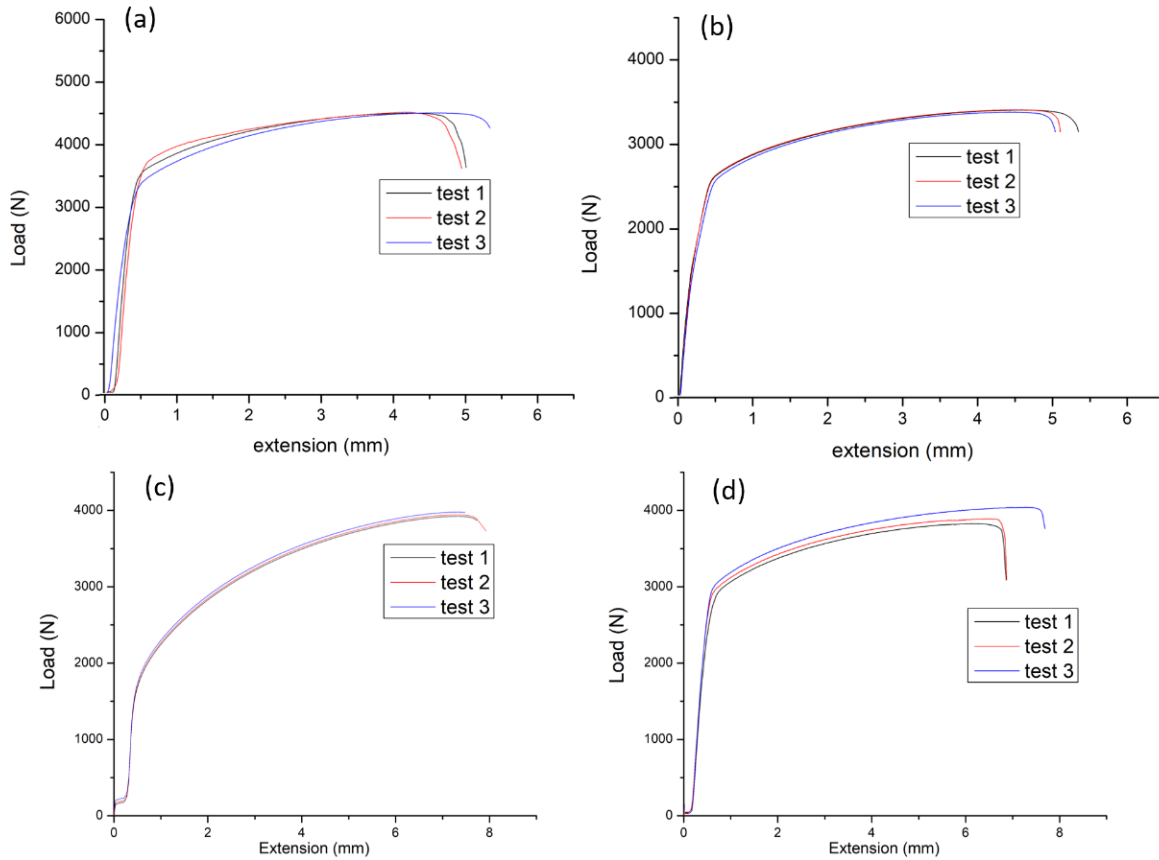


Figure 5.16 Load vs extension curves for SLM processed samples with (a) tensile strength perpendicular to the build direction (b) tensile strength parallel to the build direction; SJ processed samples with (c) tensile strength perpendicular to the build direction (d) tensile strength parallel to the build direction.

5.4 Chapter Conclusions

Our results have shown that it is possible to manufacture SS316L-WC composite parts via solvent jetting, selective laser melting and spark plasma sintering techniques. Results, however, show a significant difference in the microstructure of the parts produced by these different manufacturing techniques. These differences in microstructure have resulted in differences in the mechanical properties of the parts as seen by the values of the micro hardness measurements.

It appears from the analysis of the micrographs and the XRD patterns obtained for all processing routes that for the SS316L-WC MMC, there was some level of WC dissolution

followed by inter atomic diffusing occurring between the WC inclusions and the SS316L matrix, involving dissolved W and C atoms from the inclusions and Cr and Fe atoms from the steel matrix. The final structure of the composite system depends on the kinetics of the manufacturing process, with the SPS process favoring the precipitation of W_2C and $Cr_{23}C_6$, while the kinetics of the SJ processes favors the precipitation of Fe_3W_3C and the $Cr_{23}C_6$ carbides. The kinetics of the SLM process on the other hand favors the precipitation of CrC.

It is assumed that the formation of the CrC instead of the Fe_3W_3C or $Cr_{23}C_6$ and retention of the WC instead of the formation of W_2C in the SLM processed samples is responsible for the higher micro hardness observed for the samples.

Overall, our results on the comparison of SLM and SJ processed SS316L show that the SLM processed parts exhibit higher mechanical properties, however, results on anisotropy investigation have shown that samples processed via the SLM route exhibit higher property anisotropy as compared to samples processed via the SJ processing route.

It is also clear that the annealing operation conducted on the SLM processed SS316L samples resulted in the removal of the melt pool boundaries and the coarsening of the grains, however with a decrease in the mechanical properties. After annealing, the cellular substructure produced by the SLM process was no longer present in the microstructure.

Parts of Chapter 5 have been submitted for publication in the Journal of Materials Science and Engineering: A (I.D. Olumor, Maria, E. Torresani, A.L. Maximenko and E.A. Olevsky, (2023), “Additive manufacturing and spark plasma sintering as effective routes for manufacturing of AISI 316L Austenitic Stainless Steel-WC composites”. Journal of Materials Science and Engineering: A, submitted for publication). The dissertation author is the primary investigator and author of this paper.

Parts of Chapter 5 are also being prepared for publication (I.D. Olumor, E. Torresani, A.L. Maximenko and E.A. Olevsky, (2023), “Property anisotropy in SLM and SJ processed SS316L”. Prepared for publication). The dissertation author was the primary investigator and author of this paper.

Chapter 6

General conclusions

6.1 Summary of goals reached.

A comparative study of additive manufacturing under high and low energy processing conditions has been conducted. Case studies for the high and low energy AM processes have been the selective laser melting and the binder/solvent jetting techniques respectively. The effects of the various processing parameters of these techniques on the outcome of the process parts have been investigated.

Our results for the binder/solvent jetting AM technique have shown that the binder content and layer thickness play important roles in the integrity of the processed green part. Our results have shown that the layer thickness and the mechanism of powder spreading affects the distortion of the previously printed layers. Importantly also, our results have shown that the powder characteristics such as morphology, size and size distribution influence the relative density of the processed green parts and further influences the sinterability.

Our experiments on pressure assisted 3D printing have shown the potential of significantly increasing the packing of the printed green samples for improved sinterability. It is strongly believed that once the pressure application can be successfully done in-situ during the printing process, the observed change in part dimensions will be mitigated. This will hope will be a focus of future research endeavors.

Experiments involving SLM single tracks, processed with varying printing parameters, have been conducted. Discrete element modeling has been employed for simulating powder-bed packing for composite systems during the SLM processing of composites. Results show that the filling of the pores between ceramic particles by the molten SS316L is dependent on the laser

dwelt time, which in turn, depends on the volume fraction of ceramic reinforcement and initial pore sizes between inclusions. Our experiments, in agreement with model analysis, show that with the information of the materials property of the metal phase in a composite system such as viscosity, surface energy and initial pore sizes between ceramic inclusions, the printing parameters can be chosen to yield the appropriate dwell time for pore free composites.

Furthermore, Experiments on SLM processing of bulk components showed the need to fully account for the laser diameter and hatch spacing when estimating the energy density of the printing process, and not deal with them in isolation.

Optimization of the SLM process yielded parts with full density for both the pure stainless-steel alloy and the composite and functionally graded materials investigated.

Comparison of the SLM, SJ and SPS processed samples showed remarkable differences in their microstructures and mechanical properties. The reason for these differences has been attributed to the differences in the process kinetics. We have suggested that the various processing kinetics involved in each process investigated has resulted in the formation of unique phases, thereby imparting different mechanical properties to the processed parts.

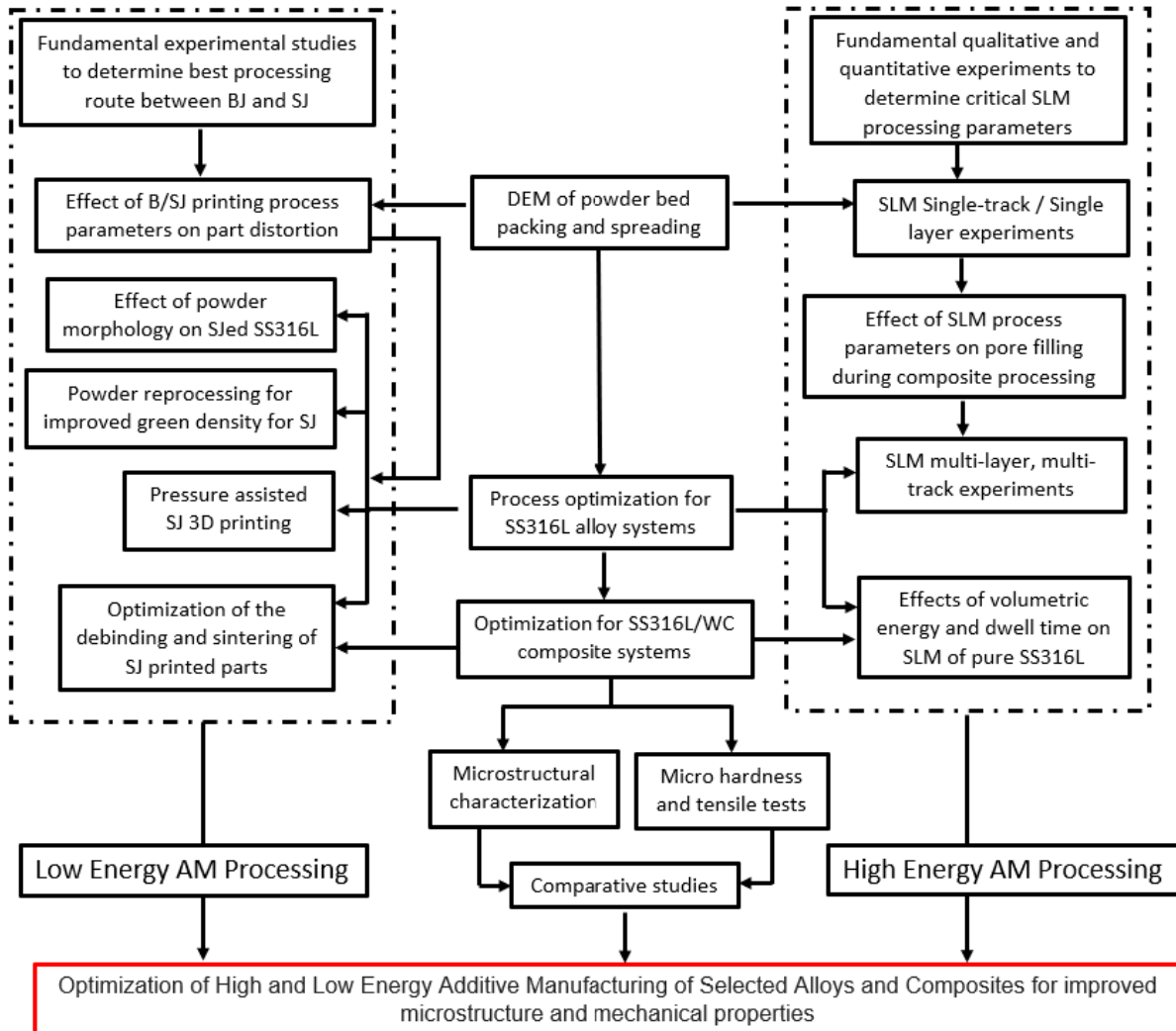


Figure 6.1 Flowchart of the completed work.

6.2 Scientific and engineering novelty of the conducted work

As AM technologies begin to find more industrial applications, it becomes imperative for comparative studies to be conducted in order to help industrial experts correctly make right choices on the proper AM techniques to employ for certain desired goals like specific microstructure and mechanical properties to be achieved. To the best of the knowledge of the authors, no such work on the direct comparison of the SLM and B/SJ AM technique has been conducted. Also, it is very important that roadmaps to optimize AM processes be explored and established. There is never enough of these fundamental optimization endeavors until the technologies are fully matured. To this end, the current work, having explored both optimization of the SLM and the B/SJ AM techniques and compared the microstructures and the mechanical properties of parts processed after optimization of these processes, is a novel endeavor.

The exploration of powder compaction to improve on the green density of BJ processed samples is also a unique and novel study. If fully exploited, this technology can be utilized in improving on the green density of binder jetting processed parts, particularly parts including ceramic powder particles which hitherto have been very difficult to produce with high enough green density. Furthermore, the utilization of DEM software for the simulation of powder packing during binder jetting with a special consideration of previously glued layers is indeed novel.

In our study on the effect of laser dwell time on pore filling in metal-matrix-composites, we have shown that, for single tracks, the appropriate laser dwell time can be established for a composite system by simply utilizing the known materials properties of the matrix phase and considering the initial pores between the ceramic inclusions. It is hoped that our condition for pore filling time is further developed to account for SLM processing of bulk composites involving the processing of multiple tracks and layers.

References

- [1] P.K. Gokuldoss, S. Kolla, J. Eckert, additive manufacturing processes: Selective laser melting, electron beam melting and binder jetting selection guidelines, *Materials*, 10 (2017) 672.
- [2] J.S. Akmal, M. Salmi, A. Makitie, R. Bjorkstrand, J. Partanen, Implementation of industrial additive manufacturing: Intelligent implants and drug delivery systems, *Journal of Functional Biomaterials*, 9 (2018) 41.
- [3] J.Y. Lee, A.P. Nagalingam, S.H. Yeo, A review on the state-of-the-art of surface finishing processes and related ISO/ASTM standards for metal additive manufactured components, *Virtual and Physical Prototyping*, 16 (2021) 68-96.
- [4] Z.Y. Liu, C. Li, X.Y. Fang, Y.B. Guo, Energy consumption in additive manufacturing of metal parts, in: 46th North American Manufacturing Research Conference (NAMRC), Texas A & M Univ, College Station, TX, (2018) 834-845.
- [5] Z.Y. Liu, C. Li, X.Y. Fang, Y.B. Guo, Energy consumption in additive manufacturing of metal parts, *procedia manufacturing*, 26 (2018) 834-845.
- [6] P. Bidare, I. Bitharas, R.M. Ward, M.M. Attallah, A.J. Moore, Fluid and particle dynamics in laser powder bed fusion, *Acta Materialia*, 142 (2018) 107-120.
- [7] C.Y. Yap, C.K. Chua, Z.L. Dong, Z.H. Liu, D.Q. Zhang, L.E. Loh, S.L. Sing, Review of selective laser melting: Materials and applications, *Applied Physics Reviews*, 2 (2015).
- [8] J.P. Kruth, P. Mercelis, J. Van Vaerenbergh, L. Froyen, M. Rombouts, Advances in selective laser sintering, in: 1st International Conference on Advanced Research in Virtual and Rapid Prototyping, Sch Technol & Management Polytechn Inst Leiria, Leiria, Portugal, (2003), 38-49.
- [9] D.G. Ahn, H.J. Lee, Investigation of novel metal additive manufacturing process using plasma electron beam based on powder bed fusion, *Cirp Annals-Manufacturing Technology*, 68 (2019) 245-248.
- [10] P.Y. Lin, F.C. Shen, K.T. Wu, S.J. Hwang, H.H. Lee, Process optimization for directed energy deposition of SS316L components, *International Journal of Advanced Manufacturing Technology*, 111 (2020) 1387-1400.
- [11] T. Do, P. Kwon, C.S. Shin, Process development toward full-density stainless steel parts with binder jetting printing, *International Journal of Machine Tools & Manufacture*, 121 (2017) 50-60.
- [12] M.P. Watters, M.L. Bernhardt, Modified curing protocol for improved strength of binder-jetted 3D parts, *Rapid Prototyping Journal*, 23 (2017) 1195-1201.
- [13] Y. Bai, C.B. Williams, An exploration of binder jetting of copper, *Rapid Prototyping Journal*, 21 (2015) 177-185.

- [14] S. Shiva, S. Brown, A. Cockburn, I.A. Palani, C.P. Paul, W. O'Neill, Evolution in additive manufacturing techniques of metals as net-shaped products, in: K. Gupta (Ed.) Near Net Shape Manufacturing Processes, (2019), 55-77.
- [15] N. Hawaldar, J. Zhang, A comparative study of fabrication of sand casting mold using additive manufacturing and conventional process, International Journal of Advanced Manufacturing Technology, 97 (2018) 1037-1045.
- [16] P. Ferro, R. Meneghello, G. Savio, F. Berto, A modified volumetric energy density-based approach for porosity assessment in additive manufacturing process design, The International Journal of Advanced Manufacturing Technology, 110 (2020) 1911-1921.
- [17] U.S. Bertoli, A.J. Wolfer, M.J. Matthews, J.P.R. Delplanque, J.M. Schoenung, On the limitations of Volumetric Energy Density as a design parameter for Selective Laser Melting, Materials & Design, 113 (2017) 331-340.
- [18] T. Larimian, M. Kannan, D. Grzesiak, B. AlMangour, T. Borkar, Effect of energy density and scanning strategy on densification, microstructure and mechanical properties of 316L stainless steel processed via selective laser melting, Materials Science and Engineering: A, 770 (2020) 138455.
- [19] K.G. Prashanth, S. Scudino, T. Maity, J. Das, J. Eckert, Is the energy density a reliable parameter for materials synthesis by selective laser melting?, Materials Research Letters, 5 (2017) 386-390.
- [20] J. Jiang, J. Chen, Z. Ren, Z. Mao, X. Ma, D.Z. Zhang, The Influence of process parameters and scanning strategy on lower surface quality of TA15 parts fabricated by selective laser melting, Metals, 10 (2020) 1228.
- [21] W.H. Wang, X.Y. Liu, Effect of linear energy density on pores of 316L stainless steel by selective laser melting, IOP Conference Series: Earth and Environmental Science, 233 (2019) 032008.
- [22] Y.L. Guo, L.N. Jia, B. Kong, Y.L. Huang, H. Zhang, Energy density dependence of bonding characteristics of selective laser-melted Nb-Si-based alloy on titanium substrate, Acta Metallurgica Sinica (English Letters), 31 (2018) 477-486.
- [23] S. Shrestha, G. Manogharan, Optimization of binder jetting using Taguchi method, JOM, 69 (2017) 491-497.
- [24] E.A. Olevsky, Theory of sintering: from discrete to continuum, Materials Science & Engineering R-Reports, 23 (1998) 41-100.
- [25] E. Torresani, M. Carrillo, C. Haines, D. Martin, E. Olevsky, Fabrication of powder components with internal channels by spark plasma sintering and additive manufacturing, Journal of the European Ceramic Society, 43 (2023) 1117-1126.

- [26] A. Cabo Rios, E. Hryha, E. Olevsky, P. Harlin, Sintering anisotropy of binder jetted 316L stainless steel: part I – sintering anisotropy, *Powder Metallurgy*, 65 (2022) 273-282.
- [27] A. Cabo Rios, E. Hryha, E. Olevsky, P. Harlin, Sintering anisotropy of binder jetted 316L stainless steel: part II – microstructure evolution during sintering, *Powder Metallurgy*, 65 (2022) 283-295.
- [28] R.K. Bordia, S.J.L. Kang, E.A. Olevsky, Current understanding and future research directions at the onset of the next century of sintering science and technology, *Journal of the American Ceramic Society*, 100 (2017) 2314-2352.
- [29] R.L. Coble, Sintering crystalline solids. I. Intermediate and final state diffusion models, *Journal of Applied Physics*, 32 (1961) 787-792.
- [30] R.M. German, Coarsening in sintering: Grain shape distribution, grain size distribution, and grain growth kinetics in solid-pore systems, *Critical Reviews in Solid State and Materials Sciences*, 35 (2010) 263-305.
- [31] I.W. Chen, X.H. Wang, Sintering dense nanocrystalline ceramics without final-stage grain growth, *Nature*, 404 (2000) 168-171.
- [32] M. Zago, N.F.M. Lecis, M. Vedani, I. Cristofolini, Dimensional and geometrical precision of parts produced by binder jetting process as affected by the anisotropic shrinkage on sintering, *Additive Manufacturing*, 43 (2021) 102007.
- [33] T. Gatsos, K.A. Elsayed, Y.W. Zhai, D.A. Lados, Review on computational modeling of process-microstructure-property relationships in metal additive manufacturing, *JOM*, 72 (2020) 403-419.
- [34] J.W. Pegues, S. Shao, N. Shamsaei, N. Sanaei, A. Fatemi, D.H. Warner, P. Li, N. Phan, Fatigue of additive manufactured Ti-6Al-4V, Part I: The effects of powder feedstock, manufacturing, and post-process conditions on the resulting microstructure and defects, *International Journal of Fatigue*, 132 (2020) 105358.
- [35] A.M. Kiss, A.Y. Fong, N.P. Calta, V. Thampy, A.A. Martin, P.J. Depond, J. Wang, M.J. Matthews, R.T. Ott, C.J. Tassone, K.H. Stone, M.J. Kramer, A. van Buuren, M.F. Toney, J.N. Weker, Laser-induced keyhole defect dynamics during metal additive manufacturing, *Advanced Engineering Materials*, 21 (2019) 1900455.
- [36] J.P. Kruth, J. Deckers, E. Yasa, R. Wauthle, Assessing and comparing influencing factors of residual stresses in selective laser melting using a novel analysis method, *Proceedings of the Institution of Mechanical Engineers Part B-Journal of Engineering Manufacture*, 226 (2012) 980-991.
- [37] C. April, S. John, Properties of metal powders for additive manufacturing: A review of the state of the art of metal powder property testing, in, *NIST Interagency/Internal Report (NISTIR)*, National Institute of Standards and Technology, Gaithersburg, MD, (2012).

- [38] A. Zwiren, C.T. Schade, Hoeganaes, Cinnaminson, S. Hoeges, Additive manufacturing using water atomized steel powders, *Metal Powder Report*, 72 (2017) 111-117.
- [39] M.N. Ahsan, A.J. Pinkerton, R.J. Moat, J. Shackleton, A comparative study of laser direct metal deposition characteristics using gas and plasma-atomized Ti-6Al-4V powders, *Materials Science and Engineering: A*, 528 (2011) 7648-7657.
- [40] C. Zhong, T. Biermann, A. Gasser, R. Poprawe, Experimental study of effects of main process parameters on porosity, track geometry, deposition rate, and powder efficiency for high deposition rate laser metal deposition, *Journal of Laser Applications*, 27 (2015) 042003.
- [41] S. Hoeges, A. Zwiren, C. Schade, Economic additive manufacturing using water atomized steel powders, *Metal Powder Report*, 72 (2017) 111-117.
- [42] T. Fedina, J. Sundqvist, J. Powell, A.F.H. Kaplan, A comparative study of water and gas atomized low alloy steel powders for additive manufacturing, *Additive Manufacturing*, 36 (2020) 101675.
- [43] L. Cordova, T. Bor, M. de Smit, M. Campos, T. Tinga, Measuring the spreadability of pre-treated and moisturized powders for laser powder bed fusion, *Additive Manufacturing*, 32 (2020) 101082.
- [44] J.A. Muñoz-Lerma, A. Nommeots-Nomm, K.E. Waters, M. Brochu, A comprehensive approach to powder feedstock characterization for powder bed fusion additive manufacturing: a case study on AlSi7Mg, *Materials (Basel)*, 11 (2018) 2386.
- [45] F. Persson, C.N. Hulme, P.G. Jönsson, Particle morphology of water atomised iron-carbon powders, *Powder Technology*, 397 (2022) 116993.
- [46] Y. Nie, J. Tang, J. Huang, S. Yu, Y. Li, A Study on internal defects of PREP metallic powders by using x-ray computed tomography, *Materials (Basel)*, 14 (2021) 1177.
- [47] S.M.Q.M. Ramli, N.A. Fadzil, H. Ghazali, P. Viklund, W.F.F.W. Ali, Essential characterization of metal powder for additive manufacturing, *IOP Conference Series: Materials Science and Engineering*, 1173 (2021) 012062.
- [48] T. Abu-Lebdeh, R. Dampney, V. Lamberti, S. Hamoush, Powder packing density and its impact on SLM-based additive manufacturing, in: *TMS 2019 148th Annual Meeting & Exhibition Supplemental Proceedings*, Springer International Publishing, Cham, (2019), 355-367.
- [49] A. Averardi, C. Cola, S.E. Zeltmann, N. Gupta, Effect of particle size distribution on the packing of powder beds: A critical discussion relevant to additive manufacturing, *Materials Today Communications*, 24 (2020) 100964.
- [50] H.W. Mindt, M. Megahed, N.P. Lavery, M.A. Holmes, S.G.R. Brown, Powder bed layer characteristics: The overseen first-order process input, *Metallurgical and Materials Transactions A*, 47 (2016) 3811-3822.

- [51] Y. Zhao, Y. Cui, Y. Hasebe, H. Bian, K. Yamanaka, K. Aoyagi, T. Hagsawa, A. Chiba, Controlling factors determining flowability of powders for additive manufacturing: A combined experimental and simulation study, *Powder Technology*, 393 (2021) 482-493.
- [52] D.A. Augenstein, R. Hogg, Friction factors for powder flow, *Powder Technology*, 10 (1974) 43-49.
- [53] Z.W. Xiang, M.D. Zhang, R. Yan, Q. Yin, K.F. Zhang, Powder-spreading dynamics and packing quality improvement for laser powder bed fusion additive manufacturing, *Powder Technology*, 389 (2021) 278-291.
- [54] J.A. Slotwinski, E.J. Garboczi, Metrology needs for metal additive manufacturing powders, *JOM*, 67 (2015) 538-543.
- [55] T. Cheng, H. Chen, Q. Wei, The role of roller rotation pattern in the spreading process of polymer/short-fiber composite powder in selective laser sintering, *Polymers (Basel)*, 14 (2022) 2345.
- [56] R. Freeman, Measuring the flow properties of consolidated, conditioned and aerated powders: A comparative study using a powder rheometer and a rotational shear cell, *Powder Technology*, 174 (2007) 25-33.
- [57] M. Marcello Vertamatti, P. Carlos Eduardo, N. Maurício David Martins das, Perspective of additive manufacturing selective laser melting in Co-Cr-Mo alloy in the consolidation of dental prosthesis, in: A.D. Leszek (Ed.) *Biomaterials in Regenerative Medicine*, IntechOpen, Rijeka, (2017), Ch. 6.
- [58] J. Clayton, D. Millington-Smith, B. Armstrong, The application of powder rheology in additive manufacturing, *JOM*, 67 (2015) 544-548.
- [59] Z. Snow, R. Martukanitz, S. Joshi, On the development of powder spreadability metrics and feedstock requirements for powder bed fusion additive manufacturing, *Additive Manufacturing*, 28 (2019) 78-86.
- [60] G.E. Amidon, P.J. Meyer, D.M. Mudie, Chapter 10 - Particle, powder, and compact characterization, in: Y. Qiu, Y. Chen, G.G.Z. Zhang, L. Yu, R.V. Mantri (Eds.) *Developing Solid Oral Dosage Forms (Second Edition)*, Academic Press, Boston, (2017), 271-293.
- [61] J.A. Slotwinski, E.J. Garboczi, K.M. Hebenstreit, Porosity measurements and analysis for metal additive manufacturing process control, *J Res Natl Inst Stand Technol*, 119 (2014) 494-528.
- [62] S. Tammam-Williams, H. Zhao, F. Léonard, F. Derguti, I. Todd, P.B. Prangnell, XCT analysis of the influence of melt strategies on defect population in Ti-6Al-4V components manufactured by Selective Electron Beam Melting, *Materials Characterization*, 102 (2015) 47-61.
- [63] R. Cunningham, A. Nicolas, J. Madsen, E. Fodran, E. Anagnostou, M.D. Sangid, A.D. Rollett, Analyzing the effects of powder and post-processing on porosity and properties of electron beam melted Ti-6Al-4V, *Materials Research Letters*, 5 (2017) 516-525.

- [64] A. Mostafaei, A.M. Elliott, J.E. Barnes, F.Z. Li, W.D. Tan, C.L. Cramer, P. Nandwana, M. Chmielus, Binder jet 3D printing process parameters, materials, properties, modeling, and challenges, *Progress in Materials Science*, 119 (2021) 100707.
- [65] A.L. Maximenko, I.D. Olumor, A.P. Maidaniuk, E.A. Olevsky, Modeling of effect of powder spreading on green body dimensional accuracy in additive manufacturing by binder jetting, *Powder Technology*, 385 (2021) 60-68.
- [66] G.K. Meenashisundaram, Z. Xu, M.L.S. Nai, S. Lu, J.S. Ten, J. Wei, Binder jetting additive manufacturing of high porosity 316l stainless steel metal foams, *Materials*, 13 (2020) 3744.
- [67] G. Lee, M. Carrilo, J. McKittrick, D.G. Martin, E.A. Olevsky, Fabrication of ceramic bone scaffolds by solvent jetting 3D printing and sintering: Towards load-bearing applications, *Additive Manufacturing*, 33 (2020) 101107.
- [68] A. Mostafaei, E.L. Stevens, E.T. Hughes, S.D. Biery, C. Huila, M. Chmielus, Powder bed binder jet printed alloy 625: Densification, microstructure and mechanical properties, *Materials & Design*, 108 (2016) 126-135.
- [69] P. Nandwana, A.M. Elliott, D. Siddel, A. Merriman, W.H. Peter, S.S. Babu, Powder bed binder jet 3D printing of Inconel 718: Densification, microstructural evolution and challenges, *Current Opinion in Solid State & Materials Science*, 21 (2017) 207-218.
- [70] Y. Bai, G. Wagner, C.B. Williams, Effect of particle size distribution on powder packing and sintering in binder jetting additive manufacturing of metals, *Journal of Manufacturing Science and Engineering-Transactions of the Asme*, 139 (2017) 081019.
- [71] G.X. Miao, W.C. Du, Z.J. Pei, C. Ma, Binder jetting additive manufacturing of ceramics: analytical and numerical models for powder spreading process, in: 14th ASME International Manufacturing Science and Engineering Conference, Erie, PA, (2019).
- [72] A. Mostafaei, C. Zhao, Y. He, S. Reza Ghiaasiaan, B. Shi, S. Shao, N. Shamsaei, Z. Wu, N. Kouraytem, T. Sun, J. Pauza, J.V. Gordon, B. Webler, N.D. Parab, M. Asherloo, Q. Guo, L. Chen, A.D. Rollett, Defects and anomalies in powder bed fusion metal additive manufacturing, current opinion in solid state and materials science, 26 (2022) 100974.
- [73] A.L. Maximenko, E.A. Olevsky, Pore filling during selective laser melting - assisted additive manufacturing of composites, *Scripta Materialia*, 149 (2018) 75-78.
- [74] A.V. Gusarov, I. Yadroitsev, P. Bertrand, I. Smurov, Heat transfer modelling and stability analysis of selective laser melting, *Applied Surface Science*, 254 (2007) 975-979.
- [75] J. Liu, D.D. Gu, H.Y. Chen, D.H. Dai, H. Zhang, Influence of substrate surface morphology on wetting behavior of tracks during selective laser melting of aluminum-based alloys, *Journal of Zhejiang University-Science A*, 19 (2018) 111-121.

- [76] M. Grasso, A.G. Demir, B. Previtali, B.M. Colosimo, In situ monitoring of selective laser melting of zinc powder via infrared imaging of the process plume, *Robotics and Computer-Integrated Manufacturing*, 49 (2018) 229-239.
- [77] M. Tang, P.C. Pistorius, J.L. Beuth, Prediction of lack-of-fusion porosity for powder bed fusion, *Additive Manufacturing*, 14 (2017) 39-48.
- [78] Q.L. Guo, C. Zhao, L.I. Escano, Z. Young, L.H. Xiong, K. Fezzaa, W. Everhart, B. Brown, T. Sun, L.Y. Chen, Transient dynamics of powder spattering in laser powder bed fusion additive manufacturing process revealed by in-situ high-speed high-energy x-ray imaging, *Acta Materialia*, 151 (2018) 169-180.
- [79] H. Attar, M. Calin, L.C. Zhang, S. Scudino, J. Eckert, Manufacture by selective laser melting and mechanical behavior of commercially pure titanium, *Materials Science and Engineering A-Structural Materials Properties Microstructure and Processing*, 593 (2014) 170-177.
- [80] R. Cunningham, C. Zhao, N. Parab, C. Kantzos, J. Pauza, K. Fezzaa, T. Sun, A.D. Rollett, Keyhole threshold and morphology in laser melting revealed by ultrahigh-speed x-ray imaging, *Science*, 363 (2019) 849-852.
- [81] B. Zhang, Y.T. Li, Q. Bai, Defect formation mechanisms in selective laser melting: A review, *Chinese Journal of Mechanical Engineering*, 30 (2017) 515-527.
- [82] K. Carpenter, A. Tabei, On Residual stress development, prevention, and compensation in metal additive manufacturing, *Materials (Basel)*, 13 (2020) 255.
- [83] C. Li, J.F. Liu, Y.B. Guo, Prediction of residual stress and part distortion in selective laser melting, in: *3rd CIRP Conference on Surface Integrity*, Charlotte, NC, (2016), 171-174.
- [84] B. Blakey-Milner, P. Gradl, G. Snedden, M. Brooks, J. Pitot, E. Lopez, M. Leary, F. Berto, A. du Plessis, Metal additive manufacturing in aerospace: A review, *Materials & Design*, 209 (2021) 110008.
- [85] Y. Liu, L. Blunt, Z. Zhang, H.A. Rahman, F. Gao, X. Jiang, In-situ areal inspection of powder bed for electron beam fusion system based on fringe projection profilometry, *Additive Manufacturing*, 31 (2020) 100940.
- [86] M. Shiomi, K. Osakada, K. Nakamura, T. Yamashita, F. Abe, Residual stress within metallic model made by selective laser melting process, *Cirp Annals-Manufacturing Technology*, 53 (2004) 195-198.
- [87] P. Mercelis, J.P. Kruth, Residual stresses in selective laser sintering and selective laser melting, *Rapid Prototyping Journal*, 12 (2006) 254-265.
- [88] C.L. Qiu, H.X. Chen, Q. Liu, S. Yue, H.M. Wang, On the solidification behaviour and cracking origin of a nickel-based superalloy during selective laser melting, *Materials Characterization*, 148 (2019) 330-344.

- [89] D. Grange, J.D. Bartout, B. Macquaire, C. Colin, Processing a non-weldable nickel-base superalloy by selective laser melting: role of the shape and size of the melt pools on solidification cracking, *Materialia*, 12 (2020) 100686.
- [90] A. Levy, A. Miriyev, A. Elliott, S.S. Babu, N. Frage, Additive manufacturing of complex-shaped graded TiC/steel composites, *Materials & Design*, 118 (2017) 198-203.
- [91] L.N. Carter, M.M. Attallah, R.C. Reed, Laser powder bed fabrication of Nickel-base superalloys: Influence of parameters; characterisation, quantification and mitigation of cracking, in: 12th International Symposium on Superalloys, Seven Springs, PA, (2012) 577-586.
- [92] J. Platl, D. Rainer, H. Leitner, C. Turk, F. Galbusera, A.G. Demir, B. Previtali, R. Schnitzer, Potential causes for cracking of a laser powder bed fused carbon-free FeCoMo alloy, *BHM Berg- und Hüttenmännische Monatshefte*, 167 (2022) 325-331.
- [93] I.D. Olumor, G. Lee, E. Olevsky, Effect of process route on powder three-dimensional-printing of metal powders, *Rapid Prototyping Journal*, 27 (2021) 399-406.
- [94] Y.M. Fouda, A.E. Bayly, A DEM study of powder spreading in additive layer manufacturing, *Granular Matter*, 22 (2019) 10.
- [95] S. Haeri, Optimisation of blade type spreaders for powder bed preparation in additive manufacturing using DEM simulations, *Powder Technology*, 321 (2017) 94-104.
- [96] E.J.R. Parteli, T. Poschel, Particle-based simulation of powder application in additive manufacturing, *Powder Technology*, 288 (2016) 96-102.
- [97] S. Beitz, R. Uerlich, T. Bokelmann, A. Diener, T. Vietor, A. Kwade, Influence of powder deposition on powder bed and specimen properties, *Materials*, 12 (2019) 297.
- [98] L.E. Silbert, Jamming of frictional spheres and random loose packing, *Soft Matter*, 6 (2010) 2918-2924.
- [99] R.K. Enneti, K.C. Prough, Effect of binder saturation and powder layer thickness on the green strength of the binder jet 3D printing (BJ3DP) WC-12%Co powders, *International Journal of Refractory Metals and Hard Materials*, 84 (2019) 104991.
- [100] A. Mostafaei, A.M. Elliott, J.E. Barnes, F. Li, W. Tan, C.L. Cramer, P. Nandwana, M. Chmielus, Binder jet 3D printing—process parameters, materials, properties, modeling, and challenges, *Progress in Materials Science*, 119 (2021) 100707.
- [101] R.M. German, Prediction of sintered density for bimodal powder mixtures, *Metallurgical Transactions A*, 23 (1992) 1455-1465.
- [102] U. Hassler, D. Gruber, O. Hentschel, F. Sukowski, T. Grulich, L. Seifert, In-situ monitoring and defect detection for laser metal deposition by using infrared thermography, *Physics Procedia*, 83 (2016) 1244-1252.

- [103] A.R. Nassar, M.A. Gundermann, E.W. Reutzler, P. Guerrier, M.H. Krane, M.J. Weldon, Formation processes for large ejecta and interactions with melt pool formation in powder bed fusion additive manufacturing, *Scientific Reports*, 9 (2019) 5038.
- [104] M. Qu, Q. Guo, L.I. Escano, A. Nabaa, S.M.H. Hojjatzadeh, Z.A. Young, L. Chen, Controlling process instability for defect lean metal additive manufacturing, *Nature Communications*, 13 (2022) 1079.
- [105] O.B. Holzmond, X. Li, In situ real time defect detection of 3D printed parts, *Additive manufacturing*, 17 (2017) 135-142.
- [106] D. Höfflin, C. Sauer, A. Schiffler, J. Hartmann, Process monitoring using synchronized path infrared thermography in PBF-LB/M, *Sensors*, 22 (2022) 5943.
- [107] P.M. Cordero, J. Mireles, S. Ridwan, R.B. Wicker, Evaluation of monitoring methods for electron beam melting powder bed fusion additive manufacturing technology, *Progress in Additive Manufacturing*, 2 (2017) 1-10.
- [108] F. Zhang, L. Chen, D. Bhattacharyya, In situ synchrotron and neutron characterization of additively manufactured alloys, *JOM*, 73 (2021) 174-176.
- [109] T. Hatsui, H. Graafsma, X-ray imaging detectors for synchrotron and XFEL sources, *IUCrJ*, 2 (2015) 371-383.
- [110] S.M.H. Hojjatzadeh, N.D. Parab, W. Yan, Q. Guo, L. Xiong, C. Zhao, M. Qu, L.I. Escano, X. Xiao, K. Fezzaa, W. Everhart, T. Sun, L. Chen, Pore elimination mechanisms during 3D printing of metals, *Nature Communication*, 10 (2019) 3088.
- [111] K. An, L. Yuan, L. Dial, I. Spinelli, A.D. Stoica, Y. Gao, Neutron residual stress measurement and numerical modeling in a curved thin-walled structure by laser powder bed fusion additive manufacturing, *Materials & Design*, 135 (2017) 122-132.
- [112] T. Mukherjee, T. DebRoy, Mitigation of lack of fusion defects in powder bed fusion additive manufacturing, *Journal of Manufacturing Processes*, 36 (2018) 442-449.
- [113] M. Jackson, A. Deshpande, A. Kim, F. Pfefferkorn, A study of particle size metrics using non-spherical feedstock for metal additive manufacturing, *Procedia Manufacturing*, 53 (2021) 519-524.
- [114] R.M. German, Particle packing characteristics, Metal Powder Industries Federation, NJ-USA, (1989).
- [115] R.K. McGeary, Mechanical packing of spherical particles, *Journal of the American Ceramic Society*, 44 (1961) 513-522.
- [116] G. Egger, P.E. Gyax, R. Glardon, N. Karapatis, Optimization of powder layer density in selective laser sintering, in, *International Solid Freeform Fabrication Symposium Austin-TX*, (1999) 255-263.

- [117] H. Gong, K. Rafi, T.L. Starr, B.E. Stucker, The effects of processing parameters on defect regularity in ti-6al-4v parts fabricated by selective laser melting and electron beam melting, in, Proceedings of the Solid Freeform Fabrication Symposium Austin-TX, (2013) 424-439.
- [118] P.A. Kobryn, E.H. Moore, S.L. Semiatin, The effect of laser power and traverse speed on microstructure, porosity, and build height in laser-deposited Ti-6Al-4V, Scripta Materialia, 43 (2000) 299-305.
- [119] D. Hagedorn-Hansen, M.B. Bezuidenhout, D.M. Dimitrov, G.A. Oosthuizen, The effects of selective laser melting scan strategies on deviation of hybrid parts, South African Journal of Industrial Engineering, 28 (2017) 200-212.
- [120] A. Gaikwad, R.J. Williams, H. de Winton, B.D. Bevans, Z. Smoqi, P. Rao, P.A. Hooper, Multi phenomena melt pool sensor data fusion for enhanced process monitoring of laser powder bed fusion additive manufacturing, Materials & Design, 221 (2022) 110919.
- [121] P. Yadav, O. Rigo, C. Arvieu, E. Le Guen, E. Lacoste, In situ monitoring systems of the slm process: On the need to develop machine learning models for data processing, Crystals, 10 (2020) 524.
- [122] L. Scime, J. Beuth, A multi-scale convolutional neural network for autonomous anomaly detection and classification in a laser powder bed fusion additive manufacturing process, Additive Manufacturing, 24 (2018) 273-286.
- [123] A. Butscher, M. Bohner, N. Doebelin, L. Galea, O. Loeffel, R. Muller, Moisture based three-dimensional printing of calcium phosphate structures for scaffold engineering, Acta Biomaterialia, 9 (2013) 5369-5378.
- [124] B.R. Utela, D. Storti, R.L. Anderson, M. Ganter, Development process for custom three-dimensional printing (3dp) material systems, Journal of Manufacturing Science and Engineering-Transactions of the Asme, 132 (2010) 011008.
- [125] W. Zhang, R. Melcher, N. Travitzky, R.K. Bordia, P. Greil, Three-dimensional printing of complex-shaped alumina/glass composites, Advanced Engineering Materials, 11 (2009) 1039-1043.
- [126] M. Castilho, B. Gouveia, I. Pires, J. Rodrigues, M. Pereira, The role of shell/core saturation level on the accuracy and mechanical characteristics of porous calcium phosphate models produced by 3D printing, Rapid Prototyping Journal, 21 (2015) 43-55.
- [127] M. Vaezi, C.K. Chua, Effects of layer thickness and binder saturation level parameters on 3D printing process, International Journal of Advanced Manufacturing Technology, 53 (2011) 275-284.
- [128] H. Miyajima, S.S. Zhang, L. Yang, A new physics-based model for equilibrium saturation determination in binder jetting additive manufacturing process, International Journal of Machine Tools & Manufacture, 124 (2018) 1-11.

- [129] Y.Y. Wang, P.F. Jia, W.D. Yang, K. Peng, S.X. Zhang, Simulation and experimental study of binder droplet infiltration in 3DP technology, *Modern Physics Letters B*, 32 (2018) 1850272.
- [130] A. Gaikwad, T. Chang, B. Giera, N. Watkins, S. Mukherjee, A. Pascall, D. Stobbe, P. Rao, In-process monitoring and prediction of droplet quality in droplet-on-demand liquid metal jetting additive manufacturing using machine learning, *Journal of Intelligent Manufacturing*, 33 (2022) 2093-2117.
- [131] J.M. Ravalji, S.J. Raval, Review of quality issues and mitigation strategies for metal powder bed fusion, *Rapid Prototyping Journal*, ahead-of-print (2022) 143-149.
- [132] L. Löber, C. Flache, R. Petters, U. Kühn, J. Eckert, Comparison of different post processing technologies for SLM generated 316l steel parts, *Rapid Prototyping Journal*, 19 (2013) 173-179.
- [133] Y. Kaynak, O. Kitay, The effect of post-processing operations on surface characteristics of 316L stainless steel produced by selective laser melting, *Additive Manufacturing*, 26 (2019) 84-93.
- [134] N.T. Aboulkhair, M. Simonelli, L. Parry, I. Ashcroft, C. Tuck, R. Hague, 3D printing of Aluminium alloys: Additive manufacturing of Aluminium alloys using selective laser melting, *Progress in Materials Science*, 106 (2019) 100578.
- [135] B. van Wachem, K. Thalberg, J. Remmelgas, I. Niklasson-Björn, Simulation of dry powder inhalers: Combining micro-scale, meso-scale and macro-scale modeling, *AIChE Journal*, 63 (2017) 501-516.
- [136] G.B. Less, J.H. Seo, S. Han, A.M. Sastry, J. Zausch, A. Latz, S. Schmidt, C. Wieser, D. Kehrwald, S. Fell, Micro-scale modeling of Li-Ion batteries: Parameterization and validation, *Journal of The Electrochemical Society*, 159 (2012) A697.
- [137] B.A. Bednarczyk, B. Stier, J.W. Simon, S. Reese, E.J. Pineda, Meso- and micro-scale modeling of damage in plain weave composites, *Composite Structures*, 121 (2015) 258-270.
- [138] J. Sjöström, A. Durga, G. Lindwall, Linkage of macro- and microscale modeling tools for additive manufacturing of steels, *Frontiers in Materials*, 9 (2022) 797226.
- [139] Y.C. Zhang, G. Guillemot, M. Bernacki, M. Bellet, Macroscopic thermal finite element modeling of additive metal manufacturing by selective laser melting process, *Computer Methods in Applied Mechanics and Engineering*, 331 (2018) 514-535.
- [140] H. Kruggel-Emden, E. Simsek, S. Rickelt, S. Wirtz, V. Scherer, Review and extension of normal force models for the discrete element method, *Powder Technology*, 171 (2007) 157-173.
- [141] C.J. Coetzee, Calibration of the discrete element method and the effect of particle shape, *Powder Technology*, 297 (2016) 50-70.
- [142] L. Kempton, D. Pinson, S. Chew, P. Zulli, A.B. Yu, Simulation of macroscopic deformation using a sub-particle DEM approach, *Powder Technology*, 223 (2012) 19-26.

- [143] E.A. Olevsky, J. Ma, J.C. LaSalvia, M.A. Meyers, Densification of porous bodies in a granular pressure-transmitting medium, *Acta Materialia*, 55 (2007) 1351-1366.
- [144] S. Bose, S. Vahabzadeh, A. Bandyopadhyay, Bone tissue engineering using 3D printing, *Materials Today*, 16 (2013) 496-504.
- [145] Y. Wen, S. Xun, M. Haoye, S. Baichuan, C. Peng, L. Xuejian, Z. Kaihong, Y. Xuan, P. Jiang, L. Shibi, 3D printed porous ceramic scaffolds for bone tissue engineering: a review, *Biomaterials Science*, 5 (2017) 1690-1698.
- [146] X. Du, S. Fu, Y. Zhu, 3D printing of ceramic-based scaffolds for bone tissue engineering: an overview, *Journal of Materials Chemistry B*, 6 (2018) 4397-4412.
- [147] A. Yegyan Kumar, J. Wang, Y. Bai, S.T. Huxtable, C.B. Williams, Impacts of process-induced porosity on material properties of copper made by binder jetting additive manufacturing, *Materials & Design*, 182 (2019) 108001.
- [148] M. Salehi, S. Maleksaeedi, M.A.B. Sapari, M.L.S. Nai, G.K. Meenashisundaram, M. Gupta, Additive manufacturing of magnesium–zinc–zirconium (ZK) alloys via capillary-mediated binderless three-dimensional printing, *Materials & Design*, 169 (2019) 107683.
- [149] Y. Shanjani, J.N. De Croos, R.M. Pilliar, R.A. Kandel, E. Toyserkani, Solid freeform fabrication and characterization of porous calcium polyphosphate structures for tissue engineering purposes, *J Biomed Mater Res B Appl Biomater*, 93 (2010) 510-519.
- [150] R. Chumnanklang, T. Panyathanmaporn, K. Sitthiseripratip, J. Suwanprateeb, 3D printing of hydroxyapatite: Effect of binder concentration in pre-coated particle on part strength, *Materials Science and Engineering: C*, 27 (2007) 914-921.
- [151] H. Kakisawa, K. Minagawa, K. Ida, K. Maekawa, K. Halada, Dense P/M component produced by solid freeform fabrication (SFF), *Materials Transactions*, 46 (2005) 2574-2581.
- [152] R.M. German, *Sintering Theory and Practice*, Wiley NJ-USA, (1996).
- [153] T. Do, T.J. Bauder, H. Suen, K. Rego, J. Yeom, P. Kwon, Additively manufactured full-density stainless steel 316l with binder jet printing, in: *ASME 2018 13th International Manufacturing Science and Engineering Conference*, 1 (2018).
- [154] Y. Wang, Y.F. Zhao, Investigation of sintering shrinkage in binder jetting additive manufacturing process, *Procedia Manufacturing*, 10 (2017) 779-790.
- [155] M. Ziaee, E.M. Tridas, N.B. Crane, Binder-jet printing of fine stainless steel powder with varied final density, *JOM*, 69 (2017) 592-596.
- [156] A. Kumar, Y. Bai, A. Eklund, C.B. Williams, Effects of hot isostatic pressing on copper parts fabricated via binder jetting, *Procedia Manufacturing*, 10 (2017) 935-944.

- [157] A. Mostafaei, P. Rodriguez De Vecchis, I. Nettleship, M. Chmielus, Effect of powder size distribution on densification and microstructural evolution of binder-jet 3D-printed alloy 625, *Materials & Design*, 162 (2019) 375-383.
- [158] Z.C. Cordero, D.H. Siddel, W.H. Peter, A.M. Elliott, Strengthening of ferrous binder jet 3D printed components through bronze infiltration, *Additive Manufacturing*, 15 (2017) 87-92.
- [159] B. Derby, Additive manufacture of ceramics components by inkjet printing, *Engineering*, 1 (2015) 113-123.
- [160] K. Lu, W.T. Reynolds, 3DP process for fine mesh structure printing, *Powder Technology*, 187 (2008) 11-18.
- [161] M. Asadi-Eydivand, M. Solati-Hashjin, A. Farzad, N.A. Abu Osman, Effect of technical parameters on porous structure and strength of 3D printed calcium sulfate prototypes, *Robotics and Computer-Integrated Manufacturing*, 37 (2016) 57-67.
- [162] E. Sachs, M. Cima, J. Cornie, Three-dimensional printing: Rapid tooling and prototypes directly from a CAD model, *CIRP Annals*, 39 (1990) 201-204.
- [163] S. Haeri, Y. Wang, O. Ghita, J. Sun, Discrete element simulation and experimental study of powder spreading process in additive manufacturing, *Powder Technology*, 306 (2017) 45-54.
- [164] Q. Han, H. Gu, R. Setchi, Discrete element simulation of powder layer thickness in laser additive manufacturing, *Powder Technology*, 352 (2019) 91-102.
- [165] Z. Xiang, M. Yin, Z. Deng, X. Mei, G. Yin, Simulation of forming process of powder bed for additive manufacturing, *Journal of Manufacturing Science and Engineering*, 138 (2016) 081002.
- [166] Y. Lee, A.K. Gurnon, D. Bodner, S. Simunovic, Effect of particle spreading dynamics on powder bed quality in metal additive manufacturing, *Integrating Materials and Manufacturing Innovation*, 9 (2020) 410-422.
- [167] J.T. Zhang, Y.Q. Tan, T. Bao, Y.L. Xu, X.W. Xiao, S.Q. Jiang, Discrete element simulation of the effect of roller-spreading parameters on powder-bed density in additive manufacturing, *Materials*, 13 (2020).
- [168] D.M. Mueth, Measurements of particle dynamics in slow, dense granular couette flow, *Phys Rev E Stat Nonlin Soft Matter Phys*, 67 (2003) 011304.
- [169] C.H. Rycroft, K. Kamrin, M.Z. Bazant, Assessing continuum postulates in simulations of granular flow, *Journal of the Mechanics and Physics of Solids*, 57 (2009) 828-839.
- [170] D. Howell, R.P. Behringer, C. Veje, Stress Fluctuations in a 2D granular couette experiment: A continuous transition, *Physical Review Letters*, 82 (1999) 5241-5244.

- [171] L.C. Li, G.E. Peck, The effect of moisture content on the compression properties of maltodextrins, *J Pharm Pharmacol*, 42 (1990) 272-275.
- [172] H. Miyajima, M. Orth, J.M. Akbar, L. Yang, Process development for green part printing using binder jetting additive manufacturing, *Frontiers of Mechanical Engineering*, 13 (2018) 504-512.
- [173] X. Xu, S. Meteyer, N. Perry, Y.F. Zhao, Energy consumption model of binder-jetting additive manufacturing processes, *International Journal of Production Research*, 53 (2015) 7005-7015.
- [174] I.D. Olumor, L. Geuntak, E. Olevsky, Effect of process route on powder three-dimensional-printing of metal powders, *Rapid Prototyping Journal*, 27 (2021) 399-406.
- [175] P. Ferro, R. Meneghello, G. Savio, F. Berto, A modified volumetric energy density-based approach for porosity assessment in additive manufacturing process design, *International Journal of Advanced Manufacturing Technology*, 110 (2020) 1911-1921.
- [176] J.L. Bartlett, F.M. Heim, Y.V. Murty, X. Li, In situ defect detection in selective laser melting via full-field infrared thermography, *Additive Manufacturing*, 24 (2018) 595-605.
- [177] T. Craeghs, S. Clijsters, J.P. Kruth, F. Bechmann, M.C. Ebert, Detection of process failures in layerwise laser melting with optical process monitoring, *Physics Procedia*, 39 (2012) 753-759.
- [178] J.L. Bartlett, X. Li, An overview of residual stresses in metal powder bed fusion, *Additive Manufacturing*, 27 (2019) 131-149.
- [179] K.R. Riedmuller, M. Liewald, L. Kertesz, Manufacturing of composite and hybrid materials by semi solid forming, in: *12th International Conference on Semi-Solid Processing of Alloys and Composites (S2P 2012)*, Cape Town, SOUTH AFRICA, (2012) 89-94.
- [180] J. Liu, J. Li, C.Y. Xu, Interaction of the cutting tools and the ceramic-reinforced metal matrix composites during micro-machining: A review, *Cirp Journal of Manufacturing Science and Technology*, 7 (2014) 55-70.
- [181] D. Bandhu, A. Thakur, R. Purohit, R.K. Verma, K. Abhishek, Characterization & evaluation of Al7075 MMCs reinforced with ceramic particulates and influence of age hardening on their tensile behavior, *Journal of Mechanical Science and Technology*, 32 (2018) 3123-3128.
- [182] S.a. B, C. G, B. C, P. T, S. R, Production and characterization of mechanical and microstructural behaviour of friction stir welded Al6063 composites reinforced with Gr/B4C/SiC particles, *Journal of Ceramic Processing Research*, 19 (2018) 69-74.
- [183] J. Yang, J.L. Guo, A.G. Mikos, C. He, G. Cheng, Material processing and design of biodegradable metal matrix composites for biomedical applications, *Annals of Biomedical Engineering*, 46 (2018) 1229-1240.
- [184] S.P. Rawal, Metal-matrix composites for space applications, *JOM*, 53 (2001) 14-17.

- [185] S.A. Sajjadi, H.R. Ezatpour, H. Beygi, Microstructure and mechanical properties of Al–Al₂O₃ micro and nano composites fabricated by stir casting, *Materials Science and Engineering: A*, 528 (2011) 8765-8771.
- [186] C. Suryanarayana, N. Al-Aqeeli, Mechanically alloyed nanocomposites, *Progress in Materials Science*, 58 (2013) 383-502.
- [187] V. Sivananth, S. Vijayarangan, N. Rajamanickam, Evaluation of fatigue and impact behavior of titanium carbide reinforced metal matrix composites, *Materials Science and Engineering: A*, 597 (2014) 304-313.
- [188] D. Herzog, V. Seyda, E. Wycisk, C. Emmelmann, Additive manufacturing of metals, *Acta Materialia*, 117 (2016) 371-392.
- [189] Y. Lakhdar, C. Tuck, J. Binner, A. Terry, R. Goodridge, Additive manufacturing of advanced ceramic materials, *Progress in Materials Science*, 116 (2021) 100736.
- [190] M. Gelinsky, T. Ahlfeld, Chapter 10 - Additive manufacturing of polymers and ceramics for tissue engineering applications, in: A.R. Boccaccini, P.X. Ma, L. Liverani (Eds.) *Tissue Engineering Using Ceramics and Polymers (Third Edition)*, Woodhead Publishing, (2022) 385-406.
- [191] D.A. Türk, R. Kussmaul, M. Zogg, C. Klahn, B. Leutenecker-Twelsiek, M. Meboldt, Composites part production with additive manufacturing technologies, *Procedia CIRP*, 66 (2017) 306-311.
- [192] S.L. Sing, L.P. Lam, D.Q. Zhang, Z. Liu, C.K. Chua, Interfacial characterization of SLM parts in multi-material processing: Intermetallic phase formation between AlSi10Mg and C18400 copper alloy, *Materials Characterization*, 107 (2015) 220-227.
- [193] C.K. Chua, K.F. Leong, *3D Printing and Additive Manufacturing: Principles and applications*, World Scientific publishing, NJ-USA, (2014).
- [194] F. Zok, F.F. Lange, J.R. Porter, Packing density of composite powder mixtures, *Journal of the American Ceramic Society*, 74 (1991) 1880-1885.
- [195] J. von Seckendorff, K. Achterhold, F. Pfeiffer, R. Fischer, O. Hinrichsen, Experimental and numerical analysis of void structure in random packed beds of spheres, *Powder Technology*, 380 (2021) 613-628.
- [196] V. Lampitella, M. Trofa, A. Astarita, G. D'Avino, Discrete element method analysis of the spreading mechanism and its influence on powder bed characteristics in additive manufacturing, *Micromachines*, 12 (2021) 392.
- [197] T. Roessler, A. Katterfeld, Scaling of the angle of repose test and its influence on the calibration of DEM parameters using upscaled particles, *Powder Technology*, 330 (2018) 58-66.

- [198] Z. Yan, S.K. Wilkinson, E.H. Stitt, M. Marigo, Discrete element modelling (DEM) input parameters: understanding their impact on model predictions using statistical analysis, *Computational Particle Mechanics*, 2 (2015) 283-299.
- [199] R.M. German, Coordination number changes during powder densification, *Powder Technology*, 253 (2014) 368-376.
- [200] A.S. Sangani, A. Acrivos, Slow flow through a periodic array of spheres, *International Journal of Multiphase Flow*, 8 (1982) 343-360.
- [201] Y. Liu, C. Liu, W. Liu, Y. Ma, S. Tang, C. Liang, Q. Cai, C. Zhang, Optimization of parameters in laser powder deposition AlSi10Mg alloy using Taguchi method, *Optics & Laser Technology*, 111 (2019) 470-480.
- [202] R.C. Van Nostrand, Design of experiments using the Taguchi approach: 16 steps to product and process improvement, *Technometrics*, 44 (2002) 289-289.
- [203] N. Singh, R. Ummethala, P.S. Karamched, R. Sokkalingam, V. Gopal, G. Manivasagam, K.G. Prashanth, Spark plasma sintering of Ti6Al4V metal matrix composites: Microstructure, mechanical and corrosion properties, *Journal of Alloys and Compounds*, 865 (2021) 158875.
- [204] C. Manière, E. Torresani, E.A. Olevsky, Simultaneous spark plasma sintering of multiple complex shapes, *Materials (Basel)*, 12 (2019) 557.
- [205] M. Diego, C. Flaviana, K. Manickavasagam, C. Riccardo, A. Elisa Paola, B. Sara, U. Daniele, P. Matteo, F. Paolo, Additive manufacturing of Al alloys and Aluminium matrix composites (AMCs), in: A.M. Waldemar (Ed.) *Light Metal Alloys Applications*, IntechOpen, Rijeka, (2014) Ch. 1.
- [206] S. Kumar, J.P. Kruth, Composites by rapid prototyping technology, *Materials & Design*, 31 (2010) 850-856.
- [207] W.E. Frazier, Metal additive manufacturing: A review, *Journal of Materials Engineering and Performance*, 23 (2014) 1917-1928.
- [208] I.D. Olumor, A.L. Maximenko, E.A. Olevsky, Effect of laser dwell time on pore elimination in powder bed fusion of metal matrix composites: Experimentally validated modeling, *Journal of Materials Research and Technology*, 21 (2022) 4994-5003.
- [209] I.M. Anne, L.B. Jacqueline, On the role of interfacial reactions, dissolution and secondary precipitation during the laser additive manufacturing of metal matrix composites: A review, in: V.S. Igor (Ed.) *New Trends in 3D Printing*, IntechOpen, Rijeka, (2016) Ch. 9.
- [210] X.-B. Liu, S.-H. Shi, J. Guo, G.-Y. Fu, M.-D. Wang, Microstructure and wear behavior of γ /Al₄C₃/TiC/CaF₂ composite coating on γ -TiAl intermetallic alloy prepared by Nd:YAG laser cladding, *Applied Surface Science*, 255 (2009) 5662-5668.

- [211] P. Xu, C. Lin, C. Zhou, X. Yi, Wear and corrosion resistance of laser cladding AISI 304 stainless steel/Al₂O₃ composite coatings, *Surface and Coatings Technology*, 238 (2014) 9-14.
- [212] N. Li, W. Liu, Y. Wang, Z. Zhao, T. Yan, G. Zhang, H. Xiong, Laser additive manufacturing on metal matrix composites: A review, *Chinese Journal of Mechanical Engineering*, 34 (2021) 38.
- [213] J. Dutta Majumdar, A. Kumar, L. Li, Direct laser cladding of SiC dispersed AISI 316L stainless steel, *Tribology International*, 42 (2009) 750-753.
- [214] R. Anandkumar, A. Almeida, R. Vilar, Microstructure and sliding wear resistance of an Al–12wt.% Si/TiC laser clad coating, *Wear*, 282-283 (2012) 31-39.
- [215] K.H. Lo, F.T. Cheng, C.T. Kwok, H.C. Man, Improvement of cavitation erosion resistance of AISI 316 stainless steel by laser surface alloying using fine WC powder, *Surface and Coatings Technology*, 165 (2003) 258-267.
- [216] F. Chang, D. Gu, D. Dai, P. Yuan, Selective laser melting of in-situ Al₄SiC₄+SiC hybrid reinforced Al matrix composites: Influence of starting SiC particle size, *Surface and Coatings Technology*, 272 (2015) 15-24.
- [217] L. Emanuelli, A. Molinari, M. Pellizzari, Interaction between WC and Inconel 625 under solid and liquid state sintering conditions, *Metals*, 11 (2021) 666.
- [218] P. Priya, B. Mercer, S. Huang, M. Aboukhatwa, L. Yuan, S. Chaudhuri, Towards prediction of microstructure during laser based additive manufacturing process of Co-Cr-Mo powder beds, *Materials & Design*, 196 (2020) 109117.
- [219] S.S. Babu, S.A. David, R.P. Martukanitz, K.D. Parks, Toward prediction of microstructural evolution during laser surface alloying, *Metallurgical and Materials Transactions A*, 33 (2002) 1189-1200.
- [220] F.T. Cheng, C.T. Kwok, H.C. Man, Laser surfacing of S31603 stainless steel with engineering ceramics for cavitation erosion resistance, *Surface and Coatings Technology*, 139 (2001) 14-24.
- [221] J.C. Betts, B.L. Mordike, M. Grech, Characterisation, wear and corrosion testing of laser-deposited AISI 316 reinforced with ceramic particles, *Surface Engineering*, 26 (2010) 21-29.
- [222] A.D. Warren, I.J. Griffiths, P.E.J. Flewitt, Precipitation within localised chromium-enriched regions in a Type 316H austenitic stainless steel, *J Mater Sci*, 53 (2018) 6183-6197.
- [223] A. Emamian, M. Alimardani, A. Khajepour, Correlation between temperature distribution and in situ formed microstructure of Fe–TiC deposited on carbon steel using laser cladding, *Applied Surface Science*, 258 (2012) 9025-9031.
- [224] I.V. Shishkovskii, A.G. Makarenko, A.L. Petrov, Conditions for SHS of intermetallic compounds with selective laser sintering of powdered compositions, *Combustion, Explosion and Shock Waves*, 35 (1999) 166-170.

- [225] T. Dash, B.B. Nayak, Preparation of WC–W₂C composites by arc plasma melting and their characterisations, *Ceramics International*, 39 (2013) 3279-3292.
- [226] L. Sun, X. Ji, L. Zhao, W. Zhai, L. Xu, H. Dong, Y. Liu, J. Peng, First principles investigation of binary chromium carbides Cr₇C₃, Cr₃C₂ and Cr₂₃C₆: Electronic structures, mechanical properties and thermodynamic properties under pressure, *Materials (Basel)*, 15 (2022).
- [227] A.T. Olanipekun, M. Nthabiseng, O.O. Ayodele, M.R. Mphahlele, B.M. Mampuya, P.A. Olubambi, Datasets on the measurement of mechanical properties of ferrite and austenite constitutive phases using nanoindentation and micro hardness techniques, *Data in Brief*, 27 (2019) 104551.
- [228] F. Almeida Costa Oliveira, B. Granier, J.-M. Badie, J. Cruz Fernandes, L. Guerra Rosa, N. Shohoji, Synthesis of tungsten sub-carbide W₂C from graphite/tungsten powder mixtures by eruptive heating in a solar furnace, *International Journal of Refractory Metals and Hard Materials*, 25 (2007) 351-357.
- [229] G. Liu, D. Du, K. Wang, Z. Pu, B. Chang, Epitaxial growth behavior and stray grains formation mechanism during laser surface re-melting of directionally solidified nickel-based superalloys, *Journal of Alloys and Compounds*, 853 (2021) 157325.
- [230] R. Casati, J. Lemke, M. Vedani, Microstructure and fracture behavior of 316L austenitic stainless steel produced by selective laser melting, *Journal of Materials Science & Technology*, 32 (2016) 738-744.
- [231] M. Rasch, F. Huber, L. Butzhammer, C. Merz, M. Schmidt, Effect of scanning sequence on subsurface porosity at laser beam melting in powder bed, in: *Rapid.Tech – International Trade Show & Conference for Additive Manufacturing*, (2017) 255-268.